The Dissertation Committee for Junhao Zhou Certifies that this is the approved version of the following dissertation:

Interactions of Organic-Rich Shale with Water-Based Fluids

Committee:

Mukul M. Sharma, Supervisor

Benny D. Freeman, Co-Supervisor

David A. DiCarlo

Chun Huh

Kishore K. Mohanty

Martin E. Chenevert

Interactions of Organic-Rich Shale with Water-Based Fluids

by

Junhao Zhou, B.A.; M.S.E.

Dissertation

Presented to the Faculty of the Graduate School of

The University of Texas at Austin

in Partial Fulfillment

of the Requirements

for the Degree of

Doctor of Philosophy

The University of Texas at Austin

August 2015

Dedication

I dedicate this dissertation to my mother Aifang Wang, father Daming Zhou and wife Tiantian Zhang for being by my side all these years.

Acknowledgements

This dissertation could not have been completed without the help from a number of people. First and foremost, I would like to thank my supervisor Dr. Mukul Sharma for the opportunity to work on the topic of shale characterization. His guidance and encouragement have made this journey very fruitful and enjoyable. I have learned a lot from him as a scholar and as a person during my graduate studies. I also want to express my gratitude to Dr. Martin Chenevert for his contributions to this work. I am very grateful to my co-supervisor Dr. Benny Freeman, and my other committee members Dr. David DiCarlo, Dr. Chun Huh and Dr. Kishore Mohanty for their valuable feedback and comments on this dissertation.

I am very thankful to Dr. Hugh Daigle for his help with the gas adsorption and NMR experiments and Dr. Jon Holder for his support with the acoustic wave velocity and indentation measurements. I also want to acknowledge Glen Baum, Gary Miscoe, Daryl Nygaard, Jin Lee, Frankie Hart, Cheryl Kruzie, Lydia Pruneda, Carol Assadourian, Roger Terzian, and John Cassibry for their technical, administrative and IT assistance. Many thanks go to RPSEA (Project # 09122-41) and the Hydraulic Fracturing and Sand Control JIP at the University of Texas at Austin for the financial support of this work.

I want to thank the past and present shale group members for their company. Mac Pedlow, Evan Gilmore, JP Gips, Chang Min Jung, Weiwei Wu, Pratik Kakkar, Murtada Al Tammar, Peng Zhang and Rod Russell are wonderful colleagues and friends. I am also indebted to many friends who have made my time at UT a memorable experience. In particular, I want to thank Jongsoo Hwang, Chris Blyton, Haryanto Adiguna, Xiaoyan Shi, Bo Gao, Peila Chen, Xianhui Kong, Wei Yu, Kan Wu, Wei Li, Haiyan Zhou, Liangping Li, Ming Gu, Qing Tao, Guangwei Ren, Li Ji, Kaimin Yue, Zhitao Li, Yuhao

Sun, Weiwei Wang, Xiangyu Liu, Chunbi Jiang, Tianbo Liang, Pengpeng Qi, Shan Huang, Haotian Wang, Andrew Chiang, and Qinshan Yang. Also, I am very grateful to Shun-Yang Lee for the friendship since our college days at Bard.

Finally, none of this could have been possible without my wife Tiantian Zhang. She is my soulmate and a great listener and is always there for me. I cannot thank her enough for her understanding and sacrifices throughout these years.

Interactions of Organic-Rich Shale with Water-Based Fluids

Junhao Zhou, PhD

The University of Texas at Austin, 2015

Supervisor: Mukul M. Sharma

Co-Supervisor: Benny D. Freeman

The success of horizontal drilling and hydraulic fracturing has enabled the economic production of hydrocarbons from shale formations. However, wellbore instability and proppant embedment remain two major concerns during drilling and completion of wellbores in unconventional shale reservoirs. Both issues are largely controlled by shale-fluid interactions. Understanding the interactions of organic-rich shale with water-based fluids is the first step towards selecting appropriate drilling and fracturing fluids. The main objective of this study is to investigate the interactions of organic-rich shale with various water-based fluids.

A series of measurements were performed to determine shale mineralogy, native water activity, fluid content, pore size distribution, Brinell hardness, Young's modulus, P-wave and S-wave velocities. It was shown that XRD and XRF yield consistent shale mineralogy, allowing us to make rapid determinations of shale mineralogy. Large variations in mineralogy were observed with shale samples from different formations. Even samples from the same well and at adjacent depths exhibited very different mineralogical makeup. The NMR T_1/T_2 ratio and T_2 secular relaxation were used to distinguish pore fluids of different viscosity in pores of various sizes. A good correlation was established between the clay content and the amount of low-viscosity fluid in small

pores, indicating that the water-saturated microporosity was in clay minerals. Combined N_2GA and MICP measurements showed that a majority of the shale pores were found to be in the micropore to mesopore size range.

Changes in shale mechanical properties were measured before and after shale samples came into contact with water-based fluids. The small degree of swelling and mechanical properties changes suggests that these organic-rich shales were only slightly sensitive to fluid exposure. Anisotropic swelling perpendicular and parallel to bedding planes could be due to the clay fabric anisotropy. The importance of using preserved shale samples was clearly demonstrated. Temperature and fluid pH were found to have significant impact on the reduction in shale mechanical stability after fluid exposure. Changes in both shale hardness and Young's modulus were observed with fluid exposure. Shales with higher clay content tend to experience greater reduction in modulus and hardness after contact with water-based fluids. A comparison between the measured fracture permeability damage and the calculated fracture permeability damage due to proppant embedment alone reveals that proppant embedment caused by shale softening is only partially responsible for the decrease in fracture permeability. Other mechanisms such as fines mobilization may be the dominant factors controlling fracture conductivity damage.

Together these measurements allow us to rapidly screen drilling and fracturing fluids that are compatible with a particular shale by studying changes in shale mechanical properties before and after contact with water-based fluids. Potentially troublesome shales can be identified and possible solutions can also be evaluated using this measurement procedure.

Table of Contents

Table of Contents ix

List of Tables xiii

List of Figures xv

Chapter 1: Introduction 1

1.1. Motivation and Objectives 1

1.2. Outline of Chapters 3

Chapter 2: Background and Literature Review 5

2.1. Developing Shale Reservoirs 5

2.1.1. Horizontal Drilling 6

2.1.2. Hydraulic Fracturing 7

2.2. Shale Petrophysical Properties 8

2.2.1. Native Water Activity 9

2.2.2. Shale Mineralogy 13

2.2.3. Organic Matter 17

2.2.4. Porosity and Pore Size Distribution 19

2.2.5. Fluid Saturation 23

2.2.6. Wettability 24

2.2.7. Cation Exchange Capacity 25

2.2.8. Membrane Efficiency 26

2.3. Shale Mechanical Properties 27

2.3.1. Young's Modulus 28

2.3.2. Poisson's ratio 29

2.3.3. Acoustic Wave Velocity 30

2.3.4. Brinell Hardness 34

2.4. Shale Swelling and Softening 36

2.4.1. Shale Swelling Mechanisms 37

2.4.2. Wellbore Instability 38

2.4.3. Proppant Embedment 39

2.4.4. Shale Swelling and Softening Reduction....41

Chapter 3: Materials and Experimental Procedures....43

3.1. Materials....43

3.1.1. Preserved Shale Samples....43

3.1.2. Brines....44

3.1.3. Fracturing Fluids....45

3.2. Characterization of Shale Petrophysical Properties....47

3.2.1. Adsorption Isotherm Test....47

3.2.2. XRD and XRF....48

3.2.3. Pore Size Distribution: N_2 adsorption and MICP....50

3.2.4. NMR....53

3.3. Characterization of Shale-Fluid Interactions....54

3.3.1 Swelling Test....54

3.3.2 Acoustic Wave Velocity....55

3.3.3 Brinell Hardness....56

Chapter 4: Measurement of Shale Petrophysical Properties....62

4.1. General Description of Shale Plays in the US....62

4.2. Mineralogy and Elemental Composition....67

4.3. Native Water Activity....80

4.4. NMR....83

4.4.1. T_1 and T_2 Distributions....83

4.4.2. Secular Relaxation....91

4.5. Pore Size Distribution....97

4.5.1. N_2 Adsorption....97

4.5.2. MICP....112

4.5.3. Integration of N_2GA and MICP....116

4.6. Results and Discussion....123

4.7. Conclusions....128

Chapter 5: Shale-Brine Interactions 130
5.1 Background on Water/Ion Movement in Shale 130
5.2 Gravimetric Test 132
5.2.1. Gravimetric Test Procedure 133
5.2.2. Gravimetric Test Results and Discussion 134
5.2.2.1 Water/Ion Movement with BEF-1 Shale 134
5.2.2.2 Comparison between BEF-1 and Pierre I 138
5.3 Swelling Behavior 144
5.3.1. TGS-F Shale 144
5.3.2. WBS Shale 147
5.3.3. WGS-B Shale 150
5.3.4. Comparison with the Pierre I Shale 152
5.4 Mechanical Properties 157
5.4.1 TGS-F Shale 157
5.4.2 WBS Shale 160
5.4.3 WGS-B Shale 163
5.5 Impact of Shale Preservation on Mechanical Properties 167
5.6 Conclusions 172

Chapter 6: Shale-Fracturing Fluids Interactions 175
6.1 Background on Fracturing Fluid 175
6.1.1 Slickwater 176
6.1.2 Gelled Fluids 177
6.1.3 Energized Fluids 179
6.2 Desiccator Test 180
6.2.1 TGS-F Shale 181
6.2.2 HUT 1-70 and HUT 4-39 Shales 185
6.3 Change in Shale Mechanical Properties 193
6.3.1 BEF-1 Shale 194
6.3.2 BUT Shale 196
6.3.3 BEF-2 Shale 207

6.3.4 Dynamic versus Static Young's Modulus.....222
6.3.5 Fracture Width and Conductivity.....225
6.4 Conclusions.....231
Chapter 7: Conclusions and Future Work.....234
7.1. Conclusions.....234
7.2. Future Work.....239
References.....241
Vita.....256

List of Tables

Table 2.1: Mineralogy of the Eagle Ford shale in different counties (Stegent et al., 2011). 14

Table 2.2: Diffraction angles of typical minerals found in shale samples (adapted from Breeden and Shipman, 2004). 15

Table 2.3: Guidelines for thermal maturity assessment for the Barnett shale with vitrinite reflectance (adapted from Jarvie et al., 2005). 18

Table 3.1: Concentrations of major ions in simulated Eagle Ford field brine. 44

Table 3.2: Compositions of fracturing fluids for the Utica shale. 46

Table 3.3: Compositions of fracturing fluids for the Eagle Ford shale. 46

Table 3.4: Saturated salt solutions and their respective relative humidity. 47

Table 3.5: Energy of emitted photon and the analysis depth of the XRF analysis for some elements (Kaiser, 2013). 50

Table 4.1: Whole rock mineralogy of 12 shales using XRD. 68

Table 4.2: Clay mineralogy of 12 shales using XRD. 70

Table 4.3: Elemental composition of 13 shales from XRF measurements. 75

Table 4.4: Elemental composition of illite and kaolinite (after www.webmineral.com). 77

Table 4.5: The native water activity of 11 shales. 81

Table 4.6: Porosity component based the T_{2sec}-T_1/T_2 contour map and the partition scheme shown in Figure 4.23 95

Table 4.7: Total porosity obtained from the NMR T_2 measurement and the T_{2sec}-T_1/T_2 map respectively for the seven shales. 95

Table 4.8: Shale pore parameters obtained with N_2GA and MICP measurements for all the seven samples. PV_{total} refers to the total pore volume. 122

Table 4.9: ρ_2 derived from the NMR T_2 and pore size distribution measured with N_2GA and MICP based on Eq. 4.8. 125

Table 5.1: Whole rock mineralogy of the Pierre I shale (Zhang, 2005). 139

Table 5.2: Clay mineralogy of the Pierre I shale (Zhang, 2005). 139

Table 6.1: Test matrix of the change in Brinell hardness of BEF-2 after being exposed to various fluids at 175^{o}F. 208

Table 6.2: Mineralogy of the BEF-2 shale samples used in the indentation test and the corresponding fluids that they were exposed to.....209

List of Figures

Figure 2.1: Ternary diagram of mineralogy for four Barnett shale wells (Rickman et al., 2008). 14

Figure 2.2: An AMF image of nano-pores and nano-grooves in a shale sample (Javadpour, 2009). 21

Figure 2.3: SEM images of 9 shale samples. The darker porous holes are kerogen (Curtis et al., 2010) 21

Figure 2.4: (a) 3D volumetric visualization of a shale sample from stacking a series of 2-D FIB-SEM images; (b) Volume rendering of the pore space from the stacked 3D FIB-SEM volume in (a) (Josh et al., 2012). 22

Figure 3.1: A de-aerated desiccator with saturated $K_2Cr_2O_7$ salt solution (red) on the bottom to store shale samples. 48

Figure 3.2: Bruker Tracer IV-SD System XRF Analyzer with a vacuum pump for determining the shale elemental composition. 50

Figure 3.3: Micromeritics 3Flex gas adsorption system for N_2GA measurement. 52

Figure 3.4: Micromeritics Autopore III mercury porosimeter for the MICP measurement. 52

Figure 3.5: N_2GA and MICP (MIP as shown in the plot) curves used to determine the complete pore size distribution of the shale sample (Schmitt et al., 2013). 53

Figure 3.6: Side view of one displacement indicator with a shale sample. 55

Figure 3.7: Rex durometer for determining the shale Brinell hardness. 56

Figure 3.8: Experimental setup of the spherical indentation test. 57

Figure 3.9: A load-displacement plot during the loading process with a spherical indenter of 5 mm diameter. The blue dots show the non-linear part of the curve at the early stage of loading and the red dots represent the linear part of the curve that is used for the Brinell hardness calculation. ...58
Figure 3.10: Contact geometry between a spherical indenter and the shale sample.59
Figure 3.11: The load-displacement plot during loading and unloading with a spherical indenter of 5 mm diameter. The filled dots represent the loading process. The unfilled red dots represent the linear part of the load-displacement curve during early unloading. The unfilled blue dots represent the remaining unloading process until the load is completely recovered. 61
Figure 4.1: A map of the current and prospective shale plays in the US (EIA, 2015). 62
Figure 4.2: Contour map of the depth of the Utica Shale (King, 2011). 64
Figure 4.3: Contour map of the depth of the Utica Shale (King, 2011). 64
Figure 4.4: A map of the Eagle Ford shale play with the oil (green), gas condensate (pink) and dry gas zones (orange) (EIA, 2011). 66
Figure 4.5: Ternary diagram of the relative abundance of quartz, carbonate and clay for the 12 shales using XRD. 69
Figure 4.6: Cross-plot of clay and calcite content of Eagle Ford shales....69
Figure 4.7: The quartz content of samples from a Utica well as a function of depth. 71
Figure 4.8: The calcite content of samples from a Utica well as a function of depth. 72

Figure 4.9: The total clay content of samples from a Utica well as a function of depth. 72
Figure 4.10: Ternary diagram of the relative abundance of quartz, carbonate and clay for the samples from a Utica well (using XRD). 73
Figure 4.11: Cross-plot of quartz and silicon (Si) content of some shales (using XRF). 76
Figure 4.12: Cross-plot of calcite and calcium (Ca) content of some shales (using XRF). 76
Figure 4.13: Cross-plot of clay and aluminum (Al) content of some shales. 77
Figure 4.14: Ternary diagram of the relative abundance of quartz, calcite and clay for shale samples using elemental composition obtained with the handheld ED-XRF instrument. 78
Figure 4.15: Comparison of the relative abundance of clay from the XRD and XRF measurements for 11 shales. 79
Figure 4.16: Comparison of the relative abundance of carbonate from the XRD and XRF measurements for 11 shales. 79
Figure 4.17: Comparison of the relative abundance of quartz from the XRD and XRF measurements for 11 shales. 80
Figure 4.18: Adsorption isotherms for determining the native water activities of shales from the Eagle Ford formation. 82
Figure 4.19: Adsorption isotherms for determining the native water activities of the other six shale samples. 82
Figure 4.20: NMR T_2 distribution for seven shale samples. 87
Figure 4.21: T_1-T_2 contour map of the seven shale samples. The peaks are labeled with a red dot. 90

Figure 4.22: T_1/T_2-T_2 plot for seven shale samples. 91
Figure 4.23: Partition of the T_{2sec}-T_1/T_2 map into seven zones based on the fluid viscosity and pore size (modified from Daigle et al., 2014). 92
Figure 4.24: T_{2sec}-T_1/T_2 contour map for seven shale samples. 94
Figure 4.25: Plot of the total porosity from the T_{2sec}-T_1/T_2 map and that from the T_2 alone for seven shale samples. 96
Figure 4.26: Plot of the total clay content against the porosity from Zone 4 of the T_{2sec}-T_1/T_2 map. 97
Figure 4.27: N_2 adsorption and desorption isotherms for seven shale samples. GOM-12 is a non-hydrocarbon-bearing shale while the rest all contain organic materials. The filled dots represent the adsorption isotherm and the unfilled dots represent the desorption isotherm. 101
Figure 4.28: Pore size distribution for all the seven samples using the BJH model.104
Figure 4.29: Pore size distribution for all the seven samples using the dV/d(logD) plot and the BJH model. 105
Figure 4.30: BJH pore size distribution for all the seven samples with the dV/dD plot. 106
Figure 4.31: Specific surface area of the seven shales calculated using the BET model with the N_2 adsorption isotherm. 109
Figure 4.32: Cross-plot of the BET specific surface and the total clay content of seven shales. 110
Figure 4.33: Incremental pore surface area based on the BET model as a function of pore size for seven shales. 111
Figure 4.34: Capillary pressure curves of all the seven shales. 115

Figure 4.35: N_2GA and MICP curves used to determine the intersection pore diameter from which the complete pore size distribution can be constructed.118
Figure 4.36: Overlaid N_2GA and MICP curves for TGS-D and GOM-12 shales with the incremental pore volume as the y-axis that exhibit peak shifts 119
Figure 4.37: Combined pore size distribution for all seven shales with the dV/d(logD) plot using the BJH N_2GA and MICP curves.....121
Figure 4.38: Combined pore size distribution from the BJH N_2GA and MICP curves and the NMR T_2 distribution for five shales. 124
Figure 4.39: Plot of the transverse surface relaxivity ρ_2 against the total clay content. 125
Figure 4.40: Plot of the transverse surface relaxivity ρ_2 against the iron content.126
Figure 4.41: Cross-plot of the total pore volume per unit weight from the pore size distribution and the total NMR porosity based on the T_{2sec}-T_1/T_2 measurements for five shale samples.....127
Figure 4.42: Cross-plot of the native water activity and the total NMR porosity based on the T_{2sec}-T_1/T_2 measurements for four shale samples. 128
Figure 5.1: Water and ion movement into and out of BEF-1 shale using NaCl, KCl and $CaCl_2$ brines, plotted against salt concentration.....135
Figure 5.2: Water and ion movement into and out of BEF-1 shale using NaCl, KCl and $CaCl_2$ brines, plotted against water activity difference between brine and shale.....137
Figure 5.3: Water and ion movement into and out of Pierre I shale using NaCl, KCl and $CaCl_2$ brines, plotted against salt concentration (Zhang, 2005).140
Figure 5.4: Water activity of NaCl, KCl and $CaCl_2$ brines at different concentrations (adapted from Zhang, 2005). 140

Figure 5.5: Water and ion movement into and out of Pierre I shale using NaCl, KCl and $CaCl_2$ brines, plotted against the water activity difference between brine and shale (Zhang, 2005). 141
Figure 5.6: Net weight change of the BEF-1 shale after being exposed to NaCl, KCl and $CaCl_2$ solution at room temperature. 143
Figure 5.7: Net weight change of the Pierre I shale after being exposed to NaCl, KCl and $CaCl_2$ solution at room temperature (adapted from Zhang, 2005).143
Figure 5.8: Swelling behavior of the TGS-F shale with fresh water, 4% NaCl, and 2% KCl solutions at room temperature. 146
Figure 5.9: Weight change of the TGS-F shale after being exposed to fresh water, 4% NaCl, and 2% KCl solutions for 24 hours at room temperature. 147
Figure 5.10: Plot of the weight change of the TGS-F shale vs. the corresponding swelling perpendicular and parallel to bedding planes after 24 hours' exposure fresh water, 4% NaCl, and 2% KCl for solutions at room temperature. 147
Figure 5.11: Swelling behavior of the WBS shale with fresh water and 4% seawater at room temperature. 149
Figure 5.12: Weight change of the WBS shale after being exposed to fresh water and 4% seawater for about 24 hours at room temperature. 150
Figure 5.13: Swelling behavior of the WGS-B shale with fresh water, 4% NaCl and 2% KCl at room temperature. 151
Figure 5.14: Weight change of the WGS-B shale after being exposed to fresh water, 4% NaCl and 2% KCl for 24 hours at room temperature. 152

Figure 5.15: Swelling behavior of the Pierre I shale with DI water, NaCl, KCl and $CaCl_2$ solutions with Aw = ~0.95 at room temperature (adapted from Zhang, 2005). 154
Figure 5.16: Cross-plot of the swelling perpendicular to bedding planes after 24 hours of contact with fresh water and the clay content of the TGS-F, WBS, WGS-B and the Pierre I shales. 155
Figure 5.17: Cross-plot of the net weight change after 24 hours of contact with fresh water and the clay content of the TGS-F, WBS, WGS-B and the Pierre I shales. 156
Figure 5.18: Cross-plot of the net weight change and the swelling perpendicular to bedding planes after 24 hours of contact with fresh water for the TGS-F, WBS, WGS-B and the Pierre I shales. 157
Figure 5.19: Brinell hardness of the TGS-F shale before and after being immersed in fresh water, 4% NaCl and 2% KCl for 24 hours. 158
Figure 5.20: P-wave and S-wave velocities of the TGS-F shale before and after being immersed in fresh water, 4% NaCl and 2% KCl for 24 hours (a) perpendicular and (b) parallel to bedding planes. 159
Figure 5.21: (a) Dynamic Young's modulus and (b) Poisson's ratio of the TGS-F shale before and after being immersed in fresh water, 4% NaCl and 2% KCl for 24 hours perpendicular to bedding planes. 160
Figure 5.22: Brinell hardness of the WBS shale before and after being immersed in fresh water and 4% seawater for 24 hours. 161
Figure 5.23: P-wave and S-wave velocities of the WBS shale before and after being immersed in fresh water and 4% seawater for 24 hours (a) perpendicular and (b) parallel to bedding planes. 162

Figure 5.24: (a) Dynamic Young's modulus and (b) Poisson's ratio of the WBS shale before and after being immersed in fresh water and 4% seawater for 24 hours perpendicular to bedding planes. 163
Figure 5.25: Brinell hardness of the WGS-B shale before and after being immersed in fresh water, 4% NaCl and 2% KCl for 24 hours.....164
Figure 5.26: P-wave and S-wave velocities of the WGS-B shale before and after being immersed in fresh water, 4% NaCl and 2% KCl for 24 hours (a) perpendicular and (b) parallel to bedding planes. 165
Figure 5.27: (a) Dynamic Young's modulus and (b) Poisson's ratio of the WGS-B shale before and after being immersed in fresh water, 4% NaCl and 2% KCl for 24 hours perpendicular to bedding planes. 166
Figure 5.28: Cross-plot of the change in P-wave velocity after 24 hours of contact with fresh water and the clay content of the TGS-F, WBS, WGS-B and the Pierre I shales. 167
Figure 5.29: Weight change of the dry and preserved WGS-B shale samples after being immersed in 4% NaCl for 24 hours at room temperature. 169
Figure 5.30: Change in Brinell hardness of the dry and preserved WGS-B shale samples after being immersed in 4% NaCl for 24 hours at room temperature. 170
Figure 5.31: Change in P-wave and S-wave velocities of the dry and preserved WGS-B shale samples perpendicular to bedding planes after being immersed in 4% NaCl for 24 hours at room temperature.....171
Figure 5.32: Change in the dynamic Young's modulus and Poisson's ratio of the dry and preserved WGS-B shale samples after being immersed in 4% NaCl for 24 hours at room temperature.....172

Figure 6.1: Structures of (a) a linear gel polymer, (b) a crosslinked gel polymer.178
Figure 6.2: Change in Brinell hardness of the TGS-F shale as a result of water adsorption and desorption on the sample plotted against water activity. 182
Figure 6.3: Change in indentation Young's modulus of the TGS-F shale as a result of water adsorption and desorption on the sample plotted against water activity.....183
Figure 6.4: Change in Brinell hardness of the TGS-F shale as a result of water adsorption and desorption on the sample plotted against weight change. 184
Figure 6.5: Change in indentation Young's modulus of the TGS-F shale as a result of water adsorption and desorption on the sample plotted against weight change. 185
Figure 6.6: Change in Brinell hardness of the HUT 1-70 and HUT 4-39 shales as a result of water adsorption and desorption on the sample plotted against water activity.....186
Figure 6.7: Comparison of Brinell hardness of the HUT 1-70 and HUT 4-39 shales at a water activity of 0.96.....187
Figure 6.8: Change in indentation Young's modulus of the HUT 1-70 and HUT 4-39 shales as a result of water adsorption and desorption on the sample plotted against water activity. 188
Figure 6.9: Comparison of the indentation Young's modulus of the HUT 1-70 and HUT 4-39 shales at a water activity of 0.96. 189

Figure 6.10: Change in Brinell hardness of the HUT 1-70 and HUT 4-39 shales as a result of water adsorption and desorption on the sample plotted against weight change. The weight of HUT 4-39 is shown on the horizontal axis on the top, and that of HUT 1-70 is shown on the horizontal axis on the bottom. 190
Figure 6.11: Change in indentation Young's modulus of the HUT 1-70 and HUT 4-39 shales as a result of water adsorption and desorption on the sample plotted against weight change. The weight of HUT 4-39 is shown on the horizontal axis on the top, and that of HUT 1-70 is shown on the horizontal axis on the bottom.....191
Figure 6.12: Change in Brinell hardness of the HUT 1-70, HUT 4-39 and TGF-S shales against the weight change of the shale samples. 192
Figure 6.13: Change in Young's modulus of the HUT 1-70, HUT 4-39 and TGF-S shales against the weight change of the shale samples. 193
Figure 6.14: Change in the absolute Brinell hardness of the BEF-1 shale after exposure to various water-based fluids at room temperature as a function of time. 195
Figure 6.15: Change in the normalized Brinell hardness of the BEF-1 shale after exposure to various water-based fluids at room temperature as a function of time. 196
Figure 6.16: Hardness of the BUT shale samples at their native state. 198
Figure 6.17: Histogram of the hardness of the BUT shale samples at their native state. 198

Figure 6.18: Change in the absolute Brinell hardness of the BUT shale after being exposed to Solutions 1, 2 and 4 for more than 40 hours at room temperature. 199
Figure 6.19: Change in the normalized Brinell hardness of the BUT shale after being exposed to Solutions 1, 2 and 4 for more than 40 hours at room temperature. 200
Figure 6.20: Change in the absolute indentation Young's modulus of the BUT shale after being exposed to Solutions 1, 2 and 4 for over 40 hours at room temperature. 201
Figure 6.21: Change in the normalized indentation Young's modulus of the BUT shale after being exposed to Solutions 1, 2 and 4 for over 40 hours at room temperature. 201
Figure 6.22: Cross-plot of the Brinell hardness against the indentation Young's modulus of the HUT shale at different stages of exposure to Solutions 1, 2 and 4. 202
Figure 6.23: Change in the absolute Brinell hardness of the BUT shale after being exposed to Solutions 1, an acidic fluid and a high pH fluid at room temperature and elevated temperature. 205
Figure 6.24: Change in the normalized Brinell hardness of the BUT shale after being exposed to Solutions 1, an acidic fluid and a high pH fluid at room temperature and elevated temperature. 205
Figure 6.25: Swelling of the BUT shale perpendicular to bedding planes after being immersed in an acidic fluid and a high pH fluid for 24 hours at room temperature. 207

Figure 6.26: Ternary diagram of the relative abundance of quartz, carbonate and clay for the low-clay and high clay shales. 209
Figure 6.27: Change in the absolute Brinell hardness of the low-clay BEF-2 shale after being exposed to the field brine, an acidic fluid and a high pH fluid for over 40 hours at 175^{o}F. 210
Figure 6.28: Change in the normalized Brinell hardness of the low-clay BEF-2 shale after being exposed to the field brine, an acidic fluid and a high pH fluid for over 40 hours at 175^{o}F. 211
Figure 6.29: Change in the absolute Brinell hardness of the high-clay BEF-2 shale after being exposed to the field brine, an acidic fluid and a high pH fluid for over 40 hours at 175^{o}F. 212
Figure 6.30: Change in the normalized Brinell hardness of the high-clay BEF-2 shale after being exposed to the field brine, an acidic fluid and a high pH fluid for over 40 hours at 175^{o}F. 212
Figure 6.31: Change in the absolute Brinell hardness of the high-clay BEF-2 shale after being exposed to a high pH fluid and the fluid with various clay stabilizers for over 40 hours at 175^{o}F. 214
Figure 6.32: Change in the normalized Brinell hardness of the high-clay BEF-2 shale after being exposed to a high pH fluid and the fluid with various clay stabilizers for over 40 hours at 175^{o}F. 214
Figure 6.33: Cross-plot of change in normalized fracture permeability and change in normalized Brinell hardness of the BEF-2 shale after being exposed to various types of fluids. 216
Figure 6.34: Concentrations of the Mg and Ca in the high pH fluid and the fluid with various quaternary amine-based clay stabilizers. 217

Figure 6.35: Concentrations of the Al and Si in the acidic fluid, the high pH fluid and the high pH fluid with various quaternary amine-based clay stabilizers. 218
Figure 6.36: Cross-plot of the Brinell hardness and the relative abundance of clay of the BEF-2 shale before fluid exposure.....219
Figure 6.37: Cross-plot of the Brinell hardness and the relative abundance of calcite of the BEF-2 shale before being exposed to fluids. 219
Figure 6.38: Cross-plot of the Brinell hardness and the relative abundance of quartz of the BEF-2 shale before being exposed to fluids. 220
Figure 6.39: Cross-plot of the Brinell hardness and the relative abundance of clay of the BEF-2 shale before and after fluid exposure. Red represents the samples exposed to high pH fluids with the clay stabilizers. 221
Figure 6.40: Cross-plot of the Brinell hardness and the relative abundance of calcite of the BEF-2 shale before and after fluid exposure. Red represents the samples exposed to high pH fluids with the clay stabilizers. 221
Figure 6.41: Cross-plot of the Brinell hardness and the relative abundance of quartz of the BEF-2 shale before and after fluid exposure. 222
Figure 6.42: Comparison of the dynamic and static Young's modulus of the TGS-F shale exposed to 2% $CaCl_2$ for 24 hours. 223
Figure 6.43: Comparison of the dynamic and static Young's modulus of the BUT shale exposed to Solution 1 for four days. 224
Figure 6.44: Comparison of the dynamic and static Young's modulus of the BUT shale exposed to brine, Solutions 1, 2 and 4 for over a month. 224
Figure 6.45: Cross-plot of the dynamic and static Young's modulus of the TGS-F and BUT shales exposed to various types of water-based fluids.....225

Figure 6.46: Schematic picture of the embedment of one proppant particle on the fracture face. 227
Figure 6.47: (a) Fracture width and (b) conductivity as a function of confining stress for a fracture with monolayer coverage of proppant. 229
Figure 6.48: (a) Fracture width and (b) conductivity as a function of confining stress for a fracture with three layers of proppant. 229
Figure 6.49: (a) Fracture width and (b) conductivity as a function of confining stress for a fracture with five layers of proppant. 230
Figure 6.50: Cross-plot of measured fracture permeability damage and calculated fracture permeability damage due to proppant embedment alone. .231

Chapter 1: Introduction

1.1. Motivation and Objectives

Hydrocarbon production from low permeability formations has existed in the U.S. for more than 100 years. However, it was not until a decade ago that shale gas development and production experienced a sudden expansion, thanks to the use of horizontal drilling and hydraulic fracturing. These technologies have been instrumental in unlocking hydrocarbons from shale rocks in the subsurface and will play an increasingly important role in the next few decades to meet the growing energy demand for global economic development.

Besides organic-rich shales, non-hydrocarbon bearing shales are often encountered in the drilling process. These shales account for more than 75% of the drilled formations (Steiger and Leung, 1992). What these shales have in common with hydrocarbon bearing shales is that both types of shales can be highly reactive with water-based fluids. This reactivity can be attributed to the water-sensitive clay minerals in shale rocks. When a shale comes into contact with water-based drilling and fracturing fluids, shale swelling and softening can occur. As a result, drilling problems such as wellbore instability and fracturing problems such as proppant embedment reduce the well productivity significantly and cost the industry a lot of time and money every year. It is evident that the petroleum industry will benefit tremendously if the sensitivity of shale to water-based fluids can be reduced.

In order to investigate the factors contributing to a shale's sensitivity towards water-based fluids, shale-fluid interactions have been studied extensively to understand the various mechanisms involved in phenomena such as shale swelling (e.g.: Chenevert, 1970a and 1970b, van Oort, 2003, Caenn et al., 2011, Gazaniol et al., 1995). A majority

of the attention in the past has been dedicated to minimizing wellbore instability issues in shale intervals. Preventing water from going into shales and using chemicals to reduce clay dispersion in shales are two primary methods to enhance wellbore stability in shale formations (Beihoffer et al., 1992). However, due to the cost and environmental concerns, oil-based fluids are not always suitable for drilling through shale layers. Consequently, a great deal of effort in the petroleum industry has been dedicated to developing effective shale inhibitors such as quaternary ammonium salts and cationic polymers to improve borehole stability when drilling through shales (Himes and Vinson, 1989, Beihoffer et al., 1990, Patel et al., 1999, Smith, 2003, Brady et al., 1998). Similarly, shale stabilizers have been developed to reduce proppant embedment in hydraulic fracturing (Ali et al., 2011).

A great deal is known about the interactions of non-hydrocarbon bearing shales with water-based fluids, however, shale-water interactions need to be looked at more closely for hydrocarbon bearing shales. Fracture conductivity experiments are the most direct way to examine the permeability reduction when shales are in contact with water-based fluids. However, such experiments take a lot of time to run and are difficult to perform. A more systematic protocol to evaluate changes in shale mechanical properties when in contact with water-based fluids is needed to simplify the experimental procedure and yet provide useful information regarding changes in fracture conductivity. Previous experiences in developing shale inhibitors to reduce wellbore instability may also be applied to reduce proppant embedment in hydrocarbon bearing formations.

The main objectives of this research are to systematically characterize shale petrophysical properties and to investigate shale-fluid interactions through changes in mechanical properties after fluid exposure. The specific objectives are outlined here:

1. To systematically characterize hydrocarbon bearing shales from different formations in the U.S. Mineralogy, native water activity, porosity, pore size distribution and mechanical properties will be measured and compared with those of non-hydrocarbon bearing shales. The correlations between these properties will be explored;
2. To investigate the interactions of shales with various water-based fluids. The performance of shale inhibitors with different shale samples will be evaluated. A standard protocol will be developed and followed;
3. To correlate shale swelling behavior and changes in mechanical properties such as Brinell hardness and acoustic wave velocities with shale mineralogy, water activity and ion concentrations in water-based fluids;
4. To investigate the mechanisms contributing to shale fracture conductivity damage. The reduction in shale mechanical properties and fracture permeability after fluid exposure will be compared.

1.2. OUTLINE OF CHAPTERS

This dissertation is presented in seven chapters. This chapter (Chapter 1) introduces the problem and describes the objectives of this research.

Chapter 2 reviews the applications of horizontal drilling and hydraulic fracturing in developing shale reservoirs and the recent advances in shale characterization techniques. The associated issues when shales interact with water-based fluids are discussed and the causes and solutions that the industry has employed to mitigate such unfavorable interactions are examined.

Chapter 3 illustrates the materials, experimental set-up and procedures for shale characterization in the laboratory.

Chapter 4 presents results from measurements of petrophysical properties of shales from various plays in the U.S. The NMR T_1-T_2 relaxation times are analyzed together to determine the distribution of fluids in pores of various sizes. The N_2 gas adsorption (N_2GA) and mercury injection capillary pressure (MICP) techniques are used in combination to obtain the complete pore size distribution of shale rocks.

In Chapter 5, the shale-brine interactions are investigated systematically through gravimetric tests, swelling tests and measurement of changes in mechanical properties such as the Brinell hardness and the acoustic wave velocities after the samples' exposure to various water-based fluids. The effect of shale preservation on the change in mechanical properties after fluid exposure is demonstrated.

In Chapter 6, an overview of the properties of various water-based fracturing fluids is presented. Shale-fracturing fluids interactions are investigated through changes in mechanical properties after fluid exposure. The effect of shale mineralogy, temperature, fluid pH and clay stabilizers on the reduction in shale hardness and Young's modulus after fluid exposure are examined. The reduction in shale hardness and fracture conductivity is compared

Chapter 7 discusses the conclusions of this dissertation and recommends future research related to this work.

Chapter 2: Background and Literature Review

The success of horizontal drilling and hydraulic fracturing has led to the recent boom in production of hydrocarbons from shale reservoirs. Hydrocarbon production from these relatively impermeable rocks has become economically viable, thanks to the large area of contact with the reservoir through drilling horizontal wellbores and the additional flow channels created by pumping large amounts of fluid with proppant at a high rate.

Before extracting oil and gas from a potential shale formation, the petrophysical properties of shale are needed to determine whether the formation can be considered a shale gas or oil resource with economically recoverable reserves. These petrophysical properties include the mineralogy, organic content, porosity and permeability. Proper characterization techniques need to be developed for shale petrophysical properties. On the other hand, both drilling and fracturing require the use of a large amount of water. The water molecules can interact unfavorably with shales due to the presence of clay minerals, causing problems such as wellbore instability and proppant embedment after fracturing. The compatibility of water-based drilling and fracturing fluids with shale samples needs to be evaluated to ensure the success of drilling and fracturing activities.

This chapter reviews the application of horizontal drilling and hydraulic fracturing in enhancing hydrocarbon production from shale reservoirs and the recent advances in shale characterization techniques. The associated issues when shale interacts with water-based fluids are discussed and the causes and solutions that the industry has employed to mitigate such unfavorable interactions are examined.

2.1. Developing Shale Reservoirs

The last decade has seen shale gas and oil production going up substantially due to the technological advances in horizontal drilling and hydraulic fracturing. These two

key technologies go hand in hand in unlocking hydrocarbons from shale formations. Shale gas and oil will continue to be a significant contributor for meeting the growing energy demand in North America and other parts of the world in the future. EIA (2012) estimated that the US will be 97% self-sufficient in energy in net terms by 2035, largely due to the high volumes of gas produced from shale formations. Thousands of new horizontal wells are being drilled and tens of thousands of fracturing jobs are being performed every year to maintain and elevate the production.

2.1.1. Horizontal Drilling

Despite the long history of horizontal drilling in hydrocarbon production, the technology received little attention from the oil and gas industry after it was first utilized in the 1920s (Stark, 2003). It was not until the late 1970s and early 1980s that technological development in horizontal drilling was revived due to higher oil prices and other reasons. The first multi-fractured horizontal well was air drilled in the Devonian shale in Wayne County, WV in 1986 (Trembath et al., 2012). The first horizontal well in Barnett shale was successfully drilled by Mitchell Energy in 1991, with subsidies from the Gas Research Institute (GRI) and the Department of Energy (DOE). Mitchell Energy achieved economic production of shale gas from the Barnett formation in 1997, thanks to horizontal drilling and hydraulic stimulation. Later in the 2000s, the success in shale gas production in Barnett with horizontal drilling and hydraulic fracturing was quickly translated to other unconventional shale plays in North America, which resulted in the recent shale revolution.

There can be multiple benefits with drilling horizontal wells in low-permeability shale reservoirs. The primary advantage that a horizontal well has over a vertical well is the area of contact between the wellbore and the reservoir. Horton et al. (1982) showed

that stimulated vertical wells can only extract 10% to 20% of gas in shale formations. In contrast, horizontal wells can significantly increase the area of contact with reservoir because of the extended length of the wellbore. The lateral extension of a horizontal well in shale formations can be as long as 10,000 feet today (O'Brien, 2013). Meanwhile, the surface footprint as well as the capital and operational costs can also be reduced significantly for operators drilling long horizontal wells.

While horizontal drilling can be economically beneficial for developing shale reservoirs, multiple technical challenges still exist when horizontal wellbores are drilled. Two main problems related with drilling horizontal wells are hole-cleaning and borehole collapse due to the water-sensitive shales (Schlumberger, 1990; Piroozian et al., 2012; Jellison et al., 2013). Drill cuttings tend to settle to the bottom of the extended horizontal section of the wellbore. During hole-cleaning, the circulating drilling fluid will flow above the cuttings and not remove all of them in the horizontal wellbore. High circulation rates with viscous drilling fluids are needed to push the cuttings out of the wellbore. On the other hand, the unfavorable interactions between the water-based drilling fluids and the clay minerals in shale can cause the wellbore to collapse. As a result, a proper drilling fluid needs to be used to minimize potential problems with drilling horizontal wells in shale formations.

2.1.2. Hydraulic Fracturing

As its name suggests, hydraulic fracturing involves pumping fluids at a high rate and pressure to the subsurface to create fractures for enhanced production in the reservoir. The propping agent, called proppant, is normally mixed with the fracturing fluid before the mixture is pumped downhole to create fractures. Similar to horizontal drilling, hydraulic fracturing has a long history as a stimulation technique in the oil and

gas industry. The first hydraulic fracturing job was performed on a gas well in the Hugoton field in 1947 in Kansas (Gidley et al., 1989). Since then, over a million oil and gas wells have been stimulated by hydraulic fracturing (Groat and Grimshaw, 2012). As mentioned in the previous section, the early success of shale gas development in the Barnett formation was mimicked by operators in other shale plays across North America, resulting in today's shale boom.

Hydraulic fracturing has experienced tremendous technological development since its early days. The stimulation technique has been transformed from a low-volume, low-rate operation to a highly complex, engineering-driven procedure in the subsurface. Like horizontal drilling, the primary purpose for hydraulic fracturing is to create additional area of contact in the reservoir so that hydrocarbons can flow in the otherwise impermeable shale formations. Multiple hydraulic fractures can be created in stages on the same horizontal wellbore, enabling the well productivity to be increased many times. Academic and industrial research efforts have been focused on issues such as geomechanics, proppant transport, and formation damage due to shale-fluid interactions.

2.2. SHALE PETROPHYSICAL PROPERTIES

Shale is defined as a fine-grained detrital sedimentary rock. It is formed by the compaction of clay, silt or mud (Bates and Jackson, 1984). Shales are usually finely laminated and are found in low-energy marine depositional environments (Davidson, 1999). They are commonly found to be adjacent to sandstone or limestone layers. Due to their small grain size, the porosity of shales is generally below 10% (Ground Water Protection Council and ALL Consulting, 2009) and their permeability is typically on the order of 1,000 nD to 10 nD (Freeze and Cherry, 1979). In terms of the mineralogical composition, shale typically consists of different types of clay, fine-size quartz, and

feldspars. Carbonates (calcite), sulfides, iron oxides and organic carbon compounds also exist in a lot of shales (Davidson, 1999).

Before the shale revolution, the word "shale" usually referred to the clay-rich rock encountered during the drilling process that can cause wellbore stability problems. What differentiates oil and gas shales from these non-hydrocarbon bearing shales is the presence of organic materials. These organic materials were deposited in the form of algae-, plant-, and animal-derived organic debris at the same time when the deposition of fine-grained sediments took place (Davis, 1992). They are responsible for shales being the source rock for hydrocarbon generation. The uniqueness of shale reservoir compared with conventional reservoir systems is the integration of source rock, reservoir rock and seal into one shale formation (Ground Water Protection Council and ALL Consulting, 2009). Organic matter adds a lot of complexity to the characteristics of shales. The proper characterization of shale petrophysical properties is essential in the success of resource evaluation and drilling, completion and production planning in the later stage. However, shale petrophysical properties are not well understood due to the complexity of the mineralogical makeup and the heterogeneous nature of the shale rock. Significant efforts are underway in academia and in industry to develop a better understanding of shale petrophysical properties.

2.2.1. Native Water Activity

The shale native water activity represents the original hydration state of shale samples. It is an important fundamental property of shale and is directly related to the performance of drilling and fracturing fluids. It controls the water/ion movement into and out of shale (Hale et al, 1993; Fonseca and Chenevert, 1998). As a result, physiochemical and mechanical properties such as the pore pressure and strength can be altered

(Chenevert 1970a; Hale et al., 1993). Chenevert (1970b) pointed out that water can be adsorbed onto shale due to an imbalance of water activity between pore fluid and drilling fluid. This in turn will result in the development of excessive formation pressure, and subsequently wellbore instability. He measured the native water activity of West Texas shale and demonstrated that water adsorption by shale can be prevented by adjusting the water activity of oil-based drilling mud to that of the preserved shale. On the other hand, low-activity oil-based mud can effectively withdraw water from shale, which can enhance its strength (Hale et al., 1993). Therefore, the native water activity of shale not only indicates its hydration state, but also provides useful information regarding fluid design for drilling and completion.

The definition of water activity of a system is the ratio of the fugacity of water in the system to that of pure water (Robinson and Stokes, 1959):

$$a_w = \frac{\overline{f}}{\overline{f}_o} \tag{2.1}$$

where $\overline{f}$ is the fugacity of water in the system and $\overline{f}_o$ is the fugacity of pure water. The fugacity ratio in Eq. 2.1 can be replaced by the vapor pressure ratio, because the correction factor for converting fugacity to vapor pressure is almost equal for a pure solvent and a solution (Chenevert, 1970a and 1970b; O'Brien and Chenevert, 1973). As a result, the equation for water activity of a system can be expressed as:

$$a_w = \frac{\overline{p}}{\overline{p}_o} \tag{2.2}$$

where $\overline{p}$ is the vapor pressure of water in the system and $\overline{p}_o$ is the vapor pressure of pure water. Vapor pressure is a function of temperature. At 25^{o}C, the vapor pressure of pure water is 3.2 kPa (0.46 psi) (Sandler, 2006).

The chemical potential and water activity of the water phase of the ith component in a system are related by the following equation (Zhang et al., 2008):

$$\mu = \mu^0 + RT\ln(a_w) \tag{2.3}$$

where μ is the chemical potential of the component, μ^0 is the chemical potential of the pure liquid of that component at standard conditions, a_w is the water activity of the component, R is the gas constant and T is the absolute temperature of the system. When a shale sample of water activity a_{ws} is in contact with a fluid of water activity a_{wf}, the relationship between the chemical potential difference μ_{diff} and the water activities of the shale and the fluid is as follows:

$$\mu_{diff} = RT\ln\left(\frac{a_{ws}}{a_{wf}}\right) \tag{2.4}$$

Eq. 2.4 shows that when $a_{ws} > a_{wf}$, $\mu_{diff} > 0$, and water moves from the shale to the fluid. On the other hand, when the water activity of the fluid is higher than that of the shale, the potential energy difference is negative and water moves from the fluid to the shale.

At constant temperature, the relationship between the osmotic pressure π and the partial molar volume of the solvent $\overline{V_s}$ and a_w is as follows:

$$\pi = -\frac{RT}{\overline{V_s}}\ln a_w \tag{2.5}$$

The osmotic pressure difference $\Delta\pi$ between the water in a shale and in a fluid with activity of a_{ws} and a_{wf} can be expressed as:

$$\Delta\pi = -\frac{RT}{\overline{V_s}}\ln\left(\frac{a_{ws}}{a_{wf}}\right) \tag{2.6}$$

Even a small difference in water activity between two systems can result in a significant osmotic pressure difference. Sandler (2006) showed that an osmotic pressure difference of 2.78 MPa (403 psi) can be developed between pure water and an ideal aqueous solution containing 98 mole percent water.

The native shale water activity can be determined with the adsorption isotherm test (Chenevert, 1970b; O'Brien and Chenevert, 1973; Osisanya, 1991). Controlled humidity environments are created with saturated salt solutions in de-aerated desiccators (Winston and Bates, 1960). Placing shale samples in desiccators without directly contacting the saturated solutions ensures that only moisture enters or leaves the shale with no ion movement. Chenevert (1970a and 1970b) employed a combined gravimetric-shale density technique to create an adsorption-desorption isotherm. The shale native water activity was determined with its in-situ water content calculated from the shale density data. Osisanya (1991) used the isopiestic method developed by Robinson and Sinclair (1934) for determining the shale adsorption isotherm. Shale sample was placed in the desiccator with a specific relative humidity. The weight change of the samples due to water movement was monitored and recorded until equilibrium. The process was repeated for other relative humidity environments until no weight change was observed.

The native water activity of shale determined in the laboratory is under ambient temperature and pressure conditions. Fonseca and Chenevert (1998) measured shale water activity at elevated temperature and pressure in an attempt to extrapolate the water activity from ambient conditions to downhole conditions. They found that shale water activity increases with temperature and confining pressure. The results indicate that the native water activity of shales downhole can be higher than the surface measured value.

Native water activity is an important but often overlooked property of shale samples. It indicates the swelling pressure of shale when it comes into contact with water. A lower native water activity will lead to a greater swelling pressure should water comes the shale. Activity imbalance between the pore fluid and the drilling and fracturing fluid can cause fluid flow into or out of shale. Proper preservation of shale core samples at the

wellsite and the subsequent laboratory measurement of water activity can offer valuable guidance for drilling fluid design.

2.2.2. Shale Mineralogy

Shale usually consists of different types of clay, fine-size quartz, and feldspars. Carbonates (calcite), sulfides, iron oxides and organic carbon compounds also exist in a lot of shales (Davidson, 1999). However, there is not a typical shale mineralogical makeup. The mineralogical composition of shale varies significantly between formations. Even within the same play, the mineralogy can be very different. Figure 2.1 shows the ternary diagram of the relative abundance of quartz, carbonate and clay for four wells in the Barnett formation (Rickman et al., 2008). Different colors represent different wells. While the samples from Well 2 do not contain any carbonate, the carbonate content of the samples from Well 5 varies between zero and almost 100%. And the clay content of these samples can be as high as more than 50%. Similar observation was reported by Stegent et al. (2011) for the Eagle Ford formation (Table 2.1). The samples from the Frio county are carbonate-rich (73% carbonate) while those from the Franklin county are clay-rich (~60% clay). Britt and Schoeffler (2009) pointed out that shale rocks with clay content greater than 35% to 40% cannot be considered very prospective.

The mineralogy of shales is very important because it is related to other physiochemical and mechanical properties such as the potential for water adsorption and brittleness. These rock properties will facilitate the planning of drilling and fracturing activities. Jarvie et al. (2007) and Wang and Gale (2008) proposed mineralogy-based models to use “brittleness index” to quantify the rock brittleness, which is an important mechanical property for well location selection and completion design for shale reservoirs. Again it is important to keep in mind that no two shales are the same in terms

of mineralogy and no single fracturing design is suitable for all shales (Rickman et al., 2008).

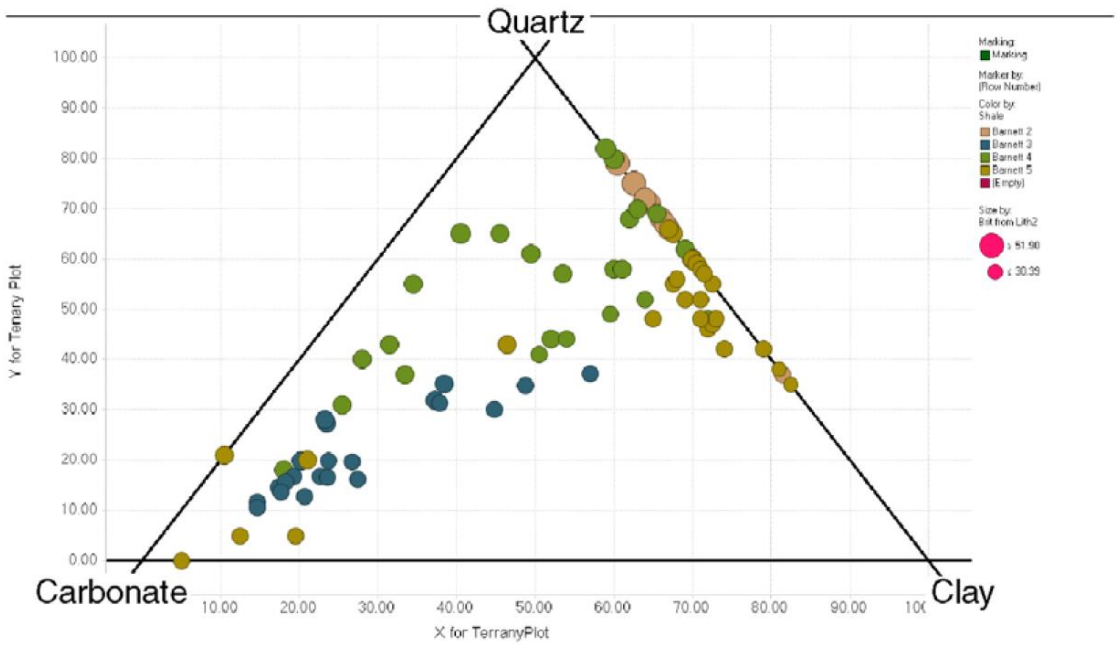

Figure 2.1: Ternary diagram of mineralogy for four Barnett shale wells (Rickman et al., 2008).

County	Dimmit	Frio	LaSalle	Live Oak	DeWitt	Robertson	Franklin	Franklin
Depth, ft	7,064–7,405	8,925–9,650	10,939–11,149	11,555– 11,669	13,296–13,513	5,800–7,000	5,475	6,868
				Mineral, wt%				
Quartz	9	9	13	18	14	34	23	20
Plagioclase	3	2	3	—	—	8	7	7
Calcite	70	70	60	52	51	12	4	12
Dolomite	1	3	1	1	Tr	—	Tr	—
Illite	11	14	4	5	6	24	26	27
Mixed Layer	3	—	15	2	9	32	32	24
Kaolinite	2	1	Tr	1	2	—	6	8
Chlorite	1	—	Tr	1	1	2	2	2
Pyrite	2	Tr	1	4	2	—	—	—

Table 2.1: Mineralogy of the Eagle Ford shale in different counties (Stegent et al., 2011).

X-ray diffraction (XRD) and X-ray fluorescence (XRF) are two commonly used methods to determine the mineralogical and elemental compositions of rocks in the oil and gas industry (Ruessink and Harville, 1992; Breeden and Shipman, 2004; Rowe et al., 2012; Marsala et al., 2012). The XRD technology is based on the specific crystalline

structure of each mineral. This results in the X-ray being diffracted with a unique pattern. The angles of diffraction of the X-ray can be measured and collected with an XRD instrument. Bragg's Law relates the lattice d-spacing and the angle of diffraction for a mineral:

$$n\lambda = 2d\sin\theta \tag{2.7}$$

where n is an integer, λ is the wavelength of the incident rays, d is the spacing between the planes of the atomic lattice (d-spacing), and θ is the angle between the incident rays and the scattering planes (angle of diffraction). Table 2.2 shows the diffraction angles of some commonly found minerals in shales. The analysis of the diffraction pattern can be used to deduce the mineralogy of the rock sample in a semi-quantitative way (Breeden and Shipman, 2004). The ratio between the measured intensities of a specific peak with a rock and with a standard mineral indicates the weight percentage of that mineral in the rock samples.

Mineral	2θ (degrees)
Quartz	26.6
Feldspar	27.5
Calcite	29.6
Dolomite	31.0
Siderite	31.8
Pyrite	33.1
Clays	19.9

Table 2.2: Diffraction angles of typical minerals found in shale samples (adapted from Breeden and Shipman, 2004).

The shape of the mineral structure plays an important role in interpreting the diffraction spectrum. Minerals such as quartz and calcite have simple crystalline structures that are easy to interpret from the XRD analysis. However, the complicated structures of clay minerals make the interpretation of their X-ray diffraction pattern

problematic. Their flaky shape and similar d-spacing between different clay minerals make the identification of individual clay difficult. The specific clay type and content cannot be determined with XRD alone. However, the swelling and softening potential of clay minerals can lead to proppant embedment and wellbore instability. Therefore, the clay content of shale samples needs to be looked at closely as well. Additional steps to impose physical and chemical changes to clay samples are necessary to distinguish clay minerals (Breeden and Shipman, 2004).

More recently, handheld energy-dispersive X-ray fluorescence (ED-XRF) technology has been developed and applied to quantify the geochemical elemental composition for both shale and carbonate rocks (Rowe et al., 2012; Wood, 2013; Marsala et al., 2012). When X-rays with sufficient energy hits an inner shell electron of an atom, the electron is ejected and the vacancy is filled by an electron from an outer shell. A photon with a specific energy is emitted and hits the detector simultaneously. This signature energy can be used to identify the element that the X-rays strike.

The handheld ED-XRF can essentially be used to quantify the composition of both major and trace elements real-time. For shale applications, Rowe et al. (2012) calibrated the instrument with a suite of five internationally-accepted commercial standards and 85 in-house reference materials obtained from five major US shale plays. The use of a wide spectrum of natural shale rock samples greatly improves the range of elemental concentration and the calibration applicability for shale rock purposes. Major elements such as silicon, calcium and aluminum obtained can be used as proxy for minerals such as quartz, carbonate and clay. An allocation scheme for converting elemental composition to mineralogy will be introduced later in Chapter 5.

Both XRD and XRF are useful tools to quantitatively analyze the mineralogical and elemental composition of shale rocks. Both require rigorous calibration of the

specific instruments with broad range of rocks and minerals. While XRD gives direct information about the mineralogy, the hand-held XRF instrument that can effectively quantify the elemental composition of shale samples in real-time has attracted significant interest from the industry lately. To understand shale-fluid interactions, the mineralogy is one of the very basic properties that we need to start with.

2.2.3. Organic Matter

The organic materials in hydrocarbon bearing shales were formed as a result of the deposition of algae-, plant- and animal-derived organic debris (Ground Water Protection Council and ALL Consulting, 2009). The properties pertinent to the organic matter include the total organic carbon (TOC), the thermal maturity (vitrinite reflectance) and organic matter type (Passey et al., 2010).

The measurement of TOC content is usually the first step to assess a potential resource play, after which the kerogen type and thermal maturity will be analyzed. To determine the TOC content of shale samples in the lab, the Leco and the Rock-Eval/TOC methods can be used (Jarvie, 1991). For the Leco method, the organic carbon is converted to carbon dioxide, which is detected by an infrared (IR) detector or a thermal conductivity detector (TCD). The Rock-Eval/TOC method is a combination of the Rock-Eval pyrolysis technique and an oxidation cycle. For Rock-Eval pyrolysis, the free hydrocarbon and cracked kerogen content are obtained with progressively heating the rock sample. The remaining TOC is then captured with the oxidation of the already pyrolyzed rock. Threshold TOC content can be used to evaluate the potential of a shale formation as a resource play. A criterion of 2% TOC was applied to define prospective resource plays in Poland (U.S. Energy Information Administration, 2013). This higher

TOC content criterion can reduce the prospective area and quantity of the estimated resources.

The thermal maturity of shale is measured with vitrinite reflectance (%Ro). Slightly different cutoffs for oil window, wet gas and dry gas windows are reported in the literature (Jarvie et al., 2005; U.S. Energy Information Administration, 2013). Table 2.3 shows an example used for assessing the hydrocarbon production potential for the Barnett shale. It is evident that the vitrinite reflectance cutoff for the oil and wet gas window differ by 0.15% with oil and condensate-wet gas windows. For the case of core samples, the oil window is between 0.55% and 1.15% Ro, the condensate-wet gas window is between 1.15% and 1.40% Ro, and the dry gas window is greater than 1.40% Ro.

Maturity	Cutting VR_o values	Core VR_o values
Immature	<0.55% VR_o	<0.55% VR_o
Oil window (peak oil at 0.90% VR_o)	0.55% to 1.00% VR_o	0.55% to 1.15% VR_o
Condensate-wet gas window	1.00% to 1.40% VR_o	1.15% to 1.40% VR_o
Dry gas window	>1.40% VR_o	>1.40% VR_o

Table 2.3: Guidelines for thermal maturity assessment for the Barnett shale with vitrinite reflectance (adapted from Jarvie et al., 2005).

The organic material in oil and gas shales consists of kerogen and bitumen. Bitumen is soluble in organic solvents and is formed from the insoluble kerogen. In general, kerogen has a higher molecular weight than bitumen. Oil and gas can be extracted from kerogen upon sufficient heating. Kerogen can be classified into different types based on the ratios of hydrogen to carbon and oxygen to carbon. Type I kerogen has a high hydrogen to carbon ratio (~1.5) and a low oxygen to carbon ratio (<0.1) (Peters and Moldowan, 1993). Oil can be produced from Type I kerogen. Type II kerogen has a hydrogen to carbon ratio between 1.2 and 1.5. Both oil and gas can be produced

from Type II kerogen. Type III kerogen has a low hydrogen to carbon ratio (<0.1) and high oxygen to carbon ratio (up to ~0.3). Natural gas can be produced from Type III kerogen. The generation of gas condensate is also possible if the thermal maturation is adequate. Type IV kerogen is has low hydrogen to carbon ratio (<0.5) and relatively high oxygen to carbon ratio (0.2 – 0.3). Type IV kerogen does not have potential for hydrocarbon production.

2.2.4. Porosity and Pore Size Distribution

Porosity and pore size distribution of shale rocks significantly affect the flow of hydrocarbon in the reservoir and the penetration of drilling and fracturing fluids in the near-wellbore regions. The porosity of shale is usually less than 10% (Ground Water Protection Council and ALL Consulting, 2009). It varies greatly from play to play. For example, the Marcellus shale typically has matrix porosity between 0.5% and 5% (Myers, 2008). However, a porosity of 9% was reported in West Virginia (Soeder, 1988). On the other hand, the average matrix porosity of the Barnett shale is 6% (Bowker, 2007). There is also significant microporosity and mesoporosity in shales due to the presence of clays and organic material (Padhy et al., 2007; Clarkson et al., 2012a). Therefore, to characterize shale porosity, inorganic porosity and organic porosity should be looked at separately.

The inorganic pores in shales are similar to those in conventional rocks. The only difference is the much smaller size of the pores in shales due to the abundant presence of fine-grained clay and silt particles. On the other hand, Loucks et al. (2009) found that most nanopores are associated with organic materials in Barnett shale. They also suggested that thermal maturity of the organic material, together with other factors, such as organic matter composition, contributes to the development of organic porosity, which

was also supported by Curtis et al. (2012). Like other petrophysical properties, the proportions of inorganic and organic pores in a shale rock also vary greatly from one formation to another. Loucks et al. (2009) classified the nano-pores in shales into three groups: 1) intra-particle pores in organic matter; 2) inter-particle pores between organic matter; 3) pores in the impermeable shale matrix unassociated with organic matter. The intra-particle organic nano-pores and the microcrystalline inorganic pores in the shale matrix were believed to be the contributors to gas storage in the Barnett shale (Loucks et al., 2009).

Several advanced analytical techniques have been employed to characterize the pore structure of shales. Atomic force microscopy (AFM) has been used to image pores as small as 5 nm (Javadpour, 2009; Javadpour et al., 2012). The advantage of using AFM is its ability to provide a three-dimensional image of the shale surface topography and it is non-destructive. Figure 2.2 shows an AFM image of nano-pores and nano-grooves in a shale sample. These nano-pores and nano-grooves are distinct at a nanometer scale. Scanning electron microscopy (SEM) together with focused ion beam (FIB) is another key technology to image the nano-pores in shale rocks. The argon-ion-beam milling technique enables the creation of a flat surface without surface topography, which is critical for high-magnification imaging (Loucks et al., 2009). Fig 2.3 shows the SEM images of shale samples from 9 major shale plays in North America. The darker porous holes represent kerogen. The 2D SEM images can be stacked to visualize a 3D volume of shale specimens. Figure 2.4 shows the 3D volumetric visualization of a shale sample and volume rendering of the pore space from stacking a series of 2-D FIB-SEM images (Josh et al., 2012).

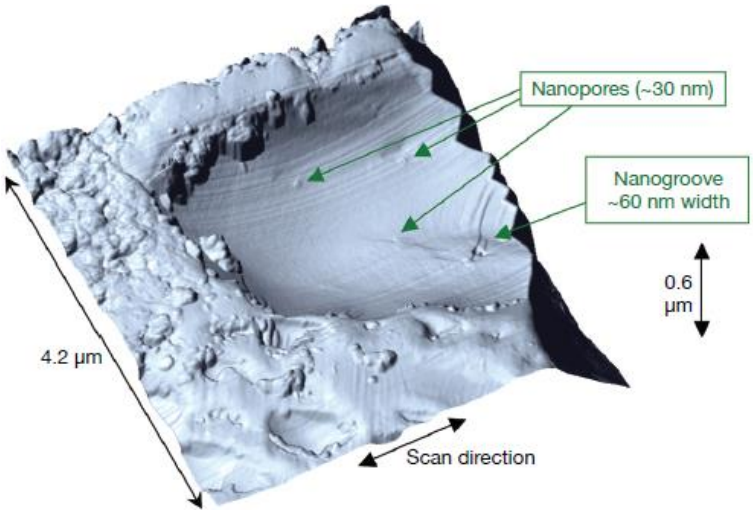

Figure 2.2: An AMF image of nano-pores and nano-grooves in a shale sample (Javadpour, 2009).

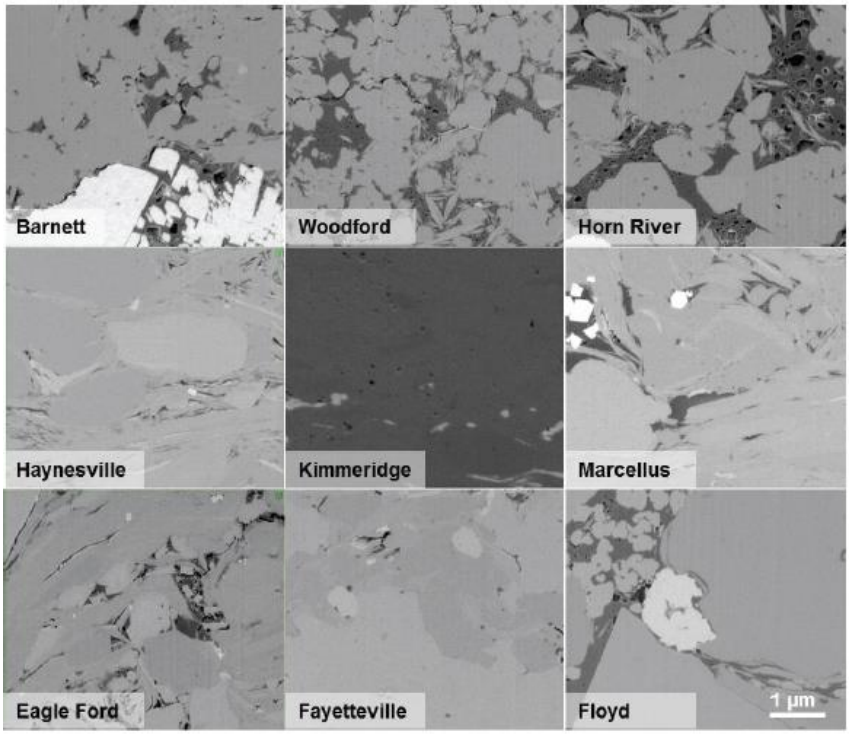

Figure 2.3: SEM images of 9 shale samples. The darker porous holes are kerogen (Curtis et al., 2010)

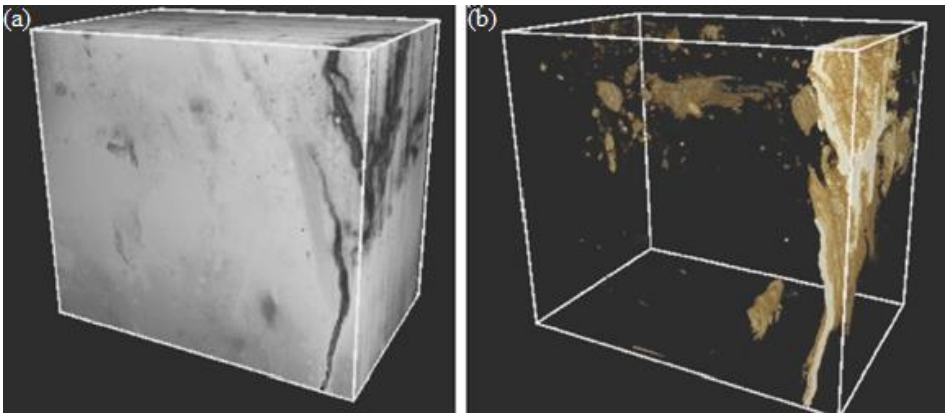

Figure 2.4: (a) 3D volumetric visualization of a shale sample from stacking a series of 2-D FIB-SEM images; (b) Volume rendering of the pore space from the stacked 3D FIB-SEM volume in (a) (Josh et al., 2012).

It is very difficult to characterize the pore size of shale samples with a single conventional analytical method because of the wide range of pore sizes present in shales. According to IUPAC recommendations, micropores have diameter smaller than 2 nm, the diameter of mesopores is between 2 nm and 50 nm, and the diameter of macropores is greater than 50 nm (Sing et al., 1985). Combined nitrogen gas adsorption (N_2GA) and mercury injection capillary pressure (MICP) were shown to be successful in characterizing the pore structure of low permeability mudrocks (Clarkson et al, 2012a & 2012b; Schmitt et al., 2013). N_2GA is suitable for characterizing the meso- and micropores while MICP can be applied to investigate the distribution of meso- and macropores. The complete pore size distribution can be obtained when these two techniques are used together. For N_2GA, crushing the shale samples is recommended because of their small pore size. Also, BJH inversion technique is preferred over the DFT inversion (Kuila and Prasad, 2013a).

Nuclear magnetic resonance (NMR) has also gained significant attention from the industry for characterizing pore structure and pore fluid distribution in shale rocks. Low-

field proton NMR responds to the presence of hydrogen nuclei in liquid and gas in the pore space, but not in the rock matrix. The measured longitudinal and transverse relaxation times (T_1 and T_2) of hydrogen nuclei in rocks are functions of pore size, pore materials and pore fluid (Kleinberg, 1999). The T_2 for an individual pore and its pore fluid is described as:

$$1/T_2 = 1/T_{2bulk} + 1/T_{2surface} + 1/T_{2diffusion} \quad (2.8)$$

where T_{2bulk} is the bulk relaxation, $T_{2surface}$ is the surface relaxation time and $T_{2diffusion}$ is the diffusion relaxation time. T_{2bulk} is a function of the pore fluid viscosity. $T_{2surface}$ is affected by the interaction between the pore wall and the wetting fluid, and is a function of the pore size. The shorter relaxation mechanism between the bulk relaxation and the surface relaxation is the dominant relaxation mechanism. Josh et al. (2012) pointed out that NMR relaxation time can be used to characterize the pore size distribution of shale if fast diffusion and uniform pore surface relaxivity for the entire sample are assumed.

2.2.5. Fluid Saturation

The in-situ fluid saturation of hydrocarbon-bearing shales plays a crucial role in resource evaluation and project economics. For conventional rocks, the Dean Stark toluene extraction and retort are two commonly used methods for fluid saturation determination (API, 1998; Sondergeld et al., 2010; Handwerger et al., 2012). The Dean Stark method utilizes boiling toluene to extract the in-situ fluid, while for a retort, fluid is extracted from rock samples through sequential heating. Unfortunately, these methods are not particularly well suited for saturation determination of shale because of the abundant presence of clay, low porosity and small amount of fluid in the pore space. Handwerer et al. (2012) found that for the same shale, the Dean Stark results show significantly higher

water saturation than the retort results. The discrepancy could be due to the structural water associated with clay that the Dean Stark method is able to extract.

More recently, NMR has shown the potential for determining the shale fluid saturation as well. Cutoffs assigned to T_2 can be used to distinguish free and bound fluids (Rylander et al, 2013). In addition, the fact that T_1/T_2 ratio is a function of the viscosity of the pore fluid can be used to differentiate the presence of water or hydrocarbon in the pore space (Rylander et al, 2013; Daigle et al., 2014). Together the unique characteristics of T_1 and T_2 response to the presence of different pore fluids points to the potential of NMR to quantify the fluid saturation in shale pore spaces.

2.2.6. Wettability

The rock surface wettability is another important petrophysical property that impacts the oil and gas flow in porous media and the penetration and flowback of fracturing fluid in shale reservoirs. There is a great deal of variation in the wettability of hydrocarbon bearing shale rocks (Borysenko et al., 2009). Shale samples from different plays can be water-wet, oil-wet or mixed-wet. Mineralogy was found to have a significant influence on shale wettability (Borysenko et al., 2009). Illitic and smectic shales tend to be hydrophilic and kaolinitic shales are likely to be hydrophobic. Hydrophilic clay minerals have the potential to become hydrophobic upon contact with crude oil.

Similar to conventional rocks, the wettability of shales is determined with contact angle, spontaneous and forced imbibition experiments. For contact angle measurements, a smooth surface is required to minimize hysteresis due to the topography on the rock surface. For the imbibition tests, the imbibition rate will be much slower for shales due to their small porosity and permeability. NMR and dielectric measurements are two of the

more recently developed techniques to characterize shale wettability (Borysenko et al., 2009; Odusina et al., 2011; Josh et al., 2012). NMR is used to detect the saturation of pore fluid in the shale pore space and can be applied during the imbibition process to investigate the movement of oil and water. The dielectric constant measures the polarizability of the rock samples. The dielectric constant can be correlated to the water saturation and mineral composition.

2.2.7. Cation Exchange Capacity

As previously described, the unique characteristics of shale rocks compared with other conventional reservoir rocks such as sandstone or carbonate arise from the presence of significant amount of clay minerals in shales. Clay is hydrous aluminum silicate where other metal atoms such as magnesium, potassium, sodium and iron can also be part of the crystalline lattice structure (Lake, 1989). In fact, the diagenesis process results in Al^{3+} being replaced by lower valence cations such as Mg^{2+} or K^{+}. Subsequently, the clay becomes negatively charged and requires cations in the pore fluid to neutralize the excess negative charges. The cation exchange capacity (CEC) is then defined as either the concentration of these negative charges (Lake, 1989), or the concentration of cations adsorbed on the clay to balance the negative charges (Caenn et al., 2011). These two definitions are essentially the same, because both of them refer to the charge concentration of clay and its capacity to form bonding with cations. The unit of CEC is milliequivalents (meq) per unit mass of substrate, which is clay in this case. The typical CEC values for common clay minerals such as montmorillonite, illite and kaolinite are 700 – 1300, 200 – 400 and 30 – 150 meq/kg of dry clay respectively (Grim, 1968). A high CEC (e.g. montomorillonite) indicates that the clay mineral is reactive and swells rapidly and vice versa.

In general, the cations with higher valence tend to have stronger bonds with the negatively charged clay and are more likely to replace the cations with lower valence in clay. The relative ease of cation adsorption on clay is as follows (Hendricks et al., 1940):

$H^+ > Ba^{2+} > Sr^{2+} > Ca^{2+} > Cs^+ > Rb^+ > K^+ > Na^+ > Li^+$

It is worth noting that the H^+ can be strongly bonded to the negatively charged clay and as a result, pH has a significant impact on the ability of clay to exchange cations.

In the laboratory, the CEC can be determined by leaching two samples of the clay, one with a suitable salt (e.g. ammonium acetate) and the other one with distilled water (Caenn et al., 2011). The ammonium acetate will remove cations in both clay and the interstitial water, while distilled water will only remove that in the interstitial water. The difference in cation type and concentration can be compared to give the individual exchanged cation concentration and the CEC. The CEC of shales can also be determined with the same measurement.

2.2.8. Membrane Efficiency

Unlike sandstone and carbonate formations, when shale is drilled, no mud cake is formed because the permeability of shale is lower than that of the mudcake. Therefore, shale itself is widely perceived as a semi-permeable membrane limiting osmotic flow (Zhang et al., 2008). However, in reality, when shale interacts with water-based fluid, not only does water move into and out of shale, but ions also are exchanged. As a result, the osmotic effect generated by shale-fluid interactions is affected by both water and ion movement into and out of the shale (Zhang et al., 2004). The concept of shale membrane efficiency was introduced to quantitatively investigate shale's ability to prevent ionic flow across it. Its value lies between zero and one. If ionic flow can be completely stopped, the shale membrane efficiency is said to be one. On the other hand, if ions can

flow without any resistance, the shale membrane efficiency is zero (Stenson and Sharma, 1989; Zhang et al, 2004).

The membrane efficiency of shale has been measured extensively in the past two decades with the pressure transmission technique (van Oort et al., 1996; Ewy and Stankovich, 2000; Mody et al., 2002; Schlemmer et al., 2003; Zhang et al., 2008). The results show that the measured shale membrane efficiency with various salt solutions was very low (<10%). Moreover, Zhang et al. (2008) revealed that the shale membrane efficiency is negatively correlated with shale permeability and positively correlated with cation exchange capacity. They further determined the membrane efficiency of shale with oil based muds. Since the semi-permeable membrane characteristics are displayed by the mud, the membrane efficiency of oil-based muds is used as that of the shale. As expected, the membrane efficiency of oil-based muds is much greater than that of shale with water-based fluids.

2.3.SHALE MECHANICAL PROPERTIES

Shale mechanical properties such as Young's modulus, Poisson's ratio, acoustic wave velocity and Brinell hardness are becoming increasingly important for the development of shale reservoirs. These mechanical properties are critical in well design and the planning and execution of hydraulic fracturing jobs. Not only are the mechanical properties of native shales of great interest to the industry, significant efforts have been devoted to investigate the changes in these mechanical properties when shale is in contact with water-based drilling and fracturing fluids. Although field-measured stress state such as the magnitude and direction of the three principal stresses is of paramount importance for fracturing planning, the focus of this dissertation is on the laboratory-based mechanical properties measurements. An overview of the laboratory-determined shale

mechanical properties will be presented in this section. The effect of shale-fluid interactions on these mechanical properties will also be discussed.

2.3.1. Young's Modulus

It is usually assumed that rock behaves as a linear elastic material. For an isotropic medium, Young's modulus and Poisson's ratio are the most commonly used elastic constants to describe the rock properties. Together, they are used to indicate the brittleness of rocks (Rickman et al., 2008). Young's modulus is the ratio of the uniaxial stress to the strain in the same direction. In Cartesian coordinate system, if stresses in the y- and z-directions are equal and constant, the Young's modulus, E, can be calculated as:

$$E = \frac{\sigma_x}{\varepsilon_x} \tag{2.9}$$

where σ_x is the uniaxial stress in the x-direction and ε_x is the strain in the x-direction.

Young's modulus can be measured in the laboratory in two ways. One way is to use the triaxial compression test. A cylindrical core with radial confining stress equal to the mean effective stress on the rock is normally compressed in the axial direction. The static Young's modulus is determined with the slope of the stress-strain curve. The term "static" is used because the load is applied at a low frequency. The corresponding dynamic properties measurement will be discussed later in Section 2.3.3.

For the static triaxial test, the ratio of the cylindrical core's length to diameter is preferably greater than two (Sondergeld et al., 2010). A variety of factors can impact the static Young's modulus measurement (Gidley et al., 1989). These factors include the confining stress, the moisture content of the rock, the strain rate during the compression test, and the coring process in the field and the sample preparation procedure in the laboratory. The presence of cracks in the rock sample can significantly impact the measured static Young's modulus as well. Because the shape of the stress-strain curve of

a rock during a compression test is not linear, there is no unique static Young's modulus for a rock. Two static moduli, the tangent and the secant moduli, are usually obtained. By definition, the tangent modulus is the slope of the tangent line to the stress-strain curve at a particular stress. On the other hand, the secant modulus is the slope of the straight line connecting the origin and the point at the stress of interest.

The Young's modulus is one of the most important rock mechanical properties. It is a measure of rocks' ability to resist deformation and thus sustain a conductive fracture after it is propped (Rickman et al., 2008). It is used as an input for computing the fracture pressure and width. It differs from rock to rock and can affect the length and height of the fracture created. Britt and Schoeffler (2009) concluded that prospective shale plays need to have a static Young's modulus greater than 3.5×10^6 psi. When water-sensitive shale comes into contact with drilling and fracturing fluid, the Young's modulus can be greatly affected. Wong (1998) observed that the Young's modulus of La Biche shale in West Canada decreased with increasing swelling caused by water/brine contact. He attributed the fact that confining stress does not affect the Young's modulus of intact shale to strong cementation. The same confining stress independence of Young's modulus was also observed by Sondergeld et al. (2010). Remvik and Skalle (1993) reported a reduction of 20% - 60% of undrained Young's modulus for shale samples after contact with deionized water, KCl and cellulose at 70^oC and 120^oC.

2.3.2. Poisson's ratio

Like Young's modulus, Poisson's ratio is also one of the most important rock elastic properties. Both of these elastic moduli are related to the axial strain when an axial stress is applied to a rock sample. Poisson's ratio is defined as the negative ratio of

radial/lateral to axial strain. In a Cartesian coordinate system, the Poisson's ratio, ν, can be calculated as:

$$\nu = -\frac{\varepsilon_y}{\varepsilon_x} = -\frac{\varepsilon_z}{\varepsilon_x} \tag{2.10}$$

where σ_x, σ_y, and σ_z are the strains in the x-, y- and z-directions respectively.

Poisson's ratio is usually measured in the laboratory together with Young's modulus. Therefore, both static and dynamic measurements can be performed on the rock to determine its Poisson's ratio. Both these elastic moduli are affected by stress or strain amplitude and frequency (Tutuncu and Sharma, 1992a, 1992b; Gidley et al., 1989).

The Poisson's ratio controls the stress in a layer and, therefore, the fracture-width distribution in each layer. As documented by Gercek (2006), typical values of Poisson's ratio lie between 0.05 and 0.325. Wong (1998) noted that Poisson's ratio is not a function of confining stress or swelling strain. However, Sondergeld et al. (2010) reported that Poisson's ratio increases with confining stress. Bustin et al. (2009) observed that Poisson's ratio as well as Young's modulus depends on the mineralogy and rock fabric, which is a function of sedimentology, diagenesis and tectonics. Little information regarding the effect of shale-fluid interactions on the Poisson's ratio of shale can be found in the literature.

2.3.3. Acoustic Wave Velocity

As mentioned in Sections 2.3.1 and 2.3.2, besides the static method, the rock elastic properties can also be determined dynamically with an acoustic wave velocity measurement in the laboratory. The term "dynamic" refers to the high frequency of loading. A typical load frequency of 1 MHz is applied to the rock sample for the acoustic wave velocity measurement.

Two types of wave velocities, the P-wave and S-wave velocities, are usually measured with rock samples. The mode of propagation for P-wave, or the compressional wave, is longitudinal, which means the wave propagates parallel to the direction of particle oscillations in the elastic medium. On the other hand, S-wave, or the shear wave propagates transversely. The direction of wave propagation is perpendicular to the direction of particle oscillations. Together, P-wave and S-wave velocities can be used to determine the rock elastic properties, because the elastic properties of the medium dictate how waves propagate through it.

When a rock sample is subject to dynamic loading, the P-wave and S-wave transit times will be measured. The subsequent P-wave and S-wave velocities can be calculated with the length of the rock sample:

$$v_p = \frac{l}{t_p} \tag{2.11}$$

$$v_s = \frac{l}{t_s} \tag{2.12}$$

where l is the length of the sample, v_p and v_s are P-wave and S-wave velocities and t_p and t_s are P-wave and S-wave transit times respectively. The dynamic Young's modulus and Poisson's ratio can then be calculated if we assume the rock behaves as a linear elastic medium:

$$E = \frac{v_s^2 \rho \left[3\left(\frac{v_p}{v_s} \right)^2 - 4 \right]}{\left[\left(\frac{v_p}{v_s} \right)^2 - 1 \right]} \tag{2.13}$$

$$\upsilon = \frac{1}{2}\frac{\left[\left(\frac{v_p}{v_s}\right)^2 - 2\right]}{\left[\left(\frac{v_p}{v_s}\right)^2 - 1\right]} \tag{2.14}$$

where E is the Young's modulus, ν is the Poisson's ratio and ρ is the density of the rock.

Acoustic wave velocity measurements were performed on rock samples in the laboratory as early as more than half a century ago (Hughes and Jones, 1950; Hughes and Cross 1951). It was observed that wave velocities increase with stress and decrease with temperature (Hughes and Jones, 1950). Very few measurements of acoustic wave velocities on shales existed in the early days because of the friable nature of shale and a shortage of high quality samples (Jones and Wang, 1981). Kaarsberg (1959) observed that the wave velocities of naturally occurring shales increase with their density and depth of burial. Podio et al. (1968) and Jones and Wang (1981) reported that wave velocities of shale increased with stress level, which is similar to Kaarsberg's (1959) conclusions. Both studies also noted the anisotropic nature of the elastic properties of shales from the measured wave velocities. Podio et al. (1968) further concluded that the subsequent dynamic Young's modulus also increased with stress level.

The effect of fluid saturation on shale acoustic wave velocities has also been extensively investigated. Both Podio et al. (1968) and Jones and Wang (1981) concluded that the P-wave velocity increases while the S-wave velocity decreases with water saturation. Podio et al. (1968) also reported that the increase in P-wave and S-wave velocities with confining stress is more pronounced when the shale sample is water saturated rather than dry. Vernik and Liu (1997) attributed the effect of NaCl saturation on shale wave velocities to significant chemical softening of swelling clay. On the other hand, they related the effect of oil saturation on shale wave velocities to the mechanical

pore fluid compressibility rather than the chemical swelling behavior. Popp (2004) studied the effect of water activity on shale wave velocities and found that both P-wave and S-wave velocities decrease with increasing water activity. The subsequent dynamic Young's modulus decreases while the Poisson's ratio increase with increasing water activity.

Extensive research has been conducted on the relationship between dynamic and static elastic moduli of rocks. For static experiment, the strain can be up to 0.01 while for dynamic measurement, the strain is about 10^{-7}. Eissa and Kazi (1988) found that the static and dynamic moduli are not well correlated. They suggested an empirical relationship between the logarithmic of static Young's modulus and the logarithmic of the product of dynamic Young's modulus and density, with a coefficient of 0.96. Tutuncu (1992) observed that the dynamic moduli of sandstone are 1 to 6 times greater than the static moduli under stress after sample length correction. She also noted that the difference between the dynamic and static moduli decreases with increasing stress. The major mechanism for such contrast is believed to be grain contact micromechanics. Furthermore, she also believed that the difference between the static and dynamic Young's modulus can be due to their different strain amplitudes. Yale and Jamieson (1994) developed corrections for dynamic to static mechanical properties correlations for clastic rocks based on lithofacies. They also reported good correlations between static and dynamic Poisson's ratio for liquid saturated samples. They dynamic properties were log-based. Britt and Schoeffler (2009) further pointed out that for shales to be prospective, dynamic to static Young's modulus correlation needs to be consistent with that of clastic rocks.

2.3.4. Brinell Hardness

Hardness is a material property that indicates its resistance to permanent deformation. The hardness of hydrocarbon bearing shales is a very important mechanical property related to proppant embedment in shale reservoirs. When shale interacts with water-based fracturing fluids, it swells and becomes soft. Subsequently, proppant will be embedded on the shale fracture surface, resulting in the reduction in fracture width and conductivity. In fact, hardness was recognized as a direct measure of rock deformation and embedment potential of proppant in the oil and gas industry long time ago (Huitt and McGlothlin, 1958).

Material hardness can be measured in a variety of ways, such as the more commonly known static indentation test, the rebound test and the scratch file test (Chandler, 1999). In the oil and gas industry, the indentation test is widely utilized, which includes the Brinell, Vickers and Rockwell testing. The Brinell test, originally proposed by Johan August Brinell in Sweden in 1900 (Brinell, 1900), involves the use of a spherical indenter to deform the flat testing surface plastically. The load and the corresponding area of the spherical impression are used to compute the Brinell hardness:

$$HBN = \frac{L}{A} \tag{2.15}$$

where HBN refers to the Brinell hardness, L is the load and A is the area of the spherical impression. Similarly, the Vickers hardness test employs a square-based pyramidal indenter to deform the smooth surface of interest (Das, 1974). The hardness is also calculated as the ratio between load and the area of the impression. The Rockwell test measures the depth of penetration of a conical or spherical indenter when a larger load is applied to the testing material after an initial preload (Chandler, 1999). Santarelli et al. (1991) examined the applicability of a wide range of testing methods for measuring the hardness of rocks and concluded that the Brinell test has the potential for rock core

mechanical testing. Kurz et al. (2013) also compared different hardness test methods and found that the Brinell technique is more suited for rock samples. Similar testing procedure was employed by Chenevert and Dwarakanath (1993) for shale hardness measurement. Halleck et al. (1995) also adopted the Brinell test to measure the rock hardness reduction in a perforation zone in a weak rock. More recently, nano-indentation has been adopted to overcome the problem of sample shortage for adequate statistical sampling for quantifying shale mechanical properties (e.g. Kumar et al., 2012). The dimension of nano-indenters is in the submicron scale.

The hardness of rock depends on a number of its intrinsic properties, such as the mineralogy, grain size, plastic behavior and modulus of elasticity (Atkinson, 1993). Van der Vlis (1970) pointed out that the sample heterogeneity affects the reproducibility of the hardness measurement directly. Big variations in local hardness can exist for even visually homogeneous samples. Boutrid et al. (2013) attributed the observed reduction in Brinell hardness test repeatability with higher clay content of the rock to greater variation in the grain size. Santarelli et al. (1991) and Chenevert and Dwarakanath (1993) obtained good correlation between the Brinell hardness and uniaxial compressive strength for homogeneous reservoir rocks and shales respectively. Similar observation was reported by Szwedzicki (1998) for ultramafic and basaltic rocks in Western Australia. Van der Vlis (1970) also showed an empirical correlation between the Brinell hardness and the elastic moduli of rock. Boutrid et al. (2013) reported similar correlation as well. Geertsma (1985) further demonstrated that the rock hardness is proportional the yield strength.

For practical fluid screening purposes, Kurz et al. (2013) also used Brinell hardness testing to differentiate the softening effect of exposing shale samples from the Bakken formation to fracturing fluids such as slickwater and gelled diesel. Slickwater appeared to have a greater tendency to soften the shale than gelled diesel. LaFollett and

Carman (2013) conducted pre- and post-immersion Brinell hardness measurements with shale samples from different plays and observed significant variation in terms of the softening behavior with fluids of different pH values. They recommended that Brinell hardness should be measured for received core sample and the same sample after at least 24-hour of exposure to fracturing fluids at reservoir temperature. Das and Achalpurkar (2013) revealed that mineralogy such as clay content can affect the hardness change of shale samples after exposure to 3% KCl fluid.

It is important to specify the indentation test procedure if the measured Brinell hardness values are to be compared. Santeralli et al. (1991) observed that an increase in the diameter of the spherical indenter and a decrease in the loading rate results smaller Brinell hardness. The use of large diameter indenter for the Brinell hardness testing is preferred for rocks so that the measurement scattering due to sample heterogeneity can be reduced.

2.4. SHALE SWELLING AND SOFTENING

It is well-known in the oil and gas industry that shales, whether hydrocarbon bearing or not, are highly reactive with water-based fluids. This reactivity is due to the presence of clay minerals in shales (Sharma, 2004). As a result, shales can swell and become soft after coming into contact with water-based fluids. This can lead to a variety of associated problems in completion and drilling practices. For organic shales, proppant embedment will result in the closure of hydraulically created fractures and thus reduced permeability, which in turn will negatively impact productivity. Meanwhile, drilled shales contribute to more than 90% of wellbore instability problems (Steiger and Leung, 1992), a lot of which are caused by shale's sensitivity with water-based drilling fluids. These instability issues also cost the industry significant rig time loss. It is unquestionable

that mitigating shale's reactivity with water-based fluids can save the industry a lot of money, time and manpower and enhance well productivity tremendously. In this section, an overview of the various shale swelling mechanisms will be presented. The related issues with proppant embedment in fractures and wellbore instability will be discussed. The industry's attempts to reduce the damage caused by these problems will also be studied in some detail.

2.4.1. Shale Swelling Mechanisms

Shale swelling and softening is largely due to the presence of clay minerals in it. Clays are composed of tiny crystal platelets, which in turn consist of octahedral aluminum layers and tetrahedral silica layers (Caenn et al., 2011). Cation exchange can take place within these thin layers of clay and result in the crystal surface being negatively charged. This phenomenon will cause water/ion movement in and out of shale when they are in contact. Among various clay minerals, smectite has the greatest swelling potential because of its expandable lattice structure (Caenn et al., 2011).

Extensive experimental research has shown that two mechanisms can be used to explain clay swelling: crystalline (also referred to as inter-crystalline) and osmotic (Norrish, 1954; Foster et al., 1954; Fink and Thomas, 1964; Zhang and Low 1989; Madsen and Müller-Vonmoos, 1989). Crystalline swelling (also known as surface hydration) is a result of adsorption of monomolecular water on the external surface of the clay lattice and within the interlayer space of the expanding clay (Gupta, 1987). This process of water molecule adsorption repeats to form multi-molecular water layers between clay sheets, depending on the relative humidity (RH) of the environment (Anderson et al., 2010). Crystalline swelling is known to be short-range, with typical interlayer spacing between 9 Å and 20 Å (Anderson et al., 2010). Madsen and Müller-

Vonmoos (1989) reported the swelling stress of more than 58,000 psi for the adsorption of the first water layer, nearly 16,000 psi for the adsorption of the second layer, and almost 4,000 psi for the adsorption of the third and fourth layer of water molecules for the pure montmorillonite in the Wyoming bentonite. Crystalline swelling can happen to all types of clay minerals.

On the other hand, osmotic swelling occurs because of the difference in the concentration of cations in the interlayer space of shale and in the bulk solution (Anderson et al., 2010; Caenn et al., 2011). Water is drawn from the less concentrated water-based fluid to the shale interlayer region with a higher cationic concentration. Osmotic swelling is only applicable to certain clay minerals that contain exchangeable cations (Anderson et al., 2010). For example, Na^+ saturated smectites tend to swell osmotically and cause potential wellbore instability problems such as the collapse of the borehole. However, compared with crystalline swelling, osmotic swelling can result in much larger volume increase of shales than crystalline swelling. The typical interlayer spacing for osmotic swelling is between 20 Å and ~130 Å (Anderson et al., 2010). On the other hand, for sodium montmorillonite, the swelling stress related to osmotic swelling is no more than 290 psi, much smaller than that due to crystalline swelling (Madsen and Müller-Vonmoos, 1989).

2.4.2. Wellbore Instability

When shale is drilled with water-based fluids, the balance between stress and shale strength in the subsurface is disturbed. Stress alteration happens because shale in the wellbore and the near-wellbore region is replaced by water-based drilling fluids during the drilling process. Meanwhile, the penetration of water-based fluids into shale can reduce shale strength and increase pore pressure (Lal, 1999). As a result, when the

altered stresses exceed the altered strength, the wellbore will become unstable, causing problems such as hole collapse and enlargement. In order to prevent shale wellbore instability, the imbalance between stress and strength caused by shale-fluid interactions should be minimized (Lal, 1999). This can be done through the selection of appropriate drilling fluid and additives and reduced exposure time of shale to the water-based drilling fluid (Lal, 1999).

Tremendous research effort has been devoted to understanding shale-fluid interactions and the impact on wellbore stability. Experimental work on the impact of shale-fluid interactions on shale mechanical properties has been carried out by various researchers to investigate potential wellbore instability problems. Steiger and Leung (1992) developed an experimental technique to accurately determine the shale stress-strain relationship using a triaxial test. The measurement of pore pressure during loading enables the calculation of effective stress and greatly improves the predictive capabilities of wellbore stability models. Hale et al. (1993) showed the movement of water into and out of shale due to chemical potential difference can significantly impact the wellbore stability. As a result, dehydration of shale can enhance its strength. Oil-based mud can create a semi-permeable membrane on the shale surface, resulting in selective water transport across the shale. The use of oil-based mud to reduce water inflow was echoed by Bol et al. (1994) and van Oort et al. (1996). A more detailed discussion on solutions to mitigate shale swelling and softening during petroleum operations will be presented in Section 2.4.4.

2.4.3. Proppant Embedment

During the stage of hydrocarbon production from shale reservoirs, the fracture conductivity is one of several factors that directly impact the well productivity. However,

it is challenging to sustain the fracture conductivity through the life of the well because it can be reduced through various mechanisms, including fines migration, proppant diagenesis, proppant crushing and proppant embedment on the fracture surface (Alramahi and Sundberg, 2012). The issue of proppant embedment is unique to shale reservoirs because of the high clay content in the shale rock compared with other conventional reservoir rocks. Prolonged exposure of shale to water-based fracturing fluids under reservoir conditions can significantly soften the shale and cause proppant to be embedded on the fracture surface, subsequently reducing the fracture conductivity.

Proppant embedment research in the petroleum industry took place as early as the 1950s. Huitt and McGlothlin (1958) used an indetation technique with rigid steel balls as the indenter to mimic the proppant embedment process. They investigated the effect of overburden pressure (for horizontal fractures), proppant size and concentraion on proppant embedment. Volk et al. (1981) performed embedment tests on shale and sandstones and concluded that when the proppant concentration is greater than 50% of a monolayer, the effect of closure stress on proppant embedment is similar for shale and sandstone. However, when the proppant concentration is lower than 50% of a monolayer, the increase in closure stress will result in more severe proppant embedment for shales. Alramahi and Sundberg (2012) found via embedment tests that after fluid exposure, the proppant embedment is greater for shale samples with higher clay content. However, they cautioned that proppant embedment should not be predicted sololy on the clay content of the shale rock. Other petrophysical properties, such as the porosity and TOC can affect the embedment potential of shale as well. They also observed a sharp increase in proppant embedment when the static Young's modulus of the shale is less than 6.89 GPa (1 MMpsi). Although water-based fluid (3% KCl) was used, no comparison was made with native core samples without being in contact with fluid. Pedlow and Sharma (2014)

addressed the effect of shale-fluid interactions on fracture conductivity reduction and observed that the shale mineralogy plays an important role in proppant embedment and loss of fracture conductivity. Zhang et al. (2014) reported that up to 88% of the fracture conductivity was lost due to the softening of shale sample after exposure to water. They concluded that proppant embedment is likely the dominant cause because of the much greater embedment depth after shale's exposure to water than to gas.

2.4.4. Shale Swelling and Softening Reduction

The petroleum industry has invested a lot of effort to counter shale-related wellbore instability and proppant embedment problems. Even though oil-based fluids are very effective in reducing shale swelling and softening, they are often not preferred for economic and environmental reasons. Developing additives compatible with water-based fluids has been the focus of the industry. O'Brien and Chenevert (1973) show that potassium and ammonium cations are more effective inhibitors to reduce shale swelling and dispersion than sodium, calcium and magnesium ions. At equal concentrations, the sodium, calcium and magnesium salts inhibit only 60% of what potassium and ammonium are capable of. For the case of potassium, its size and hydration energy give it the unique advantages for inhibiting shale swelling.

Quaternary amine compounds are another group of inhibitors that can reduce shale swelling and softening. Its main advantage over potassium and other inorganic salt is the low concentration required for treating reactive shales (Patel, 2009). These quaternary amine compounds are categorized into three types depending on their number of cationic charge: mono-cationic, oligo-cationic and poly-cationic. Mono-cationic amines include ammonium chloride, tetramethyl ammonium chloride (TMAC) and choline chloride. Examples of oligo-cationic and poly-cationic amines are amphoteric

amines and poly-cationic PHPA. Patel (2009) also points out that mono-cationic and poly-cationic amines have various performance limitations in terms of tolerance of pH and high temperature and toxicity, compared with oligo-cationic amines.

Other shale inhibitors include uncharged and charged polymers. Polyethylene glycol (PEG) and polypropylene oxides (PPO) are two uncharged polymers that inhibit shale swelling by disrupting the hydrogen bonding between water molecules and the silica or alumina function groups on the clay surface (Quintero, 2002). Charged polymers used as shale inhibitors may be cationic, anionic or amphoteric if both cationic and anionic groups are present (Anderson et al., 2010). In fact, the poly-cationic amines mentioned earlier is one type of charged shale inhibiting polymers.

Another way to lower shale swelling and softening is to reduce its effective permeability with pore-plugging agents (van Oort et al., 1996). Novel nanoparticle-based drilling fluids have been developed at the University of Texas at Austin to minimize the unfavorable reaction between shale and water-based fluids (Sensoy et al., 2009; Cai et al., 2012; Jung et al., 2013a).

Chapter 3: Materials and Experimental Procedures

3.1. MATERIALS

3.1.1. Preserved Shale Samples

Shale core samples used in this study were obtained from various operators and represent a wide range of gas and oil shale plays in the U.S. Normally the whole core samples are cylindrical in shape, with a diameter between 4 inches and 5 inches and length between 1 ft and 3 ft.

Since the focus of this study is on the interactions between shale and water-based fluids, it is imperative that preserved core samples be used. This is because shale tends to interact rapidly with moisture in the atmosphere. Such reactions can change the in-situ state of the shale core sample, resulting in the drying and cracking of the sample. Subsequently, the shale mechanical properties such as the strength and stiffness will also be altered (Ghborbani et al., 2009). As a result, the use of dried and cracked samples can render the test results inappropriate for making drilling and fracturing decisions. Therefore, great care needs to be taken both in the field and in the laboratory when shale samples are cored and retrieved. Ideally at the well-site, balanced activity oil-based mud should be used in the coring process to preserve the in-situ fluid saturation and prevent the cracking and disintegration of the shale cores. After the core is retrieved to the surface, it should be encased in epoxy immediately to avoid any exposure to the moisture in the atmosphere. The epoxy encapsulated whole core will then be transported to laboratories for further testing. For the core samples used for this study, they were covered by a layer of plastic wrap, followed by aluminum foil and then epoxy with a thickness of a few millimeters.

In the laboratory, the preserved shale samples from the field should be processed in a water-free environment. Oil-cooled coring machines can be used to cut the cores into a desired size for specific tests later. The prepared shale samples and unused remaining cores can be stored in cans filled with mineral oil to minimize exposure to the atmosphere. For water-wet rocks, as long as the capillary pressure is not exceeded, the mineral oil will not penetrate into the shale. Alternatively, after the native water activity of the shale is determined, the cored samples can be placed in the desiccator with appropriate relative humidity.

3.1.2. Brines

Common salts for brine preparation such as NaCl, KCl and $CaCl_2$ were obtained from Fisher Scientific. Deionized water was mixed with these salt crystals to prepare brines with various concentrations and water activities.

Simulated Eagle Ford field water was also used in this study. Its composition was based on the results from a water analysis. Table 3.1 shows the concentrations of major ions in the simulated Eagle Ford field brine.

Ion	Concentration
Fe^{2+}/Fe^{3+}	0.1 ppm
Na^{+}	39 ppm
Ca^{2+}	48 ppm
Mg^{2+}	5 ppm
Cl^{-}	60 ppm
SO_4^{2-}	19 ppm
HCO_3^{-}	146 ppm
Total Dissolved Solids	317 ppm

Table 3.1: Concentrations of major ions in simulated Eagle Ford field brine.

3.1.3. Fracturing Fluids

Water-based fracturing fluids were also used in this study to investigate the effect of shale-fluid interactions on shale mechanical properties. These chemical additives in the fracturing fluids were supplied by various service companies. The fracturing fluids were mixed in-house at the University of Texas at Austin. Tables 3.2 and 3.3 show the fracturing fluids used for the Utica and Eagle Ford shale tests, respectively.

Sol. #	Description	BC-140	LP-65	BE-9	Lo-Surf 300D	Cla-Web	GBW-30
		Buffering Crosslinker	Scale Inhibitor	Bactericide	Surfactant	Clay Control Additive	Breaker Agent
1	All Frac Components	2.00 gpt	0.25 gpt	0.50 gpt	1.00 gpt	0.50 gpt	0.25 gpt
2	All Frac Components – Clay Control	2.00 gpt	0.25 gpt	0.50 gpt	1.00 gpt	0	0.25 gpt
4	Clay Control Only	0	0	0	0	0.50 gpt	0

Table 3.2: Compositions of fracturing fluids for the Utica shale.

Fluid Type	General Description	Additive	Concentration
DI water	(resistance > 15MΩ)		
Simulated EF Field Water	DI water + salt mixture		
High pH Solution	DI water + Na_2CO_3 (pH = 11.3)		
Lewis Energy Chemicals + Simulated EF Field Water (pH = 5.6)	Scale Inhibitor	Flowsperse 1000A	0.2 gpt
	Surfactant	Smart Flow SP-3	0.5 gpt
	Shale Control	Shale Guard	1 gpt
Schlumberger Chemicals + Simulated EF Field Water (pH = 11.5)	Borate Crosslinker	J604	1.5 gpt
	Temporary Clay Stabilizer	L071	1 gpt
	Gelling Agent	U028	1 gpt
	Biocide	B244	0.5 gpt

Table 3.3: Compositions of fracturing fluids for the Eagle Ford shale.

3.2. CHARACTERIZATION OF SHALE PETROPHYSICAL PROPERTIES

3.2.1. Adsorption Isotherm Test

As described in Chapter 2, the shale native water activity is determined with an adsorption isotherm test. Controlled humidity environments are created with saturated salt solutions in de-aerated desiccators (Winston and Bates, 1960). This method ensures that only moisture enters or leaves the shale with no ion movement. The saturated salt solutions and their respective relative humidity are shown in Table 3.4. These solutions cover a wide range of relative humidity. Figure 3.1 shows a desiccator with saturated $K_2Cr_2O_7$ salt solution on the bottom.

Shale samples from the same core are placed in desiccators with different relative humidity. The weight change of these samples due to water movement is recorded as a function of time. Chenevert (1970b) pointed out that equilibrium is usually reached after two weeks, but 90% of the weight change is observed within a day. The relative humidity that results in no weight change overall is the shale native water activity.

Saturated Salt Solution	Relative Humidity
$K_2Cr_2O_7$	98%
KH_2PO_4	96%
KNO_3	92%
KCl	85%
NaCl	75.5%
$Ca(NO_3)_2$	50.5%
$ZnCl_2$	10%

Table 3.4: Saturated salt solutions and their respective relative humidity.

Figure 3.1: A de-aerated desiccator with saturated $K_2Cr_2O_7$ salt solution (red) on the bottom to store shale samples.

3.2.2. XRD and XRF

Shale mineralogy and elemental compositions are determined with X-ray diffraction (XRD) and X-ray fluorescence (XRF) respectively. For some core samples, their mineralogy was already measured before they were shipped to our laboratory; for other cores, samples were sent to Core Laboratories for XRD analysis. In general, shale samples are cleaned, pulverized and dried before being analyzed with an XRD instrument. Five grams of a sample around 4 μm in size is used for bulk mineralogical analysis while another five grams of the sample smaller than 4 μm is needed for determining the clay content. A Scintag automated powder diffractometer equipped with a copper source (40kV, 40mA) and a solid state detector is used for the XRD analysis. The whole rock samples are analyzed over diffraction angles (2θ) between 2^o and 60^o at a scan rate of 1^o/min. The clay fractions (separated by size) are analyzed over diffraction angles (2θ) between 2^o and 50^o at a rate of 1.5^o/min. The diffraction angles (2θ) of typical minerals present in shale samples are shown in Table 2-2. The depth of investigation of XRD varies from less than 5 nm to about 30 μm, depending on the mineral type, the

accelerating voltage and the beam diameter. Therefore, sample pulverization is needed so that a better representation of the shale mineralogy can be obtained.

Meanwhile, the shale elemental composition can be used as a proxy for estimating the relative abundance of minerals in shale rocks. Typically, aluminum (Al) is associated with the presence of clay, silicon (Si) is related to both quartz and clay, and calcium (Ca) represents calcite. The shale elemental composition is determined with a Bruker Tracer IV-SD System XRF Analyzer. As mentioned in Chapter 2, Rowe et al. (2012) calibrated the instrument with a suite of five internationally-accepted commercial standards and 85 in-house reference materials from five major US shale plays to enhance the range of covered elemental concentration and the calibration applicability for shale rock purposes. The advantage of using a handheld XRF over an XRD instrument is the capability of rapidly measuring the shale rock mineralogy/elemental composition. Minimal sample preparation is required for the XRF analysis; only a flat surface greater than 3 mm×4 mm with a thickness of at least 5 mm is required for the sample to ensure that all the X-rays will penetrate through the sample and the important elements will be detected with sufficient sample thickness. Table 3.5 shows the energy of emitted photon and the corresponding analysis depth for some elements during the XRF analysis. It can be seen that the analysis depth for most elements is in the sub-millimeter scale. Therefore, the measured shale elemental composition reflects the mineralogical makeup of the sample locally. A scan time of at least 60 seconds is needed and the vacuum pump must be turned on to obtain the concentration of major elements. Figure 3.2 shows the handheld XRF analyzer and the vacuum pump attached to it.

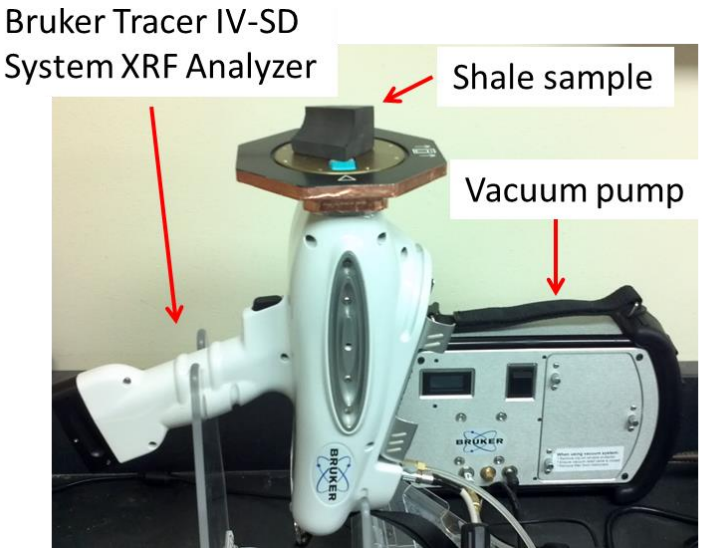

Figure 3.2: Bruker Tracer IV-SD System XRF Analyzer with a vacuum pump for determining the shale elemental composition.

Element	Energy of Emitted Photon (keV)	Analysis Depth (mm)
Na	1.04	0.007
Mg	1.2	0.0096
Al	1.47	0.017
Si	1.74	0.027
P	2.01	0.031
Ca	3.69	0.064
Cr	5.41	0.192
Fe	6.4	0.3
Cu	8.01	0.58
Zn	8.64	0.77
Pb	10.55	1.13
Zr	15.78	3.84

Table 3.5: Energy of emitted photon and the analysis depth of the XRF analysis for some elements (Kaiser, 2013).

3.2.3. Pore Size Distribution: N_2 adsorption and MICP

The complete pore size distribution of shale samples was determined with N_2 gas adsorption (N_2GA) and mercury injection capillary pressure (MICP). As described in Chapter 2, N_2GA is used to characterize the mesopores and micropores while MICP can

measure the distribution of mesopores and macropores. The N_2GA and MICP are performed with a Micromeritics 3Flex gas adsorption system (Figure 3.3) and Micromeritics Autopore III mercury porosimeter (Figure 3.4) with a maximum pressure of 412.5 MPa (60,000 psia) respectively. For N_2GA, the classical BJH model (Barret et al., 1951), based on the Kelvin equation and corrected for multilayer adsorption, relates the pressure and corresponding pore radius at which the capillary condensation of nitrogen occurs:

$$\ln\left(\frac{P}{P_o}\right) = -\frac{\alpha\sigma_{N_2}V_1}{RT\left(r_o - t\right)} \tag{3.1}$$

where P is the system pressure, P_o is the saturation vapor pressure of nitrogen (P_o = 1 atm for N_2 at 77 K), α is a shape factor for the gas/liquid interface, σ_{N_2} is the surface tension of liquid nitrogen, V_l is the molar volume of liquid nitrogen, R is the gas constant, T is the temperature of the isotherm (77K), r_o is the pore radius determined at pressure P, t is the thickness of the nitrogen gas adsorbed on the pore wall. For MICP, assuming the pores are cylindrical, the capillary pressure is related to the pore throat radius with the Washburn equation (Washburn, 1921):

$$P_c = \frac{2\sigma_{Hg}\cos\theta_{Hg}}{r_t} \tag{3.2}$$

Here P_c is the capillary pressure, σ_{Hg} is the surface tension of mercury, θ is the contact angle of mercury with the rock sample, r_t is the pore throat diameter. Schmitt et al. (2013) proposed a method to combine the N_2GA and MICP measurements to obtain the complete pore size distribution of shales. Figure 3.5 shows an example of the N_2GA and MICP (MIP as shown in the plot) experimental data that can be combined to determine the complete pore size distribution of the shale sample (Schmitt et al., 2013). In this plot, v denotes the pore volume per unit mass of the sample and D represents the pore size (diameter). The intersection of dv/dD (in this case the intersection is 85 Å) on the N_2GA

and MICP curves is the point of connection for both techniques. When D>85 Å, the pore volume from MICP is used, and when D<85 Å, the pore volume from N_2GA is used to construct the complete pore size distribution.

Figure 3.3: Micromeritics 3Flex gas adsorption system for N_2GA measurement.

Figure 3.4: Micromeritics Autopore III mercury porosimeter for the MICP measurement.

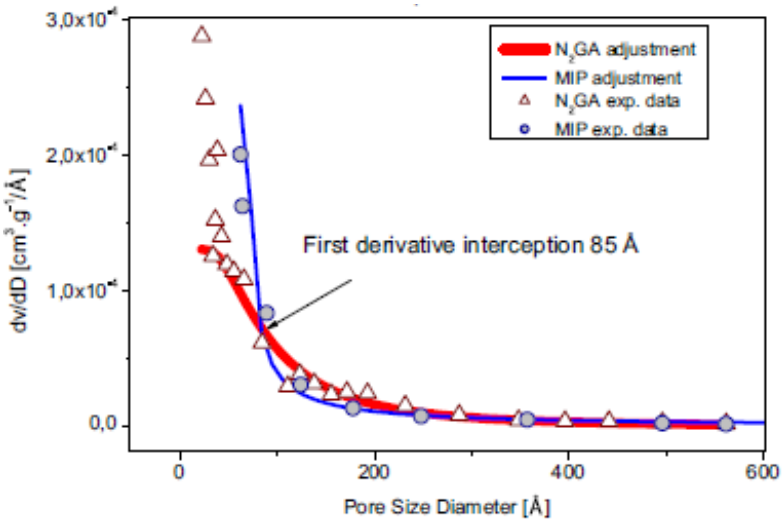

Figure 3.5: N_2GA and MICP (MIP as shown in the plot) curves used to determine the complete pore size distribution of the shale sample (Schmitt et al., 2013).

For the N_2GA measurement, the use of crushed samples smaller than 40 mesh (0.425 mm) is recommended because of the decreased path length for the gas molecules and reduced time required to reach equilibrium at 77K (Kuila and Prasad, 2013a). Crushed samples smaller than 120 mesh (0.125 mm) were used in this study. The crushed sample size is still orders of magnitude greater than the size of mesopores and micropores in shale samples.

On the other hand, larger samples can be used for MICP, as pore accessibility is not an issue for the characterization of mesopores and macropores. Samples smaller than 8 mesh (2.36 mm) were used for MICP in this study.

3.2.4. NMR

NMR T_1 and T_2 measurements were performed on preserved shale samples using an Oxford Instruments GeoSpec2 system with a frequency of 2.14 MHz at ambient conditions. T_1 and T_2 relaxation times were measured simultaneously with an inversion-recovery CPMG pulse sequence. An echo spacing of 0.086 ms was used for the CPMG

sequence. The maximum relaxation time was 1000 ms and 32 scans were averaged for each measurement to achieve a signal-to-noise ratio of greater than 100. Shale samples with weight greater than 100 g were used to improve the signal-to-noise ratio as well.

3.3. CHARACTERIZATION OF SHALE-FLUID INTERACTIONS

3.3.1 Swelling Test

The shale swelling test is an effective technique to check the sensitivity of shales to water-based and oil-based fluids. Displacement indicators are used to measure directional swelling of shales when they are immersed in the fluid of interest. Figure 3.6 shows the side view of one displacement indicator, to which a strain gauge is attached. The strain induced by the interactions of shale with fluids causes a change in electrical resistance of the strain gauge, which is measured with a Wheatstone bridge. The change in strain is recorded by the P3 strain indicator and recorder, manufactured by Vishay Precision Group. Swelling in two directions, perpendicular and parallel to bedding planes can be measured with our unique 2-D displacement indicators as a function of time. The linear swelling percentage is obtained by dividing the displacement by the original length of the shale sample and then multiplying by 100. For convenience, cubic shale samples of one inch edge length are used in all swelling tests. In this way, the displacement measured in inches can be used directly as the swelling percentage. Shale hardness and acoustic wave velocities are also measured before and after the swelling tests to investigate the effect of shale-fluid interactions on the mechanical properties changes. The results reported here were for tests conducted at ambient temperature but the test can be conducted at elevated temperature as well.

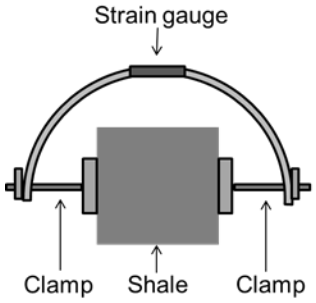

Figure 3.6: Side view of one displacement indicator with a shale sample.

3.3.2 Acoustic Wave Velocity

The acoustic wave velocity is related to the strength of shales. The P-wave (compressional wave) and S-wave (shear wave) velocities of shales are measured with a pulse transmission set-up, which consists of a pulser-receiver and an oscilloscope. An electrical pulse is generated by the pulser-receiver and is converted to acoustic waves with a transmission transducer. The acoustic waves then travel through the shale sample and are converted back into electrical signals by the receiver transducer. The electrical waveform is displayed on the oscilloscope. Dual-mode transducers with center frequencies of about 1 MHz were used in this test so that both the P-wave and S-wave transit times can be determined with the same transducer.

A viscous coupling agent is needed to make contact between the shale surface and the two transducers. To study shale-fluid interactions, an oil-based coupling agent is preferred because it does not penetrate into the shale samples to cause any alteration of the intrinsic petrophysical and mechanical properties. However, a variety of commercially available motor and engine oils were tested and none of them worked better than Molasses, a by-product from the refining of sugar cane into sugar. Molasses is water-based, so extra caution was needed to apply it onto the shale surface and avoid contamination for the acoustic wave velocity measurements. A thin layer of molasses was

coated onto the surfaces of shale and transducers before the measurement. After that, water-soaked paper towels were used to get rid of the molasses on the shale surface.

The wave velocities are calculated with the transit time displayed on the oscilloscope. The P-wave and S-wave velocities are measured perpendicular and parallel to bedding planes. For the measurement parallel to bedding planes, S-wave velocities were measured with bedding planes both perpendicular and parallel to polarization. Wave velocity measurements were performed before and after shale's contact with water-based fluids to understand of the effect of shale-fluid interactions on the dynamic properties.

3.3.3 Brinell Hardness

The shale Brinell hardness, which has potential implications for wellbore stability and proppant embedment problems, was measured with indentation techniques. A Rex multi-scale durometer (Figure 3.7) is first used to measure the Brinell hardness of shales. The durometer is equipped with different gauges that can be used on surfaces of different hardness. The shale hardness is typically measured with a type D gauge. Multiple readings are taken on the same surface and averaged. The average reading is then converted to the Brinell scale (ASTM E 140).

Figure 3.7: Rex durometer for determining the shale Brinell hardness.

The hardness obtained with the durometer is dependent on the force applied on the shale sample and the person who operates the instrument. A more reliable indentation technique was developed to investigate the hardness and Young's modulus change of shale interacting with water-based fluids. Figure 3.8 shows the experimental setup of the spherical indentation test. A hardened tungsten carbide spherical ball bearing with a diameter of 5 mm was used as the indenter. The use of large diameter indenter is to minimize the effect of surface roughness and sample heterogeneity on the measured mechanical properties.

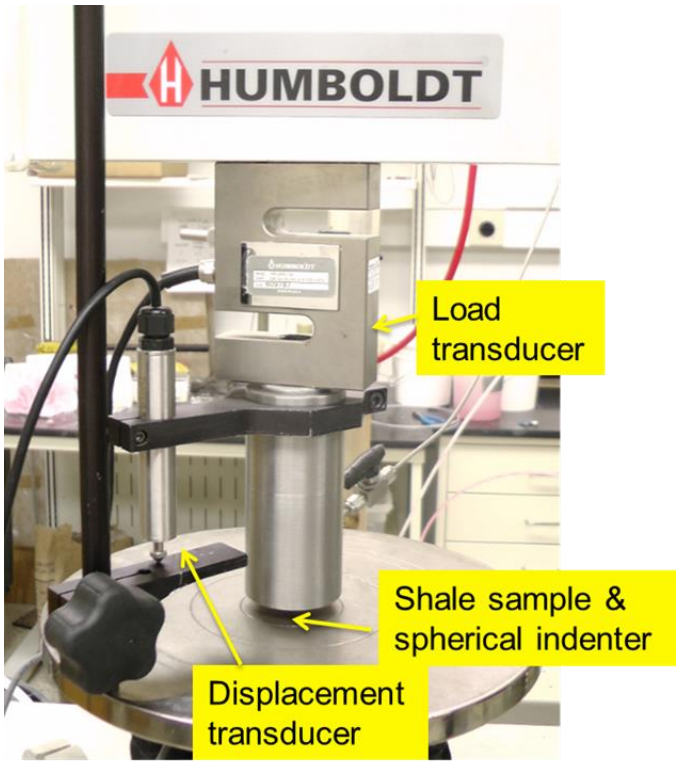

Figure 3.8: Experimental setup of the spherical indentation test.

Ideally, the shale sample used would be a circular disk with the rectangular shale in the center and the epoxy on the side (Santeralli et al., 1991; Chenevert and Dwarakanath, 1993). This would allow a clamp to be used around the circular disk to

provide confining stress, so that tensile crack formation could be delayed. However, the shortage of shale samples and the presence of laminated layers and natural fractures made the preparation of such circular disks difficult. Alternatively, shales with two parallel surfaces were used for the indentation test. The testing surface was usually sanded to make it smooth.

A constant displacement rate of 0.003 inches per minute was used in the loading and unloading process. The load and displacement were monitored and recorded simultaneously. A load not greater than 50 lbs was usually applied to avoid the creation of tensile cracks on the shale surface. The load-displacement curve is plotted and the slope of the linear part of the loading curve is used to calculate the hardness (e.g. Figure 3.9). Five measurements were taken on each sample and averaged.

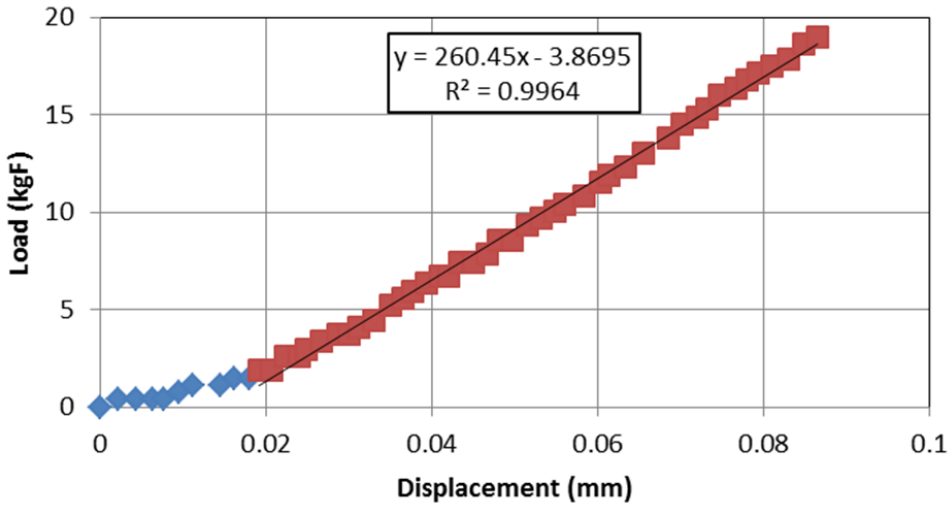

Figure 3.9: A load-displacement plot during the loading process with a spherical indenter of 5 mm diameter. The blue dots show the non-linear part of the curve at the early stage of loading and the red dots represent the linear part of the curve that is used for the Brinell hardness calculation.

According to Eq. 2.15, the Brinell hardness is defined as the ratio of the load and the area of the corresponding spherical impression:

$$HBN = \frac{L}{A} \tag{2.15}$$

From Figure 3.10, we can see that the area of the spherical impression can be calculated as:

$$A = \pi a^2 = \pi (D - d) d \tag{3.3}$$

where a is the radius of the spherical impression, D is the diameter of the spherical indenter and d is the depth of penetration. If d << D, the area of the spherical impression can be approximated as:

$$A \approx \pi D d \tag{3.4}$$

The subsequent Brinell hardness of the shale sample can be calculated as:

$$HBN = \frac{L}{\pi D d} = \frac{S}{\pi D} \tag{3.5}$$

where S is the slope of the linear part of the load-displacement curve during loading.

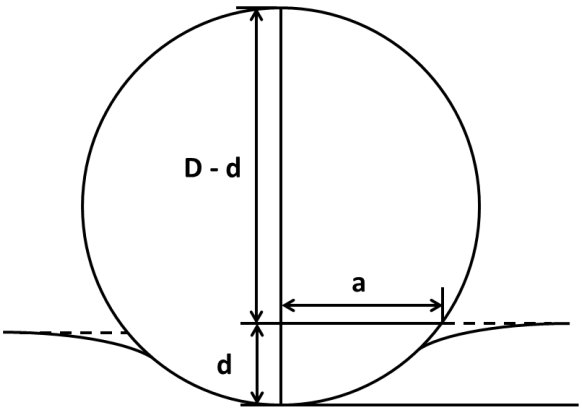

Figure 3.10: Contact geometry between a spherical indenter and the shale sample.

Meanwhile, the load-displacement curve during unloading can be used to calculate the indentation Young's modulus of the same shale sample. With the indenter

radius R_i (R_i = D/2) and the radius of the spherical impression a, the effective radius R can be calculated as:

$$R = \left(\frac{1}{R_i} + \frac{1}{a} \right)^{-1} \tag{3.6}$$

Subsequently, the slope of the linear part of the load-displacement curve during early unloading (Figure 3.11) can be related to the effective radius R and the effective Young's modulus:

$$S_{unload} = \frac{dP}{dS} = 2\sqrt{R} E_{eff} \left(h - h_f \right)^{1/2} \tag{3.7}$$

Here S_{unload} is the slope of the linear part of the load-displacement curve during early unloading, E_{eff} is the effective Young's modulus, h is the maximum displacement after loading and h_f is the permanent deformation after the load is completely recovered. The effective Young's modulus can then be related to the Young's modulus and the Poisson's ratio of the indenter and the shale sample respectively:

$$\frac{1}{E_{eff}} = \frac{1-\nu^2}{E} + \frac{1-\nu_i^2}{E_i} \tag{3.8}$$

where E and ν are the Young's modulus and Poisson's ratio of the shale sample, and E_i and ν_i are the Young's modulus and the Poisson's ratio of the indenter.

To obtain the Young's modulus of shale, the Young's modulus and Poisson's ratio of the indenter as well as the Poisson's ratio of the shale are needed. The Young's modulus of tungsten carbide is 600 – 720 GPa (Cambridge University Engineering Department, 2003), so a Young's modulus of 700 GPa was used in Eq. 3.7. Poisson's ratio of 0.24 and 0.35 were used for the tungsten carbide indenter and the shale sample respectively (source to be added).

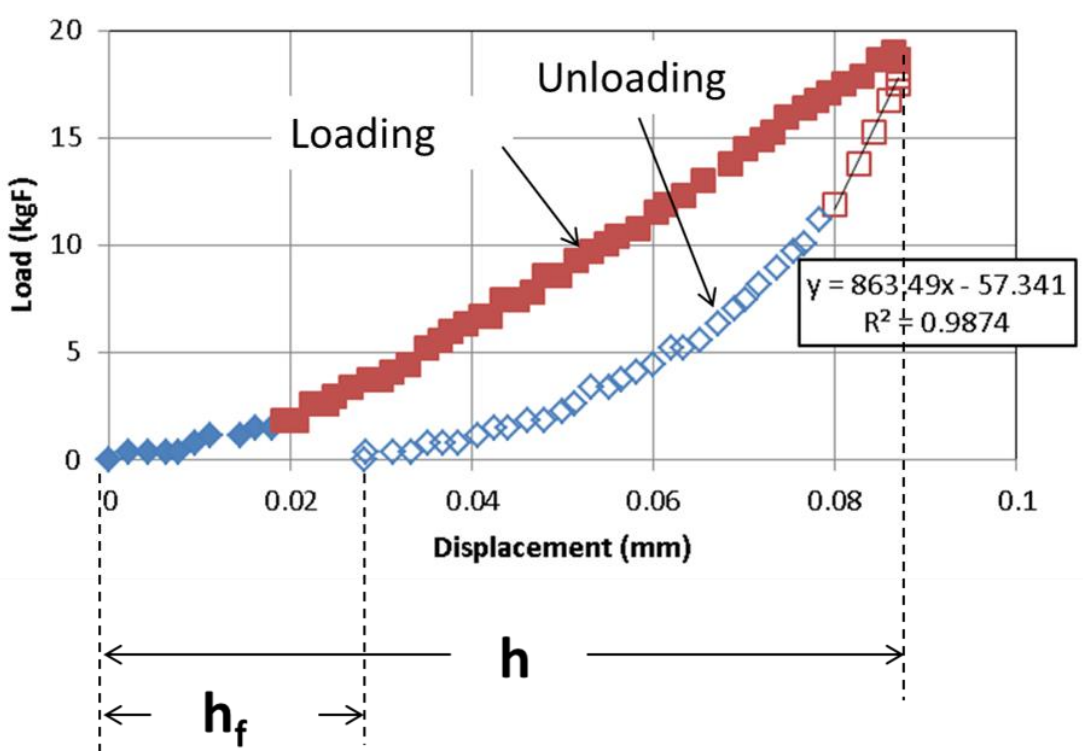

Figure 3.11: The load-displacement plot during loading and unloading with a spherical indenter of 5 mm diameter. The filled dots represent the loading process. The unfilled red dots represent the linear part of the load-displacement curve during early unloading. The unfilled blue dots represent the remaining unloading process until the load is completely recovered.

Chapter 4: Measurement of Shale Petrophysical Properties[1]

4.1. General Description of Shale Plays in the US

As mentioned in Section 2.1, the US hydrocarbon production was revived in the late 2000s, thanks to the use of horizontal drilling and hydraulic fracturing that enables the extraction of oil and gas from the previously impermeable shale rocks. Currently, more than ten shale plays are producing oil and gas in the US, and more exploration and development work is underway to unlock hydrocarbon from more shale reservoirs. Figure 4.1 shows a map of the current and prospective hydrocarbon-producing plays in the Continental US. We can see that shale gas and oil production spans large sections of the lower 48 states.

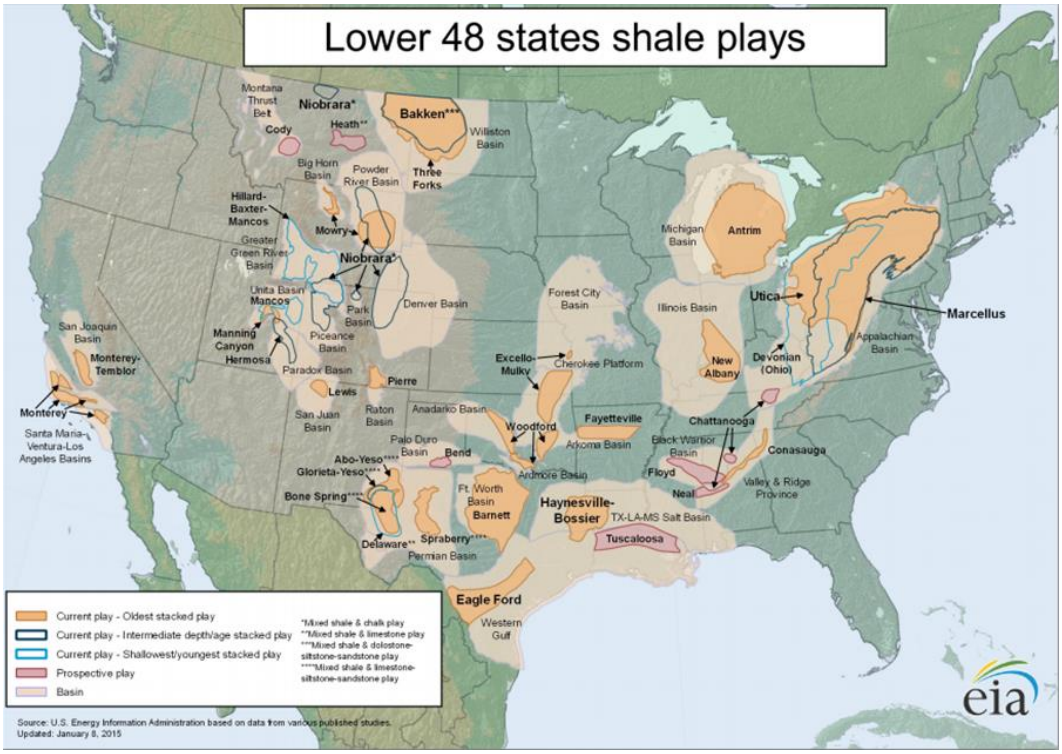

Figure 4.1: A map of the current and prospective shale plays in the US (EIA, 2015).

[1] Part of the research in this chapter was first presented in ARMA 13-546 (Zhou et al., 2013a), SPE 168792 (Zhou et al., 2013b) and SPE 166216 (Zhou et al., 2013c).

Based on the shale plays from which the core samples were received for this study, the general properties of these plays will be described below. These shale plays include Utica, Haynesville, Barnett and Eagle Ford.

The Utica shale play is a Middle Ordovician-age formation located in the northeastern US and extends into Quebec in Canada. The US part is stretched to cover the states of New York, Ohio, Pennsylvania and West Virginia. It has significant overlap with the Marcellus formation and is much deeper than the overlaying Marcellus shale. The definitive area of the Utica shale play is not available because the current exploration work is constantly extending its boundary. The depth of the Utica shale varies greatly at different locations, with the formation in Pennsylvania as deep as 14,000 ft and the boundaries in Ohio in the west and in New York in the northeast side as shallow as just 2,000 ft (Figure 4.2). Similarly, as shown in Figure 4.3, the thickness of the Utica formation also varies from place to place, with the thickness in the center of the formation over 700 ft and that gradually decreasing towards the side boundaries. A wide range of porosity up to 10% has been reported on the Utica shale (Nikhanj et al., 2014). There is also a big variation in TOC for the Utica shale, with 1 wt% to 3 wt% of TOC reported in several studies (Harper, 2011; Kirschbaum et al., 2012).

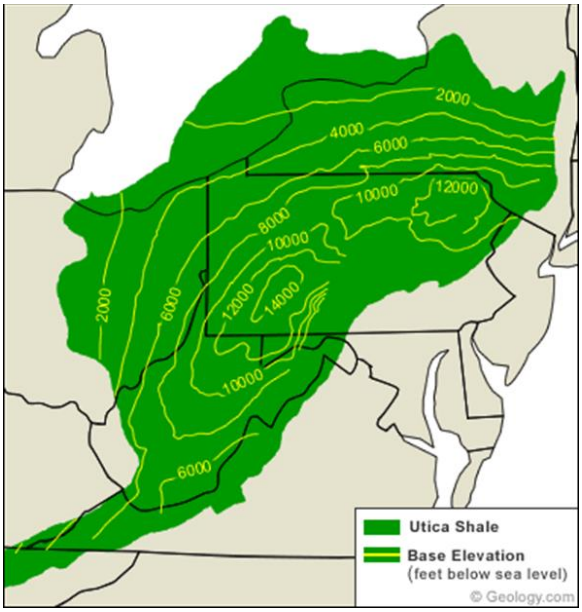

Figure 4.2: Contour map of the depth of the Utica Shale (King, 2011).

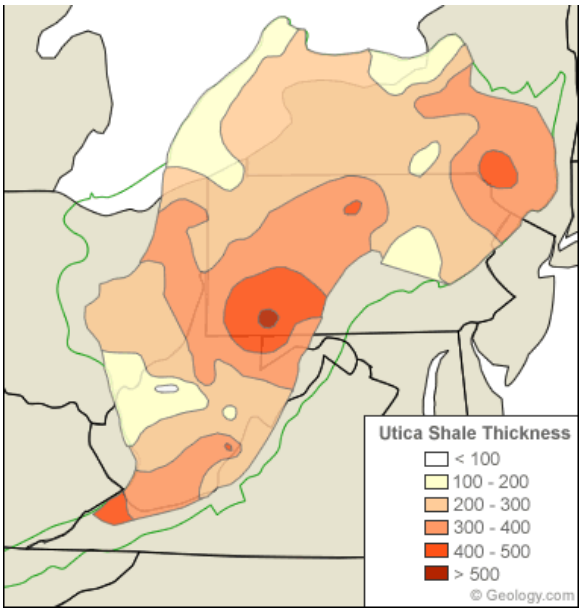

Figure 4.3: Contour map of the depth of the Utica Shale (King, 2011).

The Haynesville play, shown as "Haynesville-Bossier" in Figure 4.1, is located in east Texas and northwest Louisiana. It is a gas play and covers an area of ~9,000 square

miles (EIA, 2011). The shale reservoir in the Haynesville play is approximately between 10,500 ft and 13,500 ft in depth, with a thickness between 200 ft and 300 ft. The Haynesville shale is of Upper Jurassic age, with an average porosity of 8.5% and an average TOC of 2.25 wt% (EIA, 2011).

The Barnett shale play is to the east of the Haynesville play. It is of Mississippian age and is located in the Bend Arch-Fort Worth Basin in Texas. It has a total area of 6,458 square miles, as estimated by USGS (EIA, 2011). The average depth of the Barnett shale is 7,500 ft and the average thickness is 300 ft. It has an average porosity of 5%. The log and core measurements showed similar TOC of 4.5 wt% (Hester et al., 1990; Kuuskraa et al., 1998).

To the south of the Barnett shale in the Maverick Basin in south Texas sits the Eagle Ford formation, a Late Cretaceous age shale play. It is different from the shale plays described earlier as it contains a substantial amount of liquid hydrocarbon, which makes it a more economically valuable reservoir. Figure 4.4 shows the geographical distribution of the oil, gas condensate and gas zones in the Eagle Ford play. According to EIA (2011), the dry gas zone covers an area of ~200 square miles, while the areas of the gas condensate and oil zones were estimated to be 890 square miles and 2,233 square miles respectively. Its depth ranges from 4,000 ft to 12,000 ft, with an average depth of 7,000 ft. The reservoir thickness is between 100 ft and 300 ft, with an average thickness of 200 ft (Inamdar et al., 2010; EIA, 2011). The average porosity of the Eagle Ford shale is 9% while the average TOC is 4.25 wt% (EIA, 2011).

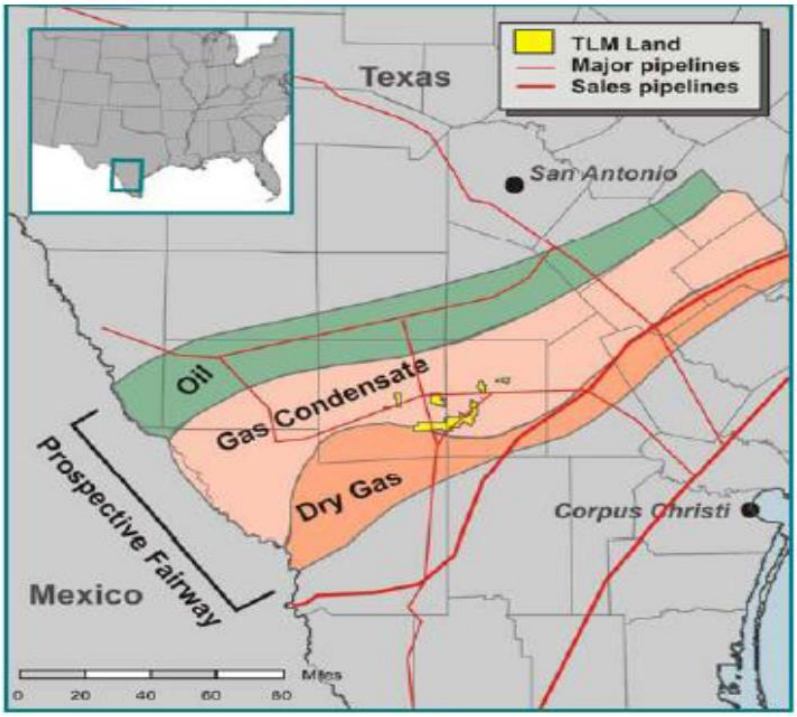

Figure 4.4: A map of the Eagle Ford shale play with the oil (green), gas condensate (pink) and dry gas zones (orange) (EIA, 2011).

The Late Devonian to Early Mississippian-age Bakken shale formation is located in the Williston Basin across the border of the US and Canada, encompassing the states of Montana and North Dakota on the US side and the provinces of Saskatchewan and Manitoba on the Canadian side. The total area of the Bakken formation is as much as 200,000 square miles, with approximately 6,500 square miles on the US side (EIA, 2005). The depth of the formation varies between 4,500 ft and 7,500 ft and is averaged around 6,000 ft. The Bakken formation can be divided into three layers: the black marine shale in the Upper and Lower Layers with a thickness of 23 ft and 50 ft respectively, and the Middle Layer which consists of limestone, siltstone, dolomite and sandstone (Grape, 2006). Up to 20 wt% TOC was reported in the organic-rich Upper and Lower Layers of

the Bakken formation (Olesen, 2010). Porosity between 4% and 10% was also observed in several fields in the Bakken shale (Olesen, 2010).

4.2. MINERALOGY AND ELEMENTAL COMPOSITION

The shale mineralogy and elemental composition were determined with the XRD and XRF measurements following the procedures illustrated in Section 3.2.1. Table 4.1 shows the whole rock mineralogy of 12 shales respectively. WGS-B, WGS-C, TGS, BEF-1, EEF are samples from the Eagle Ford formation in south Texas. BUT, HUT 2-50 and HUT 3-70 are samples from the Utica formation. WBS and NHS are samples from the Barnett and the Haynesville formations respectively, while GOM-12 is a non-hydrocarbon bearing shale from the Gulf of Mexico.

From Table 4.1, we can see that the Eagle Ford and the Haynesville formations are calcite dominated. The calcite content of the Eagle Ford samples varies between 39.8% and 60%. The two Utica samples contain the most clay among all the hydrocarbon-bearing shales. The Barnett mineralogy is quartz dominated, with 53.1% quartz. The Bakken sample is the only shale with a significant amount of dolomite (38.6%). This indicates that the sample is from the middle layer of the Bakken formation, which is not considered a shale layer. Compared with the organic-rich shales, the none-hydrocarbon-bearing GOM-12 contains much more clay, which is 65.5%. The relative abundance of quartz, carbonate (calcite and dolomite) and clay for the 12 shales is plotted in a ternary diagram and shown in Figure 4.5.

Figure 4.6 shows the cross-plot of the clay and calcite content of Eagle Ford shale samples. A good negative linear correlation exists between the clay and calcite content. This might be due to the deposition and diagenesis processes in the Eagle Ford play in south Texas.

	Whole Rock Mineralogy (wt%)							
	Quartz	K Feldspar	Plagioclase	Calcite	Dolomite & Fe-Dolomite	Pyrite	Total Clay	Other Minerals
WGS-B	8	1	4	60	1	1	25	0
WGS-C	8	1	3	56	6	2	24	0
TGS-D	13	0.7	2.4	56.9	0.6	7.3	19.1	0
BEF-1	10.6	0	3.1	57	0	3.1	25.4	0.8
EEF	7.4	0	7.6	39.8	0.9	7.5	36.8	0
BUT	24.3	0.7	5.4	19.2	3.5	3.4	43.3	0.2
HUT 2-50	23	2	4	24	3	2	38	4
HUT 3-70	12	0	0	69	6	1	11	2
WBS	53.1	0.8	2.6	2.1	1.3	5.1	35	0
NHS	12.9	0	4.2	55.1	0	5.3	22	0.5
Bakken	34.3	3.8	4.2	5.9	38.6	1.2	12.1	0
GOM-12	26.4	2.4	1.9	2.1	0	0.6	65.5	1.1

Table 4.1: Whole rock mineralogy of 12 shales using XRD.

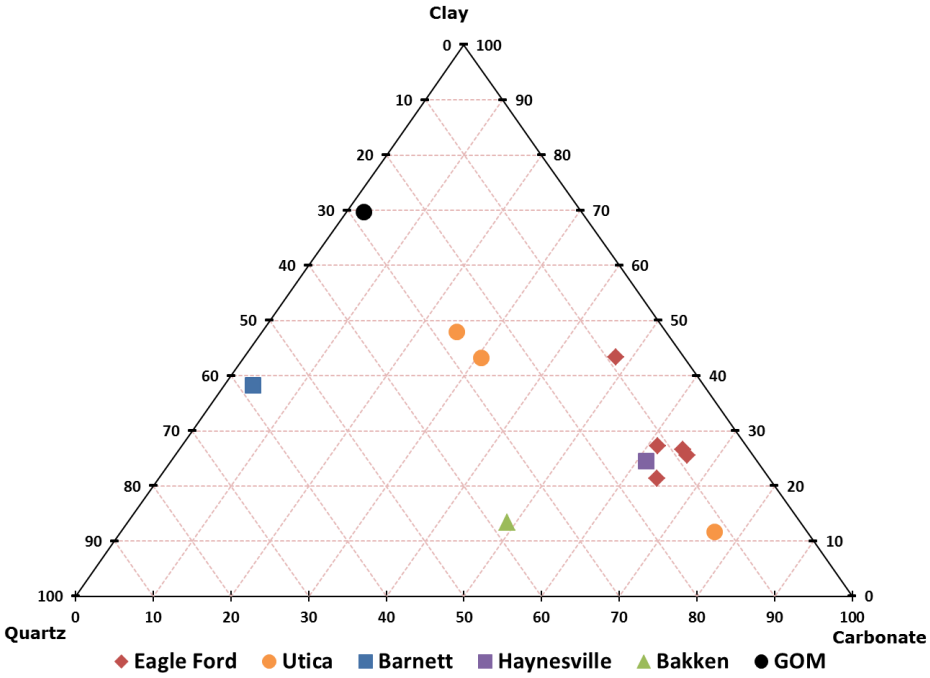

Figure 4.5: Ternary diagram of the relative abundance of quartz, carbonate and clay for the 12 shales using XRD.

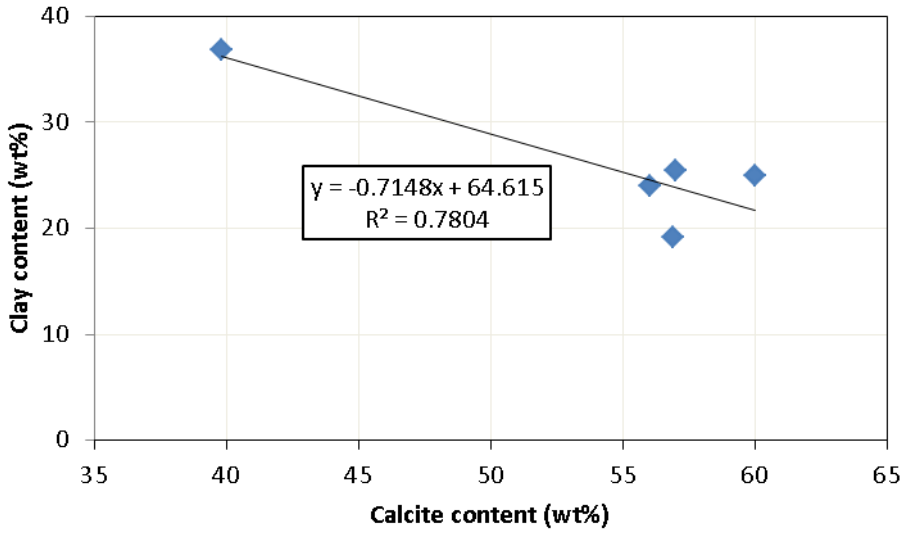

Figure 4.6: Cross-plot of clay and calcite content of Eagle Ford shales.

Table 4.2 shows the clay mineralogy of the 12 shales. Illite and mica are the most commonly found clay minerals in these shale samples. They contain the most clay minerals of all the samples except for WBS and GOM-12. Kaolinite content is very small in all the samples except for the GOM-12 sample, which has 21.8% kaolinite. Chlorite content is also extremely small for all the samples, except for BUT, which has 11.4% chlorite. It is evident that pure smectite, the most expandable clay mineral, does not exist in any of the shale samples. Diagenesis has converted smectite into other non-reactive clay minerals. The only smectite in existence is in the form of mixed illite/smectite. While most illite/smectite mixtures in these shale samples contain 10%-20% smectite, that in GOM-12 comprises 40%-50% smectite. This indicates that GOM-12 is expected to be the most water-sensitive shale.

	Clay Mineralogy (wt%)				
	Mixed Illite/Smectite	Illite & Mica	Kaolinite	Chlorite	% Smectite in Mixed I/S
WGS-B	1	22	Trace	2	N/A
WGS-C	1	21	Trace	2	N/A
TGS-D	10.7	4.8	3.6	0	10-20
BEF-1	12	11.5	0	1.9	10-20
EEF	22.6	10.6	2.1	1.5	10-20
BUT	5.9	24.1	1.9	11.4	10-20
HUT 2-50	9.5	18.3	1.5	8.7	15
HUT 3-70	0	3	0	8	20
WBS	18.5	16.5	0	0	10-15
NHS	8.9	7.9	3.5	1.7	10-20
Bakken	1.4	8.9	0.4	1.4	10-20
GOM-12	20.3	16.8	21.8	6.6	40-50

Table 4.2: Clay mineralogy of 12 shales using XRD.

Figures 4.7, 4.8 and 4.9 show the quartz, calcite and clay content of samples from a well in the Utica formation as a function of the sample depth. We can see that both the

quartz and the total clay content increases deeper into the formation, while the calcite content decreases with depth. All of these minerals exhibit a good linear correlation with the depth. The varying mineralogy of samples from the same well at various depths suggests that the mineral makeup of shale can be significantly different along the direction perpendicular to bedding planes. It will be beneficial for operators to obtain the mineralogy of core samples at different depths for the design of drilling and completion operations.

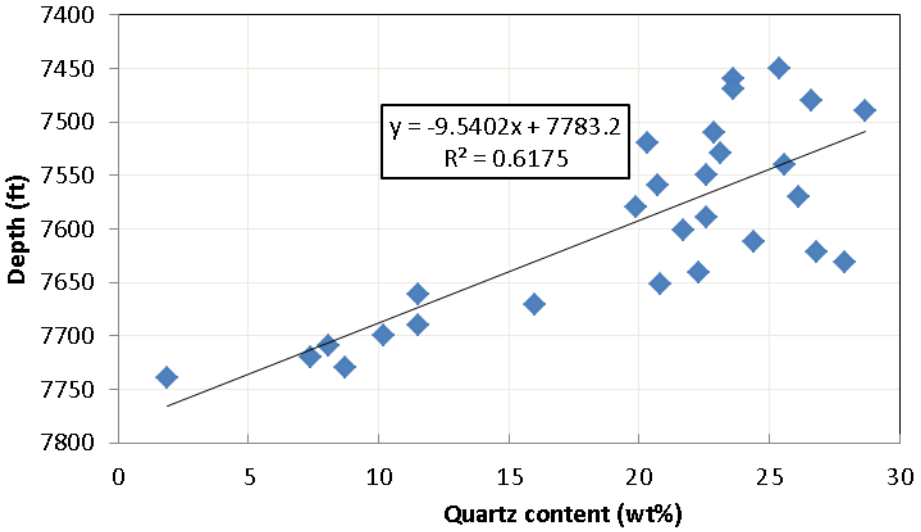

Figure 4.7: The quartz content of samples from a Utica well as a function of depth.

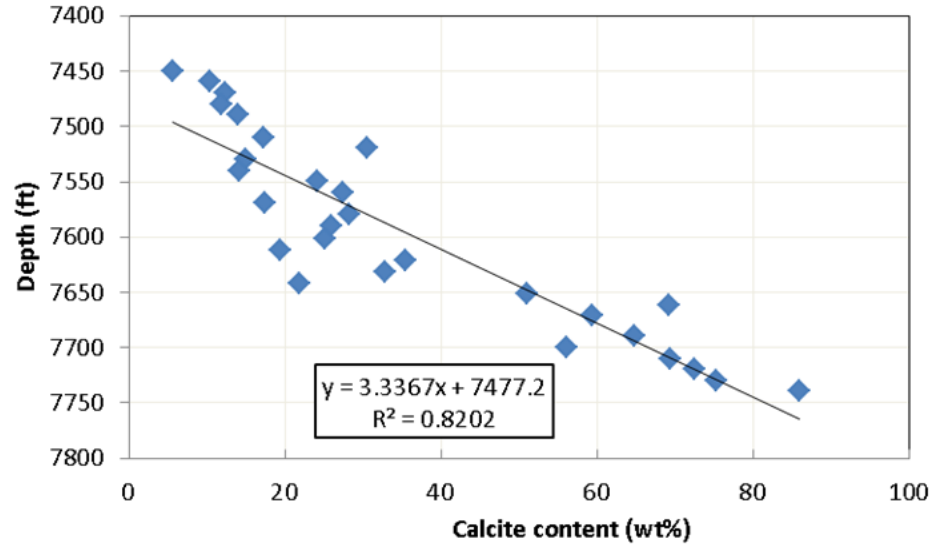

Figure 4.8: The calcite content of samples from a Utica well as a function of depth.

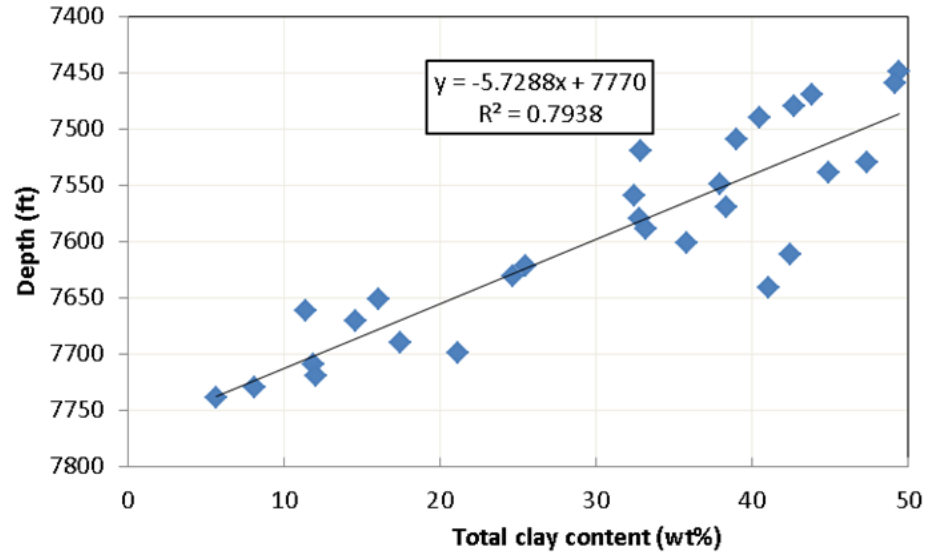

Figure 4.9: The total clay content of samples from a Utica well as a function of depth.

Figure 4.10 shows the ternary diagram of the relative abundance of quartz, carbonate and clay for the samples from the Utica well. Similar to Figures 4.7 – 4.9, Figure 10 also reveals the large variations in the composition of these minerals for

samples in the same well. Nevertheless, the dots representing different core samples fall along a straight line, marked in blue in Figure 4.10. Similar observations have reported by Brumsack (1989), Kearns (2011), Rowe et al. (2012) and Moran (2012). This straight line was called the calcite dilution line (Brumsack, 1989; Moran, 2012), which indicates the trajectory of calcite dilution for a shale with low carbonate content. It indicates that the depositional environment was mostly upwelling, through which the carbonate minerals were dissolved by the cooler water (Jenkyns, 2010).

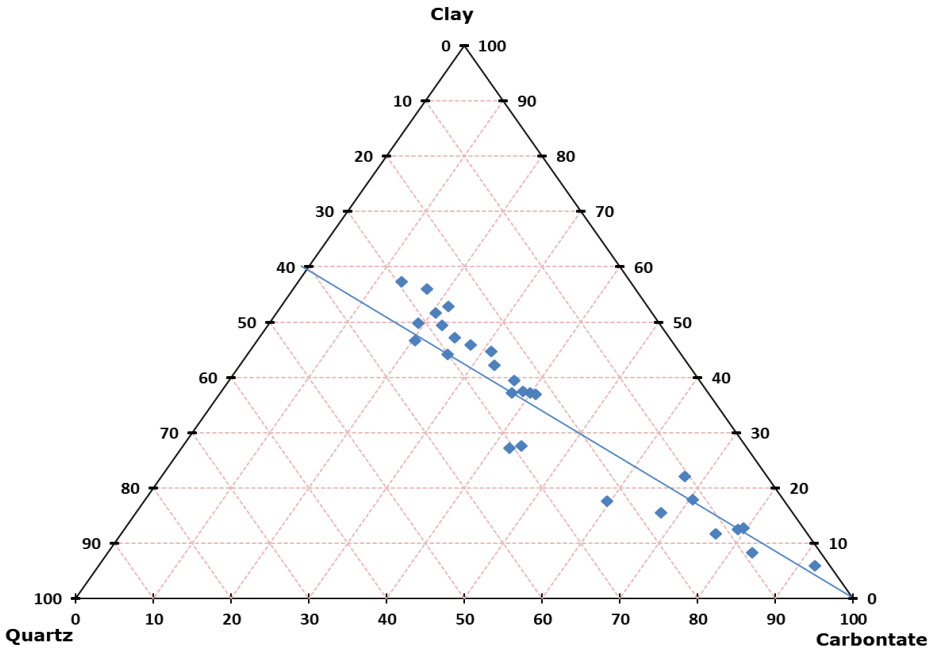

Figure 4.10: Ternary diagram of the relative abundance of quartz, carbonate and clay for the samples from a Utica well (using XRD).

The elemental composition of 13 shales is shown in Table 4.3. Most of the samples are the same as the ones in Table 4.2. Most the major elements are displayed with the unit wt%, except for bariun (Ba), vanadium (V) and chromium (Cr), whose units are parts per million (ppm). It is evident that aluminum (Al), silicon (Si) and calcium

(Ca) are the three elements that contribute to the majority of the weight of the samples. They are the major constituents of clay, quartz and calcite. Figures 4.11 – 4.13 show the cross-plots of quartz and silicon, clay and aluminum and calcite and calcium respectively. A good linear correlation exists between each of the three mineral-element pairs. The only anomaly in the calcite-calcium cross-plot (marked in red in Figure 4.12) is due to the sample having much more dolomite than calcite. Therefore, it is reasonable to use Si, Al and Ca content as proxy for quartz, clay and calcite minerals.

In order to model the content of quartz, clay and calcite minerals using the elemental composition data from the ED-XRF analysis, a simple algorithm was developed. This algorithm assumes that all Si belongs to quartz (SiO_2) and clay, and all Ca belongs to calcite ($CaCO_3$). It is possible that some Ca is part of dolomite, but from the whole rock mineralogy shown in Table 4.1, it is clear that most shale samples contain a very small amount of dolomite compared with that of calcite. Therefore, for the purpose of understanding the impact of shale mineralogy on shale-fluid interactions, the calculation of dolomite content is not included in this algorithm, and all Ca belongs to calcite.

It is more complicated to model the clay content because of the variations in individual clay type and the complex structure of clay minerals. In this study, the clay content is assumed to be the sum of the amount of illite and kaolinite, since they are the two most common clay minerals in shales. Half of the Al is assigned to illite and the other half is assigned to kaolinite. The Si content in clay can be calculated subsequently. The remaining Si will be assigned to quartz. The chemical formulas of illite and kaolinite are $(K,H_3O)(Al,Mg,Fe)_2(Si,Al)_4O_{10}[(OH)_2,(H_2O)]$ and $Al_2Si_2O_5(OH)_4$ respectively. Table 4.4 shows the elemental composition of illite and kaolinite minerals.

Sample	%Na	%Mg	%Al	%Si	%P	%S	%K	%Ca	%Ti	%Mn	%Fe	Ba (ppm)	V (ppm	Cr (ppm)
WGS-B	0.26	0.74	2.70	8.43	0.05	0.56	0.84	27.59	0.11	0.02	1.19	489	45	48
WGS-C	0.30	0.55	3.56	9.83	0.05	0.72	1.06	22.16	0.14	0.02	1.45	579	27	46
TGS-D	0.25	0.86	3.39	10.18	0.16	1.70	0.73	21.80	0.17	0.01	1.59	667	44	56
BEF-1	0.29	0.61	3.51	10.63	0.12	1.14	0.88	21.26	0.16	0.02	1.35	744	44	71
EEF	0.24	0.96	3.56	11.08	0.10	1.89	0.98	21.47	0.17	0.01	1.53	875	217	48
HUT 1-40	0.35	1.24	6.86	20.21	0.10	1.44	2.61	5.08	0.37	0.04	3.91	1042	35	53
HUT 1-70	0.35	1.21	7.17	22.30	0.09	1.65	2.60	4.67	0.39	0.03	3.52	1029	22	59
HUT 3-70	0.27	0.95	2.20	8.80	0.20	0.74	0.68	25.56	0.11	0.02	1.08	493	24	44
BUT	0.35	1.09	6.24	19.31	0.12	1.02	2.32	8.19	0.34	0.03	3.35	1217	11	54
WBS	0.38	0.55	5.79	31.70	0.09	1.23	1.65	1.94	0.32	0.03	1.80	338	120	266
Bakken	0.35	4.28	2.52	13.56	0.25	7.30	1.47	14.21	0.18	0.03	1.41	528	53	77
GOM-12	0.45	0.25	8.71	22.70	0.02	0.28	1.89	1.09	0.51	0.03	2.84	1758	66	73

Table 4.3: Elemental composition of 13 shales from XRF measurements.

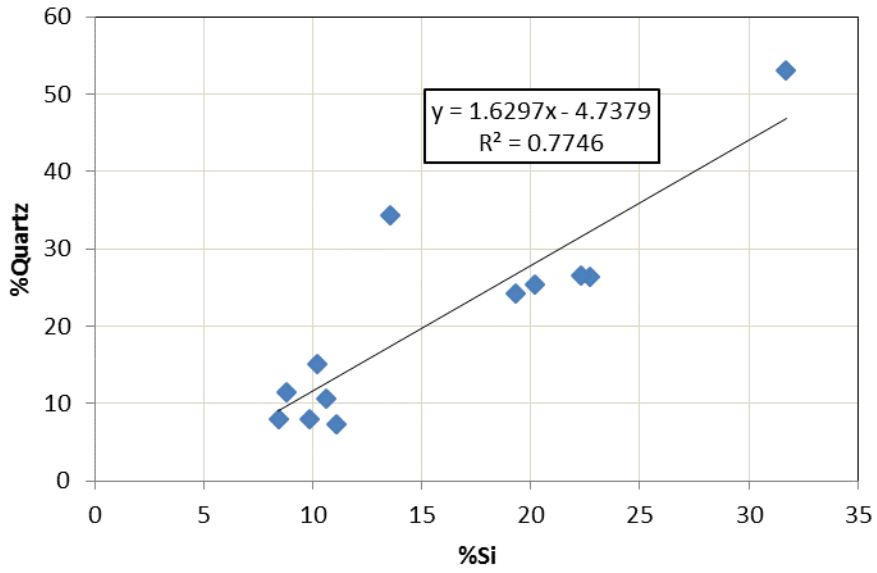

Figure 4.11: Cross-plot of quartz and silicon (Si) content of some shales (using XRF).

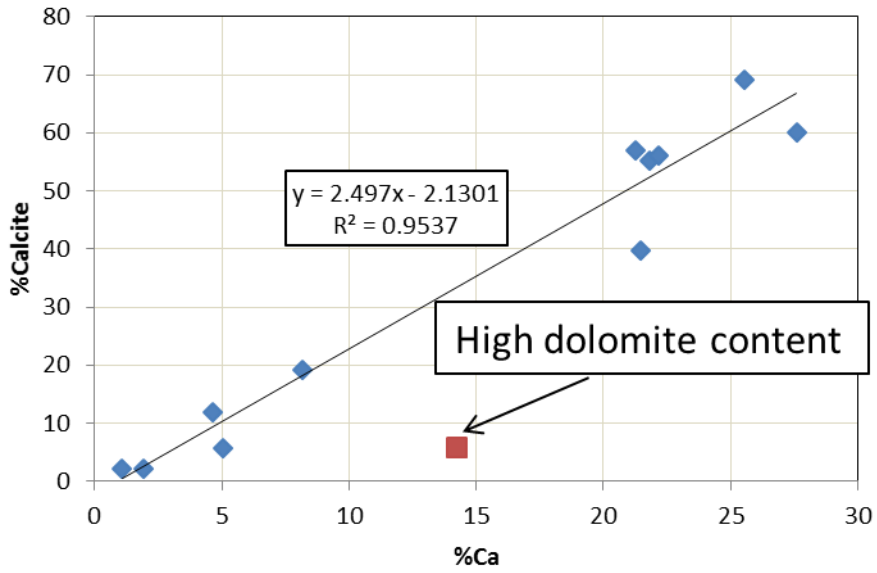

Figure 4.12: Cross-plot of calcite and calcium (Ca) content of some shales (using XRF).

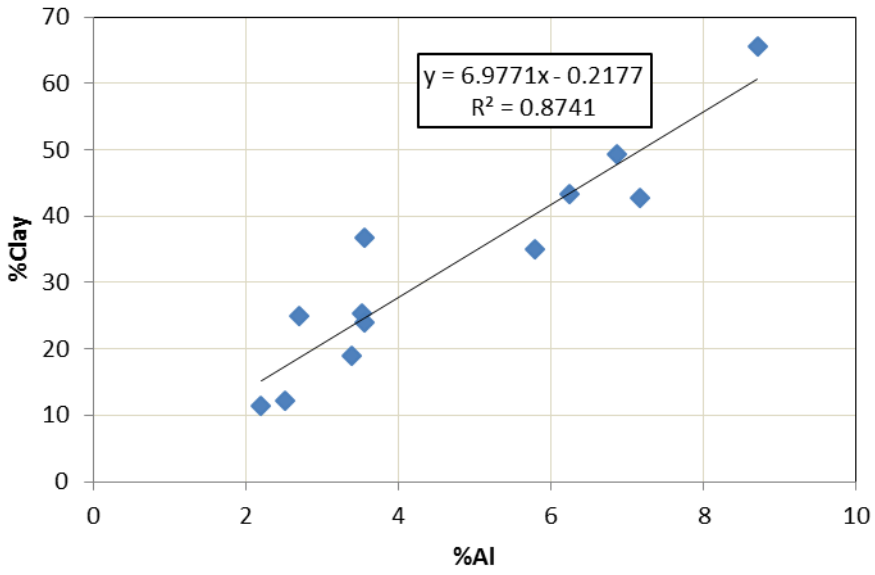

Figure 4.13: Cross-plot of clay and aluminum (Al) content of some shales.

	Elemental Composition (wt%)						
	K	Mg	Al	Fe	Si	H	O
Illite	6.03	1.87	9.01	1.43	25.25	1.35	55.06
Kaolinite	0	0	20.9	0	21.76	1.56	55.78

Table 4.4: Elemental composition of illite and kaolinite (after www.webmineral.com).

Figure 4.14 shows the ternary diagram of the relative abundance of quartz, calcite and clay for shale samples using elemental composition obtained with the handheld ED-XRF instrument. Compared with Figure 4.5, Figure 4.14 shows very similar relative abundance of the three minerals for shale samples from different plays (calcite is assumed to be the only carbonate mineral). Figures 4.15 – 4.17 show the comparison of the clay, carbonate and quartz content of 11 shales from the XRD and XRF measurements. It can be seen that XRD and XRF yield very similar mineralogy for these shales. This again proves that the elemental composition obtained with the ED-XRF instrument can be used for estimating the shale mineralogy. Rapid quantitative

measurement can be made at the wellsite or in the laboratory with the XRF instrument, a big advantage over the XRD measurement.

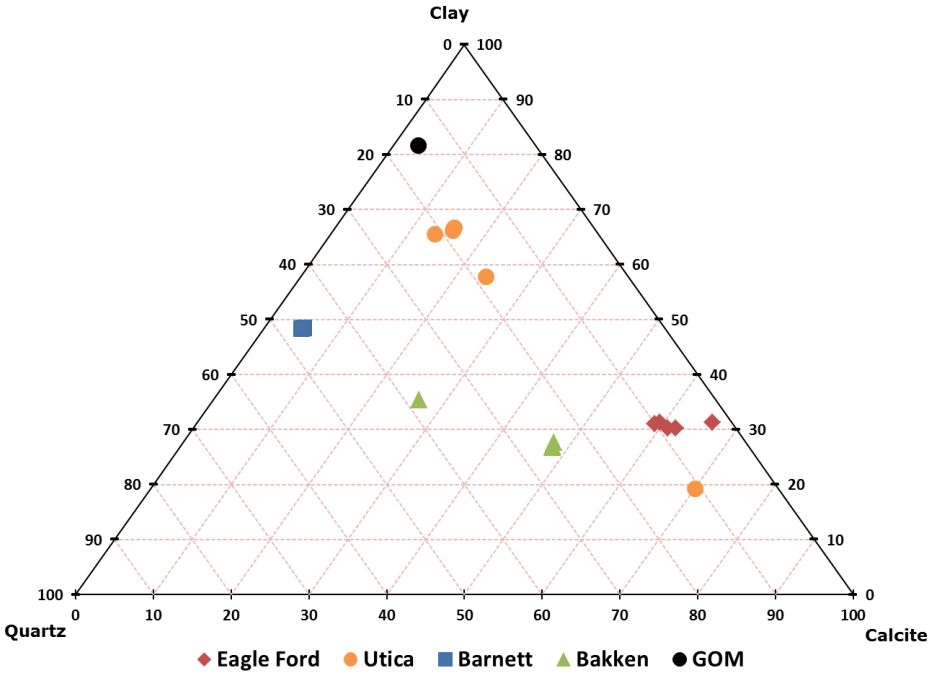

Figure 4.14: Ternary diagram of the relative abundance of quartz, calcite and clay for shale samples using elemental composition obtained with the handheld ED-XRF instrument.

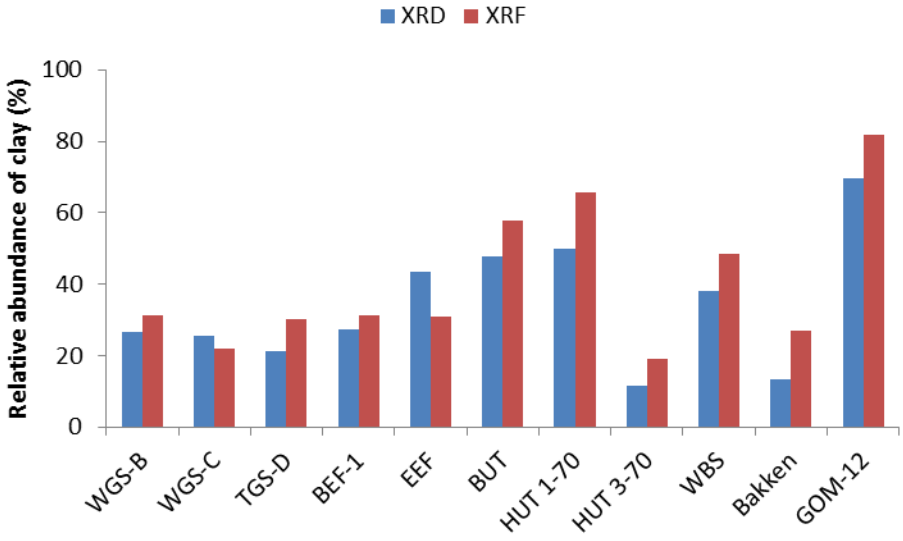

Figure 4.15: Comparison of the relative abundance of clay from the XRD and XRF measurements for 11 shales.

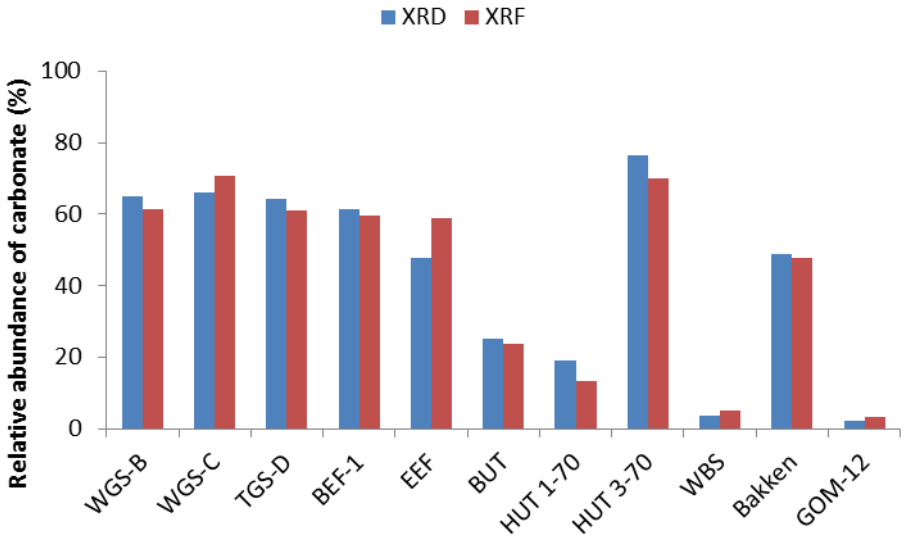

Figure 4.16: Comparison of the relative abundance of carbonate from the XRD and XRF measurements for 11 shales.

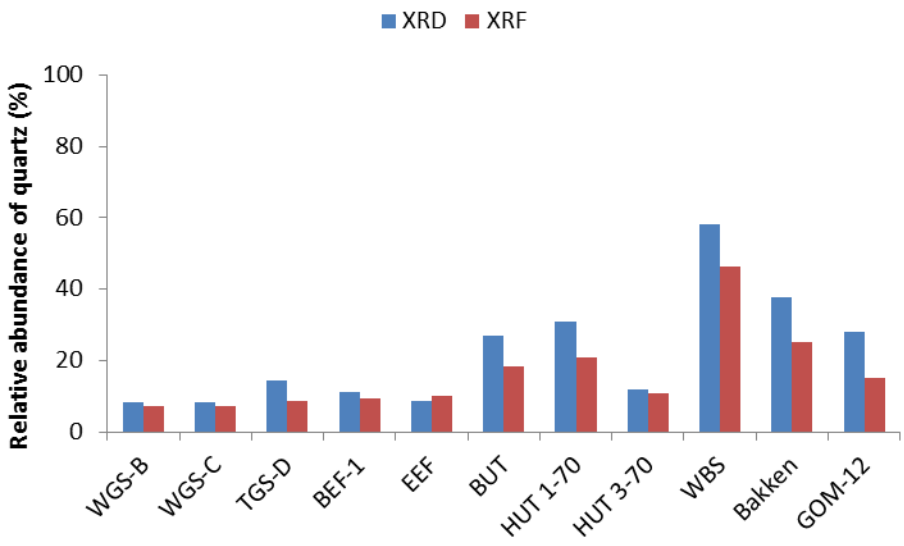

Figure 4.17: Comparison of the relative abundance of quartz from the XRD and XRF measurements for 11 shales.

4.3. NATIVE WATER ACTIVITY

Following the procedures described in Section 3.2.2, the native water activity of various shales was determined using controlled humidity desiccators with saturated salt solutions. Table 4.5 shows the native water activities of 11 shales.

The high values of the native water activity of these shales indicate that the samples were properly preserved in the field after the cores were retrieved from downhole. In contrast, the native water activity of BEF-1 is ~0.46, much lower than that of other shales in this study. The low water activity of the BEF-1 shale means that the shale was not properly preserved and was dried out. Most air conditioned buildings are maintained at a relative humidity of about 50%. Thus, a native water activity of 0.46 reflects such humidity.

Shale Sample	Native Water Activity
WGS-B	0.73
WGS-C	0.75
TGS	>0.96
BEF-1	0.46
EEF	0.96
BUT	0.85
HUT 2-50	0.75
WBS	0.92
NHS	0.83
Bakken	0.84
GOM-12	0.82

Table 4.5: The native water activity of 11 shales.

Figures 4.18 and 4.19 show the adsorption isotherms used for determining the native water activity for shales from the Eagle Ford formation and other shale plays as well as the Gulf of Mexico. A bold black line is used to indicate the x-axis at y = 0 in both figures. In Figure 4.18, the native water activities of TGS and EEF were very close to 1. For TGS, all of the shale samples lost water in controlled humidity desiccators with the highest relative humidity being 96%. Therefore, we can conclude that TGS had a native water activity very close to 1. The adsorption isotherms for WGS-B and WGS-C were very similar in shape, and so were their native water activities (~0.75). In fact, they were from the same well at different depths. This suggests that similar native water activity and hydration state can be expected for samples from nearby wells.

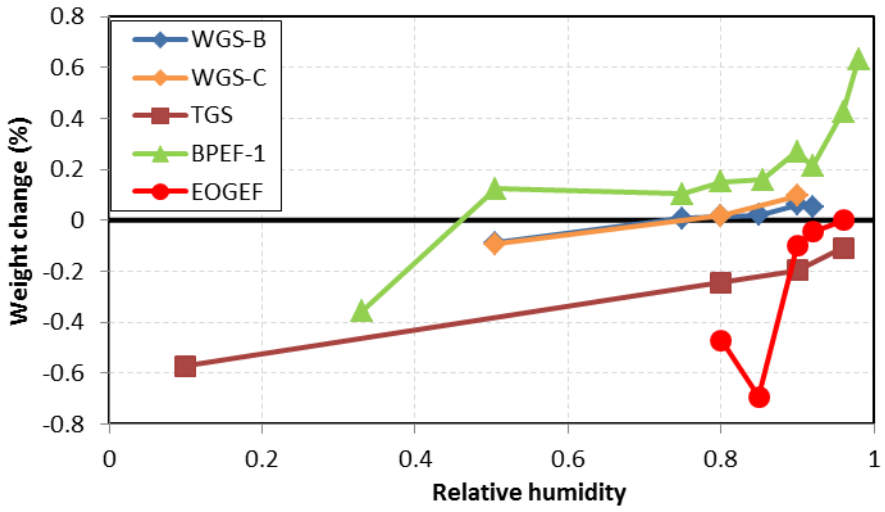

Figure 4.18: Adsorption isotherms for determining the native water activities of shales from the Eagle Ford formation.

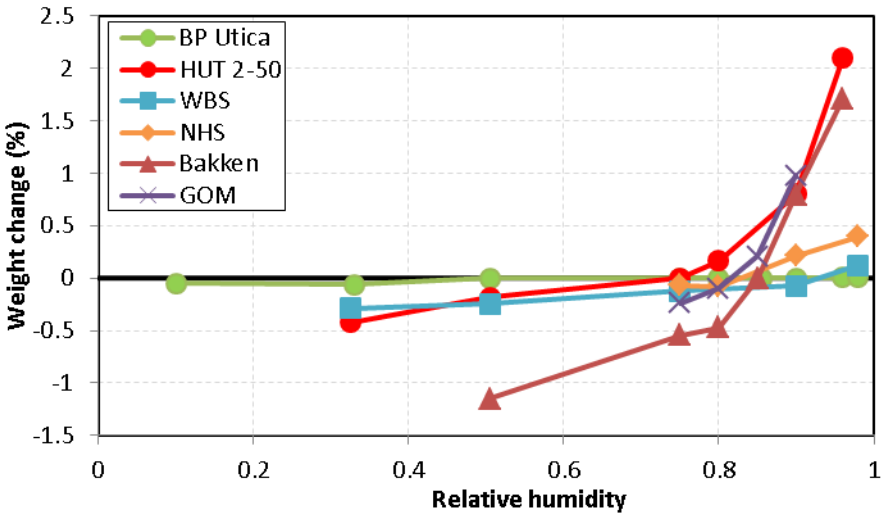

Figure 4.19: Adsorption isotherms for determining the native water activities of the other six shale samples.

It is noted that for shales with a native water activity close to one (TGS, EEF and WBS), the slope of percent weight change as a function of relative humidity is very small, irrespective of their clay content. It indicates that these shales had very little room

for water vapor adsorption, because their native water activity was close to one. On the other hand, for GOM-12, WGS-B, BUT and NHS, there is a distinct difference in the slope of their percent weight change as a function of relative humidity. It is evident that the slope of the clay-rich GOM-12 shale is much higher than that of the clay-poor WGS-B, BUT and NHS shales. This can be due to the fact that GOM-12 is more water-sensitive than WGS-B, BUT and NHS because of the significantly higher amount of clay present in the non-hydrocarbon bearing shales. One other interesting observation worth mentioning is the slope of some hydrocarbon bearing shales (TGS, WGS-B, BUT, WBS and NHS). These shales underwent very small weight gain regardless of their native water activity. Their slopes of weight change are very similar. This can be caused by the low clay content in these shales, which result in these shales being not very water-sensitive. Nevertheless, the large slope of the Bakken shale despite the fact that its clay content is low (~12%) cannot be explained by its mineral makeup.

4.4.NMR

4.4.1. T_1 and T_2 Distributions

As described in Section 3.2.4, the longitudinal relaxation time, T_1, and the transverse relaxation time, T_2, were measured on preserved shale samples. T_1 is a function of bulk relaxation within the pore fluid and surface relaxation between the pore fluid and the surface of the pore wall:

$$1/T_1 = 1/T_{1bulk} + 1/T_{1surface} \tag{4.1}$$

where T_{1bulk} is the T_1 bulk relaxation time and $T_{1surface}$ is the T_1 surface relaxation time. In addition to bulk and surface relaxation, T_2 is also affected by diffusion relaxation, which results in the diffusion of hydrogen nuclei in the presence of a magnetic field gradient. The estimation of T_2 relaxation time was described by Eq. 2.8:

$$1/T_2 = 1/T_{2bulk} + 1/T_{2surface} + 1/T_{2diffusion} \quad (2.8)$$

where T_{2bulk}, $T_{2surface}$ and $T_{2diffusion}$ are the T_2 bulk relaxation time, surface relaxation time and diffusion relaxation time respectively. For core NMR measurement, the diffusion relaxation mechanism can be neglected because no external magnetic field is applied during the measurement and the internal magnetic field gradient is negligible.

The NMR measurement is only sensitive to the hydrogen nuclei of the pore fluid. The relaxation process of the hydrogen nuclei in the rock matrix is too fast for the instrument to detect. When the shale pore space is filled with wetting fluid, surface relaxation dominates and the T_1 relaxation time in Eq. 4.1 can be expressed as:

$$1/T_1 \approx 1/T_{1surface} = \rho_1 S/V \quad (4.2)$$

where ρ_1 is the longitudinal surface relaxivity, S is the pore surface area and V is pore volume. Likewise, Eq. 2.8 for estimating T_2 can also be simplified as the following:

$$1/T_2 \approx 1/T_{2surface} = \rho_2 S/V \quad (4.3)$$

where ρ_2 is the transverse surface relaxivity. Interpretation of the NMR T_2 measurements on conventional reservoir rocks such as sandstone and limestone is based the pore size. Free fluids are expected to be in larger pores while clay-bound and capillary-bound fluids are usually found in smaller pore space.

On the other hand, if the pore space is filled with non-wetting fluid with a high viscosity, the fluid molecules will not come into contact with the pore wall, and the relaxation process will be dominated by bulk relaxation (Freedman et al., 2003). In that case, T_1 and T_2 will be a function of the fluid viscosity. The bulk relaxation time is usually longer than the surface relaxation time. Ozen and Sigal (2013) reported that T_1/T_2 ratio for brine is smaller than that for hydrocarbon in ground-up Barnett shale samples. This difference in T_1/T_2 ratio is probably due to the different dominant relaxation mechanisms for pores saturated with specific types of fluids.

Figure 4.20 shows the NMR T_2 distribution for seven shale samples. The blue and red lines represent the T_2 distribution and cumulative porosity respectively. The porosity is obtained by normalizing the measured discrete pore volume at different T_2 relaxation against the bulk volume of the shale sample, which was obtained by immersing the shale sample in mineral oil (Exxsol D110 in this case). The amplitude of the T_2 distribution is proportional of the number of hydrogen nuclei present in the shale pore space. Some of the samples are from the same core as those in Sections 4.2 and 4.3. All of these shale samples are organic-rich and contain hydrocarbons in the subsurface. HUT 1-70, HUT 3-70 and HUT 2-70 are Utica samples from the same well at different depths. WBS is a Barnett sample and NHS is a Haynesville sample. TGS-D, TGS-F, and WGS-B are Eagle Ford samples at different depths. TGS-D and TGS-F are from the same well and their depths are similar.

In Figure 4.20, three major peaks are observed. They are at $T_2 = 0.15 – 0.5$ ms, 2 – 10 ms and 150 – 300 ms respectively. This is similar to what was reported by Rylander et al. (2013). They attributed the peak with $T_2 < 1$ ms to the presence of the highly viscous bitumen. The peak with $T_2 \approx 4$ ms was believed to be a result of the presence of clay-bound water. They also observed an inflection point at $T_2 \approx 10$ ms, which is in the capillary-bound fluid region. However, this peak is not present in any of the seven shales analyzed in this study. The peak with $T_2 > 100$ ms corresponds to the presence of free fluids, according to the cutoff of 33 ms and 100 ms for sandstone and limestone respectively (Straley et al., 1997).

The pronounced peak observed at $T_2 = 0.15 – 0.5$ ms for all of the seven hydrocarbon-bearing shales indicates that significant portion of the pore space is filled with the highly viscous bitumen. Clay-bound water is also a major component of the pore fluid in HUT 1-70, HUT 3-70, NHS and TGS-F, as shown by the respective peaks at $T_2 =$

2 – 10 ms. The free fluid peak at T_2 = 150 – 300 ms has the smallest amplitude among all the peaks, which means that producible oil and water contributes the least to the pore fluid composition. This can be a result of the core retrieval process, which leaves a small amount of free fluid in the shale matrix. Meanwhile, all the samples are gas-bearing shales, therefore the presence of free oil in the pore space is not expected.

Figure 4.20 also shows that the total NMR T_2 porosity of the Utica shales is very similar (around 7.5%) among different samples. In contrast, the Haynesville sample has a lower T_2 porosity of 4.67%. The T_2 porosity of the Eagle Ford samples varies from 3.94% to 7.5%. This shows that no single number can define the porosity of a shale play. Detailed measurements need to be made on individual core samples.

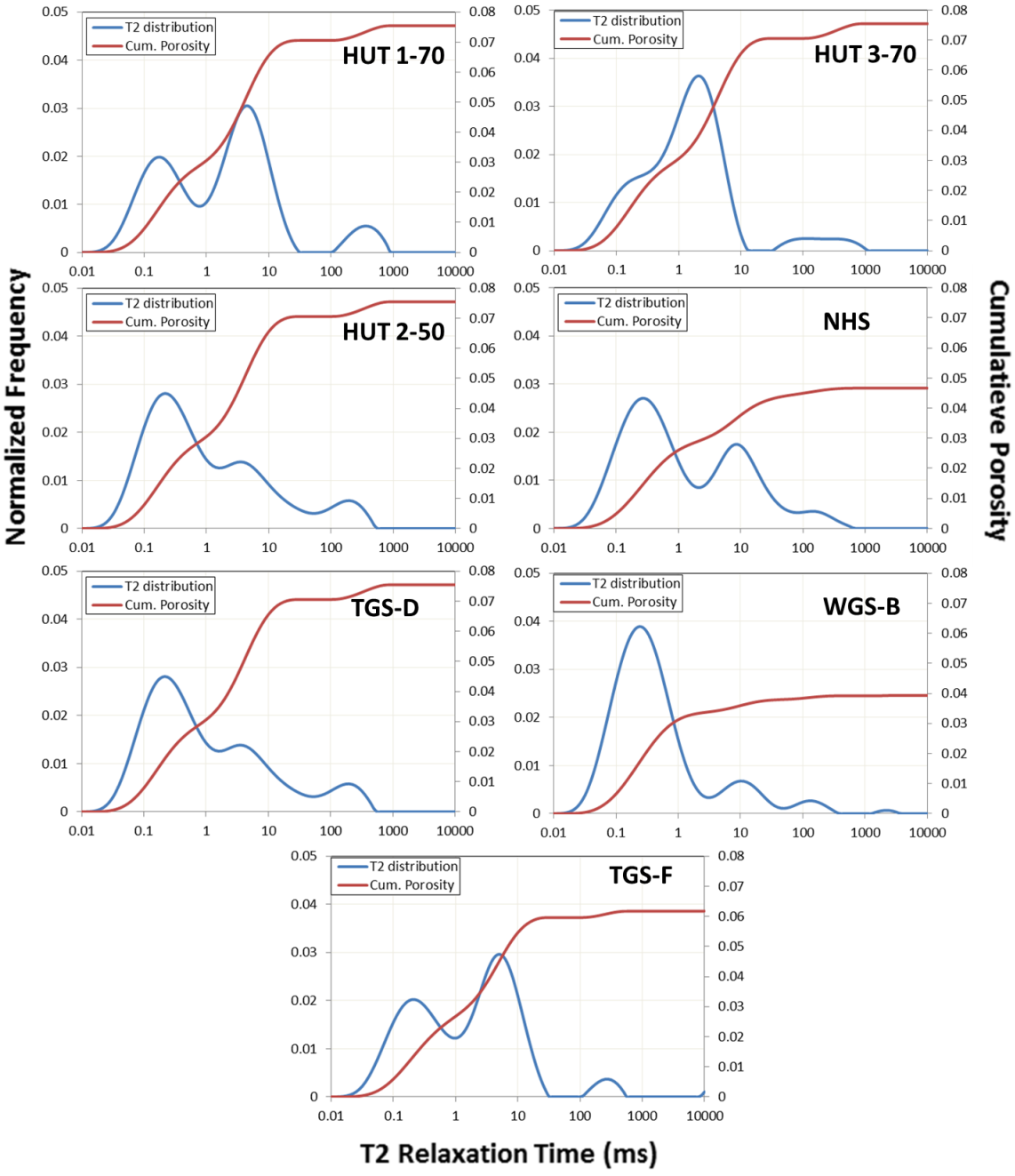

Figure 4.20: NMR T_2 distribution for seven shale samples.

Figure 4.21 shows the T_1-T_2 contour map of the seven shale samples. The color bar represents the incremental porosity at specific T_1 and T_2 relaxation times. Peaks are

identified according to the incremental volume at specific T_1-T_2 values. The corresponding T_1/T_2 ratio and T_2 is plotted in Figure 4.22. The T_1/T_2-T_2 plot is divided into four quadrants. As discussed earlier, high T_1/T_2 ratio corresponds to viscous fluid such as oil and high T_2 value can be related to larger pore size. Oil is indicated by green symbols and water is shown in blue. The top left quadrant represents oil in small pore space. This usually includes heavy oil or bitumen in tiny organic pores. The top right quadrant represents oil in large pore space. Similarly, the bottom left and right quadrants represent less viscous water in smaller and larger pores. The partition in Figure 4.22 is arbitrary and is meant to illustrate how this method can be used to investigate the presence of different types of fluids in pores of various sizes.

There is no fluid observed in the top right quadrant in Figure 4.22. This indicates that the more viscous oil is not present in the large pore space. This is consistent with the very small peaks in the T_2 distribution shown in Figure 4.20. It is possible that water is the only free fluid in the large pores. The T_2 relaxation time of all the fluids identified in Figure 4.22 is smaller than 100 ms. This indicates that all the fluids are wetting the pore space, and the subsequent dominant T_2 relaxation mechanism is surface relaxation (Rylander et al., 2013).

Regarding fluid distribution in shale samples from different plays, the Utica samples contain viscous oil in small pores or bitumen, which is not producible. Both clay-bound water and free water are observed in Utica samples as well. Oil is observed in the top left quadrant for the Eagle Ford sample, but its relatively low T_1/T_2 ratio compared with that of the Utica samples might suggest that it is water since the partition is arbitrary. Furthermore, it can be seen that water is present in pores of various sizes in the Eagle Ford samples since the T_2 relaxation time varies from close to 100 ms to less than 0.3 ms. The Haynesville sample does not show to contain oil. This can be because

Haynesville is a gas-bearing shale formation. The water in Haynesville samples is present in large pores because of its absence at T_2 close to 100 ms.

The analysis and interpretation of the T_1 and T_2 relaxation time obtained with the NMR measurement on preserved hydrocarbon-bearing shales demonstrates its capability to characterize the pore size and fluid distribution in shale samples. The results by no means can define these petrophysical properties of the shale plays comprehensively. Individual shale core samples need to be studied carefully to understand their pore and fluid properties. Another approach of utilizing T_1 and T_2 relaxation time measurements to characterize fluid distribution in shales will be illustrated in the next section.

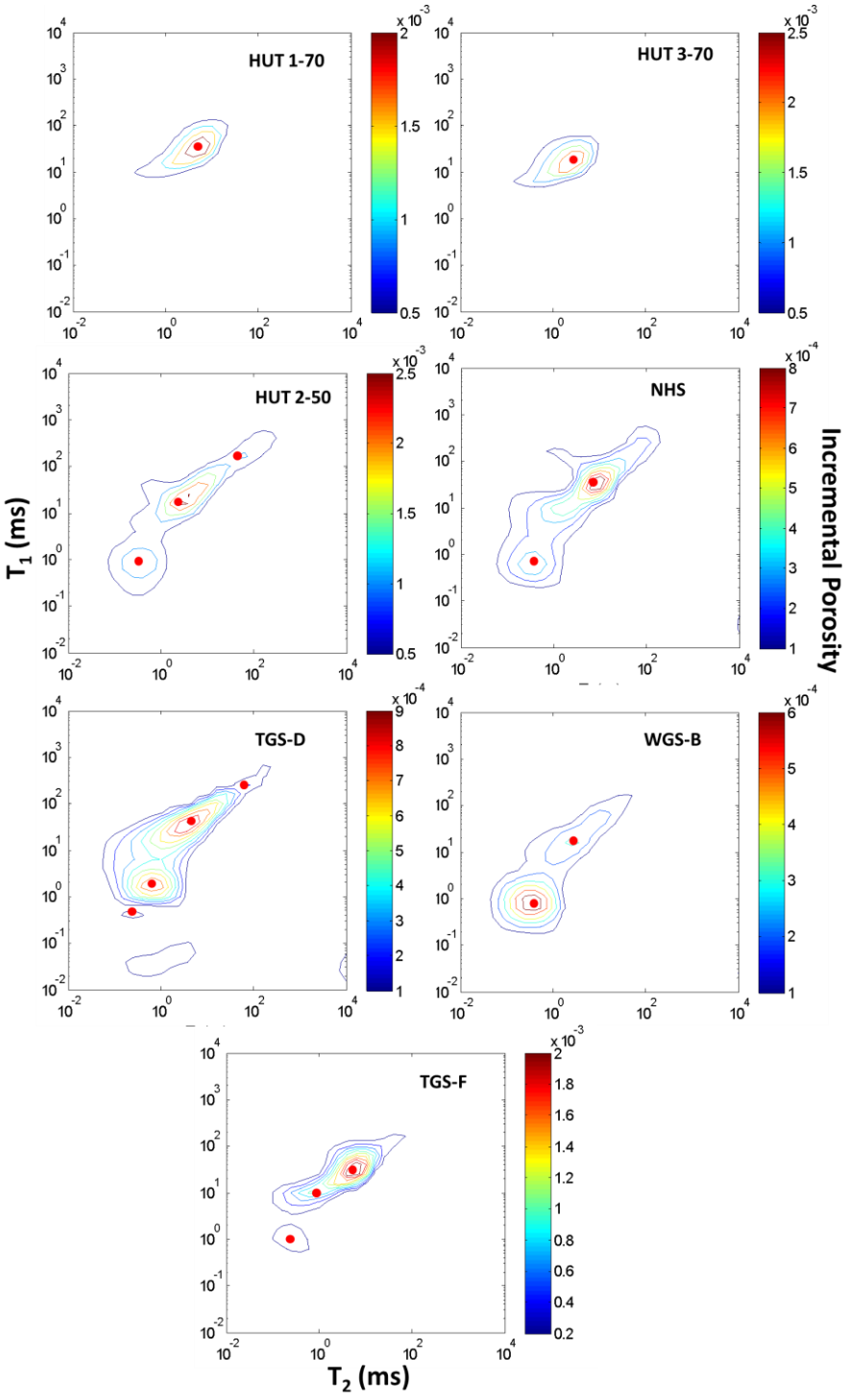

Figure 4.21: T_1-T_2 contour map of the seven shale samples. The peaks are labeled with a red dot.

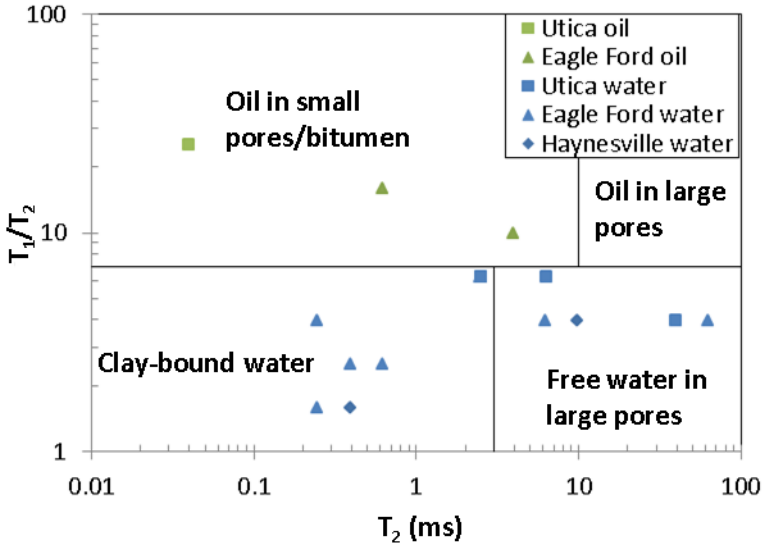

Figure 4.22: T_1/T_2-T_2 plot for seven shale samples.

4.4.2. Secular Relaxation

According to Daigle et al. (2014), the T_2 secular relaxation time, T_{2sec}, is defined as:

$$1/T_{2sec} = 1/T_2 - 1/T_1 \quad (4.4)$$

Since T_2 is generally smaller than T_1, T_{2sec} is typically greater than zero. When fluid is present in large pores or in contact with organic materials such as bitumen or kerogen, the dominant relaxation mechanism is bulk relaxation. Daigle et al. (2014) established a correlation between T_{2sec} and fluid viscosity such that T_{2sec} increases with decreasing viscosity. In comparison, as shown in Section 4.4.1, the T_2 relaxation time is shorter than 100 ms, and the dominant relaxation mechanism is surface relaxation between fluid and the surface of the pore wall in small pores. Daigle et al. (2014) showed that T_{2sec} is proportional to pore size and the T_1/T_2 ratio is independent of pore size when fluid interacts with paramagnetic ions through the surface relaxation mechanism. Therefore,

T_{2sec} together with T_1/T_2 ratio can be used to characterize the fluid type and pore size when the relaxation is surface dominated. Figure 4.23 shows the partition of a T_{2sec}-T_1/T_2 plot based on the fluid viscosity and pore size. Seven combinations of fluid viscosity and pore size are illustrated. The cutoff T_{2sec} and T_1/T_2 values are arbitrary. Further analysis needs to be conducted to fine-tune the cutoff numbers.

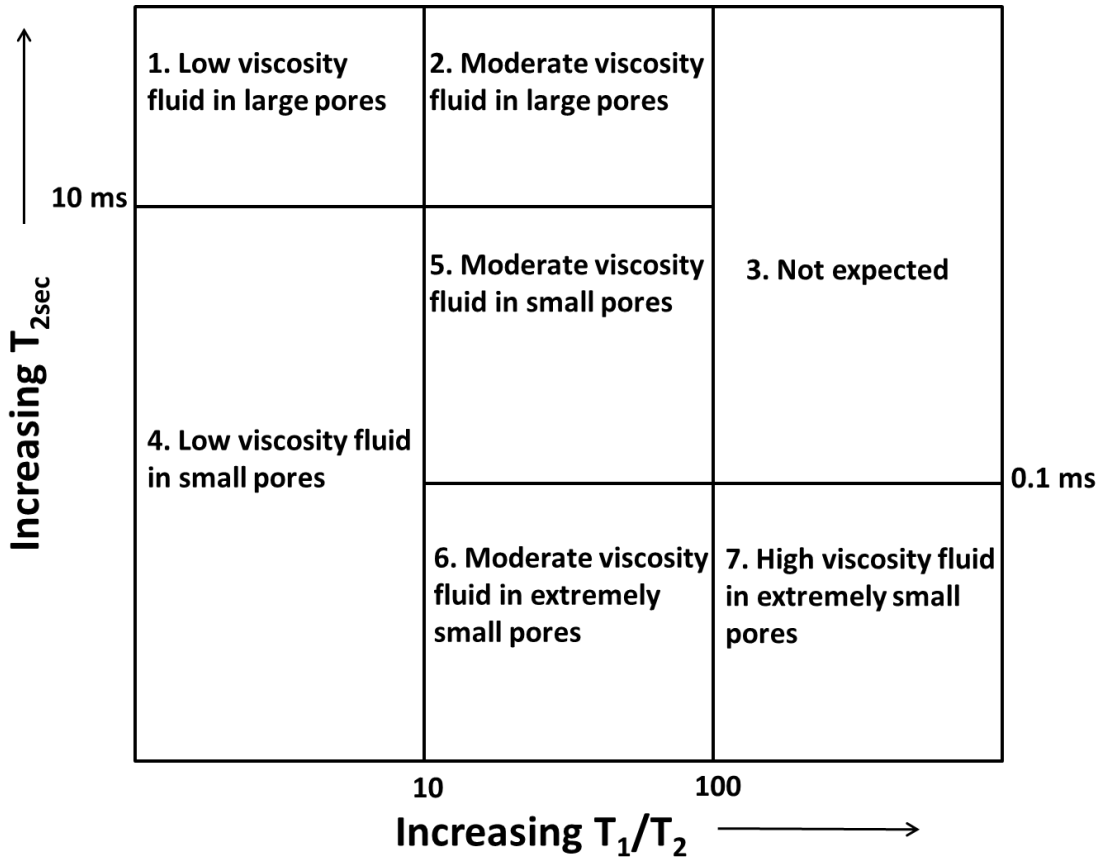

Figure 4.23: Partition of the T_{2sec}-T_1/T_2 map into seven zones based on the fluid viscosity and pore size (modified from Daigle et al., 2014).

Figure 4.24 shows the T_{2sec}-T_1/T_2 contour map for the seven shale samples. The negative T_{2sec} data are not included in the figure. Similar to that in Figure 4.23, the color bar represents the incremental porosity at specific T_{2sec} and T_1/T_2 values. It is evident that

the majority of the fluid present in these shale samples has moderate to low viscosity. More fluid belongs to the low viscosity group, as the T_1/T_2 ratio is less than 10. The pore size varies from being large to small according to the T_{2sec}. However, extremely small pores with $T_{2sec} < 0.1$ ms are very rare. There are cases (HUT 2-50, NHS and TGS-D) such that fluid is found in the unexpected zone. This can be due to the cutoff of T_{2sec} being assigned at 0.1 ms. The fluid can be characterized as high viscosity in small pores. This might be immobile heavy oil or bitumen. In terms of individual shale plays, the samples from the Eagle Ford formation have similar combinations of fluid viscosity and pore size. For the Utica samples, the contour maps of HUT 1-70 and 3-70 look similar, while the pore size of HUT 2-50 has greater variations.

Table 4.6 shows the porosity contribution from the seven zones respectively for the seven shales, based on the partition scheme shown in Figure 4.23. Similar to what Figure 4.24 shows, zone 4 contributes to the most porosity in all the seven shale samples. This suggests that clay-bound water contributes to a significant portion of the total porosity in these shales. Some shales (HUT 1-70, HUT 3-70, TGS-D, TGS-F) also have notable porosity in zone 5, which corresponds to light oil in small pores. On the other hand, some porosity is also observed in zone 1 for HUT 1-70, HUT 2-50, NHS, TGS-F, which suggests that these samples contain movable fluid in large pores.

Table 4.7 shows the total porosity based on the T_2 measurement alone and the T_{2sec}-T_1/T_2 map. The total porosity from the T_2 measurement alone is clearly greater than that from the T_{2sec}-T_1/T_2 map. This in part can be due to the exclusion of the NMR porosity when $T_1 \leq T_2$. Figure 4.25 shows that a good linear correlation exists between the total porosity from the T_{2sec}-T_1/T_2 map and that from the T_2 alone for the seven shale samples.

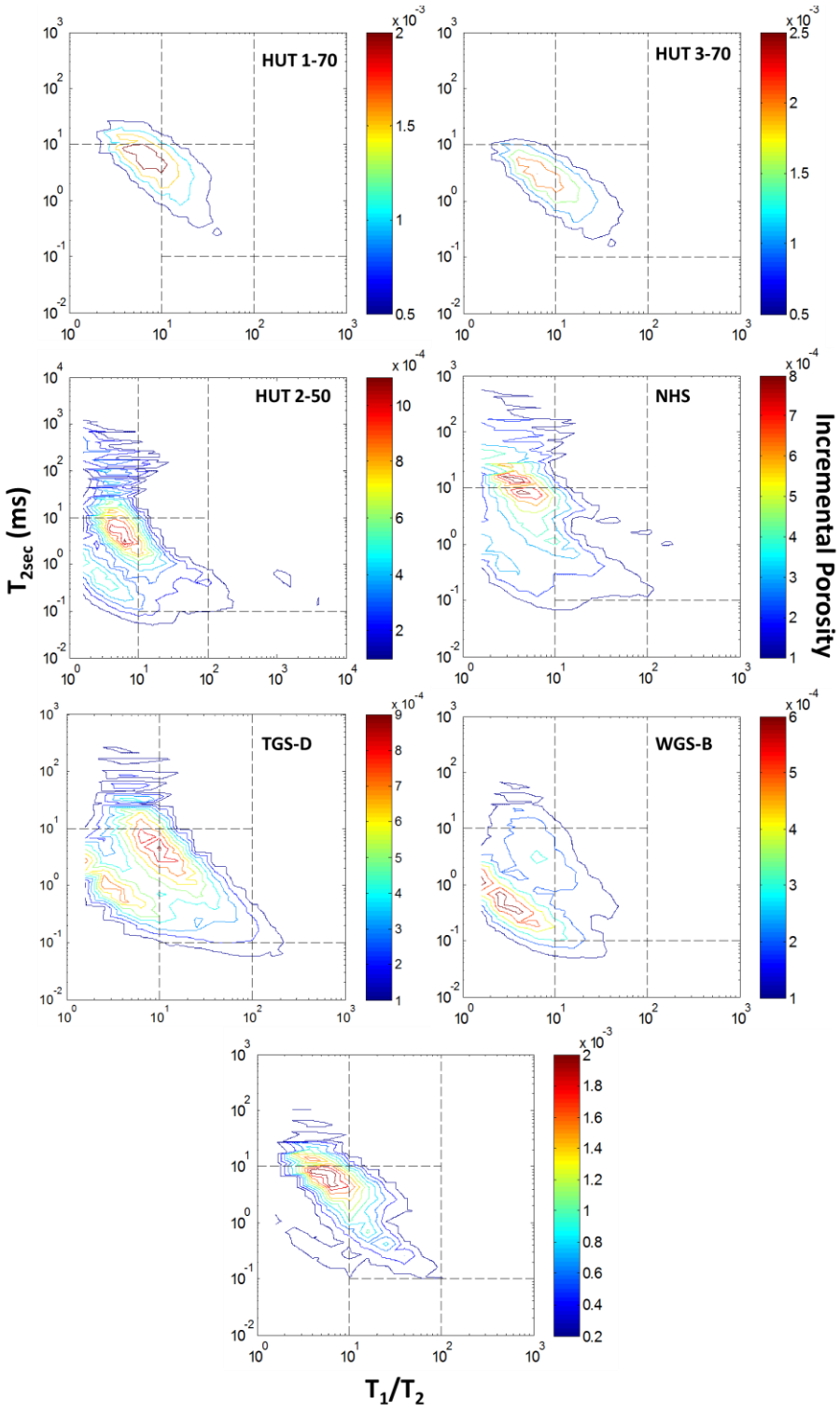

Figure 4.24: T_{2sec}-T_1/T_2 contour map for seven shale samples.

	HUT 1-70	HUT 3-70	HUT 2-50	NHS	TGS-D	WGS-B	TGS-F
Zone 1: Low viscosity fluid in large pores	0.0129	0.0049	0.0119	0.0105	0.0077	0.0034	0.0113
Zone 2: Moderate viscosity fluid in large pores	0.0006	0.0002	0.0001	0.0002	0.0006	0.0003	0.0001
Zone 3: Not expected	0.0005	0.002	0.0028	0.0012	0.0015	0.0004	0.0018
Zone 4: Low viscosity fluid in small pores	0.0215	0.0251	0.0215	0.0141	0.0185	0.0143	0.0198
Zone 5: Moderate viscosity fluid in small pores	0.0206	0.0205	0.0086	0.0058	0.0141	0.004	0.0163
Zone 6: Moderate viscosity fluid in extremely small pores	0.0004	0.0005	0.0008	0.0005	0.0006	0.0008	0.0007
Zone 7: High viscosity fluid in extremely small pores	0.0005	0.0004	0.0005	0.0003	0.0007	0.0002	0.0005

Table 4.6: Porosity component based the T_{2sec}-T_1/T_2 contour map and the partition scheme shown in Figure 4.23.

	HUT 1-70	HUT 3-70	HUT 2-50	NHS	TGS-D	WGS-B	TGS-F
Total NMR T_2 porosity	0.075	0.066	0.069	0.047	0.075	0.039	0.062
Total NMR porosity based on the T_{2sec}-T_1/T_2 map	0.057	0.054	0.046	0.033	0.044	0.023	0.051

Table 4.7: Total porosity obtained from the NMR T_2 measurement and the T_{2sec}-T_1/T_2 map respectively for the seven shales.

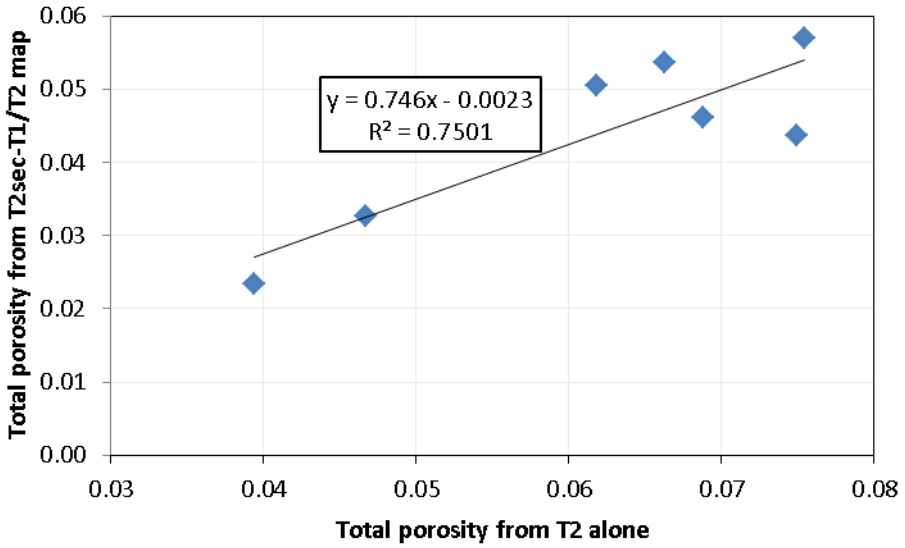

Figure 4.25: Plot of the total porosity from the T_{2sec}-T_1/T_2 map and that from the T_2 alone for seven shale samples.

Figure 4.26 shows a good linear correlation between the total clay content and the porosity in Zone 4, except for the point in red that belongs to HUT 3-70. Therefore, the low viscosity fluid in small pores might correspond to the presence of water in low-porosity clay. This shows an example of the use of the partitioned T_{2sec}-T_1/T_2 map for interpreting the fluid distribution in shale.

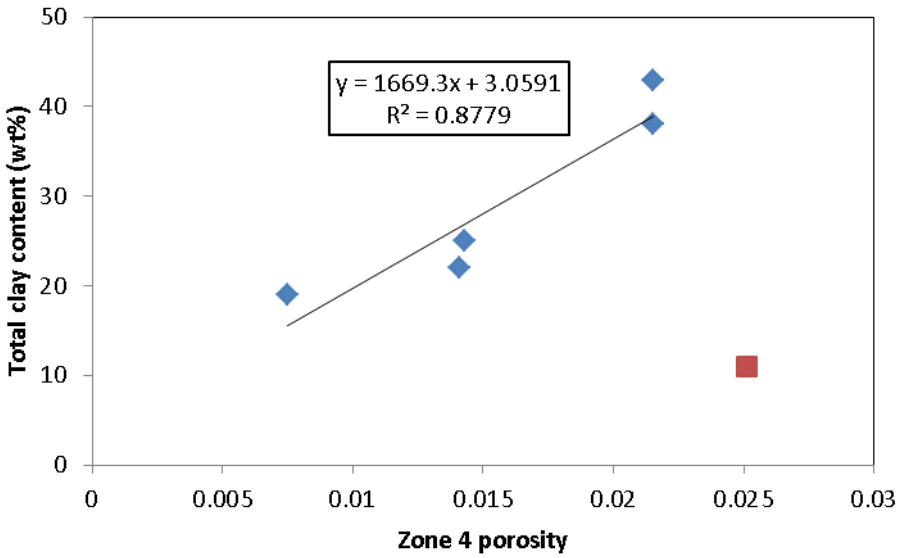

Figure 4.26: Plot of the total clay content against the porosity from Zone 4 of the T_{2sec}-T_1/T_2 map.

4.5. PORE SIZE DISTRIBUTION

4.5.1. N_2 Adsorption

As described in Section 3.2.3, the N_2GA was performed with a Micromeritics 3Flex gas adsorption system. Crushed powder samples <0.125 mm were oven dried at 105°C for 24 hours. 1 g – 1.5 g of the crushed sample was placed in the sample tube and degassed with a N_2 stream at a gradually increasing temperate at 5°C/min until 200°C for 4 – 6 hours. The sample weight after degassing was recorded and the sample tube was attached to the instrument manifold. Adsorption took place first with predefined incremental volumes of N_2 gas entering the sample tube until the relative pressure reached unity (P = 1 atm in the system), followed by desorption, through which withdrawal of N_2 gas and a reduction of system pressure happened.

Figure 4.27 shows the adsorption-desorption isotherms for seven shale samples. All of these shale samples are hydrocarbon-bearing, except for GOM-12, which is from

the Gulf of Mexico and does not contain any organic material. HUT 1-70 and HUT 3-70 are Utica samples from the same well at different depths. WBS is a Barnett sample and NHS is a Haynesville sample. TGS-D and WGS-B are Eagle Ford samples at different depths. Adsorption and desorption measurements were performed on at least two samples from the same batch simultaneously to check for reproducibility. These isotherms obtained from the same sample batch were displayed on the same plot. It is clear that the adsorption-desorption measurements have good reproducibility, as seen by the overlap of the isotherms on the same plot.

The specific shape of isotherms as well as the observed desorption hysteresis can be attributed to pore size distribution, pore geometry and connectivity (Mason, 1983; Sing et al., 1985). According to the International Union of Pure and Applied Chemistry (IUPAC) classification (Sing et al., 1985), all of the isotherms fall into a combination of Type II and Type IV (for hysteresis during desorption), except for WBS, whose isotherms exhibit negligible hysteresis during desorption. Type II isotherms with hysteresis are also called Type IIB sometimes (Rouquérol et al, 2014). The Type II isotherm indicates unrestricted monolayer-multilayers adsorption (Sing et al., 1985). At a low relative pressure, the isotherm is steep, which corresponds to monolayer adsorption. With increasing pressure, the isotherm becomes flat (almost linear), multilayer adsorption takes place. Adsorption at low relative pressure ($P/P_o < 0.05$) for all samples studied shows the presence of micropores (Clarkson et al., 2012a). Among all the samples, the GOM-12 shale exhibits the highest adsorption of 5 cm^3/g STP at low relative pressure, thus the presence of the most micropore volume as well. (maybe due to the high clay content, from mineralogy). In contrast, the WBS and NHS samples showed the lowest adsorption of ~1 cm^3/g STP at low relative pressure, which translates into the least micropore space. Other shale samples from the Utica and Eagle Ford plays had an

adsorption of ~ 2 cm^3/g STP at a low relative pressure. On the other hand, the steep slope of all the isotherms at high relative pressure ($P/P_o \rightarrow 1$) indicates the partial filling of macropores (Daigle, 2014). While the maximum adsorption at high relative pressure varies between 13 and 19 cm^3/g STP for the hydrocarbon-bearing shales, while for the GOM-12 shale it is ~ 30 cm^3/g STP, which indicates that it has significantly more macropore volume than the hydrocarbon-bearing shales.

Meanwhile, the desorption hysteresis loop observed in all samples except for WBS is a result of capillary condensation in mesopores. It is due to the pore-blocking effects in ink-bottle type of pores (Mason, 1983; Sing et al., 1985; Ravikovitch and Neimark, 2002). It is evident that these adsorption-desorption isotherms exhibit hysteresis loops at $P/P_o > \sim 0.45$ in the desorption branch. According to IUPAC classification (Sing et al., 1983), it is suggested that the hysteresis loops of all the isotherms are Type H3. Type H3 hysteresis loop indicates the presence of slit-like pores resulted from the aggregates of plate-like particles, which further proves the presence of micropores and mesopores in these shale samples. Kuila and Prasad (2013b) observed a lack of hysteresis loop with kaolinite and a Type H3 hysteresis loop with montmorillonite. They attributed the difference in the shape of isotherms to the lack of mesopores and micropores in kaolinite. However, Clarkson et al. (2012a) showed that there is a discrepancy between the pore geometry interpreted from the isotherm hysteresis loop and from the small-angle and ultra-small-angle neutron scattering. As a result, both Clarkson et al. (2012a) and Schmitt et al. (2013) cautioned the use of isotherm hysteresis loop for examining the pore geometry of natural materials such as shale.

An interesting feature observed in the isotherms with desorption hysteresis is the forced closure of the hysteresis loop at $P/P_o \approx 0.45$, which has also been reported in many other studies using N_2GA (e.g. Kuila and Prasad, 2013b; Schmitt et al., 2013; Daigle,

2014). Sing et al. (1985) stated that this particular relative pressure at which hysteresis loop closes depends mainly on the properties of the adsorbate (in this case N_2), not on that of the adsorbent (in this case the shale samples). The particular relative pressure for N_2 at 77K is approximately 0.45. This forced closure of the hysteresis loop is due to the tensile strength effect, which results in the surface tension of the liquid adsorbate reaching a state of instability and the subsequent collapse of the hemispherical meniscus during capillary evaporation for pores smaller than ~4 nm in diameter (Groen et al., 2003). As a result, the pore network effects shown in natural porous materials such as shales can affect the pore size distribution derived from the desorption isotherm (Groen et al., 2003). Therefore, the pore size distribution calculation in this study was based on the adsorption branch of the isotherm to eliminate pore accessibility effects.

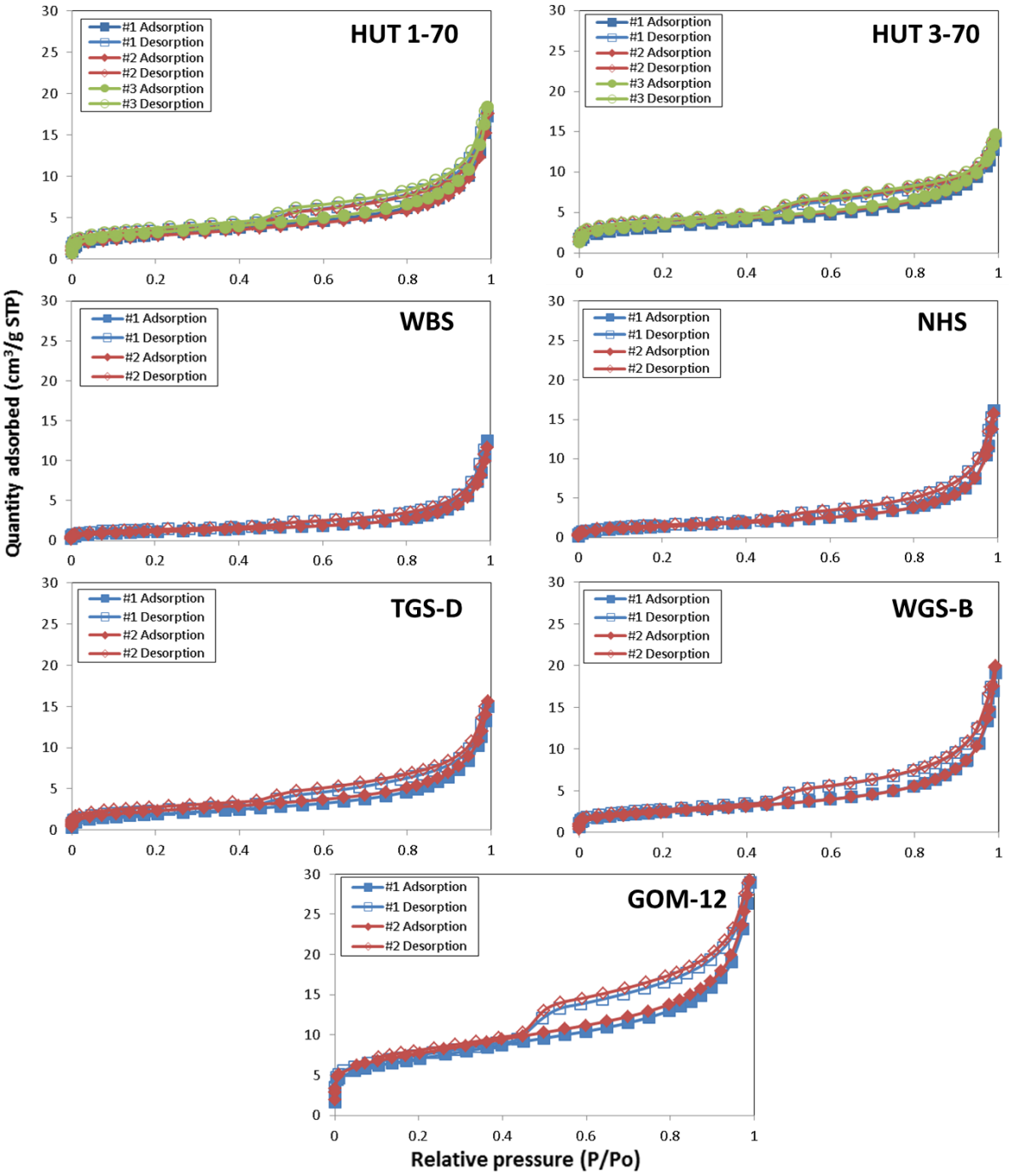

Figure 4.27: N_2 adsorption and desorption isotherms for seven shale samples. GOM-12 is a non-hydrocarbon-bearing shale while the rest all contain organic materials. The filled dots represent the adsorption isotherm and the unfilled dots represent the desorption isotherm.

Figure 4.28 shows the pore size distribution obtained using the BJH inversion method described in Section 3.2.3 from the raw adsorption isotherms for all the seven shale samples. The frequency was calculated by normalizing the incremental pore volume at a specific pressure step against the total pore volume. Figures 4.29 and 4.30 show the corresponding pore size distribution with the y-axis plotted as dV/d(logD) and dV/dD respectively. Taking the derivative of the pore volume minimizes the effect of uneven increase in pressure on the measured incremental pore volume during the adsorption test. The pore diameter on the x-axis is in log scale. We can see that these two ways of presenting the pore size distribution are very different visually. The dV/d(logD) plot focuses on the large pores while the dV/dD plot emphasizes on the small pores (Clarkson et al., 2013; Kuila and Prasad, 2013a). dV/d(logD) is mathematically equivalent to the product of dV/dD, 2.303 (ln10) and pore diameter D, and is therefore significantly magnified with large pores. It should be noted that neither of these two plots should be used directly to deduce the absolute amount of pore space for comparison. The partial porosity of pores in specific size intervals can be calculated by integrating the area under the graph. Nevertheless, caution should be taken when using the dV/d(logD) plot to interpret the relative abundance of pores of different sizes.

Figure 4.29 shows that all the shale samples exhibit a multi-modal pore size distribution. A major peak of around 100 nm is observed for all samples, indicating the presence of macropores. Other common peaks include one between 2 nm and 3 nm, one between 8 nm and 10 nm and the other one between 40 nm and 50 nm, which are in the range of micropore/fine mesopore, mesopore, and large mesopore/macropore respectively. HUT 3-70 shows a different shape compared with other samples, as its peak around 100 nm is ~0.008 cm^3/g, lower than that (the lowest is ~0.011 cm^3/g for WBS) for other samples and also lower than its own peaks at smaller pore diameter. This

means that the porosity of large mesopore/macropore is smaller for HUT 3-70 than that for other samples. On the other hand, all the peaks appear to be higher for GOM-12 than for other shales. The overall porosity and the partial porosities for different pore size ranges might be higher for GOM-12 than for other shales.

Figure 4.30 shows that a majority of the seven shale samples (except for HUT 3-70) exhibit a bimodal pore size distribution, with peaks at 2 – 3 nm and 8 – 10 nm diameter respectively. The presence of large mesopore/macropore is not captured with the dV/dD plot. The seven shale samples can be categorized into three groups based on their respectively shapes: WBS and NHS with a near flat slope, HUT 1-70, HUT 3-70, WGS-B and TGS-D with a more negative slope, and GOM-12 with the most negative slope and the largest peak. The shale samples with a more negative slope and larger peak value contain more microporosity and mesoporosity. Similar to what the dV/d(logD) suggests, the dV/dD plot also shows that the microporosity, the mesoporosity and the overall porosity of GOM-12 are the greatest among all shales.

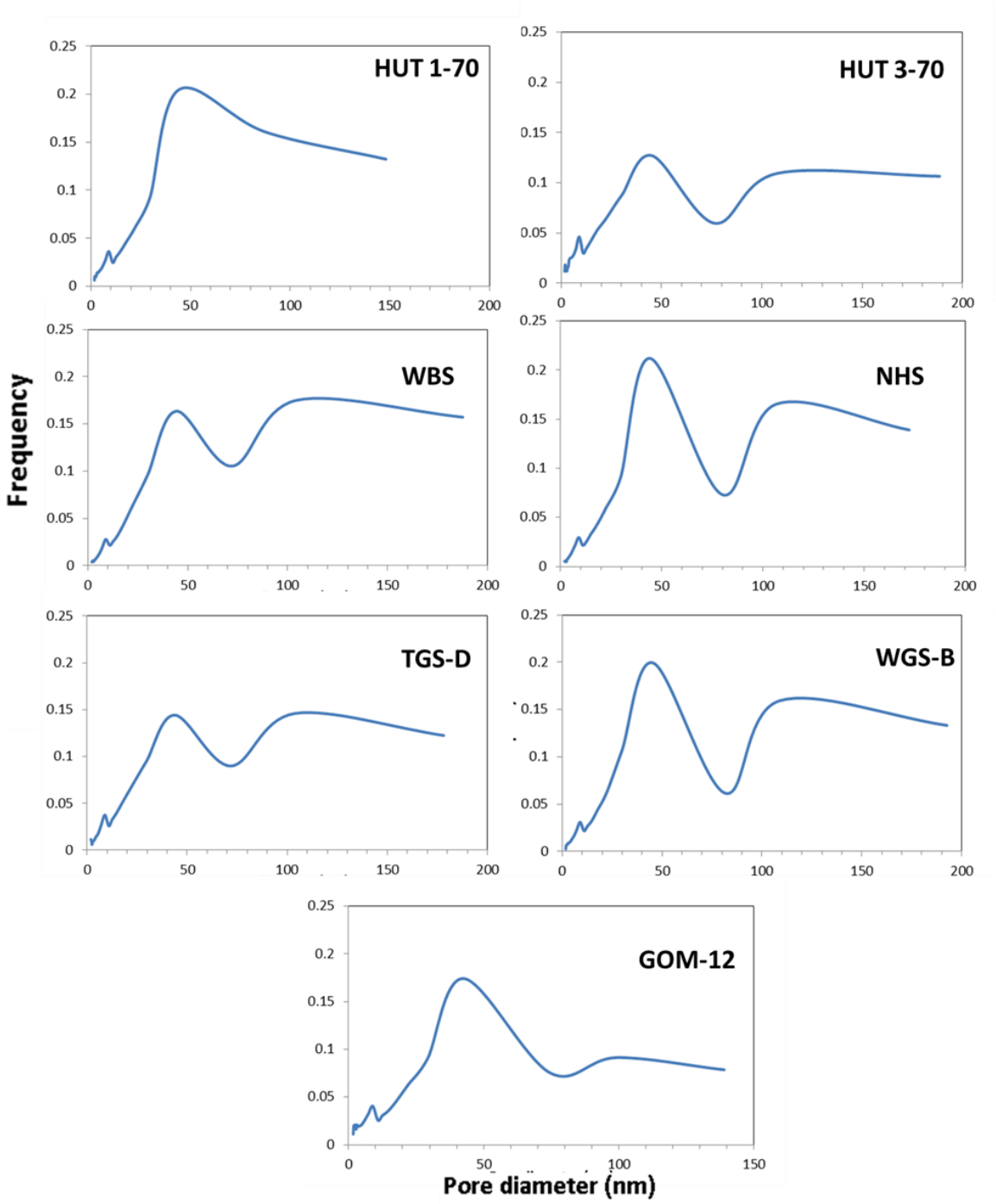

Figure 4.28: Pore size distribution for all the seven samples using the BJH model.

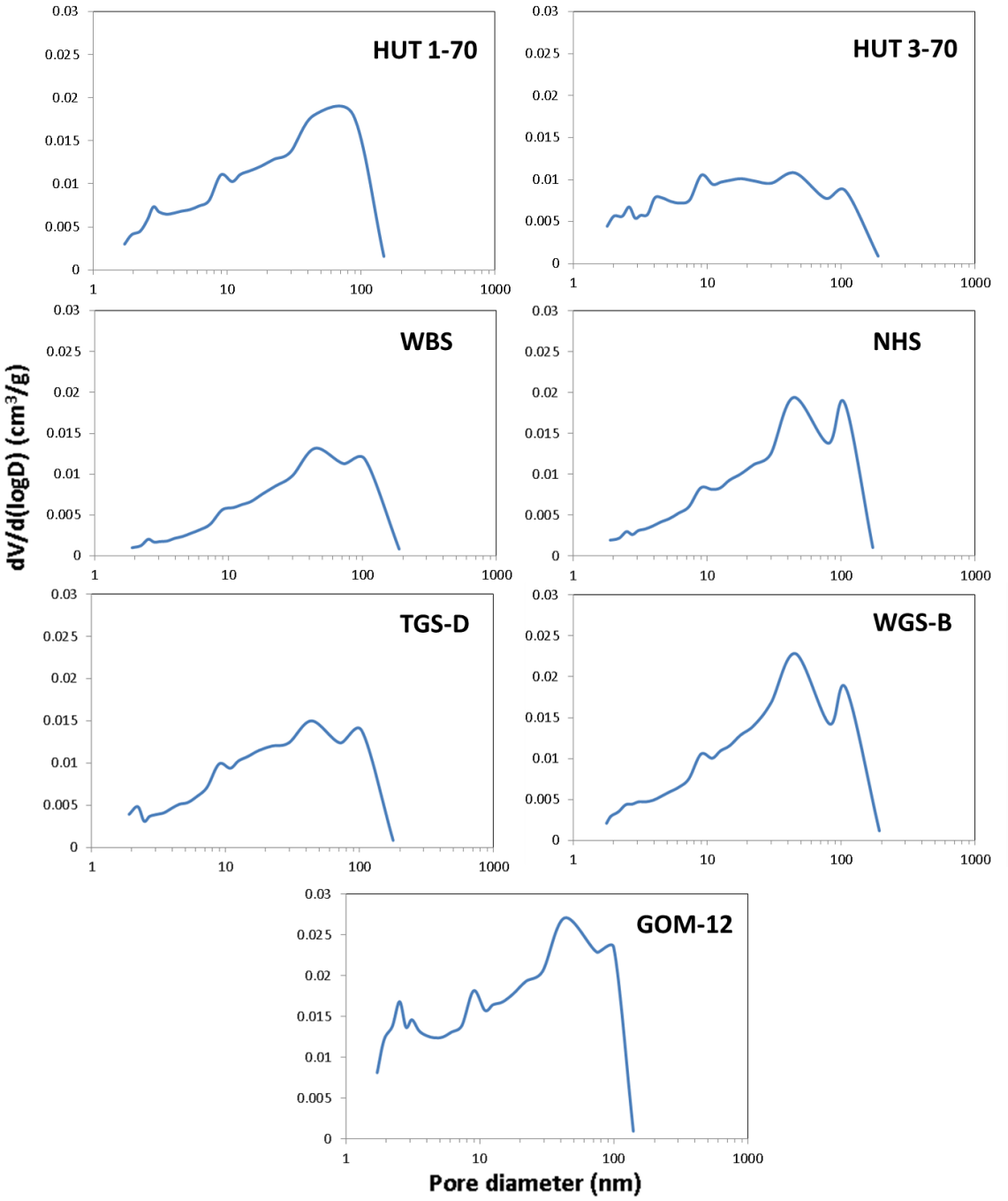

Figure 4.29: Pore size distribution for all the seven samples using the dV/d(logD) plot and the BJH model.

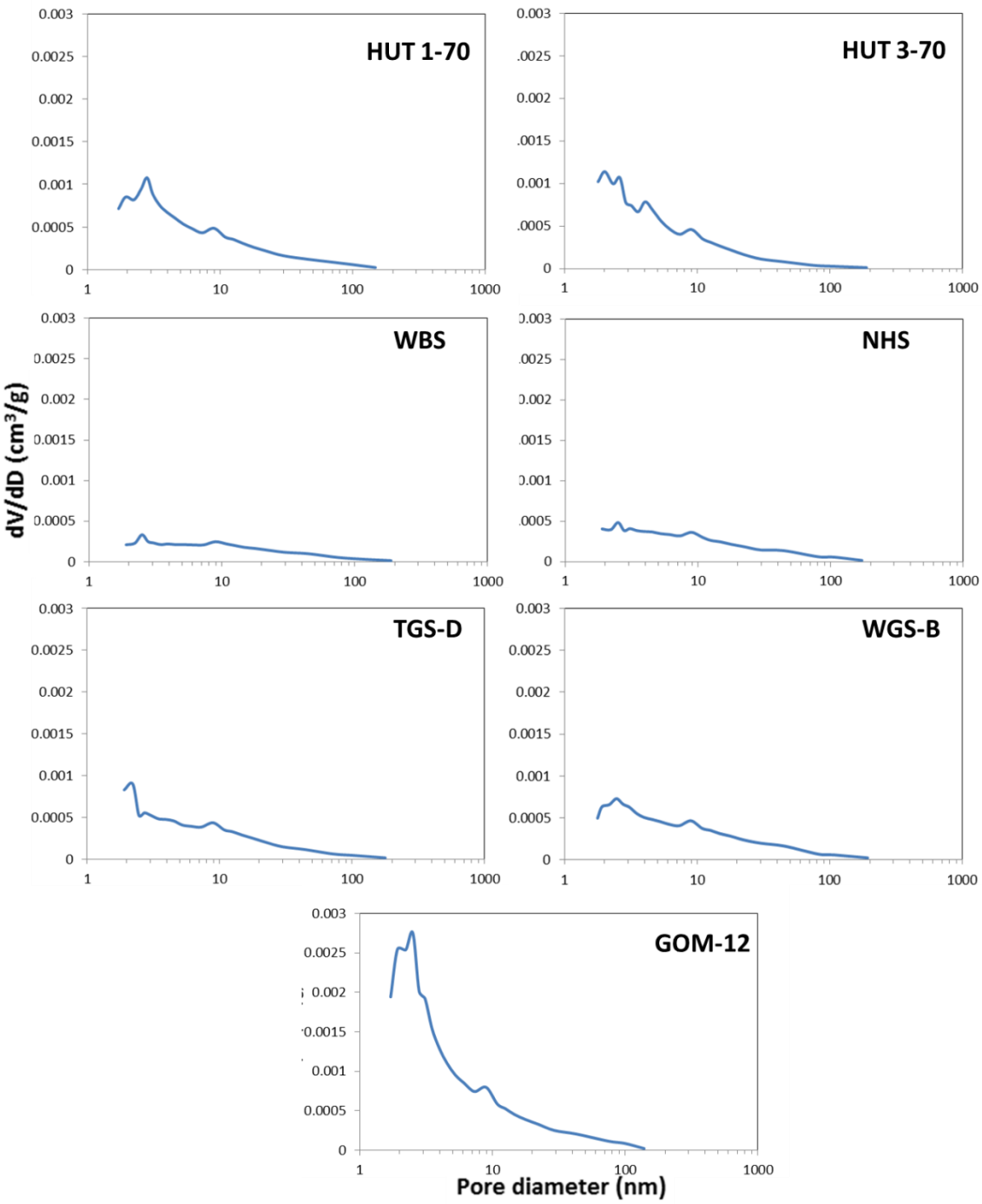

Figure 4.30: BJH pore size distribution for all the seven samples with the dV/dD plot.

The BET method (Brunauer et al., 1938) was used to determine the specific surface area of the shale rocks from the N_2 adsorption isotherms. The relative pressure (P/P_o) and the corresponding amount of adsorption are related to the monolayer capacity with the following equation:

$$\frac{\left(\frac{P}{P_o}\right)}{N\left[1-\left(\frac{P}{P_o}\right)\right]} = \frac{1}{N_o C} + \frac{C-1}{N_o C}\left(\frac{P}{P_o}\right) \tag{4.5}$$

where N is the amount of adsorption, N_o is the monolayer capacity, and C is a factor exponential related to the enthalpy of the adsorption system. The monolayer capacity is defined as the amount of adsorbate needed to completely cover the substrate surface with monolayer of molecules (Sing et al., 1985). N_o and C can be calculated from the slope and y-intercept obtained from the linear plot of $\frac{\left(\frac{P}{P_o}\right)}{N\left[1-\left(\frac{P}{P_o}\right)\right]}$ against the relative pressure. Subsequently, the specific surface area can be calculated by multiplying N_o with the atomic surface area of a N_2 molecule at 77 K (0.162 nm^2) and the Avogadro's constant (6.02×10^{23} mol^{-1}). The linear relationship is only valid for a small pressure range with the relative pressure between 0.05 and 0.30. Hence, only part of the adsorption isotherm is used to calculate the specific surface area.

Another way to estimate the specific surface area of the shale rock is the t-plot method. It determines the open specific surface area, which includes the surface area of mesopores and macropores as well as the external surface area. The surface area of the micropores is not accounted for with the t-plot method (Kuila and Prasad, 2013b). The volume of N_2 adsorption at a specific relative pressure can be plotted against the

corresponding thickness of the adsorbed layer t calculated using the Harkins-Jura model (Eq. 3.2). The slope of the linear plot will be converted to the open specific surface area.

Figure 4.31 shows the specific surface area for the seven shales obtained using the BET method and t-plot technique with the N_2 adsorption isotherm. There is good agreement between the specific surface areas obtained using these two techniques. GOM-12 exhibits the biggest discrepancy between the two specific surface areas. HUT 1-70 and HUT 3-70 also show significant (more than 10%) difference in the two specific surfaces. This can be due to the fact the t-plot method is not counting the surface area of micropores. The relationship between the difference in the two surface areas and the micropore content will be discussed later when the complete pore size distribution is obtained. On the other hand, the variation of specific surface areas between samples from the same shale play is very little (e.g. for the pair of HUT 1-70 and 3-70 from the Utica play and the pair of TGS-D and WGS-B from the Eagle Ford play). The specific surface area of the non-hydrocarbon-bearing GOM-12 shale is much greater than that of the six hydrocarbon-bearing shales. This can be due to the high clay content (65.5%) of the GOM-12 shale.

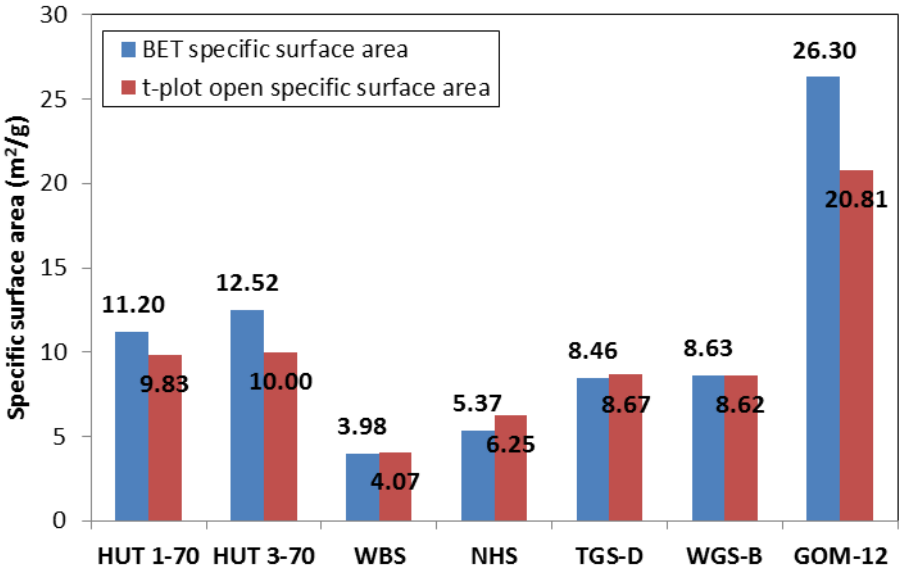

Figure 4.31: Specific surface area of the seven shales calculated using the BET model with the N_2 adsorption isotherm.

Figure 4.32 shows the cross-plot of the BET specific surface and the total clay content of seven shales. In general, the specific surface area increased with the total clay content for these shales. This is because the surface area of clay minerals is much greater than that of other minerals. The scatter of the data when the total clay content was low was probably due to the variations in clay type in these shale samples.

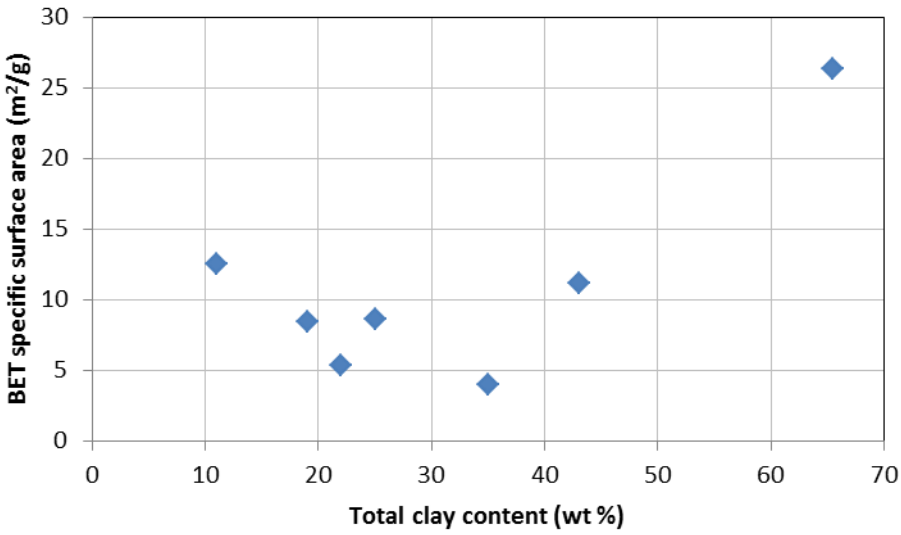

Figure 4.32: Cross-plot of the BET specific surface and the total clay content of seven shales.

Figure 4.33 shows a plot of the incremental pore surface area based on the BET model as a function of pore size for the seven shales. Peaks at pore diameters smaller than 50 nm can be observed in all the samples. This is due to the presence of clay platelets in these shales. For the organic-rich shales, the peak incremental pore volume ranged from about 0.2 m^2/g to less than 0.8 m^2/g. In contrast, the larger peak observed in the GOM-12 shale was almost 1.6 m^2/g. This can be attributed to the high clay content (65.5%) of the GOM-12 shale compared with other organic-rich shales.

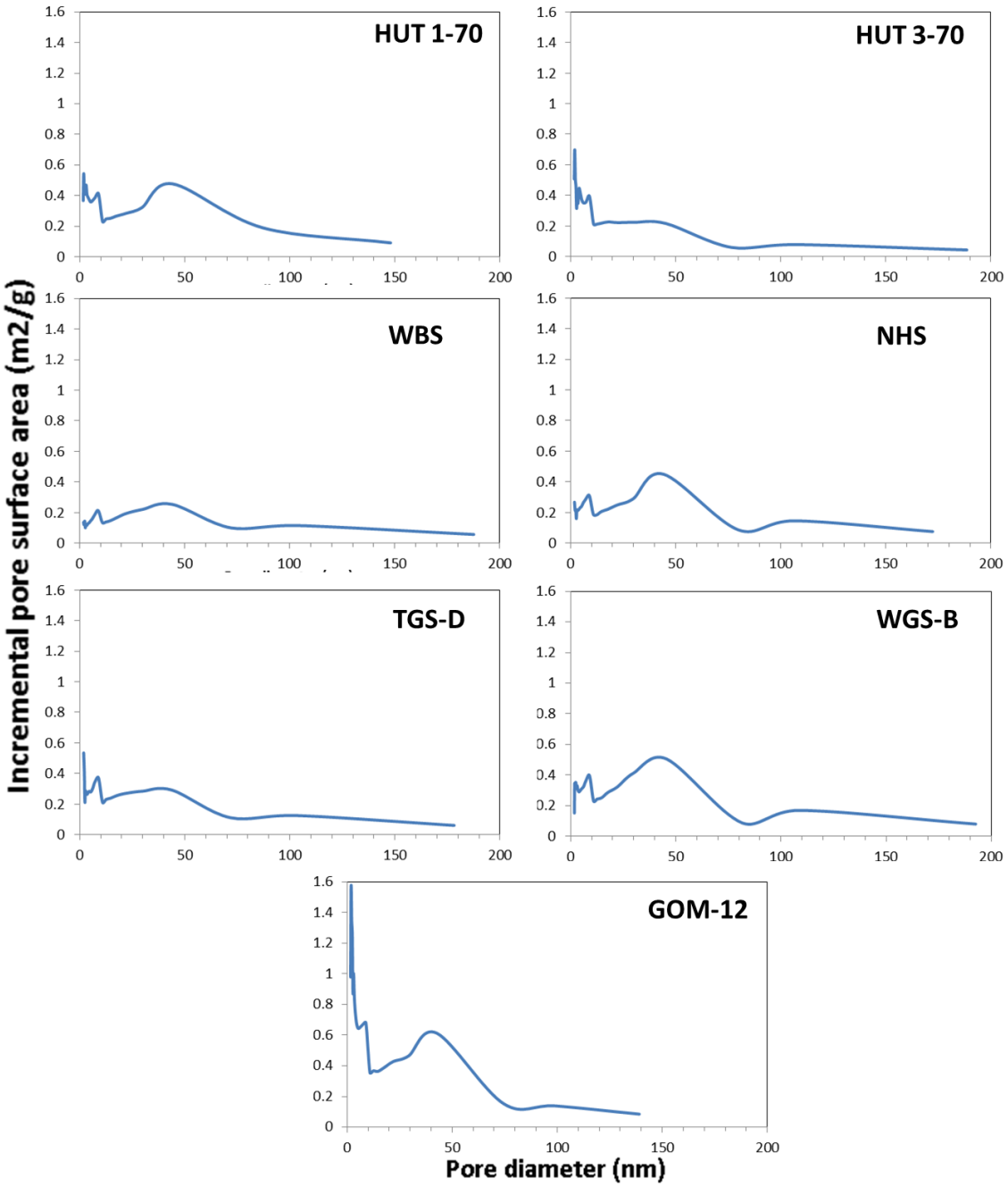

Figure 4.33: Incremental pore surface area based on the BET model as a function of pore size for seven shales.

4.5.2. MICP

As described in Section 3.2.3, the mercury injection capillary pressure was measured with the Micromeritics Autopore WIN9400 Series mercury porosimeter. Ground samples <2.36 mm were oven dried at 105^{o}C for 24 hours. 0.5 g – 2.5 g of the ground sample was used for each measurement. An injection pressure up to 60,000 psi was used. Intrusion took place before extrusion. The system compressibility was corrected by running a blank test with the penetrometer.

According to the Washburn equation (Washburn, 1921), the capillary pressure and pore throat diameter have the following relation:

$$P_c = \frac{4\sigma_{Hg}\cos\theta_{Hg}}{D} \tag{4.6}$$

where P_c is the capillary pressure, σ_{Hg} is the surface tension of mercury (σ_{hg}= 0.485 N/m is used in this study), θ_{Hg} is the contact angle of mercury with the rock sample (θ_{Hg} = 130^{o} is used in this study), and D is the pore throat diameter. The pore throat diameter was calculated based on the capillary pressure. Figure 4.34 shows the capillary pressure curve for all the seven shales. Only the intrusion curve is plotted. Note that the y-axis is the incremental pore volume.

From Figure 4.34, two major peaks can be observed in the capillary pressure curves. The first peak appears to be at an intrusion pressure between 2 psia and 3 psia (that for the GOM-12 shale is not the most pronounced peak). The large volume change at such a low intrusion pressure is probably due to conformance effects (Comisky et al., 2007; Comisky et al., 2011; Sigal, 2013). For MICP measurements with shale, mercury usually fills the container with samples at 5 psi. Occasionally, the sample container is not completely filled with mercury due to the surface irregularities of samples. Subsequently, when the injection pressure increases, mercury will enter the space between the crushed

shale particles and result in a peak due to the excessive incremental volume. From Figure 4.34, we can see that the conformance effects for GOM-12 and HUT 3-70 are much smaller than that of other samples, as the peak at $P_c = 2 – 3$ psia for GOM-12 and HUT-3-70 is 1 – 1.5 mL/g. The part of the capillary pressure curve affected by the conformance effects was not used in subsequent calculations for determining the pore size distribution.

The other peak in the capillary pressure curves was observed around 30,000 psi injection pressure. Caution needs to be taken to interpret the distribution for such fine mesopores from the capillary pressure curves. This large incremental pore volume observed at such a high intrusion pressure can be attributed to the sample compressibility, which results in pores being intruded by mercury at higher injection pressure. In fact, the pore size distribution measured using MICP is under high confining stress while that obtained with N_2GA is under ambient pressure. Furthermore, the non-uniform pore size, with the pore throat being smaller in diameter than the inner pore body, can also cause the incremental pore volume at such a high pressure to be extremely large (Labani et al., 2013).

On the right side of the left peak, zero to negative incremental pore volumes were observed between 30 psi and 300 psi of intrusion pressure, which correspond to a pore throat diameter between 6 μm and 600 nm. The reason for such incremental volume is still unknown. However, since 600 nm is three times the cutoff diameter for macropore (200 nm), it is safe to only use the positive incremental volume obtained with intrusion pressure greater than approximately 300 psi to compute the pores size distribution subsequently.

According to Sigal (2013), capillary pressure curves can be classified into four types based on their shapes. All the seven shales in this study except for HUT 3-70 have a Type 1 curve after the part of the curve due to the conformance effects is removed. Type

1 curves have a common maximum incremental intrusion volume at an intrusion pressure less than the maximum 60,000 psi. Samples with Type 1 curve would be the best reservoir rocks because of their resemblance to the capillary pressure curves obtained with conventional reservoir rocks. The capillary pressure curve for HUT 3-70 is somewhere between Type 1 and Type 2. A typical Type 2 curve has the incremental intrusion volume leveling off at 60,000. This appears to be the case for HUT 3-70, with some noise after the maximum incremental intrusion volume is reached.

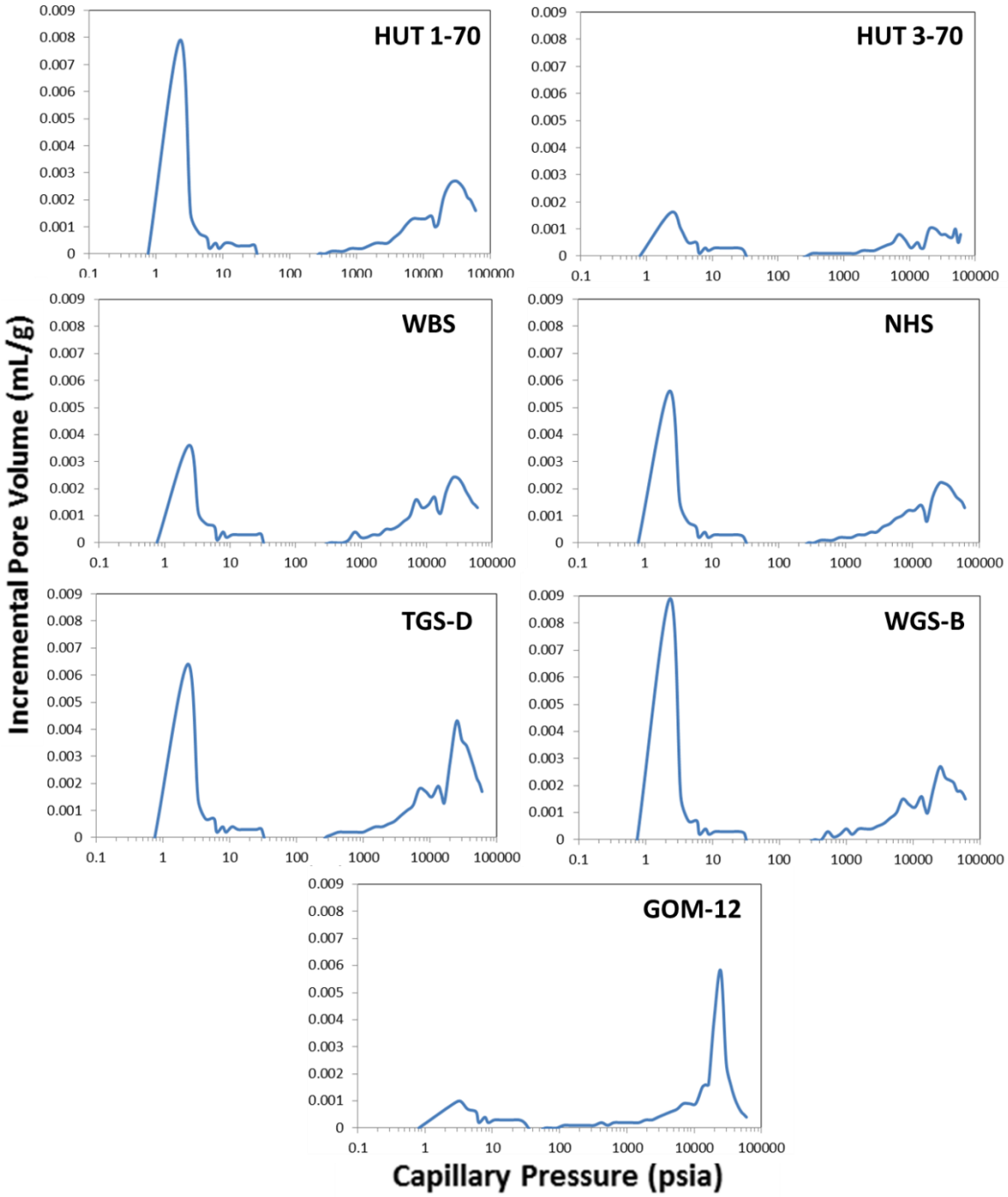

Figure 4.34: Capillary pressure curves of all the seven shales.

4.5.3. Integration of N_2GA and MICP

Following the method proposed by Schmitt et al. (2013), the complete pore size distribution of shale rocks was determined with the combined N_2GA and MICP techniques. Figure 4.35 shows the N_2GA and MICP curves used to obtain the intersection pore diameter for constructing the complete pore size distribution curve. Both curves are plotted with dV/dD as the y-axis and the pore diameter as the x-axis is. Note that the y-axis does not capture the full profile of the MICP curve when pore diameter is smaller than 10 nm. This is because the purpose of these plots is to find the intersection pore diameter where the N_2GA and MICP will merge for the complete pore size distribution. The N_2GA and MICP curves will be used for pore size smaller and greater than the intersection pore diameter respectively. The intersection of the two curves is circled in black and the intersection pore diameter is also pointed out. The intersection pore diameter ranged from 11.7 nm to 36.3 nm, which are all in the mesopore range. The most common intersection pore diameter was 36.3 nm. This proves the validity of combining both measurements to obtain the complete pore size distribution, where N_2GA is used for characterizing mesopores and micropores while MICP is used for characterizing mesopores and macropores.

Again, the effect of sample compressibility under high pressure mercury on the shape of the MICP curve is shown in Figure 4.35. For all shales, the dV/dD values for the MICP curve are consistently higher than that for the N_2GA curves for pore diameter smaller than the intersection diameter. This can be a result of the sample compressibility that causes mercury to intrude pores at a higher pressure, and the pore throat size being smaller than the pore body size, similar to what the peak near a pressure of ~30,000 psi shows in Figure 4.34. Peak shift between N_2GA and MICP pore size distribution curves due to sample compressibility has also been reported in previous works (Kuila and

Prasad, 2013b; Labani et al., 2013). High pressure mercury tends to compress the shale pores and cause the pore volume increment to be at smaller pore diameter compared with N_2GA, which works at much lower pressure. Figure 4.36 shows two examples of peak shifts observed with the TGS-D and GOM-12 shales. The incremental pore volume is plotted as the y-axis. The arrow indicates where the peak shift takes place. It can be seen that the peak shift happens at pore diameters between 10 nm and 100 nm, which is in the mesopore/macropore range. As expected, the peaks from the MICP measurement are at smaller pore diameters compared with the corresponding peaks from the N_2GA technique.

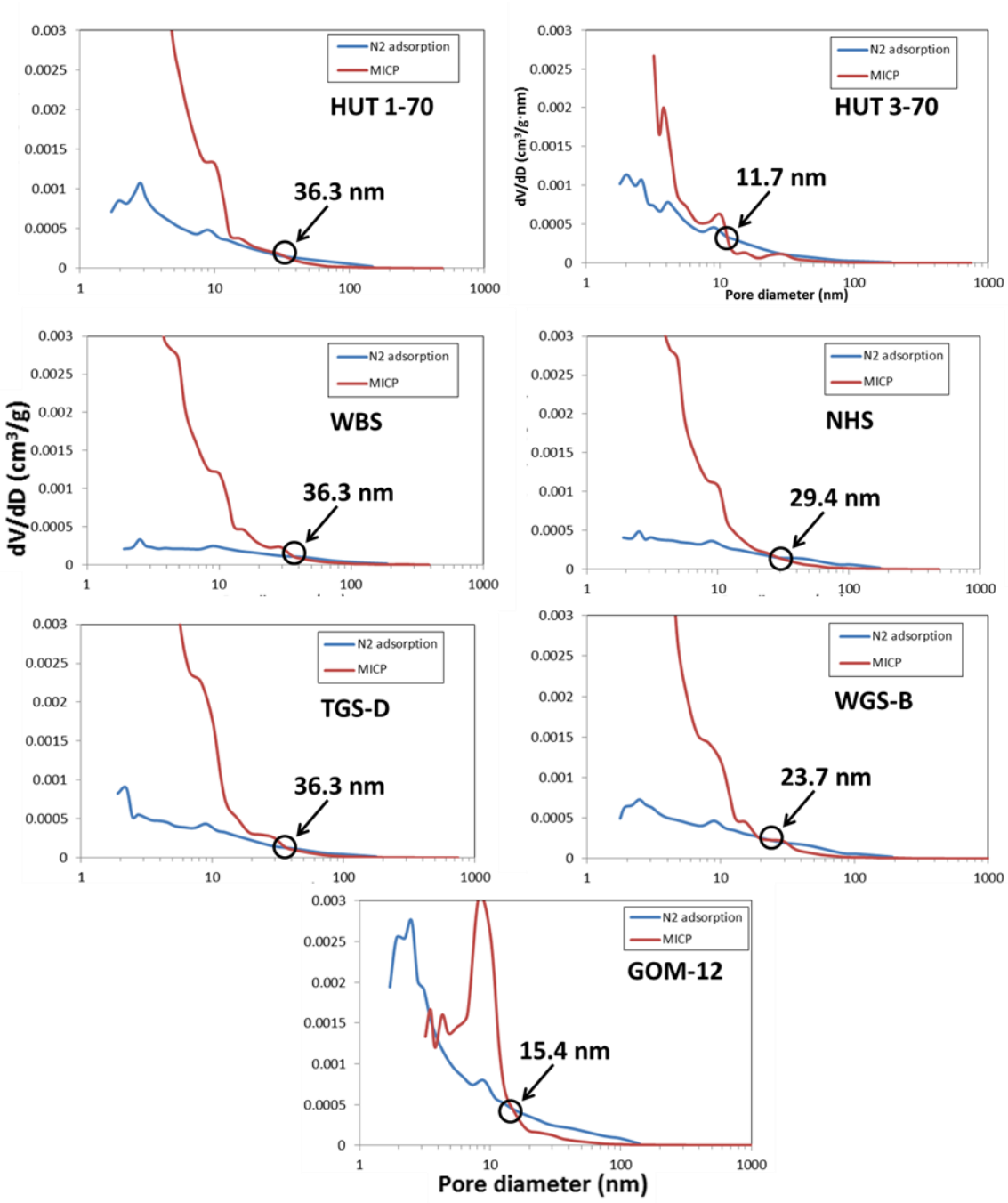

Figure 4.35: N_2GA and MICP curves used to determine the intersection pore diameter from which the complete pore size distribution can be constructed.

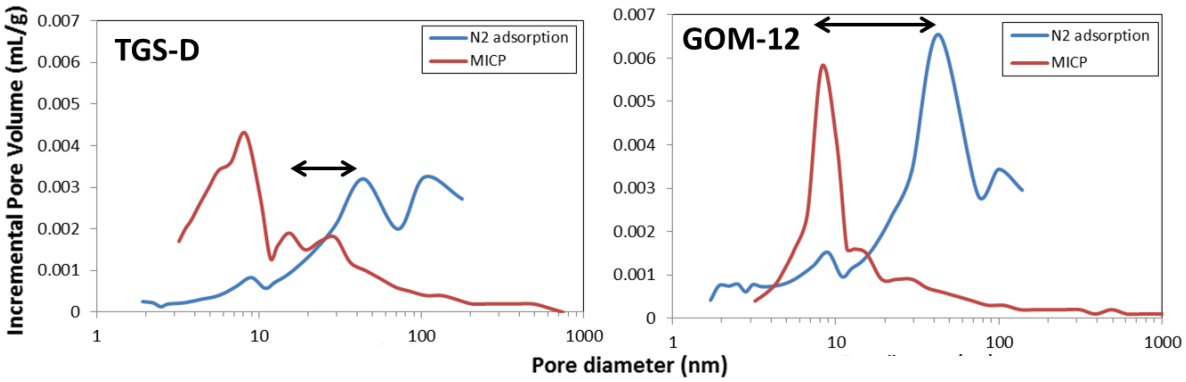

Figure 4.36: Overlaid N_2GA and MICP curves for TGS-D and GOM-12 shales with the incremental pore volume as the y-axis that exhibit peak shifts

Figure 4.37 shows complete pore size distribution for all seven shales using the combined BJH N_2GA and MICP curves, with dV/d(logD) as the y-axis. Compared with Figure 4.29 where only the BJH N_2GA data was used, we can see that the peak at ~ 100 nm pore diameter was replaced by smaller peaks stretched into pore size ranged between 400 nm and 1000 nm in Figure 4.37. This again shows the capability of the MICP technique to determine the distribution of macropores.

Table 4.8 shows the shale pore parameters obtained from N_2GA and MICP measurements separately and as a combined dataset. The total pore volume is the sum of the incremental pore volume at different pore diameters. It can be seen that single measurement (N_2GA or MICP alone) always yields higher total pore volume than the combined N_2GA and MICP results. Among these shales, the highest total pore volume was obtained with N_2GA for HUT 3-70 and GOM-12, while the other shales' highest total pore volume was measured with MICP. The combined datasets always showed the lowest total pore volume because the peak incremental pore volumes from both N_2GA and MICP techniques were not used in constructing the complete pore size distribution curve.

From the combined pore size distribution curves, we can see that for all the shale samples, the pore type is predominantly mesopores. All of the shales have a mesopore content ranged between 73.07% and 83.27%. GOM-12's micropore content of 5.04% is the highest among all shales. This can be due to the high clay content of the GOM-12 shale. The macropore content varies between 14.61% and 23.63%. While four out of the seven shales have their intersection pore diameter coincide with their respective median pore diameter from the combined N_2GA and MICP pore size distribution curve, the intersection pore diameter for the remaining three (HUT 1-70, TGS-D and GOM-12) is always slightly larger than the corresponding median pore diameter.

The proposed method of combining the N_2GA and MICP measurements to obtain the complete pore size distribution of shales should be used with caution. N_2GA measures the distribution of the entire pore system while MICP responds to the intrusion of mercury into the pore throat, not the inner pore body (Labani et al., 2013). The heterogeneous nature of shales causes the pores to be non-uniform in shape. This might be the reason for the difference observed in the pore size distribution from both measurements. On the other hand, the BJH model for interpreting the N_2GA data and the Washburn equation in the MICP analysis assume the pores to be cylindrical. This allows the measurement techniques to characterize pores of similar shapes in shales (Daigle, 2014).

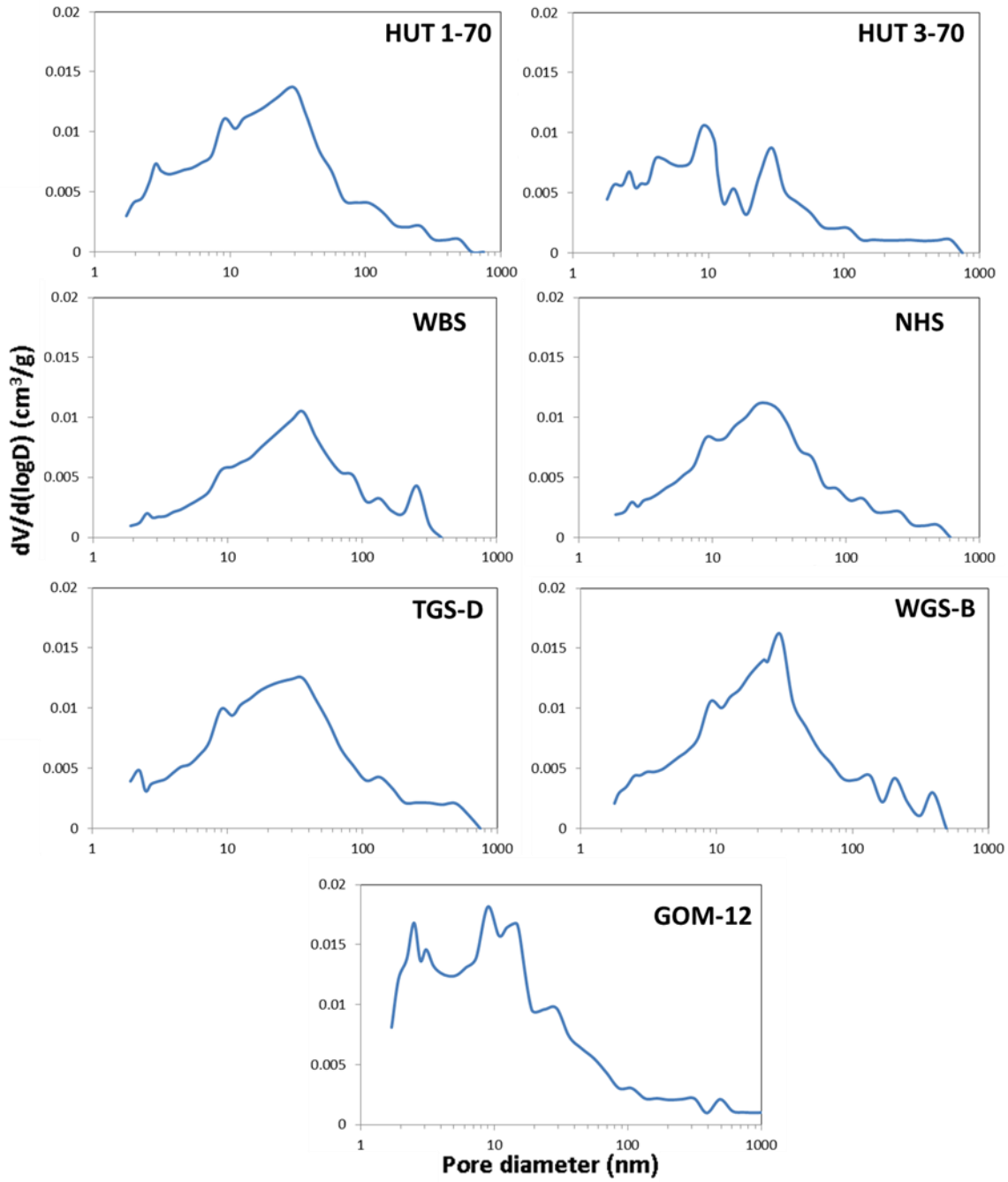

Figure 4.37: Combined pore size distribution for all seven shales with the dV/d(logD) plot using the BJH N_2GA and MICP curves.

Sample	N_2GA	MICP	Combined N_2GA + MICP					
	PV_{total} (cm^3/g)	PV_{total} (cm^3/g)	PV_{total} (cm^3/g)	Intersection Pore Diameter (nm)	% Micropore	% Mesopore	% Macropore	Median Pore Diameter (nm)
HUT 1-70	0.0258	0.0322	0.0178	36.3	2.36	80.83	16.80	22.3
HUT 3-70	0.0193	0.0127	0.0115	11.7	1.97	83.27	14.76	11.7
WBS	0.0172	0.0299	0.0118	36.3	0.56	73.07	26.37	36.3
NHS	0.0235	0.0275	0.0130	29.4	0.98	76.70	22.32	29.4
TGS-D	0.0222	0.0417	0.0174	36.3	1.47	74.90	23.63	29.7
WGS-B	0.0289	0.0311	0.0180	23.7	1.30	79.20	19.50	23.7
GOM-12	0.0376	0.0294	0.0233	15.4	5.04	80.35	14.61	12.5

Table 4.8: Shale pore parameters obtained with N_2GA and MICP measurements for all the seven samples. PV_{total} refers to the total pore volume.

4.6. RESULTS AND DISCUSSION

According to Eq. 4.3, assuming surface relaxation is the dominant relaxation mechanism, the transverse surface relaxivity ρ_2 is a function of pore size. If the pore shape is assumed to be cylindrical, then the surface to volume ration S/V can be calculated as follows:

$$S/V = 2/r = 4/D \tag{4.7}$$

Subsequent, the transverse surface relaxivity ρ_2 can be estimated with the pore diameter from the N_2GA and MICP measurements and the T_2 relaxation time from the NMR measurement:

$$\rho_2 = \frac{D}{4T_2} \tag{4.8}$$

Figure 4.38 shows the combined pore size distribution from the BJH N_2GA and MICP curves and the NMR T_2 distribution for five shales. The blue dots represent T_2 from the NMR measurement and the red line shows the pore size distribution from the combined N_2GA and MICP measurements. The axis for the pore diameter is on the top of the plot and that for T_2 relaxation time is on the bottom of the plot. The T_2 and N_2GA-MICP incremental volumes are shown on the left and right of the plots respectively. It can be seen from these plots show that both the pore size and T_2 distributions exhibit a multi-model behavior. Peaks in these plots are aligned at similar pore diameter/T_2 values to reflect that both techniques are valid in showing the presence of pores of similar sizes. However, it is evident that the curves do not overlap exactly as there is always a difference in the magnitude of some peaks when one set of the peaks in both plots are made to align with each other. This can be due to the reason that N_2GA and MICP measurements reflect the pore size while the NMR T_2 distribution is also a function of the fluid viscosity and the concentration of the paramagnetic ions on the pore wall, in

addition to the pore size. In some cases (e.g. HUT 3-70), multiple peaks from the N_2GA-MICP derived pore size distribution can appear to cover the T_2 range of a single peak.

The vertical red line in each plot is used to indicate the values of T_2 relaxation time and the corresponding pore diameter for the calculation of the transverse surface relaxivity ρ_2. It can be seen that the T_2 relaxation time used is usually 0.1 – 1 ms (except for HUT 3-70), while the pore diameter is 8 – 25 nm. Table 4.9 shows the ρ_2 derived from the T_2 and pore diameter values based on Eq. 4.8.

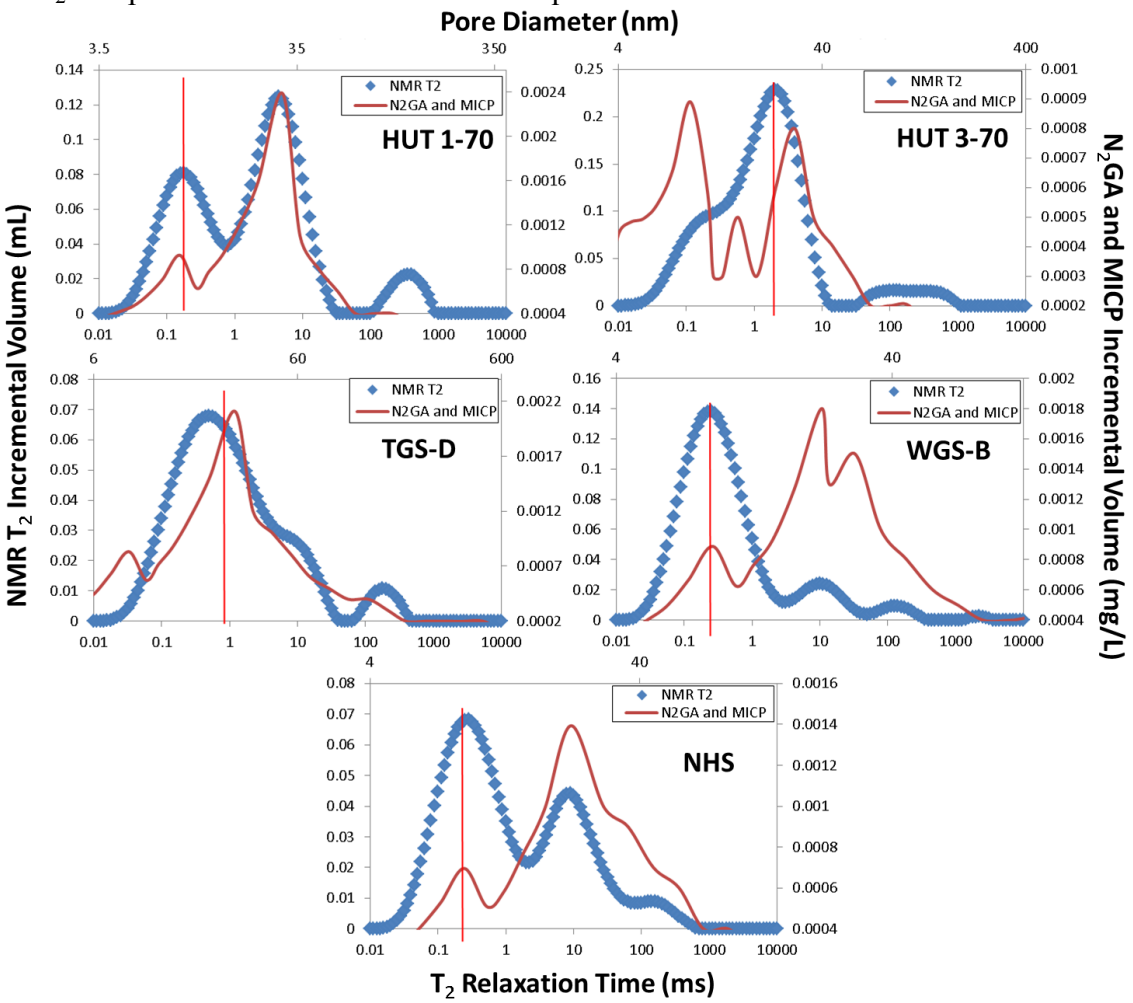

Figure 4.38: Combined pore size distribution from the BJH N_2GA and MICP curves and the NMR T_2 distribution for five shales.

Sample	ρ_2 (μm/s)
HUT 1-70	12.62
HUT 3-70	3.33
NHS	9.96
WGS-B	8.92
TGS-D	6.24

Table 4.9: ρ_2 derived from the NMR T_2 and pore size distribution measured with N_2GA and MICP based on Eq. 4.8.

As can be seen in Figure 4.39, a good linear correlation exists between the transverse surface relaxivity ρ_2 and the total clay content. Although clay is not paramagnetic but diamagnetic, the iron substitution in the lattice structure of clay might cause the clay minerals to be paramagnetic and affect the T_2 relaxation time.

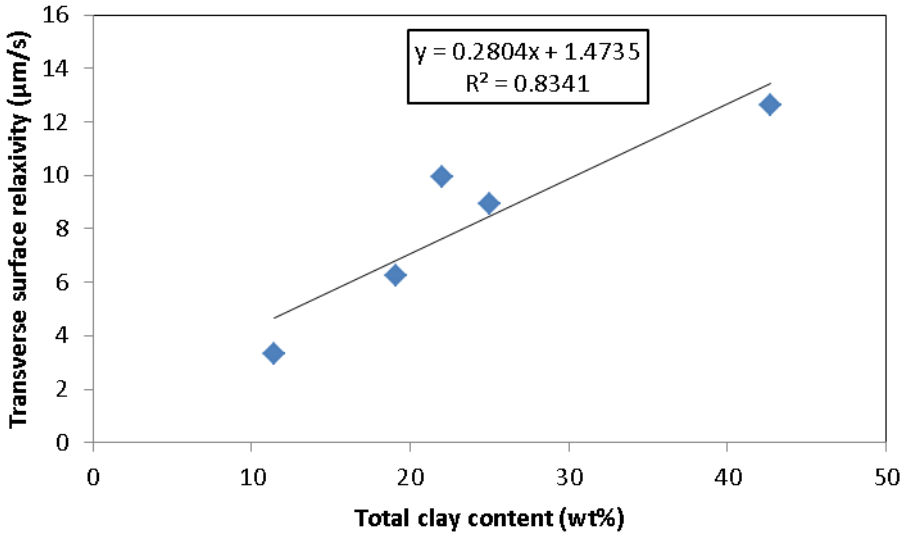

Figure 4.39: Plot of the transverse surface relaxivity ρ_2 against the total clay content.

Figure 4.40 shows a plot of the transverse surface relaxivity ρ_2 against the iron content. Only four data points were available for constructing such a plot. The linear correlation between ρ_2 and the iron content is not as good as that between ρ_2 and the total

clay content. It might be due to the lack of data that magnifies the fluctuation of data points around the best-fit line, or to the distribution of paramagnetic ions that directly affects the surface relaxivity (Daigle et al, 2014).

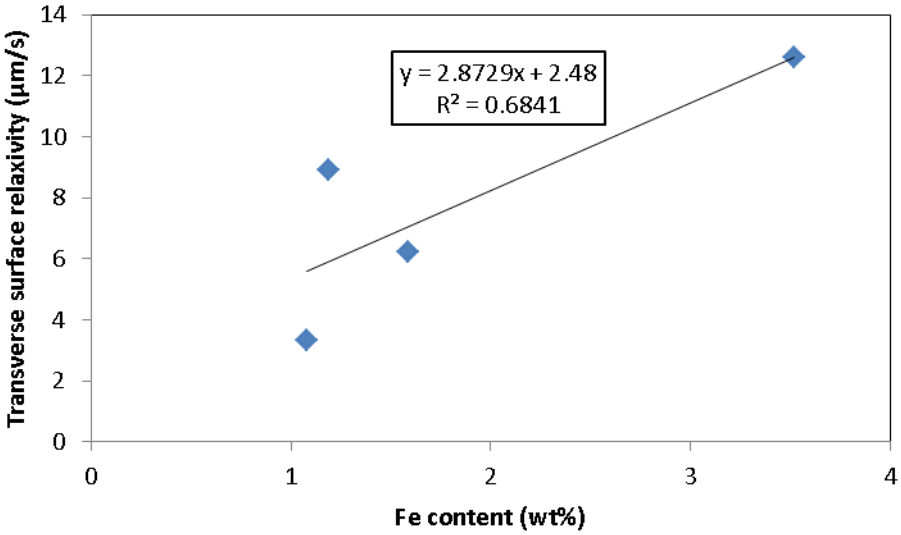

Figure 4.40: Plot of the transverse surface relaxivity ρ_2 against the iron content.

Figure 4.41 shows the cross-plot of the total pore volume per unit weight from the pore size distribution and the total NMR porosity based on the T_{2sec}-T_1/T_2 measurements for five shale samples. The porosity obtained from the combined N_2GA and MICP techniques and the NMR T_1-T_2 measurements does not exhibit a good correlation. The lack of sufficient data points for different shale samples makes it difficult to establish a clear trend. More importantly, the pore size distribution was measured with dried shale samples while the NMR T_1-T_2 measurements were performed on preserved samples. The pore size distribution covers all the pore space while the pore volume measured with NMR corresponds to the fluid-filled pore space. The pores previously filled with gas or

liquid are included in the pore size distribution, but cannot be detected by the NMR instrument.

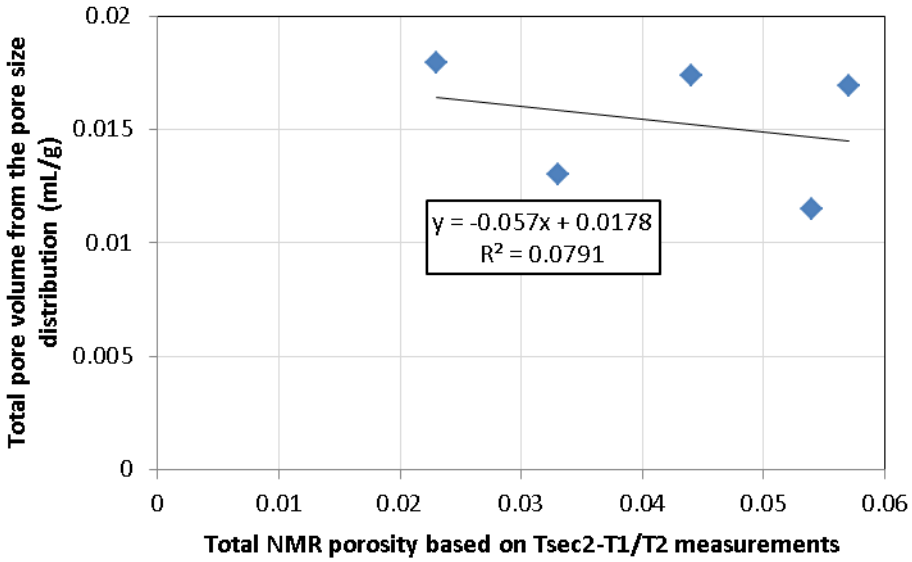

Figure 4.41: Cross-plot of the total pore volume per unit weight from the pore size distribution and the total NMR porosity based on the T_{2sec}-T_1/T_2 measurements for five shale samples.

Figure 4.42 shows the cross-plot of the native water activity and the total NMR porosity based on the T_{2sec}-T_1/T_2 measurements for five shale samples. In general, the native water activity of these four shales increased with the total porosity. Measurements of the native water activity and the corresponding total porosity on additional shale samples will be beneficial to establish a correlation between these two petrophysical properties.

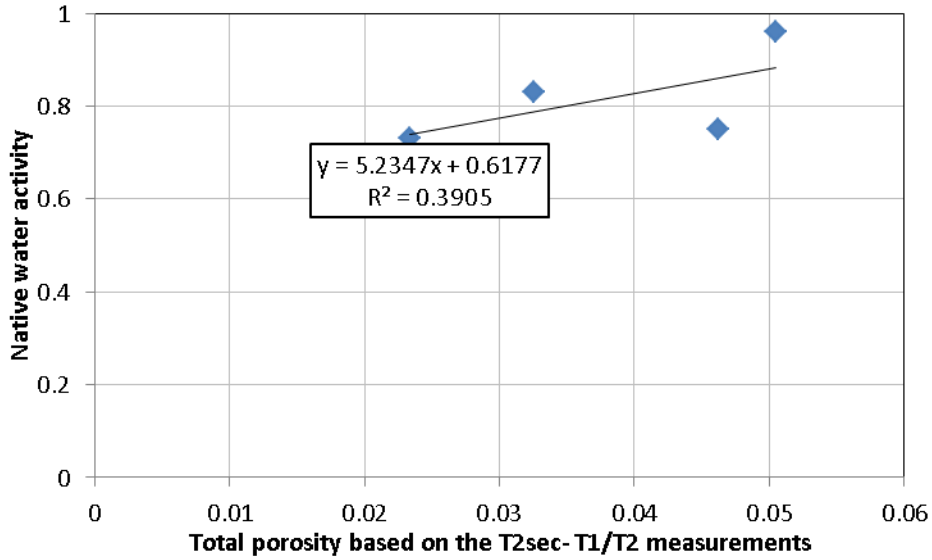

Figure 4.42: Cross-plot of the native water activity and the total NMR porosity based on the T_{2sec}-T_1/T_2 measurements for four shale samples.

4.7. CONCLUSIONS

This chapter presents new characterization techniques and results of a series of shale petrophysical properties for samples from various shale plays in the US. The XRD and XRF measurements were shown to yield consistent shale mineralogy. Therefore, the elemental composition obtained with the XRF measurement can be used to quantify the shale mineralogy accurately. The Eagle Ford formation is calcite-rich in general, and the Bakken sample contains the most dolomite. The GOM-12 shale is the most clay-rich among all the samples, and contains a greater amount of the expandable smectite mineral. A great variation in mineralogy was observed for samples even from the same well in the Utica formation. Therefore, detailed mineralogical studies need to be performed for understanding the correlation with other shale properties and studying shale-fluid interactions. A linear correlation also exists between the sample depth and the quartz, calcite and clay content for the Utica shale.

The NMR T_1-T_2 measurements were shown to be effective in distinguishing the pore fluids based on their viscosity and the pore size. The T_1/T_2 ratio and T_2 secular relaxation time were employed together to quantify the total porosity and the porosity attributed to pores with various sizes and saturated with low and high viscosity fluids respectively. A good correlation was observed between the total clay content and the porosity attributed to small pores with low viscosity fluid.

N_2GA and MICP were utilized to construct the complete pore size distribution of low porosity and ultra-low permeability shale rocks. Desorption hysteresis was observed with all the shale samples, indicating the presence of ink-bottle type of pores, which resulted in pore blockage during desorption. Sample compressibility effect was demonstrated with large peaks in the small mesopore range and greater fraction of small pores detected with MICP than with N_2GA.

The transverse surface relaxivity was calculated by peak matching the NMR T_2 distribution curve and the pore size distribution curve from N_2GA and MICP. It was shown to have a good correlation with the total clay content, suggesting the presence of paramagnetic ions in the clay mineral.

Chapter 5: Shale-Brine Interactions[2]

5.1 Background on Water/Ion Movement in Shale

When developing shale reservoirs, water-based fluids are very widely used to drill, complete and fracture wells. Inorganic salts such as KCl, NaCl and $CaCl_2$ are common additives to stabilize clay minerals in the shale rock. The transport of water molecules and ions across the shale surface can have a significant impact on the stability of shale. Water/ion movement into and out of shale can cause damage to shale stability in the form of pore pressure and swelling pressure increase and change in mechanical properties near the wellbore and on the fracture face (van Oort, 2003; Zhang et al., 2004). These effects are driven by a combination of hydraulic pressure, chemical potential, electric potential and temperature gradients (van Oort, 2003). Zhang et al. (2004) also attributed the inflow of water from the lower-activity bulk fluid to the higher-activity shale sample to the capillary effect at early time of the shale-fluid contact. Even though the shale instability problem stemming from the unfavorable interactions of shale with water-based fluids can be minimized by using oil-based or synthetic-based fluids, cost and environmental concerns still favor the use of water-based fluids in a lot of field operations. Therefore, understanding and ultimately preventing water/ion movement into and out of a shale can help improve shale stability during drilling and fracturing operations by using fluids with the appropriate concentration of additives.

When a water activity gradient exists between the bulk fluid outside the shale and the pore fluid within the shale, osmotic transport of water will occur (Chenevert, 1970b; Ewy and Stankovich, 2000; Yu et al, 2001). Previous studies have shown that shales act like leaky membranes, allowing certain ions to move across it (van Oort et al., 1995,

[2] Part of the research in this chapter was first presented in SPE 168792 (Zhou et al., 2013b), SPE 166216 (Zhou et al., 2013c) and SPE 166419 (Jung et al., 2013b).

1996; Ewy and Stankovich, 2000; Zhang et al., 2004). As a result, the presence of ionic concentration gradients for various species will cause ions to move into and out of a shale. Furthermore, the existence of a hydraulic gradient between the bulk fluid and the shale pore fluid is also very common due to the wellbore pressure being greater than the pore pressure during overbalanced drilling. This will result in the flow of the water-based drilling fluid into the shale. These coupled processes can alter the shale chemical and mechanical properties significantly and change the hydration and stress state of the shale formation in the near-wellbore region.

Van Oort (2003) compared the relative fluxes of water and ions due to the different transport processes into the shale. He pointed out that for shales with nano-Darcy permeability, ionic diffusion can be one to two orders of magnitude faster than hydraulic flow from the wellbore to the shale matrix. Even though the low permeability characteristic of shale prohibits the rapid dissipation of the elevated pore pressure far away from the wellbore, the pore pressure front still travels radially away from the wellbore into the shale one to two orders of magnitude faster than the ionic diffusion front. Ballard et al. (1994) performed transport experiments in shale with radioactive tracer and found that ion transport is dominated by diffusion in the absence of a pressure gradient across the shale surface.

Zhang et al. (2008) concluded from their experiments that the dominant mechanism for achieving higher shale wellbore stability using salt solutions such as KCl, NaCl and $CaCl_2$ lies in the subsequent change in shale mechanical properties rather than the enhanced osmotic backflow of water from the shale matrix. As a result of the change in shale stress state and mechanical properties due to the coupled transport processes of water and ions as well as the propagation of the elevated pore pressure, the shale stability may be enhanced or reduced, depending on the direction of flow and the bulk fluid

pressure relative to the pore pressure. The increase in shale pore pressure due to bulk fluid invasion (the bulk fluid being the drilling mud) and the swelling pressure developed due to adverse cation exchange at the clay surface can reduce the effective normal stresses and cause shale failure to occur. On the other hand, the weakening of the cementation bonds is manifested by a change in mechanical properties and failure parameters, shifting the Mohr-Coulomb failure envelope and resulting in the increased possibility of shale failure.

The focus of this chapter is on the interactions of hydrocarbon-bearing shale with water-based ionic solutions. The water/ion movement, the swelling behavior and the change in mechanical properties of shale samples after exposure to brines were used together to understand the sensitivity of shales to fluid exposure. The impact of cations on reducing shale reactivity was investigated with these measurements. The effect of hydraulic pressure gradient on water/ion transport and shale stability was not explored. Water and ion movement into and out of shale was studied using a gravimetric technique. The use of inorganic salt solutions to reduce the degree of shale swelling and to improve shale mechanical stability was investigated extensively. Shale preservation was shown to significantly impact the change in mechanical properties upon fluid contact.

5.2 GRAVIMETRIC TEST

A gravimetric test was employed to investigate the water/ion movement into and out of shale upon contact with various water-based brine solutions. The test procedure will be illustrated in detail below. Results from the test using hydrocarbon bearing shales will be analyzed and compared with that using non-hydrocarbon bearing shales from previous studies in our research group.

5.2.1. Gravimetric Test Procedure

The gravimetric test procedure was developed by Zhang et al. (2004) to understand water and ion movement when a shale comes to contact with water-based brine solutions. The weight change of shale samples immersed in the fluids is monitored at different stages before and after shale-fluid contact. Before any weight measurement can be taken, preserved shale samples need to be cleaned with hexane to remove any residual mineral oil on the surface.

The original water content of the shale has to be determined prior to performing any gravimetric test on shale. The weight of a native preserved shale sample is measured as W_{native}. The sample is then oven dried at 220°F (104.4°C) for 24 hours to remove any free water within the pore space and its weight is recorded as W_{dry}. The original water content of the shale can then be calculated as:

$$C_w = \frac{W_{native} - W_{dry}}{W_{native}} \times 100\% \tag{5.1}$$

where C_w is the native water content of the shale. The dried shale sample should not be used for any subsequent testing since its original hydration state and petrophysical properties have been altered due to the removal of water from its preserved state. A new preserved shale sample should be used for the immersion test with brine solutions.

The weight of a new preserved shale sample from the same core sample is measured as W_{ns}. Therefore, the weight of water in the native preserved shale sample is:

$$W_{nw} = W_{ns} \times C_w \tag{5.2}$$

where W_{nw} is the weight of water in the preserved shale at its native state. The shale sample is then immersed in a brine solution of a particular salt with a specific concentration for 24 hours. The weight after immersion is recorded as W_{ai}. Subsequently, the shale sample is oven dried at 220°F for 24 hours. The weight of the dried sample is

then recorded as W_{ad}. The total weight of water in the shale sample after immersion, W_{tw}, can be calculated as:

$$W_{tw} = W_{ai} - W_{ad} \tag{5.3}$$

Subsequently, the weight of water added to or removed from the shale, W_{wt}, can be calculated as:

$$W_{wt} = W_{tw} - W_{nw} = W_{ai} - W_{ad} - W_{ns} \times C_w \tag{5.4}$$

And the weight of ion moved into or out of the shale, W_{it}, is then calculated as:

$$W_{it} = W_{ai} - W_{ns} - W_{wt} = W_{ad} + W_{ns}\left(C_w - 1\right) \tag{5.5}$$

5.2.2. Gravimetric Test Results and Discussion

5.2.2.1 Water/Ion Movement with BEF-1 Shale

Following the procedure described in Section 5.2.1, the water and ion movement into and out of a BEF-1 shale sample at room temperature is shown in Figure 5.1. A positive weight change indicates that water or ion is added to the shale sample while a negative weight change indicates that the shale has lost water or ions. NaCl, KCl and $CaCl_2$ with concentration up to 25% by weight were used as the salt for preparing the brine solutions. The shale samples were from the same cylindrical core and their native water activity A_w and original water content C_w were assumed to be the same. As shown in Table 4.5, the native water activity of the BEF-1 shale was measured to be 0.46.

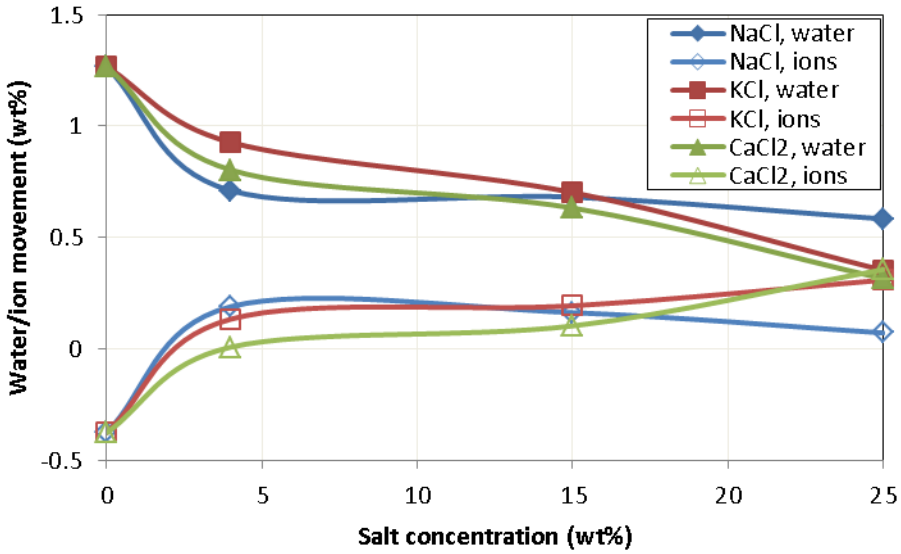

Figure 5.1: Water and ion movement into and out of BEF-1 shale using NaCl, KCl and $CaCl_2$ brines, plotted against salt concentration.

It can be seen from Figure 5.1 that in general, less water and more ions moved into the BEF-1 shale with an increasing ion concentration. The water movement into the shale decreased from about 1.3 wt% to about 0.3 wt% of the native shale when the salt concentration was increased from zero to 25% by weight for both KCl and $CaCl_2$ salts. A similar trend was observed with shale samples immersed in NaCl solutions of various concentrations as well. The decrease in the amount of water being added to the shale as a result of the salt concentration increase can be explained by osmosis. The osmotic potential as a function of the water activity difference between the bulk fluid and the shale can be expressed as:

$$\Delta\pi = \frac{RT}{V}\ln\left(\frac{a_{ws}}{a_{wf}}\right) \tag{5.6}$$

where $\Delta\pi$ is the osmotic potential, R is the gas constant (8.314 J/mol·K), T is the absolute temperature (293 K at room temperature), V is the partial molar volume of water (18 cm^3), a_{ws} and a_{wf} are the water activity of the shale and the bulk fluid respectively. In

the case with the BEF-1 shale, the water activity of the shale (0.46) was always smaller than that of the bulk fluid. Therefore, when the water activity of the bulk fluid decreased with increasing salt concentration, the osmotic potential between the shale sample and the bulk fluid also decreased. As a result, less water was drawn from the bulk salt solutions into the shale samples. Nonetheless, the fact that the water activity of these salt solutions was always greater than that of the shale sample (0.46) also causes water to move from the bulk fluid into the shale samples regardless of the salt concentration in the bulk fluid, as indicated by a positive water movement in Figure 5.1. This suggests that the in-situ fluid desaturation in the unpreserved BEF-1 shale core sample significantly impacted the water movement into the shale. Figure 5.2 shows the water and ion movement into and out of BEF-1 shale using NaCl, KCl and $CaCl_2$ brines, plotted against water activity difference between brine and shale. A positive activity difference means the water activity of the brine is greater than that of the shale. It can be seen from Figure 5.2 that the water activity of the brines was always greater than that of the shale, causing water movement from the bulk fluid into the shale.

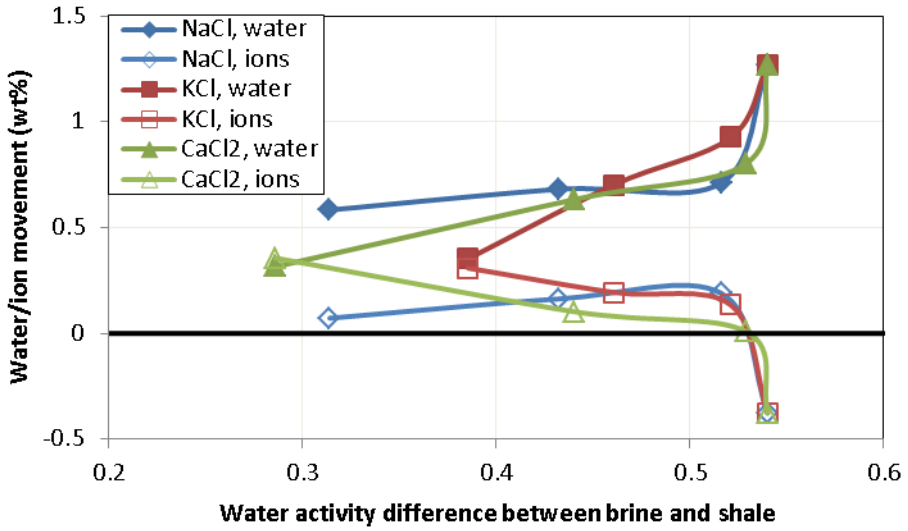

Figure 5.2: Water and ion movement into and out of BEF-1 shale using NaCl, KCl and $CaCl_2$ brines, plotted against water activity difference between brine and shale.

On the other hand, the ion movement increased from about -0.4 wt% (ions were removed from the shale to the bulk fluid) to about 0.1 wt% of the native shale when the salt concentration was increased from zero to 25 wt% for both KCl and $CaCl_2$. The ion movement is controlled by diffusion, which explains the increase in the amount of ions being added to the shale samples with higher salt concentration in the bulk fluid. The removal of ions from the shale at low salt concentration in the bulk fluid indicates the shale pore fluid has a low salinity. The concentration of Na^+, K^+, and Ca^{2+} ions in the shale pore fluid is probably less than 5 wt%, as the net ion movement changed from negative to positive values at such ion concentrations.

It can be seen from Figure 5.1 that more water was added to the shale samples when they were immersed in KCl solutions than in $CaCl_2$ solutions with the same concentrations. This can be due to the KCl solutions having a higher water activity than the $CaCl_2$ solutions at the same concentration level, as shown in Figure 5.4. As a result,

the greater water activity gradient with KCl solutions than with $CaCl_2$ solutions caused more water influx into the shale samples. Similar observation was reported by Zhang (2005) using the Pierre I shale, as shown in Figure 5.3. On the other hand, the BEF-1 shale also gained more ions when immersed in KCl solutions than in $CaCl_2$ solutions. This might be due to the fact that the ionic concentration of K^+ is smaller than that of Ca^{2+} in the pore fluid. Consequently, the concentration gradient of K^+ is greater than that of Ca^{2+} between the bulk and pore fluid, resulting in greater amount of K^+ ions being added to the shale than Ca^{2+}.

5.2.2.2 Comparison between BEF-1 and Pierre I

Zhang (2005) also performed gravimetric tests using the outcrop Pierre I shale at room temperature. Tables 5.1 and 5.2 show the bulk mineralogy and the clay mineralogy of the Pierre I shale. The resulting water and ion movement into and out of the shale using NaCl, KCl and $CaCl_2$ brines is shown in Figure 5.3. It can be seen from Figures 5.1 and 5.3 that when no salt is present in the bulk fluid (concentration = 0), there was more water movement into the BEF-1 shale than into the Pierre I shale. This is because the native water activity of the BEF-1 shale is 0.46, which is significantly lower than that of the Pierre I shale (A_w = 0.98). The greater water activity gradient between the bulk fluid and BEF-1 shale than that between the fluid and the Pierre I shale caused more water to be added to the BEF-1 shale due to the osmosis effect. When the salt concentration was increased to 25 wt%, water was still being added to the BEF-1 shale samples while water removal from the Pierre I shale took place. This again was due to the native water activity of the BEF-1 shale being much smaller than that of the Pierre I shale. Figure 5.4 shows the water activity of NaCl, KCl and $CaCl_2$ brines at different concentrations. It can be seen that at a concentration of 25 wt%, the water activity of these salt solutions range

from ~0.75 to ~0.85. Such water activity values are greater than that of the BEF-1 shale and smaller than that of the Pierre shale. Therefore, water was added to the BEF-1 shale and removed from the Pierre I shale after the samples were immersed in 25 wt% salt solutions. Figure 5.5 shows the water and ion movement into and out of the Pierre I shale using NaCl, KCl and $CaCl_2$ brines, plotted against the water activity difference between brine and shale (Zhang, 2005). Compared with the BEF-1 shale, the water activity difference between brine and shale was mostly negative, indicating that the water activity of the shale was greater than that of the brines. This is because the Pierre I shale had a high native water activity of 0.98. As a result, water moved out of the shale into the brines because of the osmotic potential.

Mineral	wt%
Quartz	19
Feldspar	4
Calcite	3
Dolomite	7
Pyrite	2
Siderite	1
Total Clay	64

Table 5.1: Whole rock mineralogy of the Pierre I shale (Zhang, 2005).

Clay Mineral	wt%
Chlorite	2.6
Kaolinite	7
Illite	12.2
Smectite	10.9
Mixed Layer Clay	31.3

Table 5.2: Clay mineralogy of the Pierre I shale (Zhang, 2005).

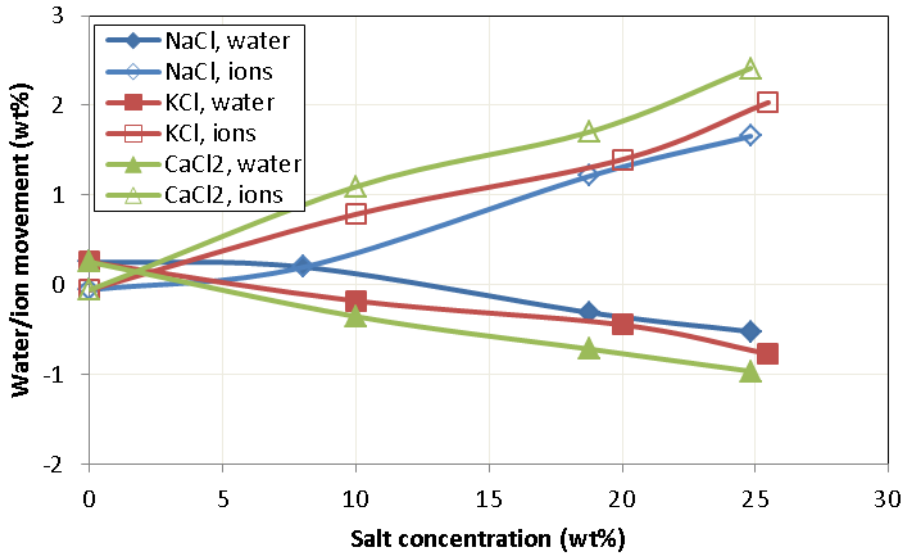

Figure 5.3: Water and ion movement into and out of Pierre I shale using NaCl, KCl and $CaCl_2$ brines, plotted against salt concentration (Zhang, 2005).

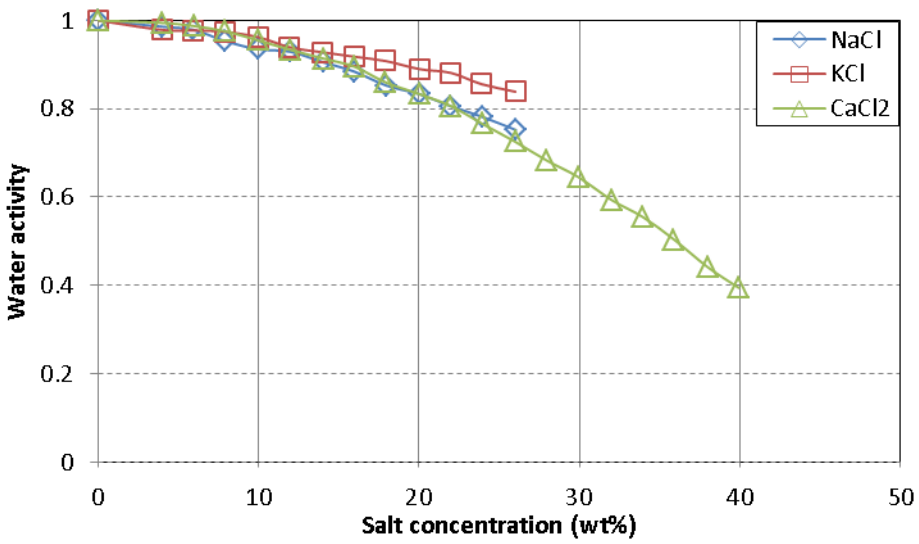

Figure 5.4: Water activity of NaCl, KCl and $CaCl_2$ brines at different concentrations (adapted from Zhang, 2005).

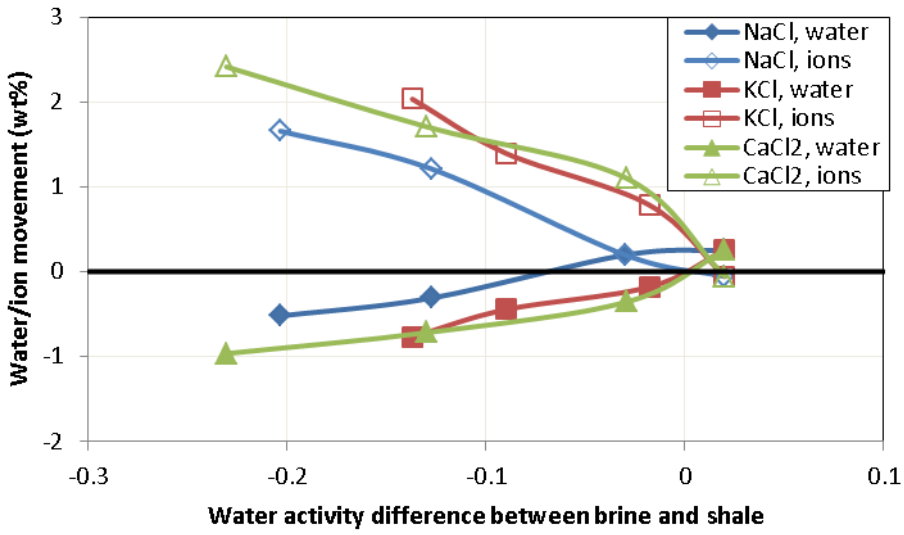

Figure 5.5: Water and ion movement into and out of Pierre I shale using NaCl, KCl and $CaCl_2$ brines, plotted against the water activity difference between brine and shale (Zhang, 2005).

On the other hand, when the ionic concentration in the bulk fluid is zero, more ions were withdrawn from the BEF-1 shale than from the Pierre I shale. This can be a result of the difference in the salinity of the pore fluid. The salinity of the pore fluid in the Pierre I shale was probably lower than that in the BEF-1 shale, resulting in a smaller salt concentration gradient between the bulk fluid and the shale pore fluid. When the salt concentration was increased to 25 wt%, the ion movement into the shale was increased to about 0.3 wt% for the BEF-1 shale and to about 2 wt% for the Pierre I shale. The pore fluid salinity certainly plays a role in the observed difference of the addition of ions. However, the difference in the ion movement into the shale as a function of the ionic concentration gradient is much greater for the Pierre I shale than for the BEF-1 shale. The amount of ions moving into the shale sample per unit change in the salt concentration was 0.027 wt%/wt% and 0.082 wt%/wt% for BEF-1 and Pierre I respectively. This can be due to the difference in the membrane efficiency of these two types of shale. The

membrane efficiency of the BEF-1 shale was probably smaller than that of the Pierre I shale, causing more ion movement across the more "leaky" shale surface.

Figures 5.6 and 5.7 show the net weight changes of the BEF-1 shale and the Pierre I shale after being exposed to NaCl, KCl and $CaCl_2$ solutions at room temperature. Both figures show that a net weight gain was observed for both shales after exposure to these salt solutions at different concentrations. This suggests that the water outflow from the Pierre I shale to the bulk fluid was not as much as the amount of ions being added to the shale matrix. The water/ion movement into and out of the Pierre I shale was dominated by the ion movement. On the other hand, for the BEF-1 shale, water was always being added to the shale matrix because the water activity of the fluid was always greater than that of the shale (A_w = 0.46) at salt concentrations smaller than 25 wt%. However, in general, the net weight change decreased with an increase in salt concentration for the BEF-1 shale. The increase in the inflow of ions was offset by the greater reduction in the inflow of water when the salt concentration was increased. In contrast, the net weight gain increased with higher salt concentration for the Pierre I shale. The increase in the inflow of ions in the Pierre I shale was greater than the reduction in water outflow from the shale matrix. A possible reason for this phenomenon is the decrease in the membrane efficiency as a result of a higher salt concentration. Zhang et al. (2008) reported a decrease in the shale membrane efficiency with greater salt concentration in the bulk solution. A reduction in the shale membrane efficiency can result in less restriction to the transport of ions across the shale surface, thus increasing the inflow of ions into shale matrix.

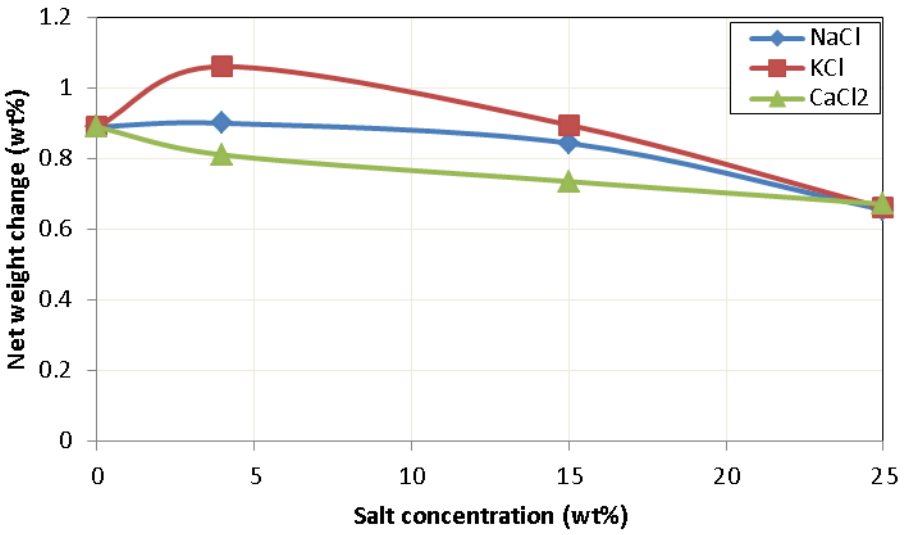

Figure 5.6: Net weight change of the BEF-1 shale after being exposed to NaCl, KCl and $CaCl_2$ solution at room temperature.

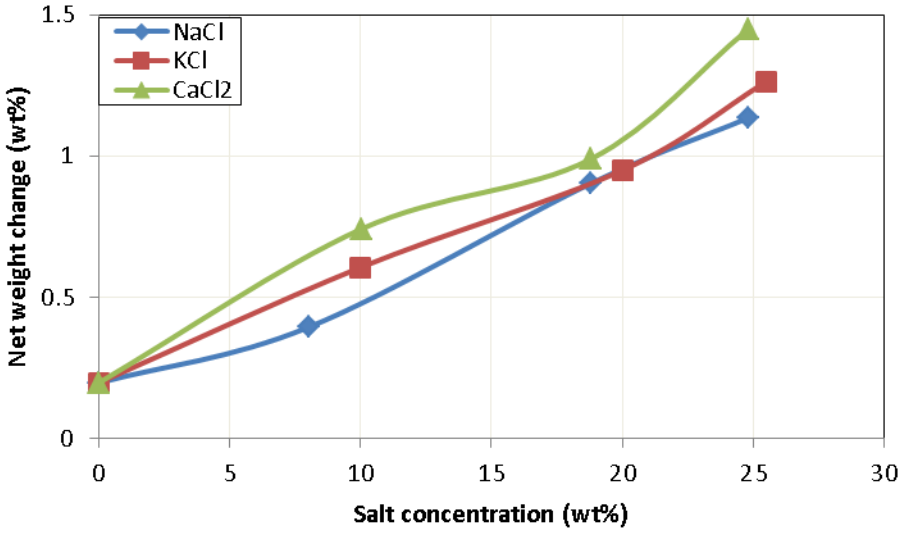

Figure 5.7: Net weight change of the Pierre I shale after being exposed to NaCl, KCl and $CaCl_2$ solution at room temperature (adapted from Zhang, 2005).

It is worth noting that capillary correction was performed on the Pierre I shale using the simulated pore fluid (Zhang, 2005). The capillary effect is typically observed

during the early stage of the shale-fluid interactions. It can affect the water movement into the shale and should not interfere with the ionic diffusion across the shale surface.

5.3 SWELLING BEHAVIOR

Following the procedure described in Section 3.3.1, the extent of shale swelling was simultaneously measured perpendicular and parallel to bedding planes at room temperature. One inch cubic shale samples were used and the duration of the swelling tests was usually 24 hours. The corresponding changes in the shale hardness and acoustic wave velocity as a result of fluid exposure were also determined and will be shown in Section 5.6.

5.3.1. TGS-F Shale

Figure 5.8 shows the swelling behavior of the TGS-F shale with fresh water, 4% NaCl, and 2% KCl solutions at room temperature. The salt concentration is expressed as percentage by weight. The maximum swelling perpendicular to bedding planes after 24 hours of fluid exposure occurred with fresh water, which was 0.17%. This suggests that the TGS-F shale was only slightly sensitive to the exposure to water-based fluids. The use of low concentrations of NaCl and KCl salts were able to significantly reduce the swelling potential of the TGS-F shale. The swelling perpendicular to bedding planes was 0.082% and 0.063% respectively when the TGS-F shale was exposed to 4% NaCl and 2% KCl solutions for about 24 hours. This is equivalent to a 52% and 63% reduction in the swelling potential compared with the exposure of the TGS-F shale to fresh water. KCl salt appears to be more effective in reducing shale swelling perpendicular to bedding planes, as 2% KCl resulted in less swelling of the TGS-F shale perpendicular to bedding planes than the more concentrated 4% NaCl salt. This can be due to the difference in the radius of the hydrated K^+ and Na^+ cations. The hydrated radius of Na^+ is 7.9 Å whereas

that of K^+ is 5.32 Å (Pruett, 1987). Even though the more concentrated NaCl solution can neutralize more negative charges on the clay surface and better stabilize the shale than the less concentrated KCl solution, the smaller number of water molecules associated with the hydrated K^+ ions resulted in less water being present between clay platelets, thus reducing the degree of shale swelling. The ability of the salts to reduce swelling indicates that they have the potential to be used in the formulation of drilling fluids to enhance wellbore stability.

Anisotropic swelling was also observed with the TGS-F shale. While the samples swelled after contact with the three fluids perpendicular to bedding, they shrank parallel to bedding planes after 24 hours of fluid contact. The degree of shrinking was not as significant as that of swelling experienced by the same shale sample. The shrinkage was less than 0.05% parallel to bedding planes, while all three samples swelled more than 0.05% perpendicular to bedding planes. This observation is similar to the Poisson effect, where rock is shortened in one direction and stretched in another direction when a uniaxial load is applied. Since the swelling perpendicular to bedding planes was much greater than the magnitude of the shrinkage parallel to bedding planes, the overall volumetric swelling of the TGS-F shale should be positive with these three types of water-based fluids. Wong (1998) and Wakim et al. (2009) also reported anisotropic swelling behavior of the La Biche shale in Canada Tournemire shale in Southern France, with the swelling perpendicular to bedding planes about three to four times that parallel to bedding planes on average. However, their swelling tests were run with cylindrical core samples. Wong (1998) was able to measure axial and radial swelling simultaneously while Wakim et al. (2009) only obtained unidirectional swelling in the axial direction of the core sample with. Shale swelling anisotropy is believed to be a result of the shale clay

fabric anisotropy. The orientation of the individual clay platelets might cause the TGS-F shale to swelling/shrink differently in various directions.

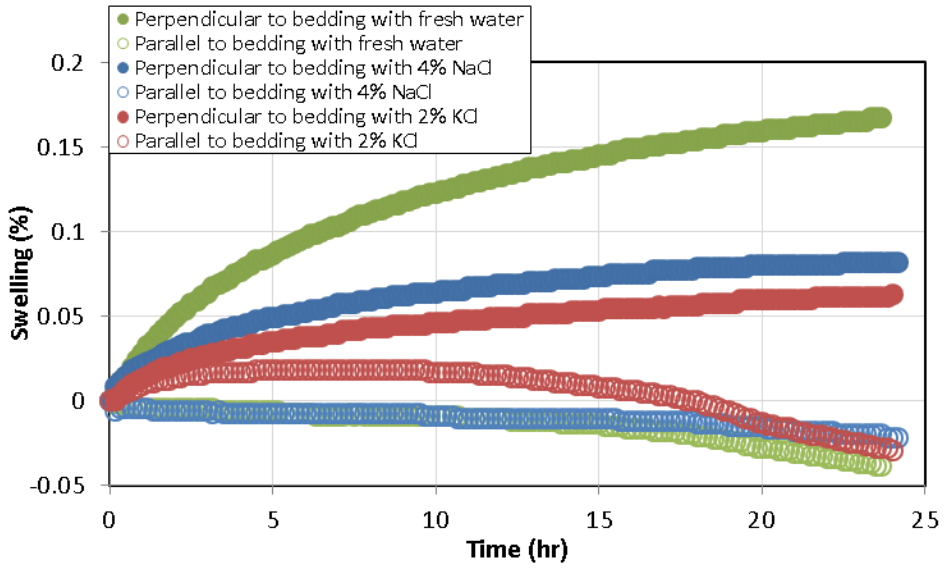

Figure 5.8: Swelling behavior of the TGS-F shale with fresh water, 4% NaCl, and 2% KCl solutions at room temperature.

Figure 5.9 shows the weight change of the TGS-F shale after being exposed to fresh water, 4% NaCl, and 2% KCl solutions for 24 hours at room temperature. It can be seen that the weight change of the TGS-F shale is consistent with the swelling behavior perpendicular to bedding planes. Fresh water resulted in the most swelling, while 2% KCl solution caused the least swelling to the TGS-F shale perpendicular to bedding planes. Figure 5.10 shows a plot of the weight change vs. the corresponding swelling perpendicular and parallel to bedding planes of the TGS-F shale after 24 hours' exposure fresh water, 4% NaCl, and 2% KCl for solutions at room temperature. Again, a positive correlation exists between the weight change and swelling perpendicular to bedding planes for the TGS-F shale.

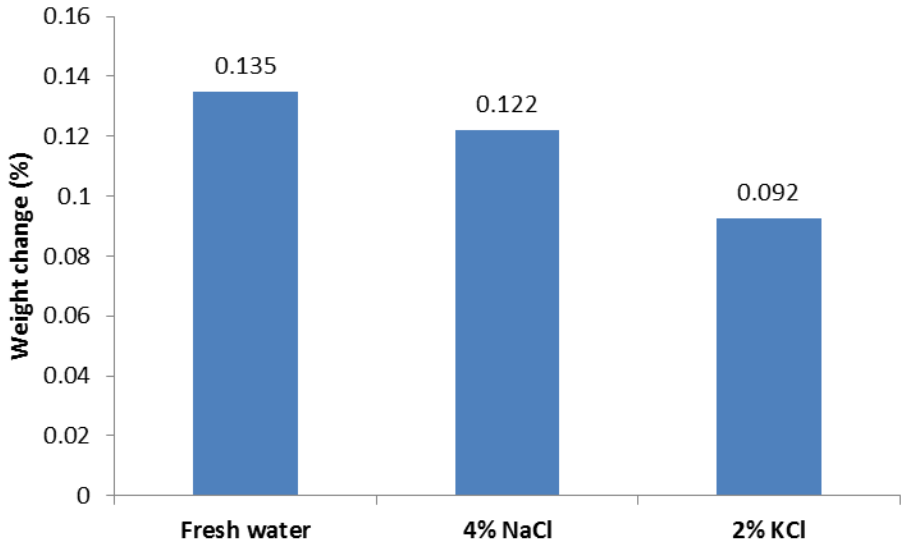

Figure 5.9: Weight change of the TGS-F shale after being exposed to fresh water, 4% NaCl, and 2% KCl solutions for 24 hours at room temperature.

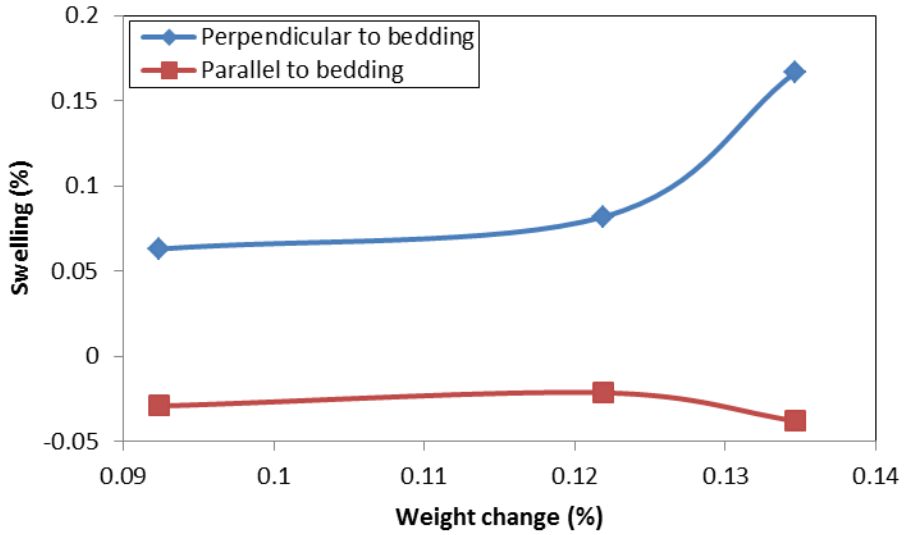

Figure 5.10: Plot of the weight change of the TGS-F shale vs. the corresponding swelling perpendicular and parallel to bedding planes after 24 hours' exposure fresh water, 4% NaCl, and 2% KCl for solutions at room temperature.

5.3.2. WBS Shale

Figure 5.11 shows the swelling behavior of the WBS shale with fresh water and 4% seawater at room temperature. The major constituents of sea salt are Na^+ and Cl^-. It

can be seen from Figure 5.11 that fresh water and 4% seawater resulted in similar degree of swelling perpendicular to bedding planes after about 24 hours. The maximum swelling of about 0.045% perpendicular to bedding planes for the WBS shale is smaller than that for the TGS-F shale, which was about 0.17%. Shale mineralogy cannot be used to explain the difference in the swelling behavior between the TGS-F and the WBS shale. Even though the mineralogy of the TGS-F is not available, it is from the same well as TGS-D and their depths are very similar. Therefore, a reasonable assumption is that TGS-F also contains about 20% clay. In contrast, the clay content of the WBS shale is about 35%. Therefore, if the clay content is the dominant factor for the dissimilar swelling behavior of the two shales, WBS should have experienced more swelling. On the other hand, both shales have a high native water activity, which should have similar impact on the water movement into the shale and the subsequent swelling. Hence, the shale membrane efficiency/permeability might be the reason for the observed difference in the swelling behavior perpendicular to bedding planes with the TGS-F shale and the WBS shale.

Similar to the swelling behavior of TGS-F, the 4% seawater resulted in less swelling perpendicular to bedding planes than fresh water. This contrast in the degree of swelling is more pronounced at early time during the shale's exposure to water-based fluids. After approximately 15 hours, the swelling perpendicular to bedding planes was similar with both fluids.

Again, anisotropic swelling was observed with the WBS shale after exposure to fresh water and 4% seawater. The shrinkage parallel to bedding was greater when the sample was exposed to fresh water than to 4% seawater. Therefore, the overall volumetric swelling is expected to be greater for the sample exposed to fresh water than that exposed to 4% seawater. This is consistent with the weight change after about 24 hours' exposure to the fluids, as shown in Figure 5.12. The WBS sample exposed to fresh

water gained much more weight than that exposed to 4% seawater. Compared with the TGS-F shale, the WBS shale gained less weight after being exposed to the two water-based fluids for about 24 hours. Again, this is consistent with the greater degree of swelling perpendicular to bedding planes experienced by the TGS-F shale. Overall, the TGS-F shale appears to be more sensitive to fluid exposure than the WBS shale.

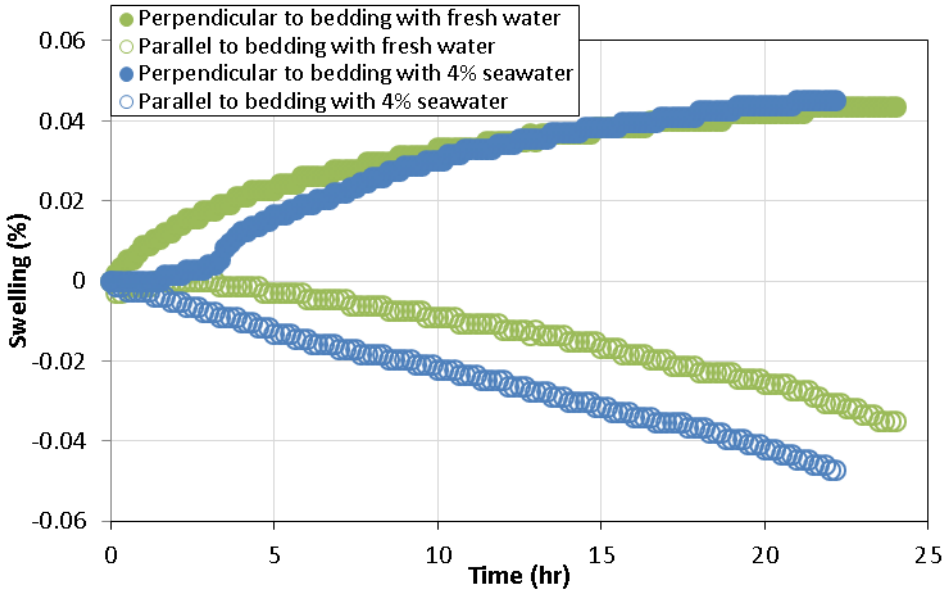

Figure 5.11: Swelling behavior of the WBS shale with fresh water and 4% seawater at room temperature.

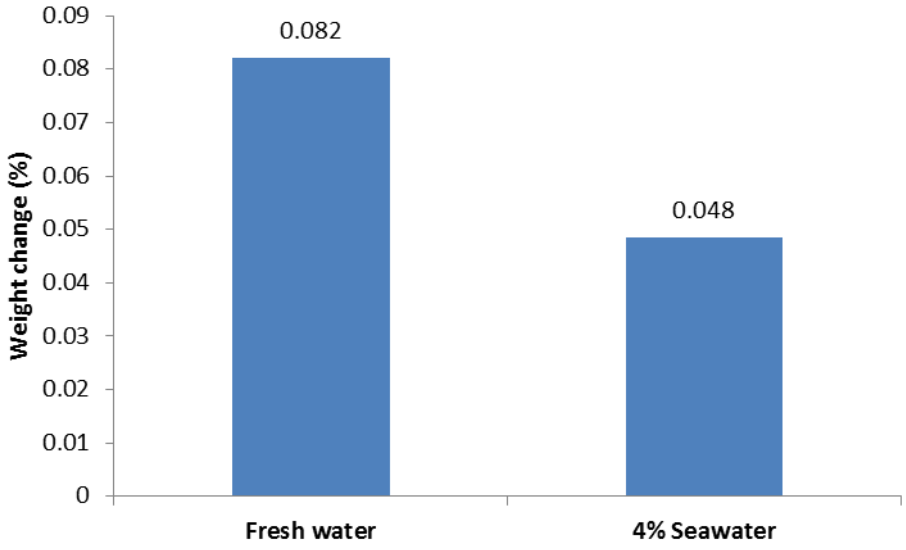

Figure 5.12: Weight change of the WBS shale after being exposed to fresh water and 4% seawater for about 24 hours at room temperature.

5.3.3. WGS-B Shale

Figure 5.13 shows the swelling behavior of the WGS-B shale with fresh water, 4% NaCl and 2% KCl at room temperature. Similar to the trend observed with the TGS-F shale, fresh water resulted in the most swelling perpendicular to bedding planes after about 24 hours for the WGS-B shale, which was 0.055%. This is also smaller than the maximum swelling occurred to TGS-F with fresh water, which was 0.17%. The shale membrane efficiency/permeability might again be reason for the difference in the maximum swelling with these two shales, because the higher clay content (25%) and lower native water activity (0.73) of WGS-B would instead suggest the shale's greater sensitivity to fluid exposure.

Like in the case with the TGS-F shale, 4% NaCl and 2% KCl were able to lower the swelling perpendicular to bedding planes to 0.037% and 0.028% respectively after 24 hours of fluid exposure. This is equivalent to a reduction of 32% and 49% respectively in

swelling perpendicular to bedding planes. The difference in the degree of swelling with these three fluids was more pronounced after about 10 hours of fluid contact.

Anisotropic swelling behavior was also observed with the WGS-B shale. The shrinkage parallel to bedding planes was the biggest with the WGS-B shale being exposed to fresh water after 24 hours of fluid exposure. The overall volumetric swelling of the WGS-B shale with the three fluids should also be positive, since the magnitude of swelling perpendicular to bedding planes was greater than that of shrinkage parallel to bedding planes. The samples exposed to 4% NaCl and 2% KCl swelled during the first 10 to 15 hours before started to shrink.

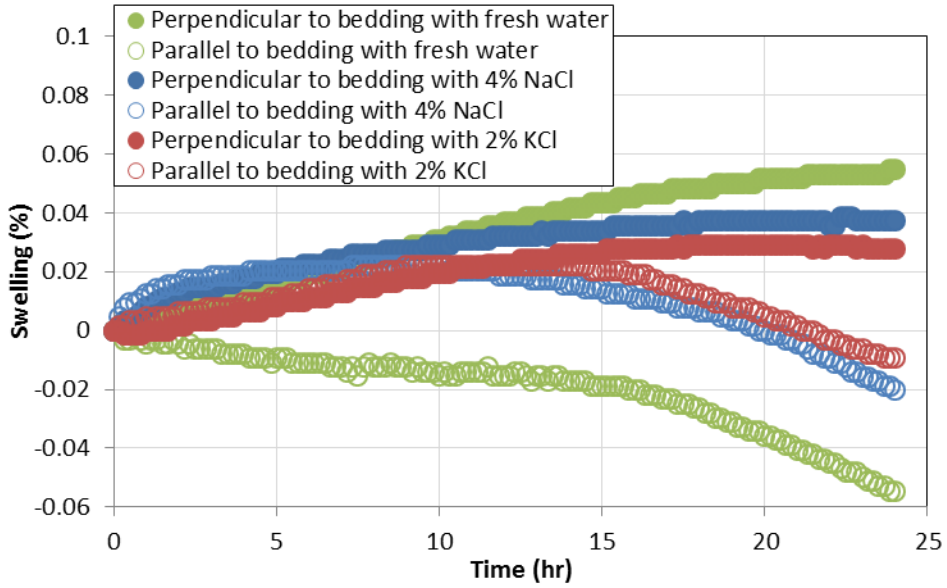

Figure 5.13: Swelling behavior of the WGS-B shale with fresh water, 4% NaCl and 2% KCl at room temperature.

The weight change of the WGS-B shale shown in Figure 5.14 after 24 hours' fluid exposure is again consistent with the swelling behavior of the shale perpendicular to bedding planes. Fresh water resulted in the most weight gain while 2% KCl added the

least weight to the WGS-B shale. Even though in general, the TGS-F shale swelled more perpendicular to bedding planes than the WGS-B shale, the weight gain was greater with the WGS-B shale after 24 hours' exposure to the three fluids. The actual swelling mechanism might have an impact on the difference in swelling and weight gain with these types of shales.

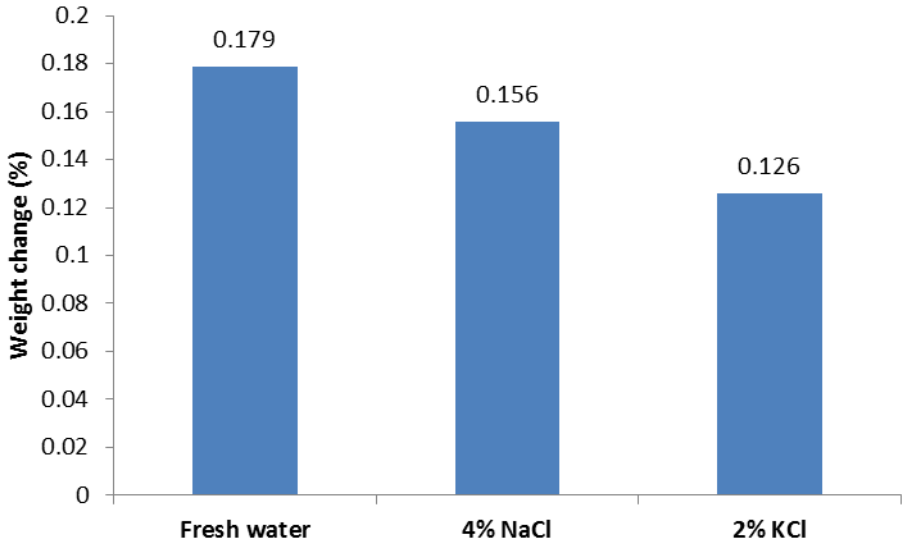

Figure 5.14: Weight change of the WGS-B shale after being exposed to fresh water, 4% NaCl and 2% KCl for 24 hours at room temperature.

5.3.4. Comparison with the Pierre I Shale

Zhang (2005) also performed the swelling test on the Pierre I shale with various water-based salt solutions. Figure 5.15 shows the swelling behavior of the Pierre I shale with DI water, NaCl, KCl and $CaCl_2$ solutions with Aw = ~0.95 at room temperature (Zhang, 2005). The direction of the measured swelling was not explicitly mentioned in the original dissertation. Nonetheless, the maximum swelling of the Pierre I shale was observed with DI water, which was 0.54% after 24 hours' fluid exposure. The maximum swelling of the Pierre I shale was 2.2 – 11 times greater than the maximum swelling of

the TGS-F, WGS-B and WBS perpendicular to bedding planes, all of which were caused by contact with fresh water. Such a large difference in the swelling behavior might be caused by the mineralogy of these shales. Table 4.1 shows that among the three shale samples in this study, WBS contains the most clay (35%), of which smectite contributes to about 2.8% of the bulk weight and is in the form of illite/smectite mixtures. In contrast, the total clay content and the smectite content of the Pierre I shale are 64% and 10.9% respectively, as shown in Tables 5.1 and 5.2. This large difference in the total clay content and the specific smectite content might explain the greater swelling experienced by the Pierre I shale. Osmotic swelling can be the dominant swelling mechanism when Pierre I was in contact with DI water as it only applies to certain clay types such as smectite that contain exchangeable cations. On the other hand, the smectite content in TGS-F, WGS-B and WBS was much smaller and the smectite exists in the form of illite/smectite mixture. Osmotic swelling should not be the main swelling mechanism of the clay in these shales. The mineralogy of TGS-F, WGS-B and WBS indicates that diagenesis has transformed a lot of the smectite into illite, resulting in these shales much less reactive to water-based fluids.

Similar to what was observed with TGS-F, WGS-B and WBS, low concentrations of NaCl, KCl and $CaCl_2$ solutions were able to reduce the degree of swelling significantly with Pierre I. In Figure 5.15, it can be seen that the swelling was reduced from 0.54% when in contact with DI water to 0.43%, 0.28%, and 0.11% respectively when the Pierre I samples were immersed in NaCl, KCl and $CaCl_2$ with a water activity of about 0.95. The swelling reduction can be a result of the suppressed osmotic swelling when the salt concentration in the bulk solution was increased, decreasing the inflow of water to the shale matrix from the bulk solution.

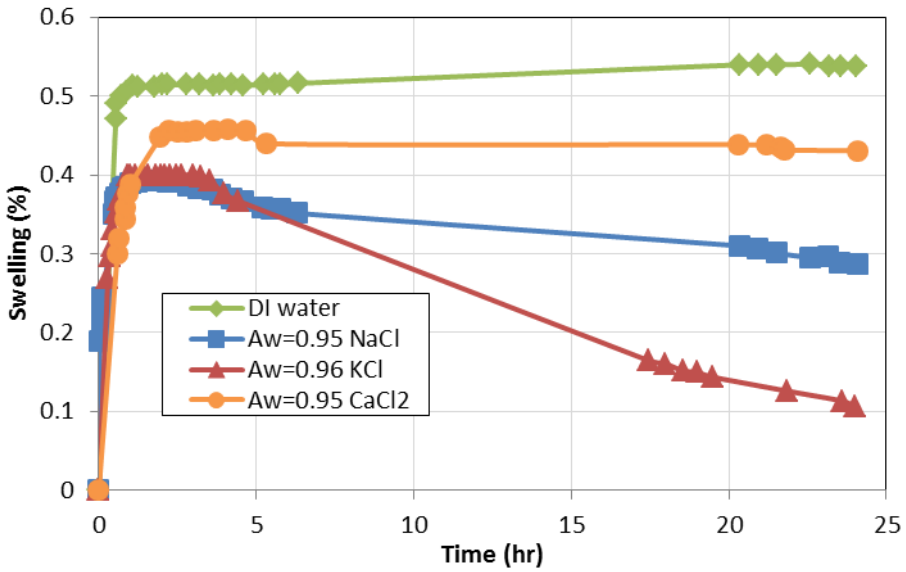

Figure 5.15: Swelling behavior of the Pierre I shale with DI water, NaCl, KCl and $CaCl_2$ solutions with Aw = ~0.95 at room temperature (adapted from Zhang, 2005).

Figure 5.16 shows the cross-plot of the swelling perpendicular to bedding planes after 24 hours of contact with fresh water and the clay content of the TGS-F, WBS, WGS-B and the Pierre I shales. In general, the degree of swelling increased with the clay content. This is expected because clay is the most water-sensitive mineral in shales. A shale with a higher clay content tends to adsorb more water. The Pierre I shale with a clay content of 68% is shown on the top right corner of Figure 5.16. Not only did the Pierre I shale contain more clay than other shale samples, but its smectite content was also 10.9%, much greater than the smectite content of other shales. Smectite clays are the most expandable clay minerals and usually cause more swelling than other clay minerals. In comparison, TGS-F, WBS and WGS-B shales all contained a smaller amount of smectite in the form of mixed illite/smectite. Therefore, these shales experienced much less swelling after exposure to fresh water. On the other hand, among the TGS-F, WBS and WGS-B shales, the degree of swelling did not increase with the clay content. This is

probably because of the difference in shale permeability and the existence of micro-fractures in these shales, which also influence the swelling behavior.

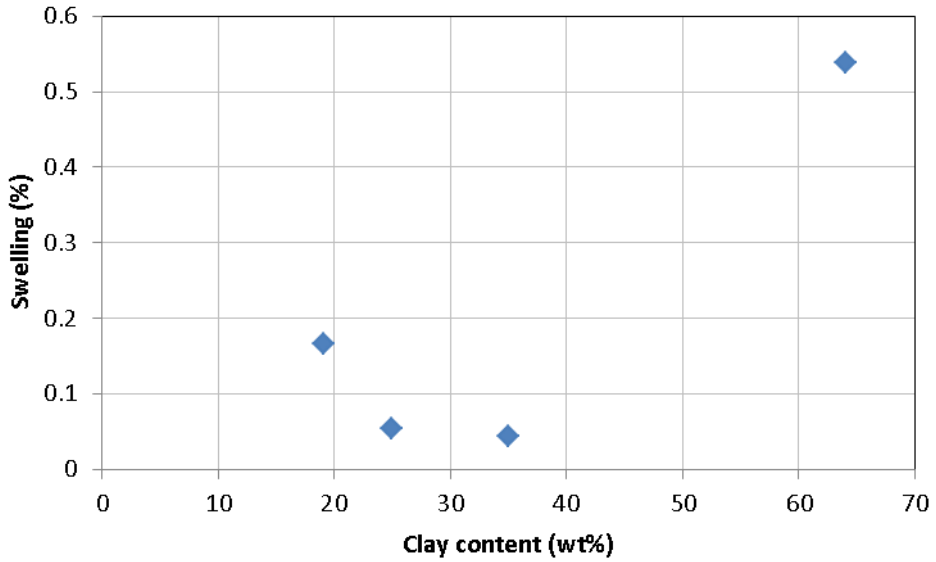

Figure 5.16: Cross-plot of the swelling perpendicular to bedding planes after 24 hours of contact with fresh water and the clay content of the TGS-F, WBS, WGS-B and the Pierre I shales.

Figure 5.17 shows the cross-plot of the net weight change after 24 hours of contact with fresh water and the clay content of the TGS-F, WBS, WGS-B and the Pierre I shales. Similar to the swelling behavior, the net weight change also increased with the clay content generally. The weight change was mostly due to water adsorption on the shale samples. The data points in Figure 5.17 appear to be scattered. This is probably due to the lack of sufficient data to establish a strong correlation.

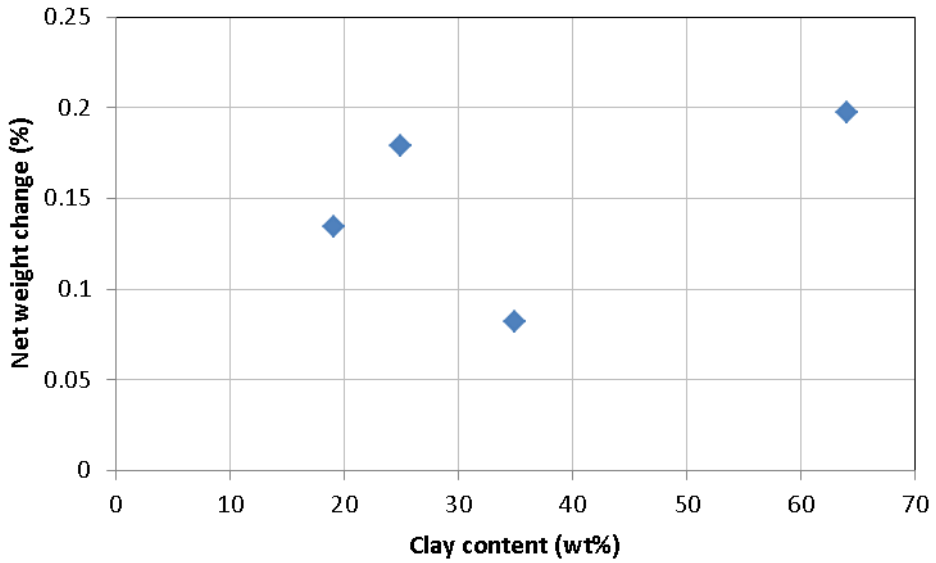

Figure 5.17: Cross-plot of the net weight change after 24 hours of contact with fresh water and the clay content of the TGS-F, WBS, WGS-B and the Pierre I shales.

Figure 5.18 shows the cross-plot of the net weight change and the swelling perpendicular to bedding planes after 24 hours of contact with fresh water for the TGS-F, WBS, WGS-B and the Pierre I shales. A positive correlation exists between the net weight change and the swelling behavior of these shales. This is because water adsorption in the interlayer space of clay minerals is usually accompanied by an expansion in the c-spacing between adjacent unit layers of clay. The Pierre I shale with the highest clay and smectite content swelled the most after contact with fresh water and also adsorbed the largest amount of water.

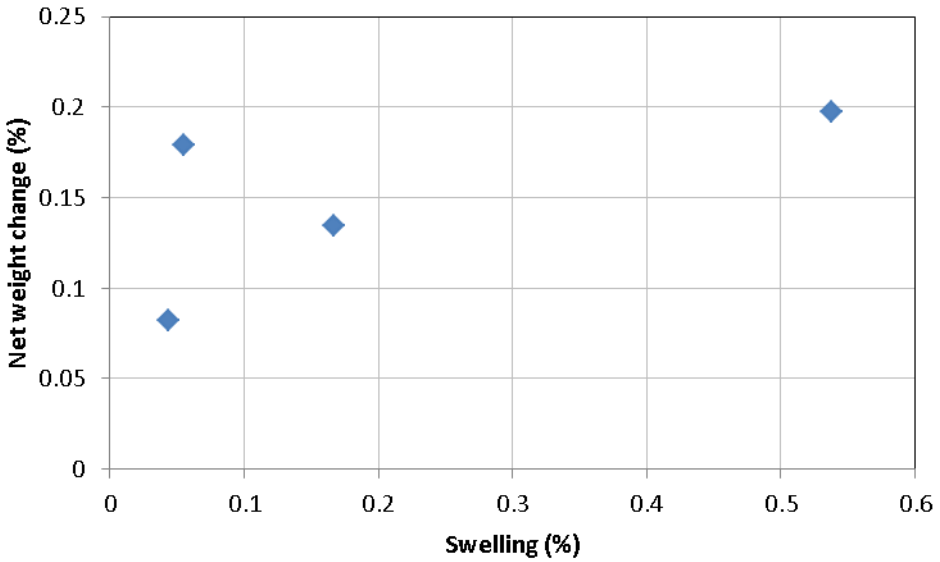

Figure 5.18: Cross-plot of the net weight change and the swelling perpendicular to bedding planes after 24 hours of contact with fresh water for the TGS-F, WBS, WGS-B and the Pierre I shales.

5.4 MECHANICAL PROPERTIES

Following the procedures described in Section 3.3.2 and 3.3.3, the change in shale mechanical properties were also measured before and after the samples were immersed in water-based fluids, along with the swelling behavior. The Brinell hardness measurement was performed with a Rex durometer and the acoustic wave velocities were determined with a pulse-transmission setup. The shale samples studied in this section were exposed to fluids at room temperature.

5.4.1 TGS-F Shale

Figure 5.19 shows the change in Brinell hardness after the TGS-F shale was exposed to fresh water, 4% NaCl and 2% KCl. HBS 10/3000 means in the vertical axis that the hardness is measured with a 10 mm diameter steel ball using a 3000 kg force. It was converted from the raw reading from the durometer. In general, there was a small decrease in hardness after the samples were immersed in these fluids. The small increase

in Brinell hardness parallel to bedding after TGS-F was immersed in fresh water was due to experimental variability. Similar to the swelling behavior and the weight change, we can conclude from the change in Brinell hardness that TGS-F was only slightly water sensitive. Furthermore, the use of low concentration salts solutions did not appear to be effective in reducing the shale softening.

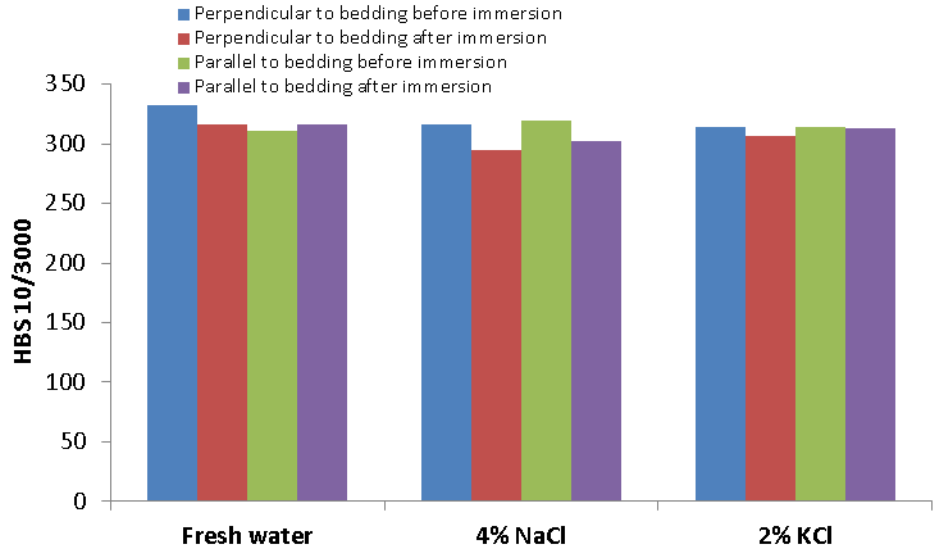

Figure 5.19: Brinell hardness of the TGS-F shale before and after being immersed in fresh water, 4% NaCl and 2% KCl for 24 hours.

Figure 5.20 shows the change in P-wave and S-wave velocities after the TGS-F samples were immersed in fresh water, 4% NaCl and 2% KCl for 24 hours. The S-wave velocity parallel to bedding planes refers to the commonly known SV-wave velocity, where the direction of particle motion is perpendicular to bedding planes (Schuster, 2007). In general, the wave velocities decreased after shale was in contact with these fluids. The decrease in the S-wave velocities parallel to bedding planes after fluid contact is consistent with Vernik and Liu (1998)'s findings on the Bakken shale from North Dakota and the Bazhenov shale from western Siberia. Again, the change in wave

velocities indicates that the TGS-F was only slightly water sensitive. The higher wave velocity parallel to bedding planes than that perpendicular to bedding planes is probably due to the preferential layering of minerals that results in less dispersion parallel to the bedding planes.

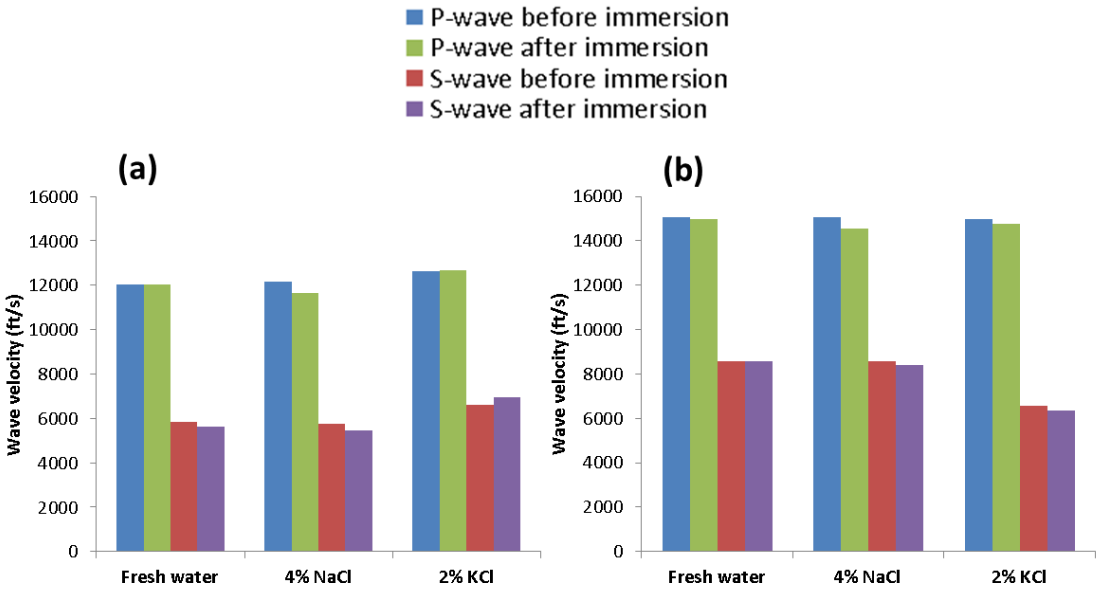

Figure 5.20: P-wave and S-wave velocities of the TGS-F shale before and after being immersed in fresh water, 4% NaCl and 2% KCl for 24 hours (a) perpendicular and (b) parallel to bedding planes.

The dynamic Young's modulus and Poisson's ratio were calculated based on the P-wave and S-wave velocities using Eq. (2.9) and Eq. (2.10). The density of the shale rock was determined from its dimension and weight change before and after immersion in fluids. The density of the TGS-F shale was approximately 2400 kg/m^3. Figure 5.21 shows the change in the dynamic Young's modulus and Poisson's ratio before and after the TGS-F shale was immersed in fresh water, 4% NaCl, and 2% KCl. The Young's modulus decreased and the Poisson's ratio increased slightly for the TGS-F shales immersed in fresh water and 4% NaCl. This indicates that the mechanical stability of the

shale was slightly reduced upon contact with these fluids. In comparison, the Young's modulus increased and the Poisson's ratio decreased after the sample was exposed to 2% KCl for 24 hours, which means the sample became more mechanically stable. Nevertheless, similar to the results from the swelling test and the Brinell hardness measurement, the elastic moduli suggest that TGS-F was only slightly sensitive to water-based fluids.

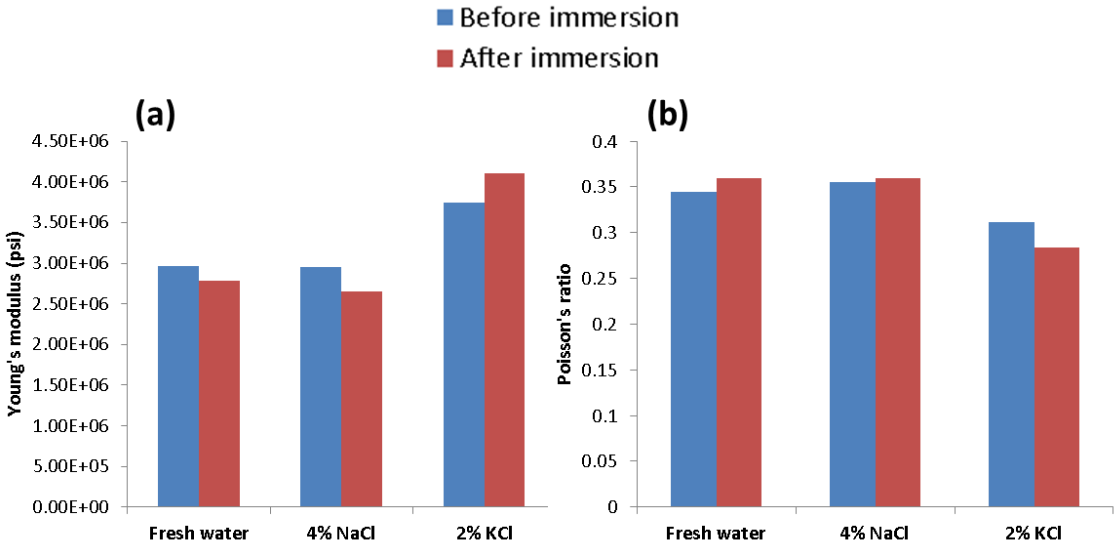

Figure 5.21: (a) Dynamic Young's modulus and (b) Poisson's ratio of the TGS-F shale before and after being immersed in fresh water, 4% NaCl and 2% KCl for 24 hours perpendicular to bedding planes.

5.4.2 WBS Shale

Figure 5.22 shows the change in Brinell hardness before and after the WBS shale was exposed to fresh water and 4% seawater for 24 hours. There was a small decrease in hardness after the shale's exposure to these fluids. Similar to the swelling behavior and the weight change after fluid exposure, the small change in Brinell hardness suggests that the WBS shale was only slightly sensitive to water-based fluids.

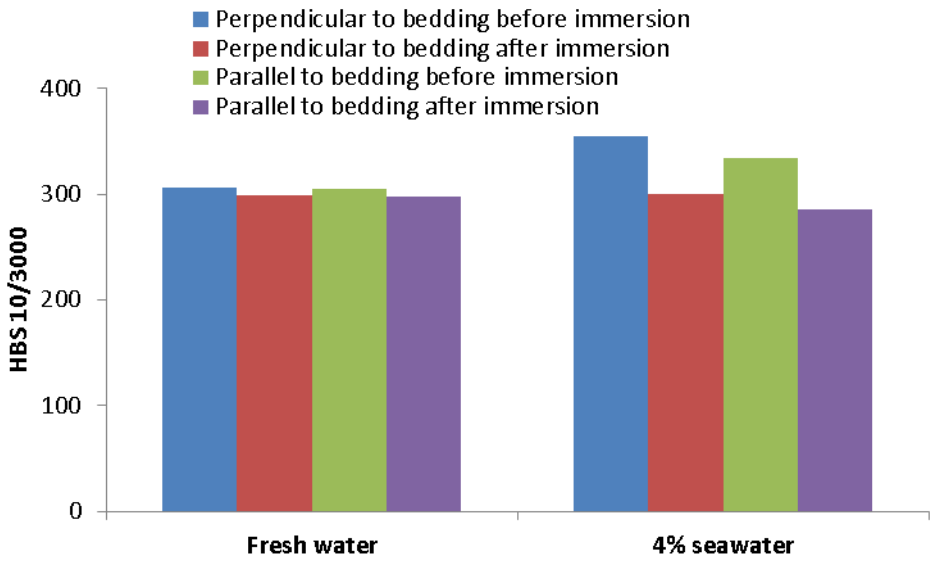

Figure 5.22: Brinell hardness of the WBS shale before and after being immersed in fresh water and 4% seawater for 24 hours.

Figure 5.23 shows the change in acoustic wave velocities after WBS was immersed in fresh water and 4% seawater for 24 hours. In general, the wave velocities of WBS underwent very little change after the shale samples were exposed to fresh water and 4% seawater. P-wave velocities perpendicular to bedding planes remained constant after the samples were immersed in the fluids for 24 hours. On the other hand, P-wave velocities parallel to bedding planes increased slightly after the samples' contact with these fluids. Again, the change in wave velocities indicates that WBS was only slightly water sensitive. Similar to TGS-F, the higher wave velocity of WBS parallel to bedding planes than that perpendicular to bedding planes is probably due to the preferential layering of minerals that results in less dispersion parallel to the bedding planes.

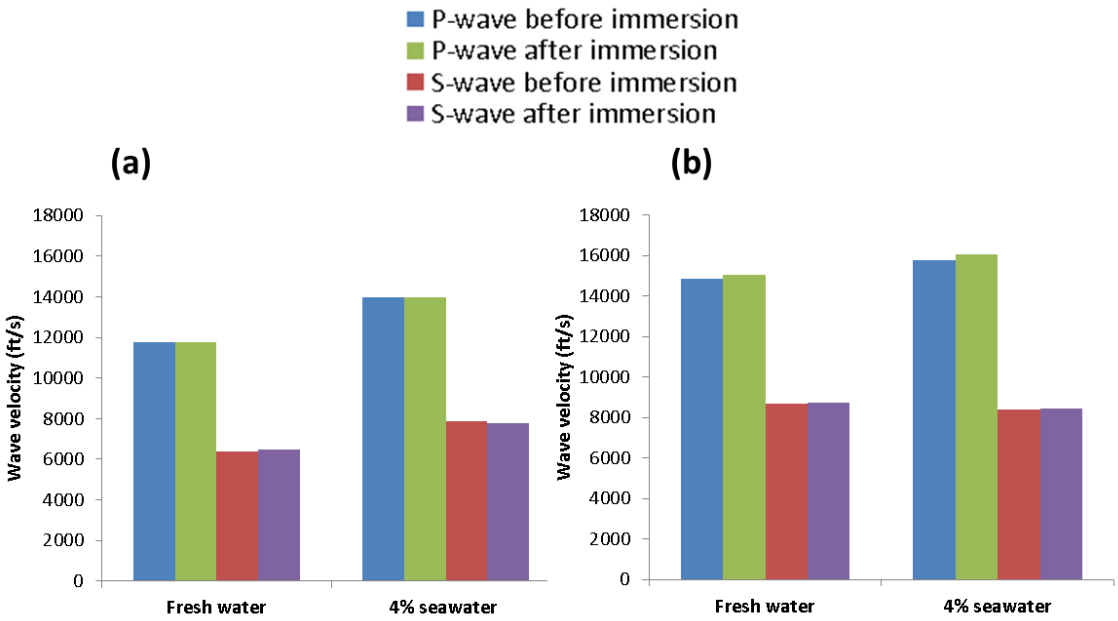

Figure 5.23: P-wave and S-wave velocities of the WBS shale before and after being immersed in fresh water and 4% seawater for 24 hours (a) perpendicular and (b) parallel to bedding planes.

Figure 5.24 shows the change in dynamic Young's modulus and Poisson's ratio of the WBS shale perpendicular to bedding planes after samples were exposed to fresh water and 4% seawater for 24 hours. The Young's modulus increased and decreased slightly with 24 hours' fresh water and 4% seawater exposure respectively. On the contrary, the Poisson's ratio decreased and increased to a small extent respectively after the samples' contact with fresh water and 4% seawater. Usually, the use of low concentration salts such as KCl and NaCl is able to reduce the damage of shale mechanical stability caused by shale-fluid interations. In the case of the WBS shale, the micro-cracks created during the core retrieval and cutting processes might result in the greater reduction in the mechanical stability of the samples. Nevertheless, similar to what the swelling behavior and the change in Brinell hardness with fluid exposure suggest, the

small change in elastic moduli of WBS upon fluid contact indicates that it was only slightly sensitive to water-based fluids.

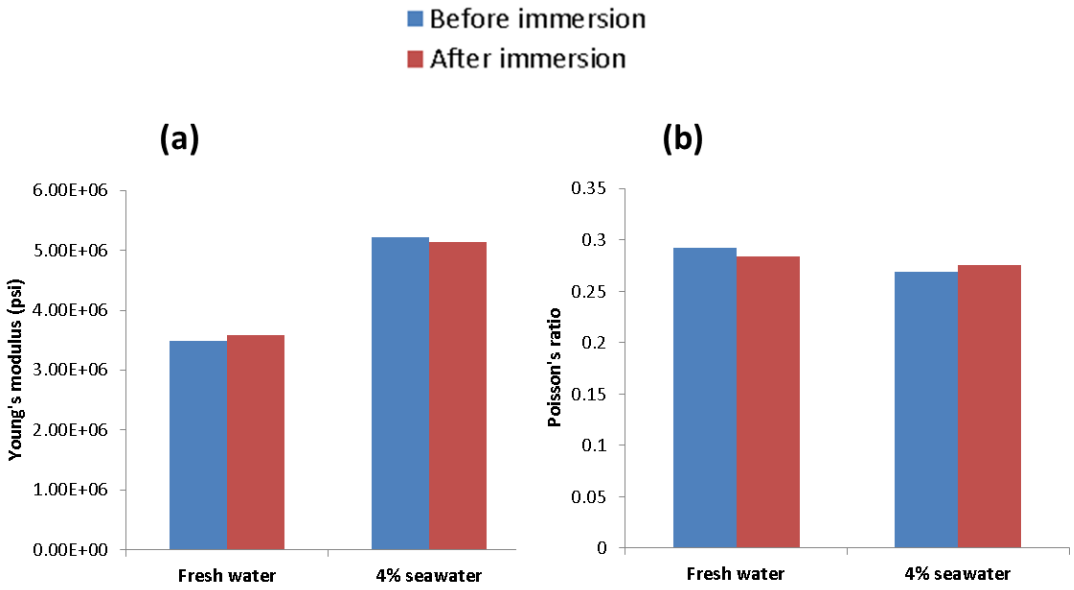

Figure 5.24: (a) Dynamic Young's modulus and (b) Poisson's ratio of the WBS shale before and after being immersed in fresh water and 4% seawater for 24 hours perpendicular to bedding planes.

5.4.3 WGS-B Shale

Figure 5.25 shows the change in Brinell hardness after WGS-B shale was exposed to fresh water, 4% NaCl and 2% KCl for 24 hours. In general, there was a small decrease in hardness after the samples were immersed in these fluids. Similar to the swelling behavior and the weight change observed after 24 hours of fluid exposure, the small change in the shale hardness suggests that TGS-B was only slightly water sensitive.

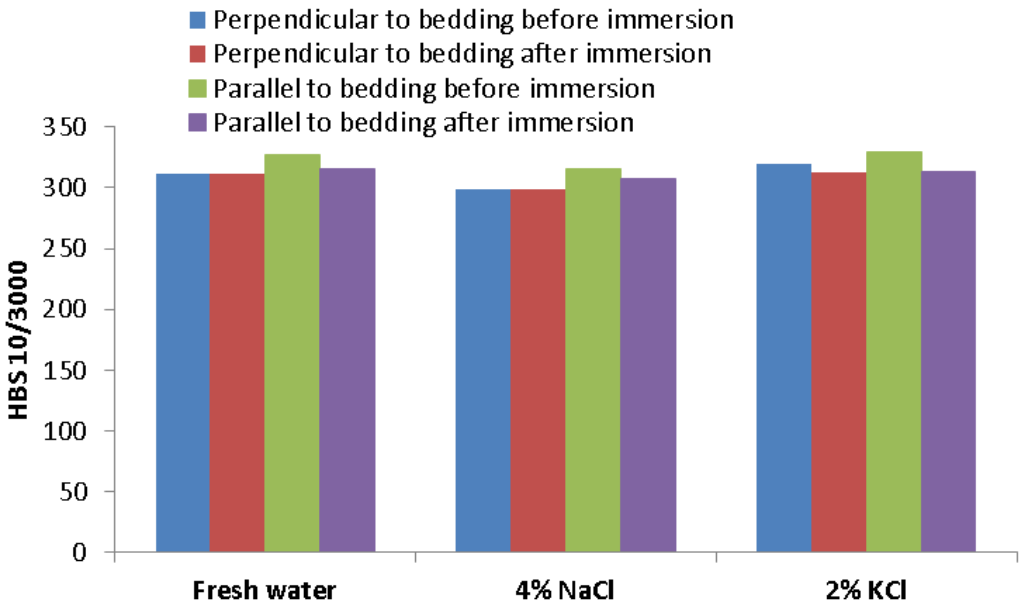

Figure 5.25: Brinell hardness of the WGS-B shale before and after being immersed in fresh water, 4% NaCl and 2% KCl for 24 hours.

Figure 5.26 shows the change in acoustic wave velocities after WGS-B was exposed to fresh water, 4% NaCl and 2% KCl for 24 hours. In general, the wave velocities of TGS-B experienced little reduction after fluid exposure. Again, the change in wave velocities indicates that TGS-B was only slightly sensitive to water-based fluids. Similar to TGS-F and WBS, the higher wave velocity of TGS-B parallel to bedding planes than that perpendicular to bedding planes is probably because of the preferential layering of minerals that results in less dispersion parallel to the bedding planes.

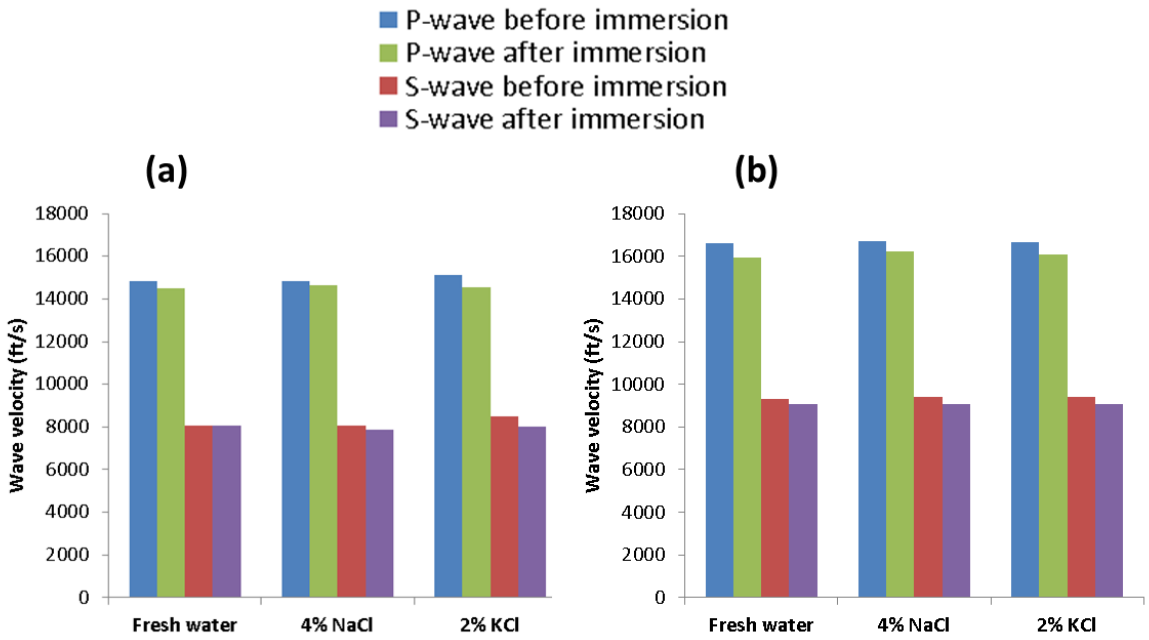

Figure 5.26: P-wave and S-wave velocities of the WGS-B shale before and after being immersed in fresh water, 4% NaCl and 2% KCl for 24 hours (a) perpendicular and (b) parallel to bedding planes.

Figure 5.27 shows the change in dynamic Young's modulus and Poisson's ratio of the WGS-B shale perpendicular to bedding planes after the samples were exposed to fresh water, 4% NaCl and 2% KCl for 24 hours. The Young's modulus decreased slightly after the samples' exposure to these fluids. The Poisson's ratio decreased after the sample's exposure to fresh water and increased after contact with 4% NaCl and 2% KCl. This indicates that the shale was only slightly sensitive to water-based fluids, similar to what the swelling behavior and the change in Brinell hardness with fluid exposure suggest.

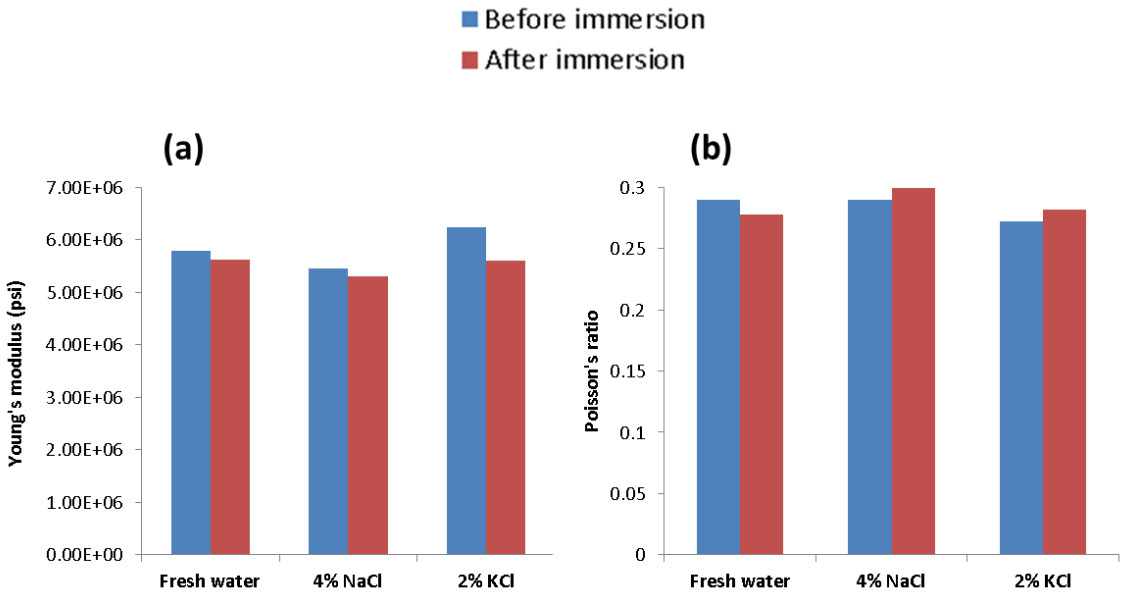

Figure 5.27: (a) Dynamic Young's modulus and (b) Poisson's ratio of the WGS-B shale before and after being immersed in fresh water, 4% NaCl and 2% KCl for 24 hours perpendicular to bedding planes.

In general, the change in shale hardness and P-wave and S-wave velocities perpendicular and parallel to bedding planes indicates that the TGS-F, the WBS and the WGS-B shales were only slightly sensitive to water-based fluids exposure. However, shale preservation was shown to impact the change in mechanical properties significantly upon shale-fluid contact. The next section will present the impact of shale preservation on mechanical properties.

Figure 5.28 shows the cross-plot of the change in P-wave velocity after 24 hours of contact with fresh water and the clay content of the TGS-F, WBS, WGS-B and the Pierre I shales. The change in wave velocity of the Pierre I shale after contact with fresh water was measured by Zhang (2005). A negative correlation exists between the shale clay content and the change in P-wave velocity after exposure to fresh water. In general, higher clay content corresponds to greater decrease in P-wave velocity after contact with

fresh water. This is because that waves travel faster through the solid rock matrix than through the pore fluid (Zhang, 2005). Therefore, water movement into the shale causes a decrease in the wave velocity. Shales with higher clay content tend to adsorb more water, thus reducing the wave velocity to a greater extent after fluid contact. The positive change in P-wave velocity observed with the TGS-F and the WBS shales might be due to experimental variability.

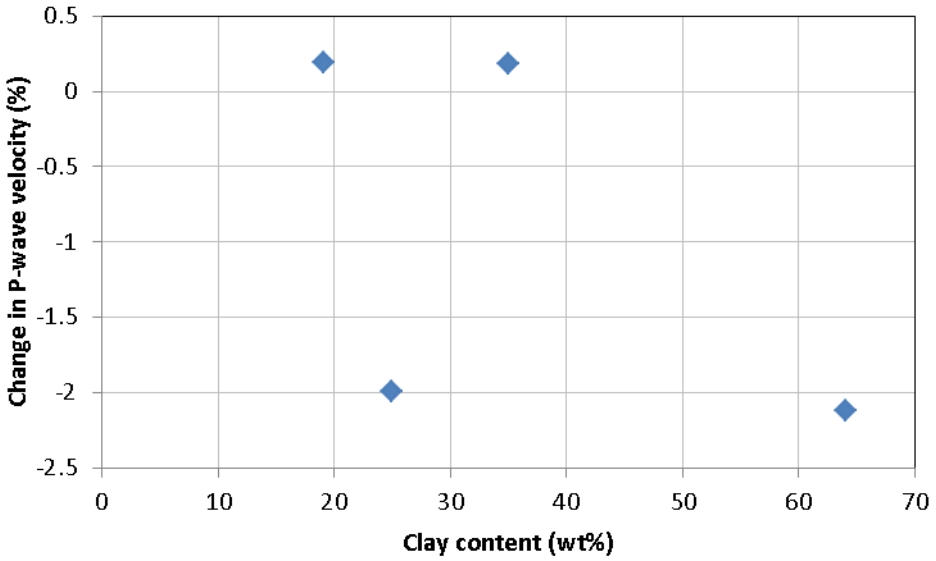

Figure 5.28: Cross-plot of the change in P-wave velocity after 24 hours of contact with fresh water and the clay content of the TGS-F, WBS, WGS-B and the Pierre I shales.

5.5 Impact of Shale Preservation on Mechanical Properties

As mentioned in Section 3.1.1, it is critical to use preserved shale samples to study shale-fluid interactions and screen drilling and fracturing fluids for their compatibility. Desiccation will alter the hydration state, petrophysical and mechanical properties of native shales. In addition, the change in shale properties will also be affected if the sample is not properly preserved. The impact of shale preservation on the

change in shale mechanical properties upon fluid contact will be presented in this section. All of the experiments were conducted at room temperature.

One inch cubic samples of the WGS-B shale were used for studying the impact of shale preservation. One preserved and one unpreserved shale sample was immersed in 4% NaCl for 24 hours. The unpreserved sample was created by drying a preserved sample in oven at 220^{o}F for 24 hours to remove the free fluid in the matrix. Changes in sample weight, Brinell hardness and acoustic wave velocities before and after fluid exposure were measured and compared for both the preserved and the unpreserved sample.

Figure 5.29 shows the weight change of the dry and preserved WGS-B shale samples after being immersed in 4% NaCl for 24 hours at room temperature. It is can be seen that the dry sample gained 0.61% of the original weight after immersion while the weight gain for the preserved sample was 0.16%. Therefore, the weight gain after fluid exposure for the unpreserved dry shale was almost four times that for the preserved shale. This clearly shows that the unpreserved shale was much more sensitive to fluid exposure, even though the WGS-B shale was shown to be only slightly sensitive to water-based fluids earlier. This difference in the weight gain can be due to the reduced water activity of the unpreserved dry shale. As a result, the osmotic potential between the shale and the bulk fluid is greater when the sample is not preserved, causing more water inflow into the shale matrix.

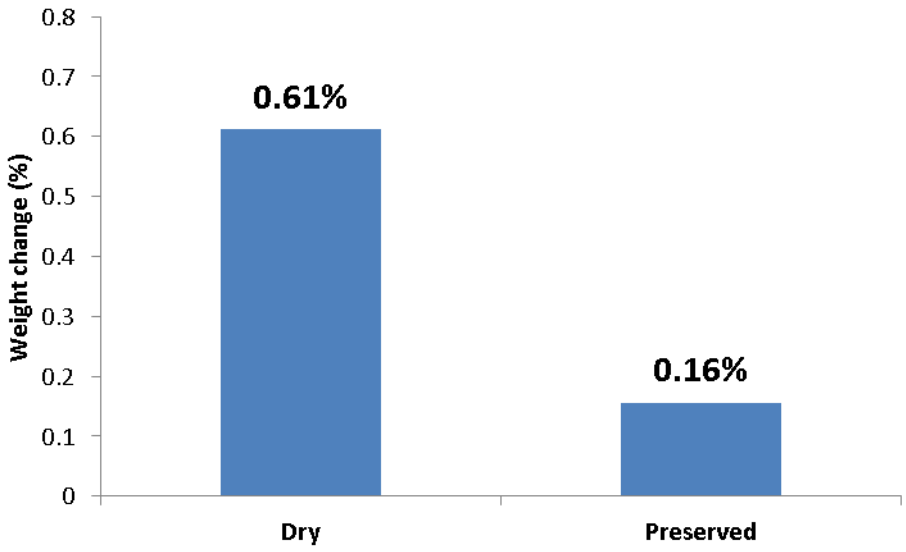

Figure 5.29: Weight change of the dry and preserved WGS-B shale samples after being immersed in 4% NaCl for 24 hours at room temperature.

Figure 5.30 shows the change in Brinell hardness of the dry and preserved WGS-B shale samples after being immersed in 4% NaCl for 24 hours at room temperature. It can be seen that the hardness reduction after the sample's exposure to water-based fluid was more significant for the unpreserved dry shale than for the preserved shale. In the direction perpendicular to bedding planes, the hardness of the unpreserved shale was reduced by 5.0% while that of the preserved sample remained unchanged. Similarly, in the direction parallel to bedding planes, the reduction of hardness of the unpreserved shale was 6.0% while that of the preserved shale was only 2.9%. Therefore, the properly preserved shale has shown to be more mechanically stable than the unpreserved dry shale in the sense that less softening of the preserved shale took place upon contact with water-based fluids. This is consistent with the weight change of the two types of shale samples shown in Figure 5.29.

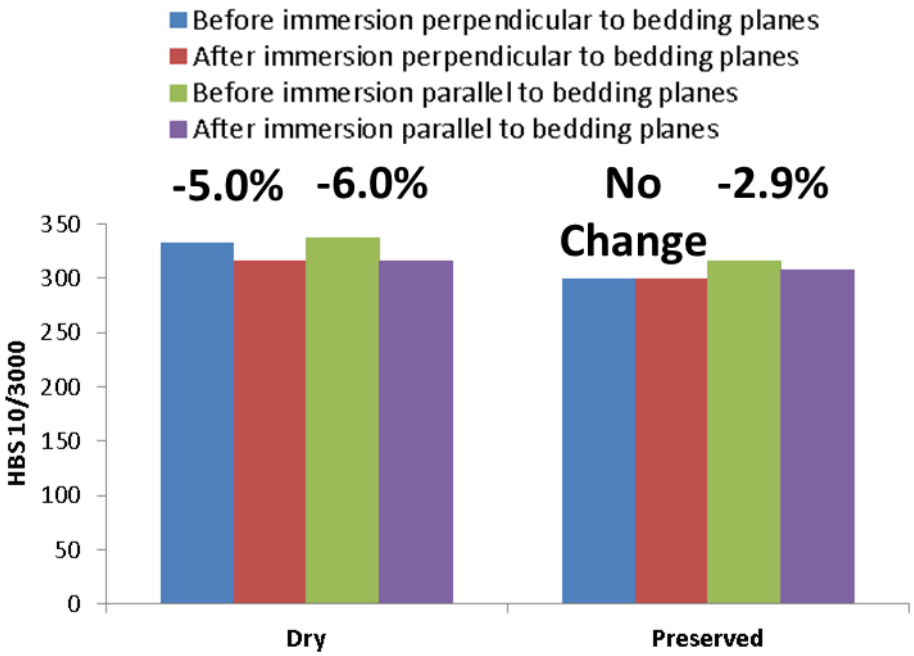

Figure 5.30: Change in Brinell hardness of the dry and preserved WGS-B shale samples after being immersed in 4% NaCl for 24 hours at room temperature.

Figure 5.31 shows the change in P-wave and S-wave velocities of the dry and preserved WGS-B shale samples perpendicular to bedding planes after being immersed in 4% NaCl for 24 hours at room temperature. The subsequent change in dynamic Young's modulus and Poisson's ratio perpendicular to bedding is shown Figure 5.32. It can be seen from Figure 5.31 that the P-wave velocity change after fluid exposure was very similar between the unpreserved and the preserved shale samples. However, the reduction in the S-wave velocity appears to be more significant for the unpreserved dry shale than the preserved shale. The greater decrease in the S-wave velocity for the unpreserved shale is magnified in the dynamic Young's modulus and Poisson's ratio. Figure 5.32 shows that the decrease in the Young's modulus for the unpreserved dry shale was 15%, five times that for the preserved shale. The contrast in the Poisson's ratio change was even more pronounced. The unpreserved shale experienced a 67% increase in Poisson's ratio

while the preserved shale only had a 3% increase. Again, the difference observed in the change in dynamic Young's modulus and Poisson's ratio of the preserved and unpreserved WGS-B shales upon fluid contact shows that the unpreserved shale was more sensitive to fluid exposure.

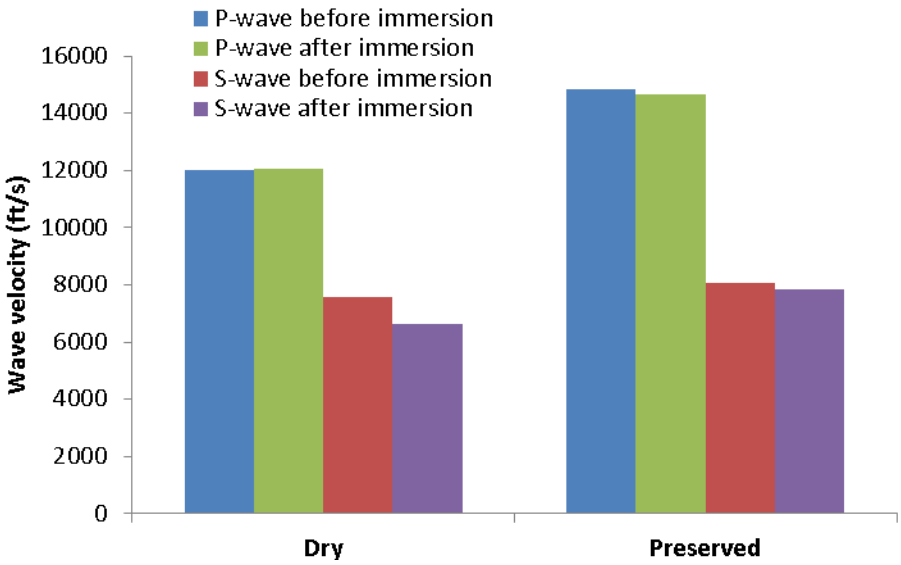

Figure 5.31: Change in P-wave and S-wave velocities of the dry and preserved WGS-B shale samples perpendicular to bedding planes after being immersed in 4% NaCl for 24 hours at room temperature.

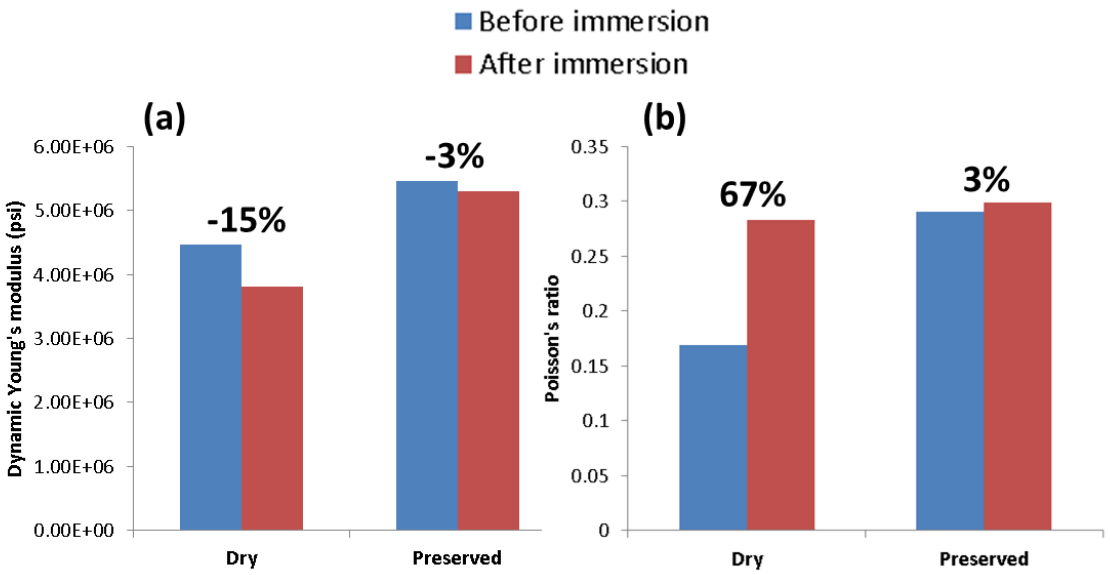

Figure 5.32: Change in the dynamic Young's modulus and Poisson's ratio of the dry and preserved WGS-B shale samples after being immersed in 4% NaCl for 24 hours at room temperature.

The results from the weight, Brinell hardness and the acoustic wave velocity changes before and after the WGS-B shale's contact with 4% NaCl show that the unpreserved shale can be much more sensitive to fluid exposure. Therefore, to understand shale-fluid interactions and to screen drilling and fracturing fluids for a particular shale oil/gas field, it is imperative that preserved core samples be used to best reflect potential compatibility issues and to test possible solutions to these problems when drilling and completing shale wells.

5.6 CONCLUSIONS

In this chapter, the shale-brine interactions were investigated systematically through gravimetric tests, swelling tests and measurements of the changes in mechanical properties such as the Brinell hardness and the acoustic wave velocities after the samples' exposure to various water-based fluids. Overall, the organic-rich shales were shown to be

only slightly sensitive to fluid exposure, as the change in weight and mechanical properties as well as the degree of swelling were fairly small after the samples were brought into contact with water-based fluids. This suggests that these shales are less likely to encounter wellbore instability and proppant embedment problems during drilling and fracturing operations. The use of salts can further reduce the reactivity of these shales to fluid exposure.

The salt concentration, the water activity of the bulk fluid, and the native water activity of the shale play an important role in the ion and water movement when shale comes to contact with water-based fluids. Since shale usually acts like a leaky membrane permitting the transfer of ions across it, the bulk fluid with a higher salt concentration tends to drive more ions into the shale because of the large ionic potential between the shale and the bulk fluid. Meanwhile, if the water activity of the shale is greater than that of the bulk fluid, the osmotic potential between the sample and the fluid will withdraw water from the shale. Increasing the salt concentration in the bulk fluid further lowers its water activity, causing a larger amount of water to be removed from the sample. This forms the basis of enhancing shale stability through the addition of salts such as KCl and NaCl. On the other hand, if the shale sample is not well preserved, its low water activity tends to trigger the inflow of water into the shale matrix.

The degree of swelling experienced by all shale samples in this study was less than 0.2% perpendicular to bedding planes. This is probably due to the expandable smectite clays being transformed into the less reactive illite clays through diagenesis. The swelling behavior was in good agreement with weight change after shale-fluid contact. Anisotropic swelling, where the samples swelled perpendicular to bedding planes and shrank parallel to bedding planes, was observed. This type of behavior was probably caused by the preferential layering of the clay platelets perpendicular to bedding planes.

The mechanical stability of the shale samples generally decreased after exposure to water-based fluids. However, the reduction in Brinell hardness, acoustic wave velocities and the Young's modulus was not significant, indicating that the samples were only slightly sensitive to fluid exposure. The changes in mechanical properties of preserved and unpreserved shale samples were shown be significantly different. The unpreserved shale was shown to be more sensitive to fluid exposure. This demonstrates the importance of using preserved shale samples for studying shale-fluid interactions and screening drilling and fracturing fluids for their compatibility.

Chapter 6: Shale-Fracturing Fluids Interactions

When shale is hydraulically stimulated, an extremely large volume of fracturing fluid is usually injected into the formation at a high rate to prop open the hydraulic and natural fractures. Typically, fracturing a deep horizontal well in the Marcellus formation requires the use of 2 – 10 million gallons of water (Kargbo et al., 2010). Prolonged exposure of shale rocks to various water-based fracturing fluids tends to alter the shale petrophysical and mechanical properties significantly. In the design of a hydraulic fracturing treatment, formation sensitivity to water and water-based fluids is one important screening criterion for choosing the appropriate fracturing fluids (Schein, 2005; Das and Achalpurkar, 2013). The degree of shale softening upon contact with water-based fracturing fluids directly impacts the fracture conductivity reduction as a result of proppant embedment, thus the well productivity as well. In this chapter, an overview of various water-based fracturing fluids and their properties is presented. Shale-fracturing fluids interactions are investigated in the form of changes in mechanical properties when a shale comes into contact with water-based fluids and clay control additives. The effect of shale mineralogy, temperature, fluid pH and clay stabilizers on the reduction in shale hardness and Young's modulus after fluid exposure is examined. The impact of water movement on shale mechanical properties is also studied.

6.1 Background on Fracturing Fluid

Fracturing fluid plays a critical role in the success of hydraulic fracturing treatment of low-permeability shale reservoirs. The viscous fracturing fluid is pumped downhole at a very high rate to open up fractures and to transport the proppant to support the natural and hydraulic fractures. As of 2000, water-based fluids made up more than 65% of all the fracturing fluids used, while only 5% of fracturing fluids were oil-based

(Gulbis and Hodge, 2000). The relatively low cost of water-based fluids' and their environmentally friendly nature have made them the preferred fluid for fracturing wells. A few commonly used water-based fracturing fluids are described below.

6.1.1 Slickwater

Slickwater is the most basic and common fracturing fluid system in use today. It contains a polyacrylamide friction reducer or a low concentration linear gel to reduce the pressure loss due to fluid friction within the pipe during pumping (Palisch et al., 2010). According to Palisch et al. (2010), there are several advantages when using slickwater for fracturing. The damage associated with the deposition of gel on the fracture face is minimized since slickwater treatment utilizes low concentrations of polymer. The cost for slickwater treatments is low in areas where water is readily available. The amount of chemical additives required in slickwater is also small, making the disposal and recycle of flowback water easier. In terms of the productivity of slickwater treatments, a complex fracture geometry is often created due to its low viscosity and high injection rate. Fractures are also less likely to grow out of the targeted zone vertically, which makes fracture containment less difficult to achieve.

On the other hand, the biggest concern with slickwater treatment is its low viscosity and the subsequent poor ability to transport and place proppant in fractures. As a result, a lot of times both lateral and vertical placement of proppant is not adequate to sustain the opening of fractures under high in-situ stress. This can shorten the propped fracture length and vertical coverage if the producing interval is thick. Proppant settling can limit the fracture height to cover the entire pay zone. In order to offset the drawbacks of slickwater treatments, a large volume of water is usually pumped to transport more proppant into the fracture. This can result in more formation damage in the near-wellbore

region due to water invasion. If the formation is water sensitive, the effect of fluid exposure will be magnified and impact the well productivity. Therefore, shale-fracturing fluid interactions need to be studied carefully to assess the compatibility of the fluid with the particular shale formation.

6.1.2 Gelled Fluids

In order to increase the viscosity of fracturing fluids, linear and crosslinked gels are usually added. Figure 6.1 shows the structures of a linear polymer and a crosslinked gel polymer. The complex network structure formed by crosslinking the linear polymer chains can significantly increase the fluid viscosity.

Guar gum, a natural agricultural product, was one of the earliest polymers used as a gelling agent. The guar particles swell and hydrate readily in water, unfolding and extending the polymer chains (Gulbis and Hodge, 2000). Other guar derivatives used to viscosify fracturing fluids include hydroxypropyl guar (HPG), carboxymethyl guar (CMG), and carboxymethyl hydroxypropyl guar (CMHPG). Cellulose derivatives are also used to enhance the viscosity in fracturing fluids. Such polymers include hydroxyethyl cellulose (HEC) and carboxymethyl hydroxyethyl cellulose (CMHEC). The concentration of these polymers in fracturing fluids is typically less than 1% by weight (Hodge, 2011). One common issue with these polymers is that they thin significantly with an increase in temperature (Gulbis and Hodge, 2000). Therefore, crosslinking these polymers can increase their effective molecular weight, thus improving the fluid viscosity, especially at high temperature.

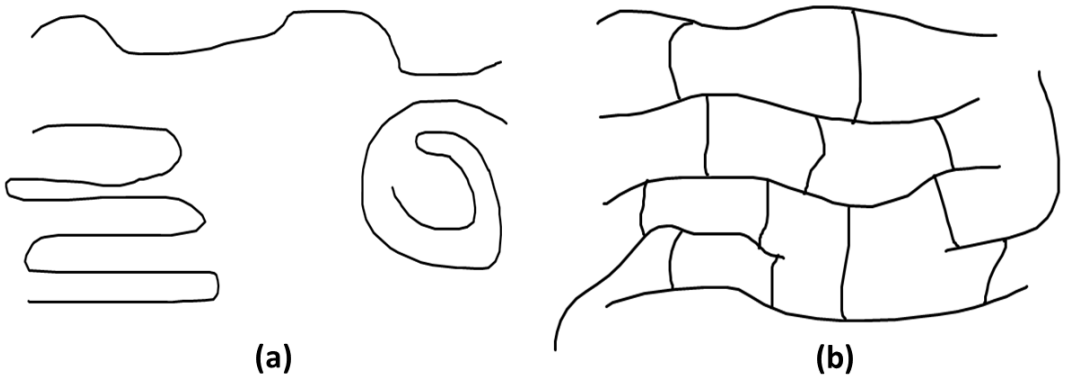

Figure 6.1: Structures of (a) a linear gel polymer, (b) a crosslinked gel polymer.

Borate, Ti (IV), Zr (IV) and Al (III) compounds are commonly used crosslinkers in water-based fracturing fluids. These crosslinkers function under various temperature and pH conditions with different types of polymers. For examples, highly viscous gels can be generated from guar and HPG using the borate ion crosslinker. The crosslinked gels are stable up to 325^{o}F (Gulbis and Hodge, 2000). Typically, a high pH environment is needed to maintain sufficient concentration of the borate crosslinker in solution. On the other hand, when the temperature increases, the fluid pH will decrease. Borate crosslinkers might not be able to produce gels with adequate viscosity. Instead, transition metal crosslinkers such as Ti (IV) and Zr (IV) compounds were developed for high temperature and low pH applications (Gulbis and Hodge, 2000). They can still crosslink polymers even when the pH is as low as 3. After the fracturing treatment, breakers are required to reduce the polymer weight and the fluid viscosity. Oxidizers and enzymes are the most common breakers for crosslinked gels. Even though the enhanced viscosity of gelled fluids is from the introduction of polymers, water is still the base fluid, and its compatibility with shale rocks at different temperature and pH conditions still impacts the success of a fracturing treatment significantly.

6.1.3 Energized Fluids

Due to cost, environmental and logistical limitations, water-based fluids might not always be the best choice for fracturing. Alternatively, energized fluids, which contain at least one compressible gaseous component, can be used to fracture tight formations such as shale. Energized fluids commonly exist in the form of multi-phase mixtures such as foams, even though single-phase gases such as N_2 and CO_2 have also been used for fracturing applications (Ribeiro, 2013). It was reported that over 40% of fracturing operations in horizontal wellbores in Canada were performed with energized fluids (Jacobs, 2014).

The benefits associated with energized fracturing technology are many-fold. The large amount of water needed for multi-staged hydraulic fracturing can be greatly reduced. Even proppant usage can be lowered to achieve a desired well productivity (Jacobs, 2014). Reynolds et al. (2014) reported that in the Montney formation in Canada, energized fracturing was able to reduce the fresh water volume by 79% and the proppant mass by 32% compared with the conventional slickwater treatment on an individual well basis. Even more encouraging was the enhanced well productivity as a result of the energized treatment. Meanwhile, gel damage and permeability impairment due to the multiphase effect in the near-wellbore region can be minimized because of the smaller amount of polymer and water used with the energized fracturing treatment. Enhanced fracture clean-up can also be accomplished with energized fluids. Furthermore, energized fluids are especially attractive to operators when water supply and disposal become challenging in the field.

Foam is one of the most widely used energized fracturing fluids. Foam is a stable two-phase mixture of liquid and gas, which is stabilized by the use of surfactants (Gulbis and Hodge, 2000; Ribeiro, 2013). The continuous liquid-phase can be water-based, oil-

based or viscoelastic surfactant-based, while the discontinuous gas-phase is usually N_2 or CO_2. The ratio of the gas and the foam volume is known as the foam quality. When the foam quality is 52% – 95%, the effective foam viscosity increases with the quality as the high gas concentration allows gas bubbles to connect with each other (Gulbis and Hodge, 2000; Friehauf and Sharma, 2009). For foams with a quality of 65% – 95%, their viscosity depends on the foam quality and shear rate (Blauer et al., 1974). Crosslinked polymers can be used with foams to further enhance fluid viscosity.

Even though fracture conductivity reduction due to proppant embedment and fines mobilization is expected to be less of an issue with energized fluids, oftentimes the base fluid is still water-based, and its interactions with the clay minerals in shale rocks can still negatively impact the performance of hydraulically fractured wells. Therefore, even when energized fluids are used for fracturing wells, shale-fluid interactions still need to be studied in order to understand and mitigate formation sensitivity to water.

6.2 DESICCATOR TEST

To investigate the effect of water adsorption and desorption on shale mechanical properties quantitatively, a series of desiccator tests were performed on preserved TGS-F, HUT 4-39 and HUT 1-70 shale samples. Samples were placed in desiccators with different humidity environments sequentially to achieve water adsorption and desorption. The use of saturated salt solutions in deaerated desiccators was to ensure that only water transfer into and out of shale takes place. The atmosphere on top of the salt solutions acts as a perfect semipermeable membrane to prevent the movement of ions. The humidity of the deaerated desiccators used in this test was 96%, 85% and 50.5%, corresponding to the native water activities of saturated KH_2PO_4, KCl and $Ca(NO_3)_2$ respectively. The shale samples were first conditioned at a water activity of 0.96, subsequently being moved to

lower humidity desiccators during desorption and back to higher humidity environments during adsorption. The indentation test procedure illustrated in Section 3.3.3 was followed to obtain the change in Brinell hardness and Young's modulus of the shale when water was adsorbed to and desorbed from the sample. Five indentation measurements were taken on different spots of the surface perpendicular to bedding planes to account for variations due to heterogeneity of the shale sample. The weight change of the samples was also measured simultaneously. The desiccators were placed at room temperature and the indentation measurements were performed at room temperature as well. Each sample was placed in one desiccator for a period of six days before being taken out for measurement so that equilibrium could be reached.

6.2.1 TGS-F Shale

Figure 6.2 shows the change in Brinell hardness of the TGS-F shale as a result of water adsorption and desorption on the sample. The error bars refer to one standard deviation of the measured data. Again, the TGS-F shale is assumed to have similar mineralogy of the TGS-D shale, which contains 56.9% calcite and 19.1% clay. As expected, during desorption, the removal of water from the shale sample resulted in an increase in shale hardness. On the other hand, the addition of water to the shale sample caused the hardness to decrease. The change in shale hardness appears to be reversible with regard to fluid content, over this range of fluid content, as the reduced hardness was restored when water was moved back into the shale sample. The change in the shale hardness was also more rapid at higher water activity than at lower water activity, as the slope was steeper when the water activity was greater than 0.85.

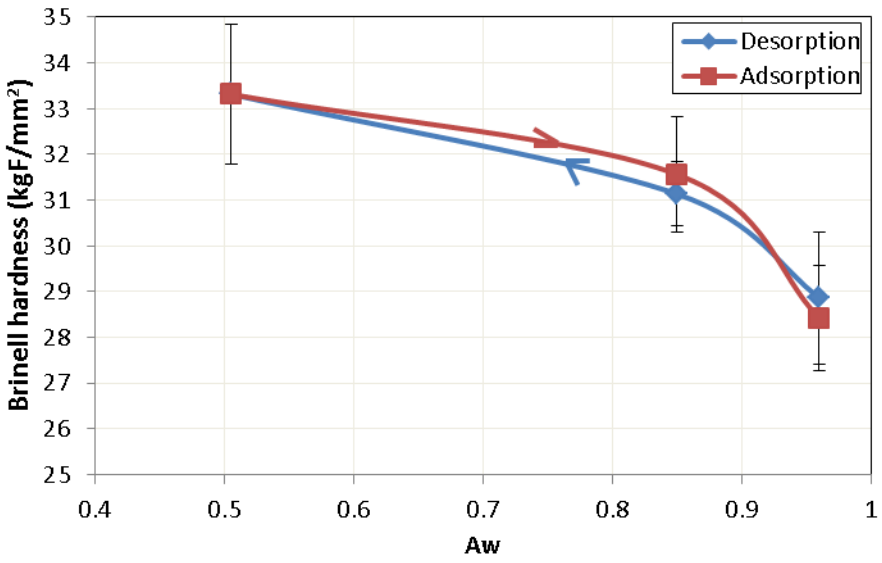

Figure 6.2: Change in Brinell hardness of the TGS-F shale as a result of water adsorption and desorption on the sample plotted against water activity.

Figure 6.3 shows the change in Young's modulus of the TGS-F shale obtained with the indentation measurement as a result of water adsorption and desorption on the sample. Similar to the trend of hardness change, the Young's modulus of the TGS-F shale increased when water was removed from the shale and decreased when water was added. Like the change in hardness, the change in Young's modulus as a result of water movement was also reversible. A similar reduced modulus was reached when water was added to the sample. In addition, the change in Young's modulus was also more rapid at higher water activity as indicated by the steeper slope when the activity was greater than 0.85.

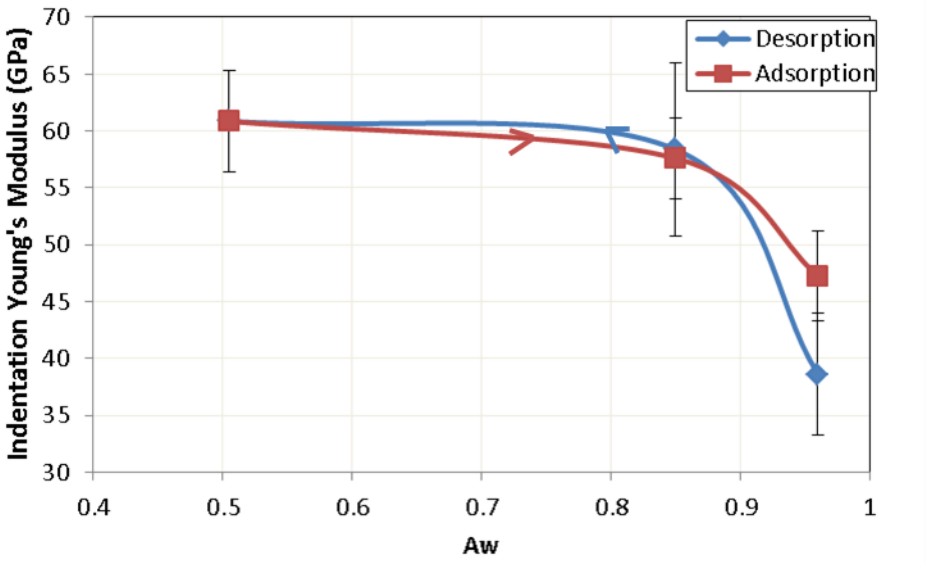

Figure 6.3: Change in indentation Young's modulus of the TGS-F shale as a result of water adsorption and desorption on the sample plotted against water activity.

Figure 6.4 shows the change in Brinell hardness of the TGS-F shale as a function of the sample weight change. Any observed weight change on the shale sample was due to water movement. It can be seen that the weight change as a result of changing relative humidity was very small. The maximum weight loss of the shale was 0.202% when the relative humidity was reduced from 96% to 50.5%. The small amount of water movement can be due to the small permeability of the shale sample. During desorption, the slope of the curve was fairly constant. In comparison, the slope of the curve was steeper during adsorption when the humidity was greater than 85%. The Brinell hardness of the shale sample increased from 29 kgF/mm^2 to 33 kgF/mm^2, when 0.202 wt% of water was removed from the shale sample. This is equivalent to a 15% increase in the hardness. Even though the sample weight change was extremely small, noticeable hardness change was observed on the TGS-F shale. The weight of the sample at the same water activity

(e.g. a_w = 0.85 and 0.96) was smaller during adsorption than during desorption, suggesting that the water movement into and out of shale was irreversible.

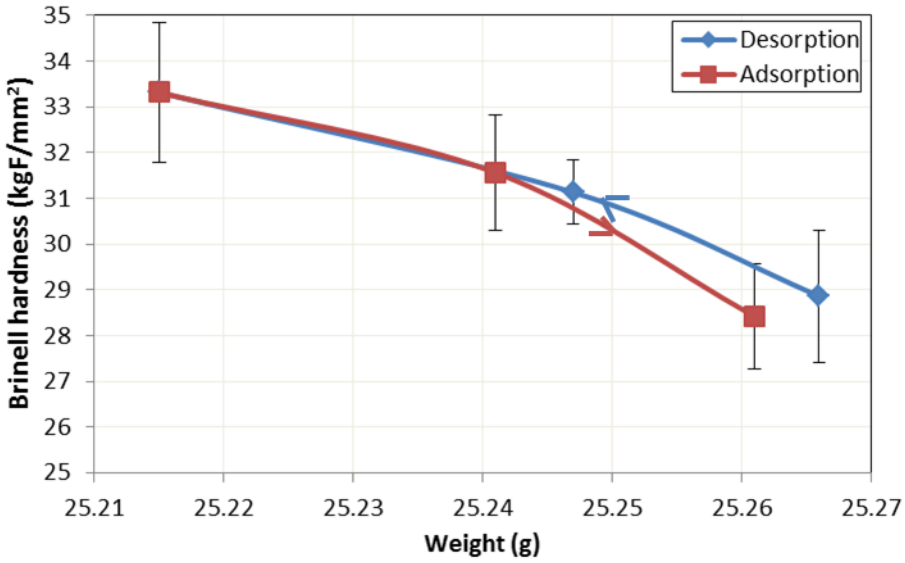

Figure 6.4: Change in Brinell hardness of the TGS-F shale as a result of water adsorption and desorption on the sample plotted against weight change.

Figure 6.5 shows the change in indentation Young's modulus of the TGS-F shale as a function of the sample weight change. The slope was slightly steeper during desorption when the humidity was greater than 85%. The Young's modulus of the shale sample increased from 39 kgF/mm^2 to 61 kgF/mm^2, a 58% increase when 0.202 wt% of water was withdrawn from the shale sample. The 58% increase in the Young's modulus compared with a 15% increase in the hardness of TGS-F shale indicates that the elastic properties of the shale are more sensitive to water movement than the plastic properties.

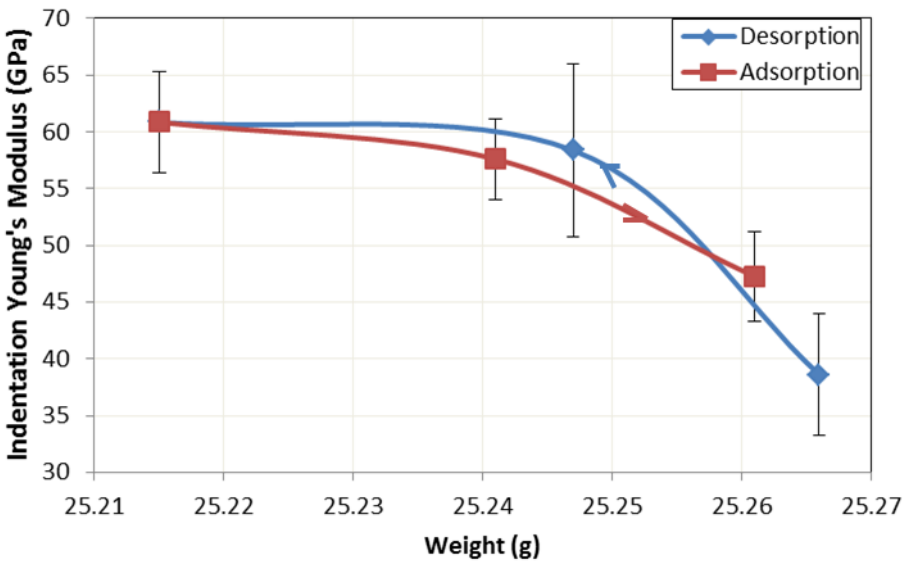

Figure 6.5: Change in indentation Young's modulus of the TGS-F shale as a result of water adsorption and desorption on the sample plotted against weight change.

6.2.2 HUT 1-70 and HUT 4-39 Shales

The effect of water movement on the shale Brinell hardness and Young's modulus of the HUT 1-70 and HUT 4-39 shales is discussed in this section. Once again, both HUT shales are from the same well in the Utica formation. The clay content of HUT 1-70 and HUT 4-39 was 43% and 12% respectively. To investigate the effect of clay content on the change in mechanical properties, HUT 1-70 is considered a high-clay shale while HUT 4-39 is taken as a low-clay shale.

Figure 6.6 shows the change in Brinell hardness of HUT 1-70 and HUT 4-39 as a result of water adsorption and desorption on the sample. Similar to the TGS-F shale, the Brinell hardness of both shales increased and decreased when water was removed from and added to the sample respectively. The slope of the adsorption and desorption curves was also steeper when the water activity was greater than 0.85 for both shales, except for HUT 4-39, where the slope was almost constant during adsorption. The change in

hardness was reversible for the low-clay HUT 4-39 shale. In contrast, an irreversible change in the hardness was observed with the HUT 1-70 shale, as the hardness at the same water activity during adsorption was smaller than that during desorption. The difference in the reversibility might be caused by the non-uniform water distribution and water activity in the shale pore space (Santos, 1997). More water might be permanently adsorbed to the clay minerals in the high-clay HUT 1-70 shale, resulting in the irrecoverable alterations in the mechanical properties. The reduction in humidity was not able to remove as much water from the high-clay shale, causing more shale softening when water was added again during adsorption.

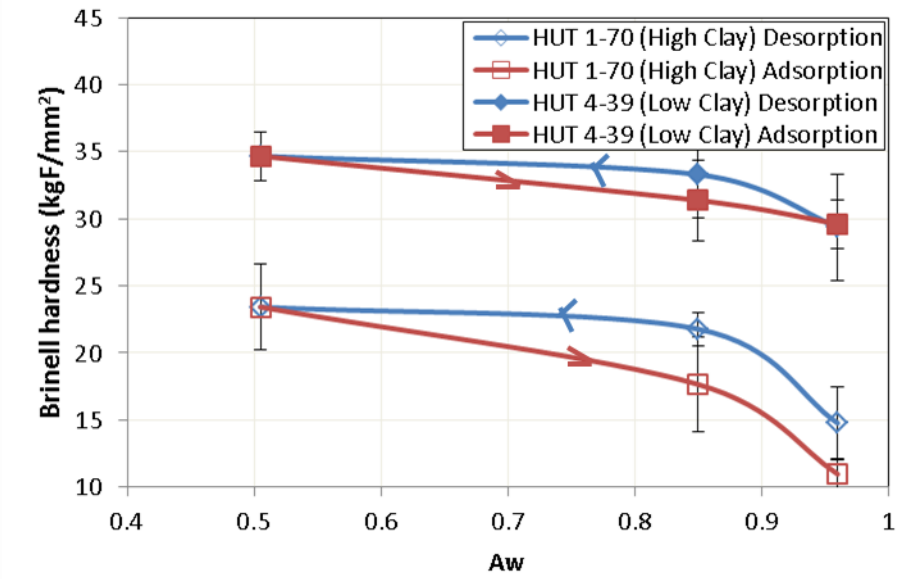

Figure 6.6: Change in Brinell hardness of the HUT 1-70 and HUT 4-39 shales as a result of water adsorption and desorption on the sample plotted against water activity.

Figure 6.7 shows the comparison of the Brinell hardness of both shales after they were first conditioned in the 0.96 water activity desiccator. It can be seen that the initial Brinell hardness of the low-clay HUT 4-39 shale was almost twice that of the high-clay

HUT 1-70 shale. Figure 6.6 also shows that throughout the adsorption and desorption processes, the Brinell hardness of the high-clay shale was always smaller than that of the low-clay shale. This suggests that the shale mineralogy, specifically the clay content, plays an important role in the hardness of the native sample as well as the change in hardness due to water movement. The soft nature of clay caused the high-clay HUT 1-70 shale to have a smaller hardness than the low-clay HUT 4-39. On the other hand, clay being more sensitive to water also resulted in HUT 1-70 being softer during adsorption and desorption. This suggests that the high-clay HUT 1-70 shale was more susceptible to proppant embedment at its native state. The issue of embedment could be much worse when large amount of water was pumped to fracture the formation.

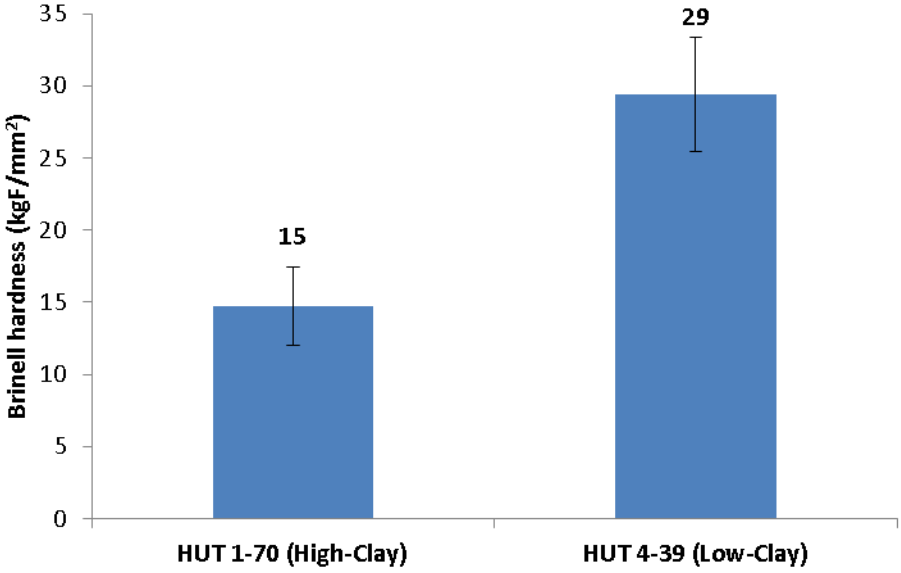

Figure 6.7: Comparison of Brinell hardness of the HUT 1-70 and HUT 4-39 shales at a water activity of 0.96.

Figure 6.8 shows the change in indentation Young's modulus of the HUT 1-70 and HUT 4-39 shales as a result of water adsorption and desorption on the sample. Similar to the trend of hardness change, the Young's modulus of both shales increased

when water was removed from the shale and decreased when water was added. Like the change in hardness, the change in Young's modulus as a result of water movement was reversible for HUT 4-39 and irreversible for HUT 1-70. For HUT 1-70, the Young's modulus during adsorption was smaller than that during desorption at the same water activity. The rate of change in Young's modulus during adsorption and desorption was fairly constant for both shales. The slope during adsorption was always steeper than that during desorption, indicating a more rapid change in Young's modulus when water was added to the shale samples. .

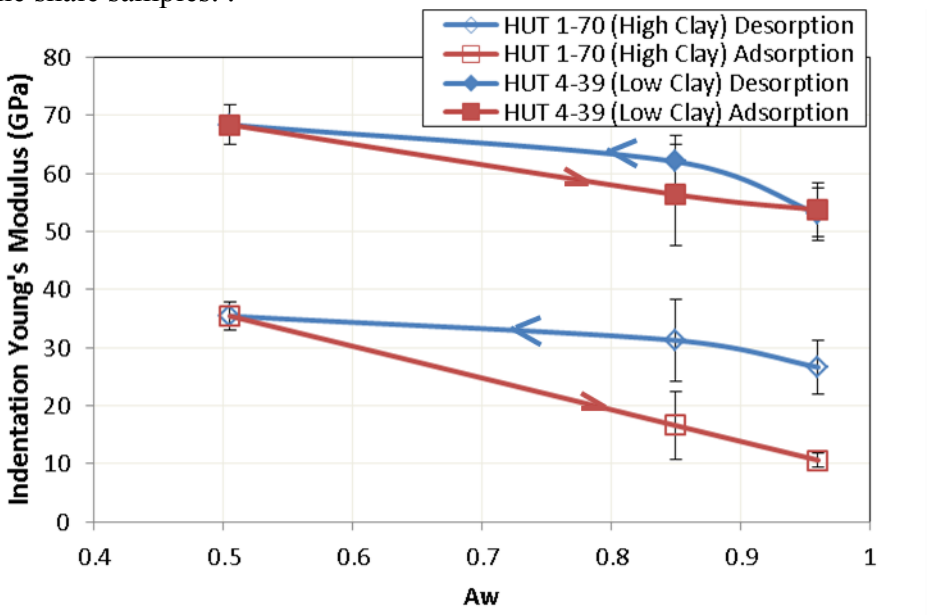

Figure 6.8: Change in indentation Young's modulus of the HUT 1-70 and HUT 4-39 shales as a result of water adsorption and desorption on the sample plotted against water activity.

Figure 6.9 shows the comparison of the indentation Young's modulus of both shales after they were first conditioned in the 0.96 water activity desiccator. Similar to the hardness at A_w = 0.96, it can be seen that the initial Young's modulus of the low-clay HUT 4-39 shale was almost twice that of the high-clay HUT 1-70 shale. Figure 6.8 also

shows that throughout the adsorption and desorption processes, the Young's modulus of the high-clay shale was always smaller than that of the low-clay shale. Again, similar to the hardness, it can be concluded that the clay content also significantly impacts the native shale's Young's modulus and the change in Young's modulus as a result of water movement.

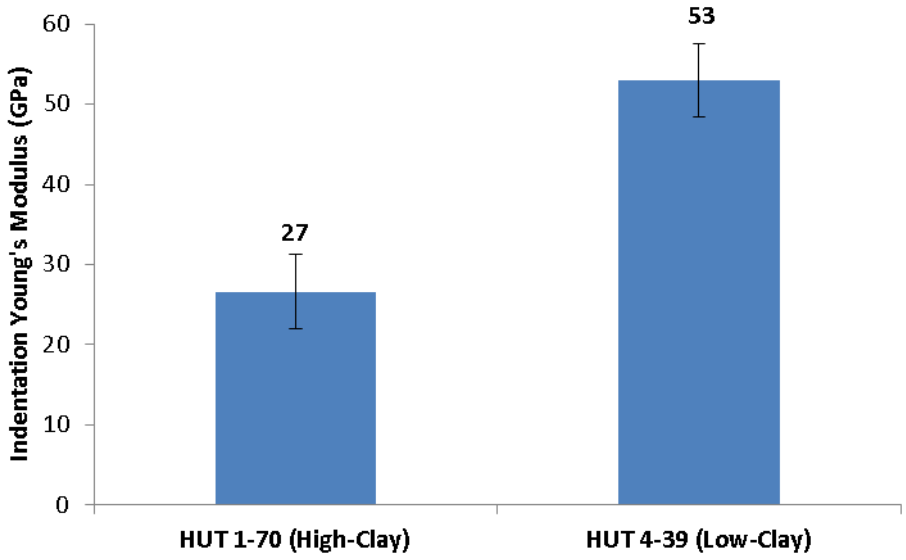

Figure 6.9: Comparison of the indentation Young's modulus of the HUT 1-70 and HUT 4-39 shales at a water activity of 0.96.

Figure 6.10 shows the change in Brinell hardness of the HUT 1-70 and HUT 4-39 shales as a function of the sample weight change. The weight changes of HUT 4-39 and HUT 1-70 are shown on the horizontal axes on the top and bottom of the plot respectively. Again any weight change of the shale samples was due to water movement. The major units of the two horizontal axes are the same for easier comparison. It can be seen that the weight change as a result of changing relative humidity in the desiccators was very small for both shales. In particular, the maximum weight loss of HUT 1-70 was 0.458% when the relative humidity was reduced from 96% to 50.5%, twice that of HUT

4-39, which was 0.205%. For both shales, during desorption, the slope of the curve was slightly steeper when the humidity was greater than 85%. In comparison, the slope of the curve was steeper during adsorption when the humidity smaller than 85%. The Brinell hardness of the high-clay HUT 1-70 increased from 15 kgF/mm^2 to 23 kgF/mm^2, a 53% increase in the hardness when the water activity was reduced from 0.96 to 0.505. In comparison, the hardness of the low-clay HUT 4-39 increased from 29 kgF/mm^2 to 35 kgF/mm^2 as a result of the same water activity change, equivalent to a 18% increase in hardness. The greater hardness change of the high-clay HUT 1-70 was consistent with the weight change observed with these shales. Similar to the TGS-F shale, the weight of the HUT 1-70 and HUT 4-39 shales at the same water activity (e.g. a_w = 0.85 and 0.96) was smaller during adsorption than during desorption. Again this behavior shows that the water movement into and out of these shales was irreversible.

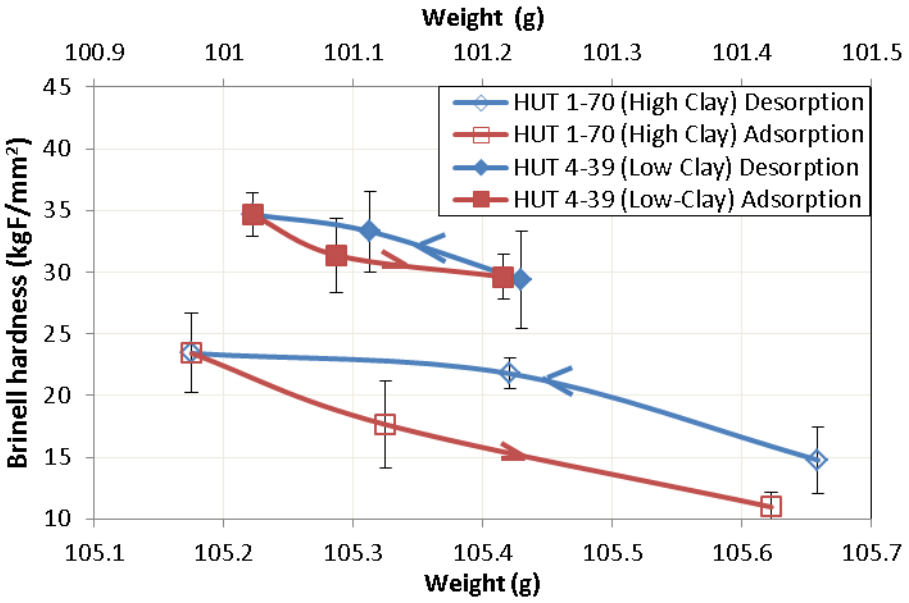

Figure 6.10: Change in Brinell hardness of the HUT 1-70 and HUT 4-39 shales as a result of water adsorption and desorption on the sample plotted against weight change. The weight of HUT 4-39 is shown on the horizontal axis on the top, and that of HUT 1-70 is shown on the horizontal axis on the bottom.

Figure 6.11 shows the change in indentation Young's modulus of the HUT 1-70 and HUT 4-39 shales as a function of the sample weight change. The slope during adsorption was steeper when the water activity was smaller than 0.85 for both shales. For HUT 1-70, when the water activity was greater than 0.85, the slope was similar to that during desorption. The Young's modulus of the high-clay HUT 1-70 increased by 33% from 27 GPa to 35 GPa when the water activity was reduced from 0.96 to 0.505. In comparison, the Young's modulus of HUT 4-39 increased by 29% from 53 GPa to 68 GPa due to the same water activity change. Again, this is consistent with the weight change (0.458% for HUT 1-70 and 0.205% for HUT 4-39 respectively) of the shale samples. The clay content of the shale has shown to directly impact the change in shale elastic properties as a result of water movement.

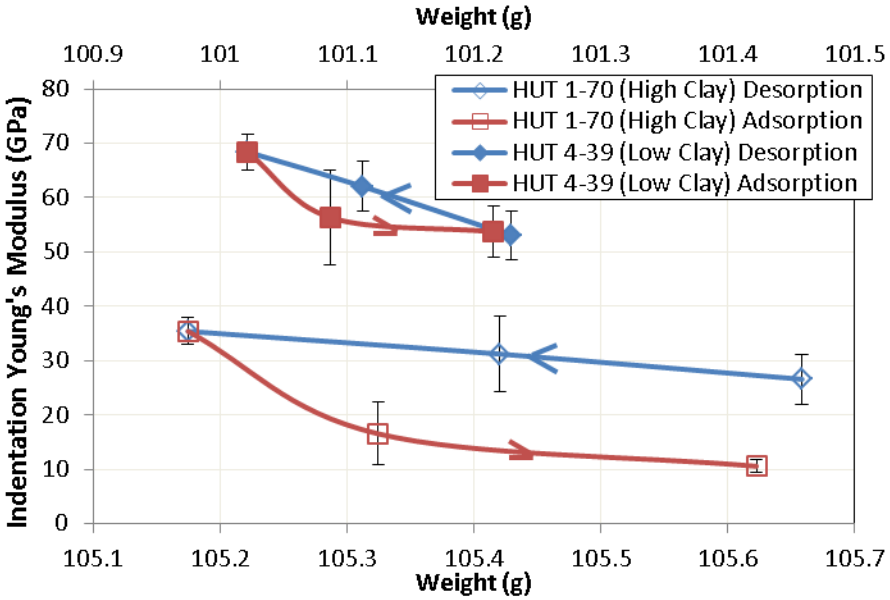

Figure 6.11: Change in indentation Young's modulus of the HUT 1-70 and HUT 4-39 shales as a result of water adsorption and desorption on the sample plotted against weight change. The weight of HUT 4-39 is shown on the horizontal axis on the top, and that of HUT 1-70 is shown on the horizontal axis on the bottom.

Figures 6.12 and 6.13 show the changes in Brinell hardness and Young's modulus of the three shales as a function of the shale weight change. It is evident that both hardness and Young's modulus decreased when water was added to the samples. The changes in mechanical properties and weight of HUT 1-70 shale were more scattered than that of HUT 4-39 and TGS-F. This could be due to the higher clay content of HUT 1-70 (43%) than that of HUT 4-39 (12%) and TGS-F (19.1%). Since clay is the most water-sensitive mineral, shale samples with more clay tend to adsorb more water and cause greater change in mechanical properties.

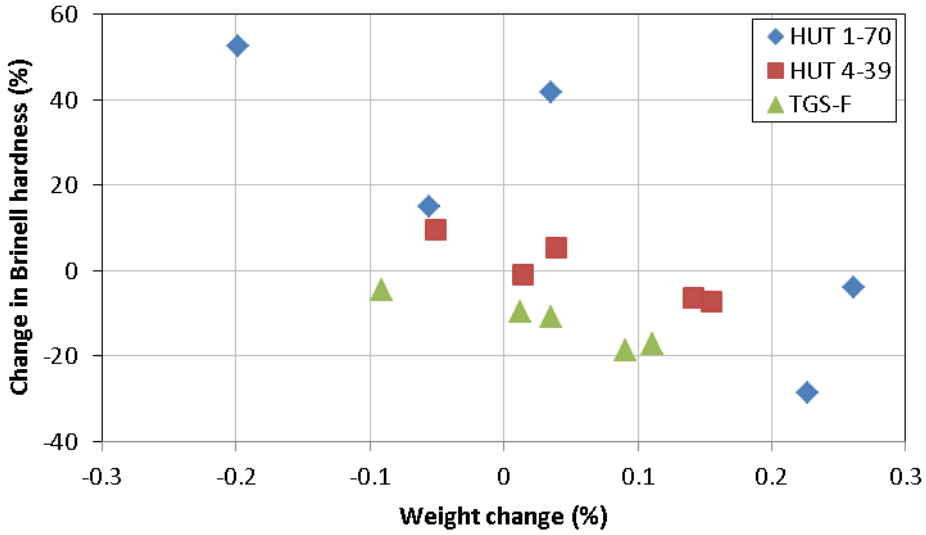

Figure 6.12: Change in Brinell hardness of the HUT 1-70, HUT 4-39 and TGF-S shales against the weight change of the shale samples.

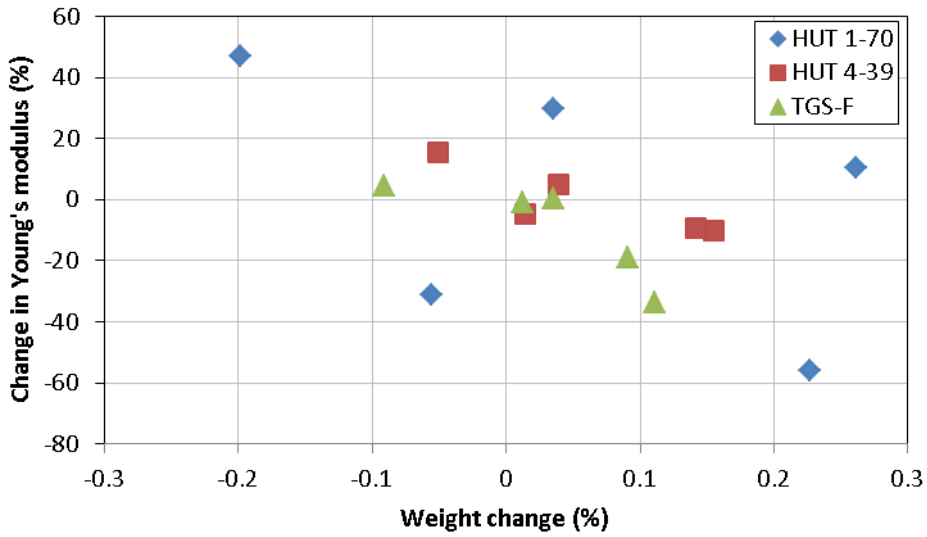

Figure 6.13: Change in Young's modulus of the HUT 1-70, HUT 4-39 and TGF-S shales against the weight change of the shale samples.

6.3 Change in Shale Mechanical Properties

In the previous section we presented results for changes in shale mechanical properties due to the gain or loss of water from the shale. In most wellbore environments the shale is exposed to the water with additives. In this section we study how the shale properties are affected by direct exposure to different fracturing fluids. Here, both water and ions and other chemicals interact with the shale and as we shall see the changes are complicated by these interactions.

Using the indentation technique illustrated in Section 3.3.3, the change in the mechanical properties of shale samples from various major plays was investigated after the samples were exposed to water-based fluids. Specifically, the effect of shale mineralogy, the fluid pH and temperature on the change in shale mechanical properties were studied. Correlations between the change in shale hardness and Young's modulus as well as the dynamic and static moduli were also established.

6.3.1 BEF-1 Shale

The change in the hardness of the BEF-1 shale was measured when the samples were immersed in various fluids shown in Table 3.3 at room temperature. The Lewis fluid was a weakly acidic fracturing fluid with a clay stabilizer (pH = 5.6). The SLB fluid was a high pH fluid with a temporary clay stabilizer (pH = 11.5). The BEF-1 shale was calcite-rich, with a calcite content of 57% and a clay content of 25.4%. As shown in Table 4.5, the BEF-1 core was not well preserved. Its native water activity was 0.46. Measurements were taken on surfaces parallel to bedding planes.

Figures 6.14 and 6.15 show the change in the absolute and normalized Brinell hardness of the BEF-1 shale after being exposed to DI water, a Na_2CO_3 solution (pH = 11.4), a low pH fracturing fluid (Lewis fluid) and a high pH fluid (SLB fluid) for up to 36 hours at room temperature. It can be seen from Figure 6.14 that the initial hardness of the native BEF-1 shale varies from sample to sample. This can impact the subsequent change in the hardness as the sample exposure to fluids continued. Sample heterogeneity certainly plays an important part as shown by the variations in hardness observed before fluid immersion.

The subsequent change in the hardness was normalized against the initial shale hardness and is shown in Figure 6.15. The least damaging fluid to the shale hardness was the low pH fluid, which caused less than 20% reduction in shale hardness after more than 30 hours of exposure. The clay stabilizer in the low pH fluid might decrease the sensitivity of the BEF-1 shale to fluid exposure. On the other hand, the high-pH Na_2CO_3 solution and the SLB fluid resulted in the most softening of the BEF-1 shale. An over 60% reduction in the hardness was observed with these two fluids. Particularly with the Na_2CO_3 solution, only one hardness measure could be obtained after the sample was immersed, because the sample fell apart along the bedding planes after being immersed in

the bulk fluid. The excess hydroxyl ions in an alkaline solution destabilize the reactive clay. The desaturation of the BEF-1 shale in the atmosphere could also be the reason for the rapid disintegration of the sample when in contact with water-based fluids. The clay stabilizer in the SLB fluid was not effective in reducing the softening of the BEF-1 shale. It can be seen from Figure 6.15 that most of the shale softening happened at early time. Not much additional hardness reduction on the samples was observed after about 13 hours of fluid exposure.

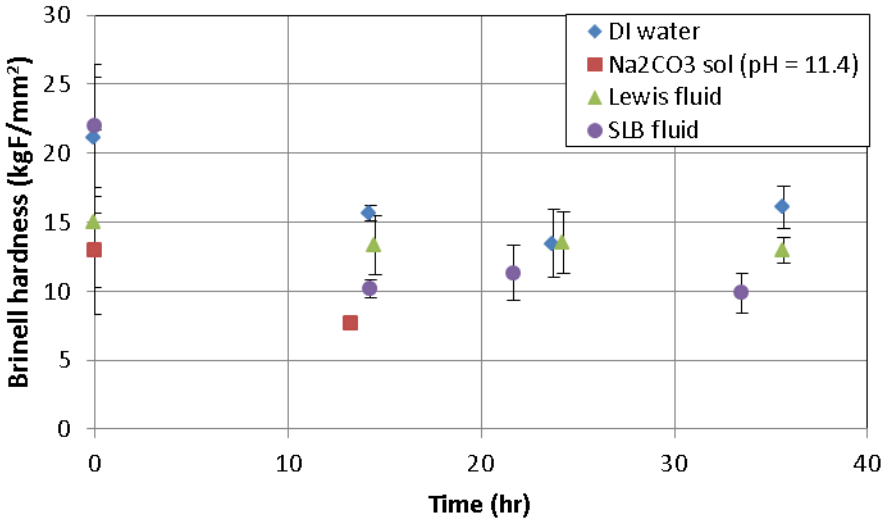

Figure 6.14: Change in the absolute Brinell hardness of the BEF-1 shale after exposure to various water-based fluids at room temperature as a function of time.

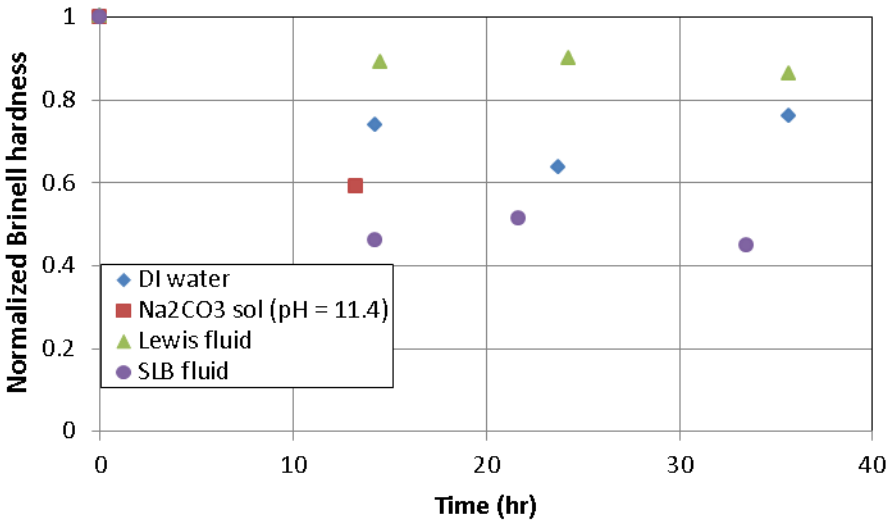

Figure 6.15: Change in the normalized Brinell hardness of the BEF-1 shale after exposure to various water-based fluids at room temperature as a function of time.

6.3.2 BUT Shale

The change in hardness and Young's modulus of the BUT shale was also measured after the samples were exposed to three water-based fluids shown in Table 3.2 for up to 40 hours. Solution 1 contains all the components of a fracturing fluid; Solution 2 contains the same components as Solution 1 except for the clay control additive; Solution 4 contains only the clay control additive with a concentration of 0.5 gpt (gallons per thousand gallons). The shale samples were immersed in these three fluids at room temperature. A high pH fluid and an acidic fluid were used to investigate the effect of pH on the change in shale mechanical properties. The high pH fluid was made by dissolving Na_2CO_3 in DI water to make the pH = 11.35. The acidic fluid was prepared by adding acetic acid to DI water to make the pH = 3.34.

The effect of temperature on the change in hardness was also studied when the temperature was raised to 175^{o}F using the high pH fluid and the acidic fluid. For each

sample at a particular time, five or more indentation measurements were made and averaged. Measurements were taken on surfaces perpendicular to bedding planes when the BUT samples were immersed in Solutions 1 and 2 and on surfaces parallel to bedding planes when the samples were immersed in Solution 3, the high pH fluid and the acidic fluid (both at room temperature and at 175^{o}F). The BUT shale was clay-rich, with a clay content of 43.3% and a calcite content of 19.2%, as shown in Table 4.1.

Figure 6.16 shows the hardness of the BUT shale samples at their native state. It can be seen that the average hardness of the surfaces perpendicular and parallel to bedding planes was very similar. The average hardness of the surfaces perpendicular to bedding planes was 33.3 kgF/mm^2 while that of the surfaces parallel to bedding planes was 33.6 kgF/mm^2. Overall, the average hardness of the BUT shale in different directions was 33.5 kgF/mm^2. This may suggest that the compressive strength of the BUT shale was also similar in different directions, as Santarelli et al. (1991) reported a good linear correlation between the Brinell hardness and the uniaxial compressive strength of various reservoir rocks. Meanwhile, the ratio of the standard deviation of the hardness to the average value of the surfaces perpendicular to bedding planes was 13.3% and that of the surfaces parallel to bedding planes was 30.9%. This difference in the hardness variation might be due to more measurements being taken on surfaces parallel to bedding planes. It could also be caused by the HUT shale being more heterogeneous parallel to the bedding planes than perpendicular to bedding planes on a core scale. Figure 6.17 shows the histogram of all the hardness measurements of the native BUT shale. The measured hardness was normally distributed and was skewed towards the right.

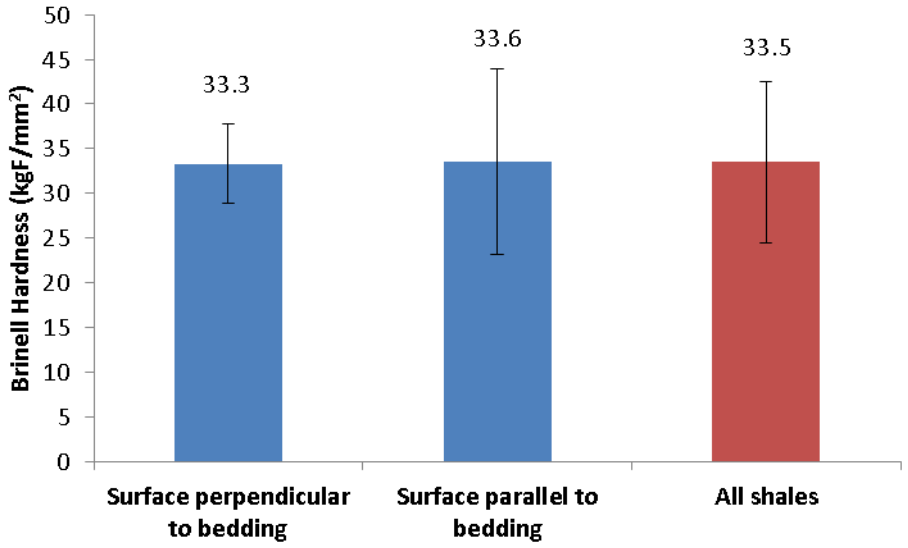

Figure 6.16: Hardness of the BUT shale samples at their native state.

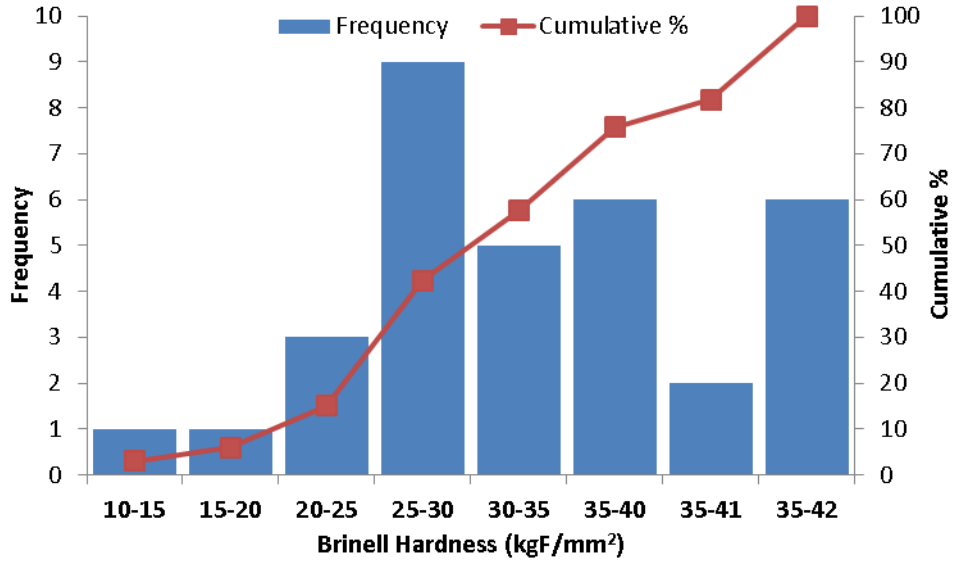

Figure 6.17: Histogram of the hardness of the BUT shale samples at their native state.

Figures 6.18 and 6.19 show the changes in the absolute and normalized Brinell hardness of the BUT shale after being exposed to Solutions 1, 2 and 4 for more than 40 hours at room temperature respectively. Overall, the shale hardness did not change

significantly when interacting with these water-based fracturing fluids. A30% reduction in hardness was observed after 40 hours of fluid exposure. The shale hardness appears to decline exponentially over time. The clay control additive was not effective in reducing softening of the BUT shale, as the reduction in hardness of the sample in Solution 2 was not greater than that in Solutions 1 and 4 during fluid exposure.

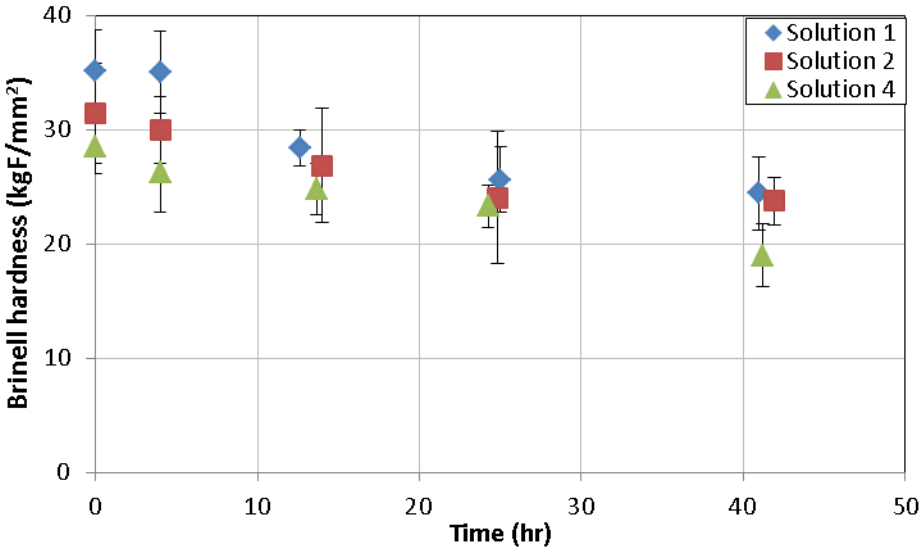

Figure 6.18: Change in the absolute Brinell hardness of the BUT shale after being exposed to Solutions 1, 2 and 4 for more than 40 hours at room temperature.

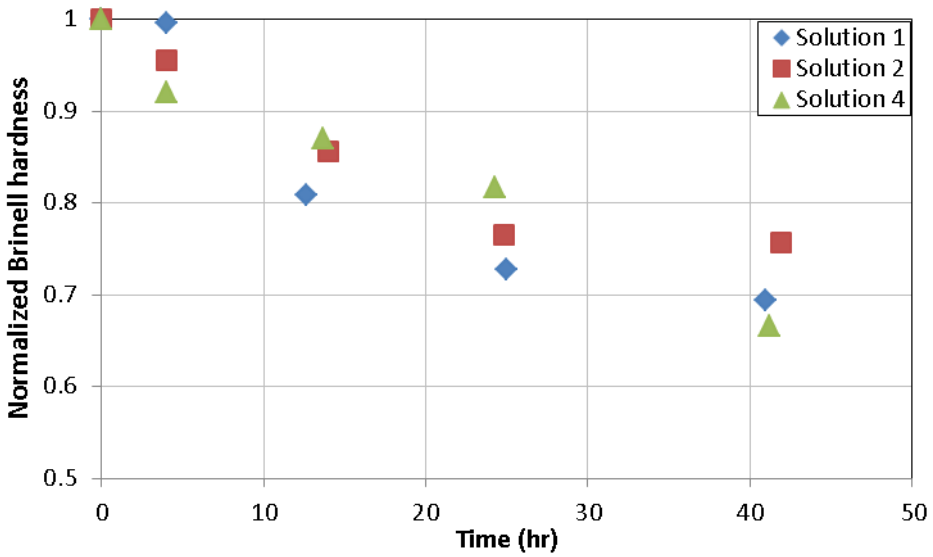

Figure 6.19: Change in the normalized Brinell hardness of the BUT shale after being exposed to Solutions 1, 2 and 4 for more than 40 hours at room temperature.

Figures 6.20 and 6.21 show the change in the absolute and normalized Young's modulus of the BUT shale after being exposed to Solutions 1, 2 and 4 for over 40 hours at room temperature respectively. Similar to the change in hardness, the shale Young's modulus did not decrease significantly after the samples were immersed in these water-based fracturing fluids. The Young's modulus was reduced by about 30% after 40 hours of fluid exposure. Again, the clay control additive was not effective in mitigating the reduction in the Young's modulus of the BUT shale, as the samples in Solutions 1 and 4 experienced greater reduction in Young's modulus than that in Solution 2 after 40 hours of fluid exposure.

Overall, at room temperature, the shale hardness and Young's modulus were reduced by about 30% after exposure to these three fracturing fluids. The clay control additive in the fluids was unable to improve the shale mechanical stability after fluid exposure.

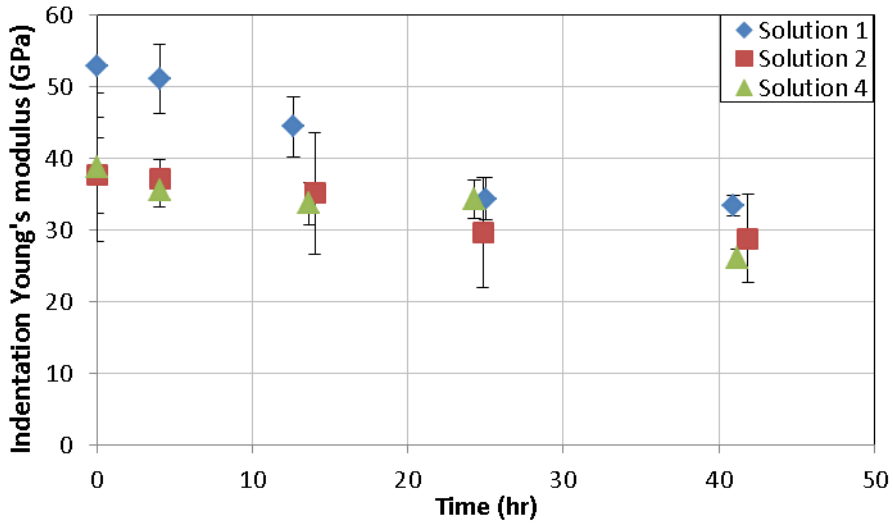

Figure 6.20: Change in the absolute indentation Young's modulus of the BUT shale after being exposed to Solutions 1, 2 and 4 for over 40 hours at room temperature.

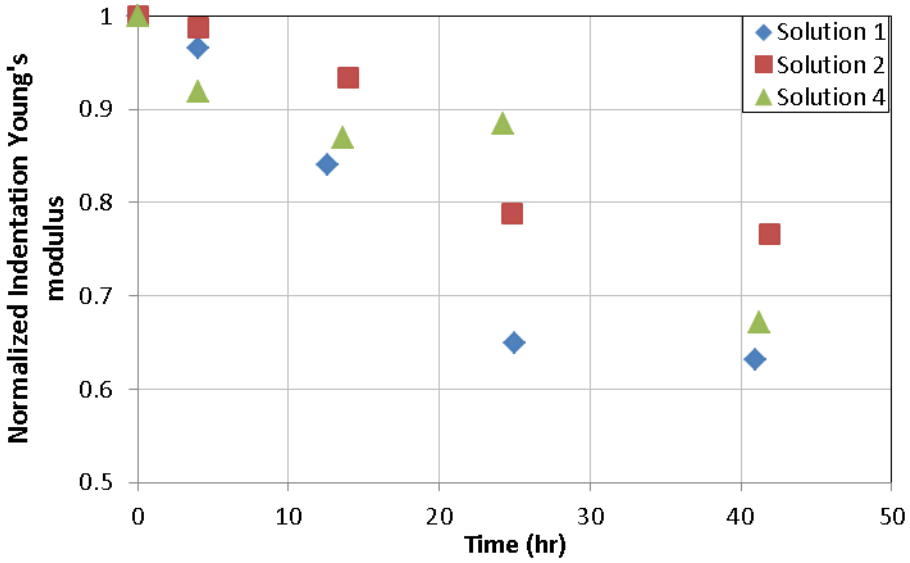

Figure 6.21: Change in the normalized indentation Young's modulus of the BUT shale after being exposed to Solutions 1, 2 and 4 for over 40 hours at room temperature.

Figure 6.22 shows the cross-plot of the Brinell hardness and the indentation Young's modulus of the BUT shale at different stages of exposure to Solutions 1, 2 and 4. There is a good linear correlation between these two mechanical properties. This means that the reduction in shale hardness coincides with a decrease in its elastic properties, when shale comes into contact with water-based fluids. The same correlation between the shale hardness and Young's modulus was also reported in a previous study by Kumar et al. (2012). On the other hand, a slope of 0.5378 indicates that the change in Young's modulus was more rapid than the change in hardness when the samples were exposed to water-based fluids. This observation is similar to the results shown in Section 6.2, where the BEF-1 shale experienced a greater increase in the Young's modulus than the hardness when water was removed from the shale samples.

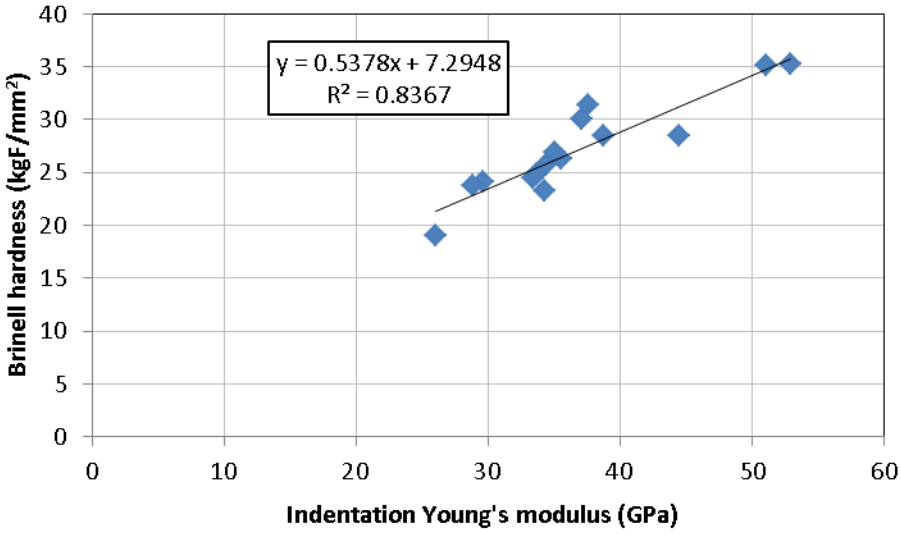

Figure 6.22: Cross-plot of the Brinell hardness against the indentation Young's modulus of the HUT shale at different stages of exposure to Solutions 1, 2 and 4.

Figures 6.23 and 6.24 show the change in the absolute and normalized Brinell hardness of the BUT shale after being exposed to Solution 1, an acidic fluid (pH = 3.34)

and a high pH fluid (pH = 11.35) at both room temperature and elevated temperature (175^{o}F). It can be seen from Figure 6.23 that there is a large variation in the Brinell hardness of the BUT samples at their native state (Time = 0). The sample hardness varies from about 45 kgF/mm^2 to slightly more than 20 kgF/mm^2. The variation in the hardness could be due to the sample heterogeneity.

It can be seen from Figures 6.23 and 6.24 that most of the shale softening took place at early time during fluid exposure. For example, the hardness of the sample exposed to the acidic fluid at 175^{o}F was 33.1 kgF/mm^2 when t = 4.65 hours and was 30.9 kgF/mm^2 when t = 42.78 hours. Fluid pH has a large impact on the shale hardness reduction. The high pH fluid tends to reduce the shale hardness more throughout the process than the acidic fluid. Solution 1, which did not contain any pH buffer, caused the least shale softening (0.4% hardness reduction) during the first four hours of fluid exposure at room temperature, as shown in Figure 6.24. In contrast, four hours of exposure to the high pH and the acidic fluid resulted in a 22% and 12% reduction in the hardness of the BUT samples respectively. Similarly, at 175^{o}F, a hardness reduction of 41.6% was observed with the sample exposed to the high pH fluid, greater than the 31.0% softening experienced by the sample immersed in the acidic fluid after more than 40 hours of fluid exposure. The impact of the fluid pH on shale softening was similar to that observed with the BEF-1 shale earlier. Often, crosslinkers in fracturing fluids function optimally at a specific pH range. The borate crosslinker works the best at a pH of 8 – 12 (Gulbis and Hodge, 2000). Appropriate shale inhibitors need to be added to such high pH fluids to minimize the damage caused by shale softening.

The reduction in shale hardness caused by the high pH fluid is likely a result of destabilization of the clays. At high pH, the pH dependent charge on the edges of clay particles becomes negative according to the following surface reaction:

$$MOH_2^+ \overset{H^+}{\rightleftharpoons} MOH \overset{OH^-}{\rightleftharpoons} MO^- + H_2O$$

Here M is the metal ion and for clays is typically Si or Al. The iso-electric point for SiOH and AlOH is is 2.5 and 8.5 respectively. Above this pH both hydroxides are deprotonated and will be negatively charged. This can cause clay dispersion and/or swelling.

On the other hand, the low pH solution will dissolve the carbonate minerals in the shale. The removal of carbonate minerals will result in shale softening since calcite is in general harder than the clay or the organic material in the shale. Therefore, the mechanisms of changes in the hardness of the shale at low pH and high pH are different.

Temperature also significantly impacts the degree of shale softening when being exposed to water-based fluids. Figure 6.24 shows that the higher temperature caused more hardness reduction when samples were exposed to the high pH fluid and the acidic fluid. After about 24 hours of fluid exposure, the high pH fluid resulted in a 21.4% hardness reduction at room temperature and a 40.0% hardness reduction at 175^{o}F. Likewise, the hardness of the example exposed to the acidic fluid was reduced by 12.5% at room temperature and by 31.7% at 175^{o}F. Therefore, a high pH fluid at a high reservoir temperature could cause the most damage to the mechanical stability of the BUT shale. Great care needs to be taken to mitigate the formation damage to the shale wells at such temperature and pH conditions.

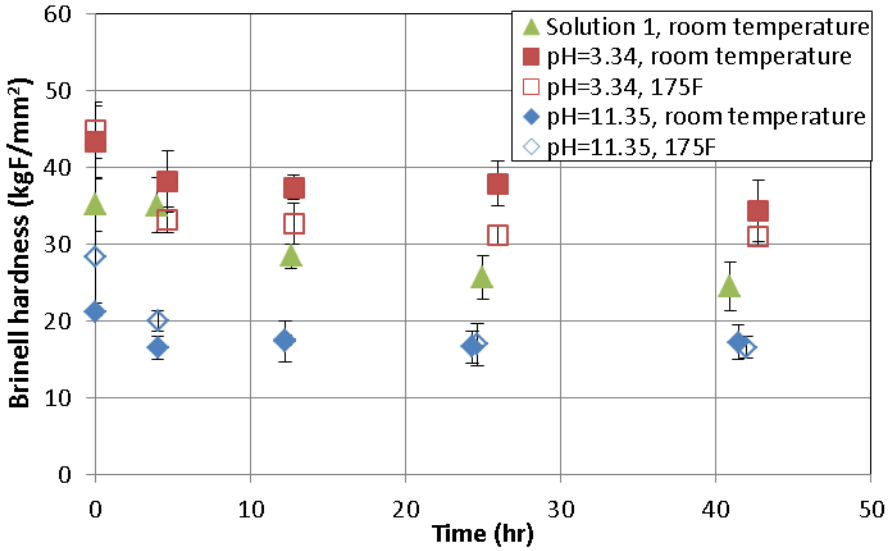

Figure 6.23: Change in the absolute Brinell hardness of the BUT shale after being exposed to Solutions 1, an acidic fluid and a high pH fluid at room temperature and elevated temperature.

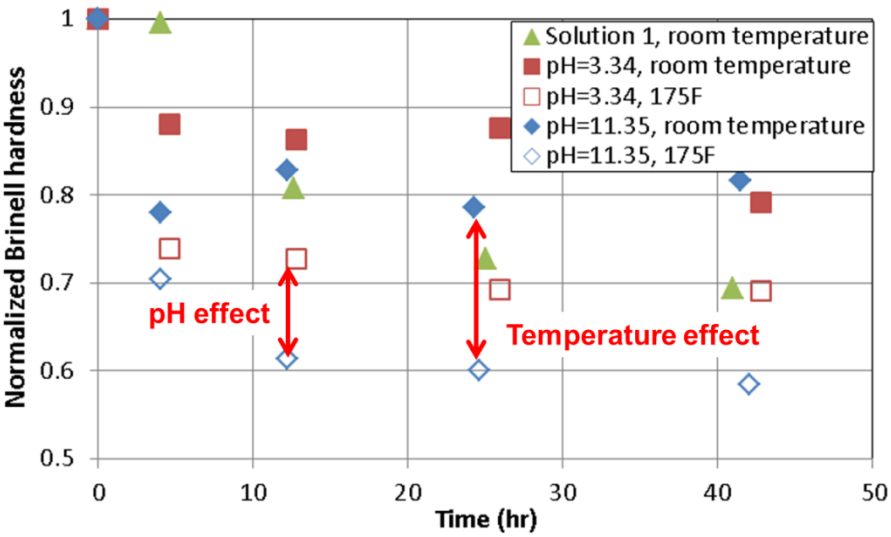

Figure 6.24: Change in the normalized Brinell hardness of the BUT shale after being exposed to Solutions 1, an acidic fluid and a high pH fluid at room temperature and elevated temperature.

The impact of fluid pH on the swelling behavior of the BUT shale was also investigated. Figure 6.25 shows the swelling of two BUT samples perpendicular to bedding planes after being immersed in an acidic fluid and a high pH fluid at room temperature respectively. The samples were of cubic shape with an edge length of approximately 1.25 inches.

It can be seen from Figure 6.25 that both shale samples underwent a short period of shrinkage when they were first immersed in these two fluids. This shrinkage behavior was unique and was not observed with other organic-rich shale samples exposed to brines earlier in Chapter 5. For the sample exposed to the acidic fluid with a pH of 3.34, the low pH probably accelerated the dissolution of the carbonate in the shale sample. As a result, the sample dimension could be reduced early during the swelling test. On the other hand, the excess negative charges in the high pH fluid could disrupt the structure of the previously aggregated and flocculated clay minerals. Some of the dispersed clay particles could be locked in the matrix and some could be mobilized. The mobilization of the clay particles and other fines might cause the shale sample to shrink at early time. After about two hours of exposure to these fluids, the swelling caused by water movement into the shale started to dominate and a positive displacement was observed with each shale sample perpendicular to bedding planes. After 24 hours of exposure, greater swelling was observed with the sample exposed to the high pH fluid than with the acidic fluid. This is consistent with the softening behavior of the BUT shale shown in Figure 6.24. The acidic fluid caused less swelling and smaller hardness reduction to the BUT shale than the high pH fluid.

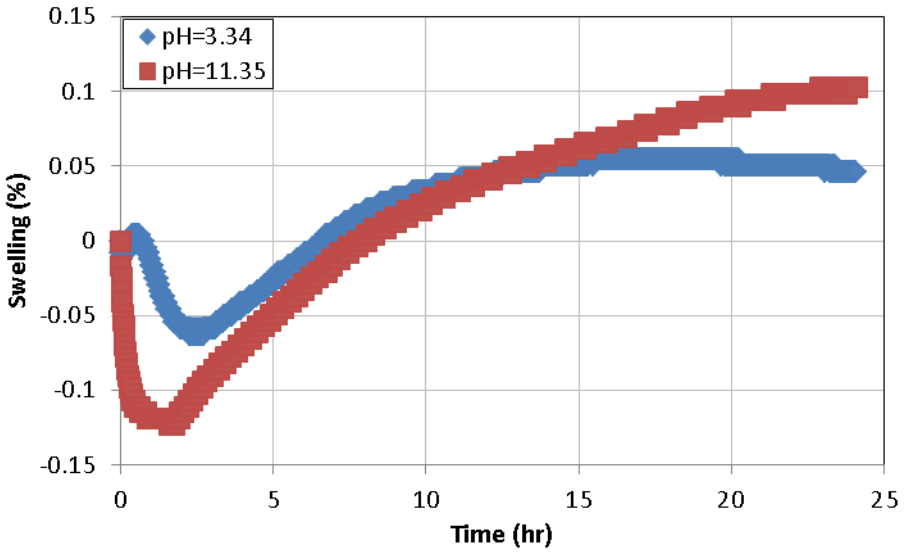

Figure 6.25: Swelling of the BUT shale perpendicular to bedding planes after being immersed in an acidic fluid and a high pH fluid for 24 hours at room temperature.

6.3.3 BEF-2 Shale

The change in Brinell hardness of the BEF-2 shale was measured when the samples were immersed in various fluids at 175°F. BEF-2 was a preserved Eagle Ford core sample. Table 6.1 shows the test matrix of the shale-fluid interactions. Brine refers to the field water, whose composition is shown in Table 3.1. The acidic fluid had a pH of about 3, and was made by adding acetic acid to the field water. The high-pH fluid was made by mixing Na_2CO_3 with the field water. Its pH was about 11. Choline chloride and TMAC are two mono-cationic quaternary amine clay stabilizers. PC-1952 and PC-1955 were also quaternary amine clay stabilizers.

The elemental composition of each shale sample was measured with the handheld ED-XRF instrument before and after the fluid exposure. The relative abundance of clay, quartz and calcite minerals was estimated using the algorithm discussed in Section 4.2. Samples were divided into a high-clay and a low-clay group, based on their relative

abundance of clay. It was found that the depth of the low-clay and high-clay group only differed by 0.5 ft. Table 6.2 shows the mineralogy of the BEF-2 shale samples used in the indentation test and the corresponding fluids that they were exposed to. The large difference in the clay content between core samples taken at virtually the same depth again shows that the shale mineralogy can change rapidly within a short depth range. In order to study shale-fluid interactions and to screen drilling and fracturing fluids for compatibility, the mineralogy of the specific shale rock at the depth of interest needs to be determined very carefully. Figure 6.26 shows the ternary diagram of the relative abundance of quartz, carbonate and clay for the low-clay and high clay shales.

	Shale Type	
Fluid	Low clay shale	High clay shale
Brine	✓	✓
Brine + acetic acid (pH≈3)	✓	✓
Brine + Na_2CO_3 (pH≈11)	✓	✓
Brine + Na_2CO_3 (pH≈11) + 0.5 gpt choline chloride		✓
Brine + Na_2CO_3 (pH≈11) + 0.5 gpt TMAC		✓
Brine + Na_2CO_3 (pH≈11) + 0.5 gpt PC-1952		✓
Brine + Na_2CO_3 (pH≈11) + 0.5 gpt PC-1955		✓

Table 6.1: Test matrix of the change in Brinell hardness of BEF-2 after being exposed to various fluids at 175^{o}F.

Shale Type	Test Fluid	Normalized clay	Normalized Quartz	Normalized Calcite
Low clay	Brine, (brine + acetic acid), (brine + Na_2CO_3)	17.29%	15.39%	67.32%
High clay	Brine, (brine + acetic acid), (brine + Na_2CO_3)	37.50%	24.44%	38.06%
	Brine + Na_2CO_3 + 0.5 gpt choline chloride	53.04%	20.77%	26.22%
	Brine + Na_2CO_3 (pH ≈ 11) + 0.5 gpt TMAC	58.54%	19.42%	22.04%
	Brine + Na_2CO_3 (pH ≈ 11) + 0.5 gpt PC-1952	60.77%	15.65%	23.58%
	Brine + Na_2CO_3 (pH ≈ 11) + 0.5 gpt PC-1955	63.73%	17.23%	19.04%

Table 6.2: Mineralogy of the BEF-2 shale samples used in the indentation test and the corresponding fluids that they were exposed to.

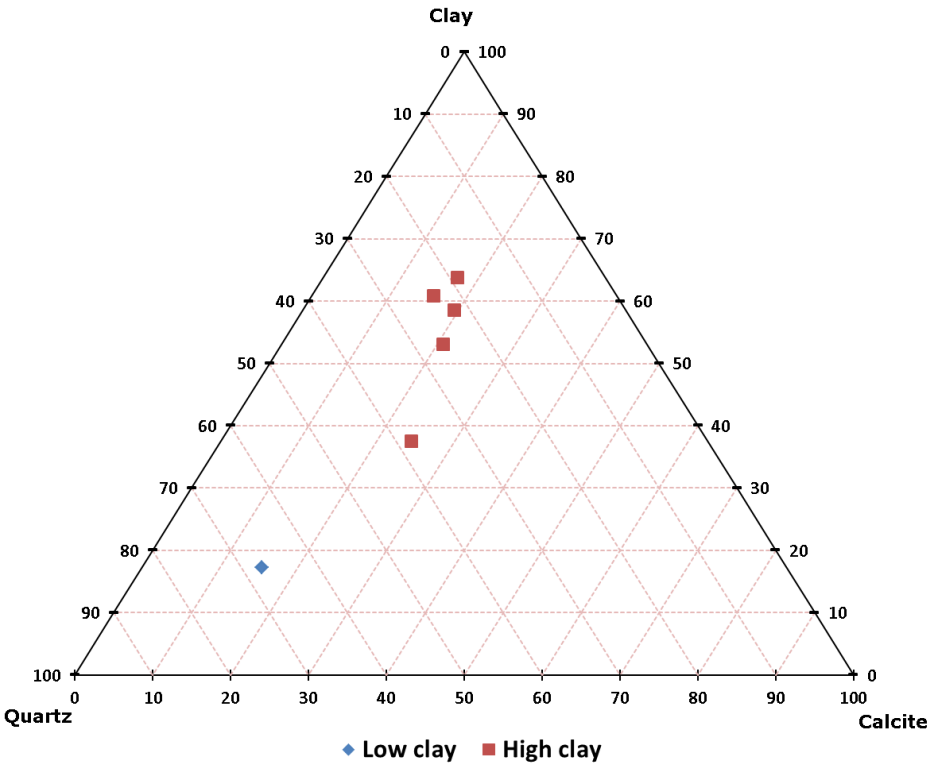

Figure 6.26: Ternary diagram of the relative abundance of quartz, carbonate and clay for the low-clay and high clay shales.

Figures 6.27 and 6.28 show the change in the absolute and normalized Brinell hardness of the low-clay BEF-2 shale after being exposed to the field brine, an acidic fluid and a high pH fluid for over 40 hours at 175°F. In general, a 10% – 20% reduction in the hardness of the BEF-2 shales was observed after 40 hours of fluid exposure. The slight increase in the hardness of the sample exposed to the acidic fluid was probably due to measurement variability. The low-clay samples experienced little softening when exposed to these water-based fluids. They were not very sensitive to fluid exposure. Meanwhile, fluid pH did not appear to have a big impact on the degree of softening with these shales.

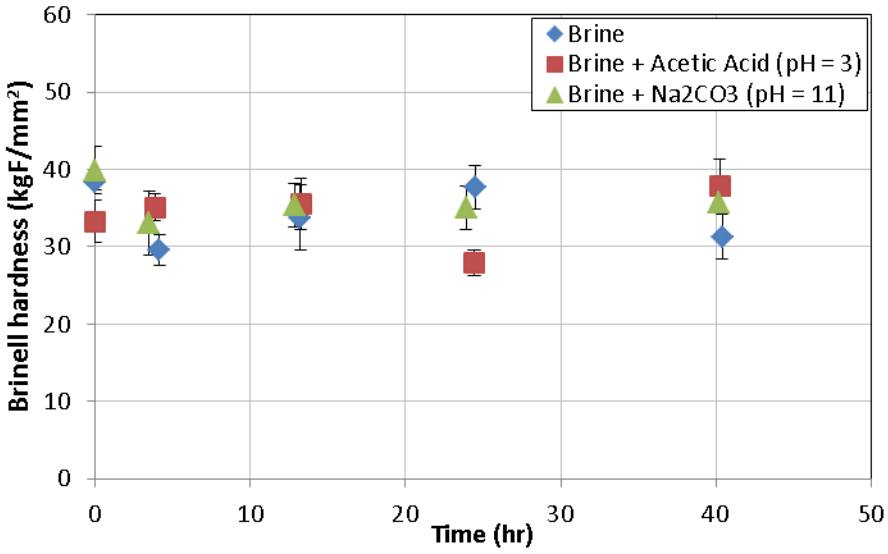

Figure 6.27: Change in the absolute Brinell hardness of the low-clay BEF-2 shale after being exposed to the field brine, an acidic fluid and a high pH fluid for over 40 hours at 175°F.

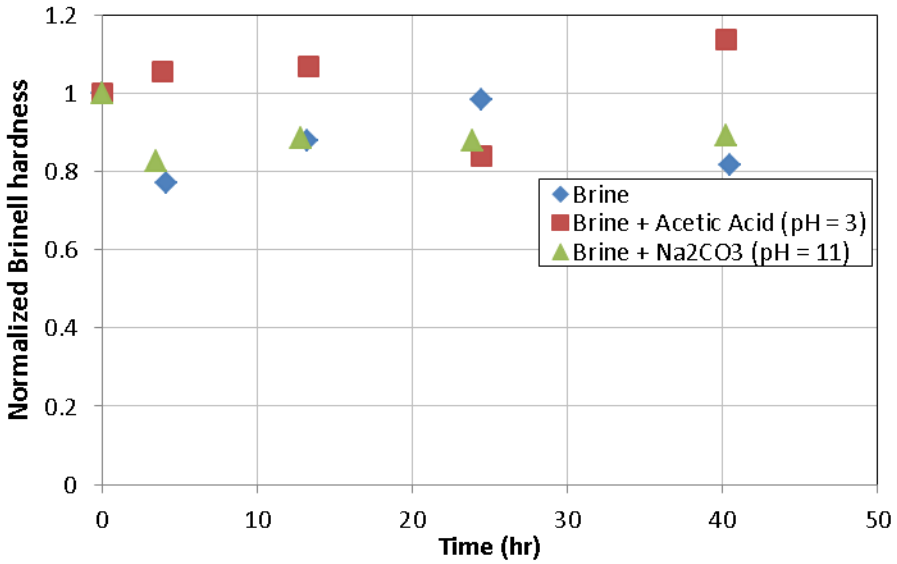

Figure 6.28: Change in the normalized Brinell hardness of the low-clay BEF-2 shale after being exposed to the field brine, an acidic fluid and a high pH fluid for over 40 hours at 175°F.

Figures 6.29 and 6.30 show the change in the absolute and normalized Brinell hardness of the high-clay BEF-2 shale after being exposed to the field brine, an acidic fluid and a high pH fluid for more than 40 hours at 175°F. The shale hardness declined exponentially with time. The hardness of the high-clay samples was reduced by about 60% after 40 hours of fluid exposure. This is three times the softening experienced by the low-clay samples. Therefore, clay content can significantly affect the change in shale hardness after exposure to water-based fluids. The effect of pH on shale softening was also more pronounced with these high-clay samples. After about 13 hours of fluid exposure, brine resulted in the least softening of the high-clay shale, reducing its hardness by 24%. In contrast, the acidic fluid and the high pH fluid reduced the hardness of the high-clay samples by 45% and 52% respectively. The impact of fluid pH on the hardness reduction was similar to the trend observed with the BUT shale in Section 6.3.2. Overall, the high-clay BEF-2 samples were more sensitive to exposure to water-based fluids than

the low-clay samples. Meanwhile, the effect of fluid pH on shale softening was also more significant with the high-clay samples.

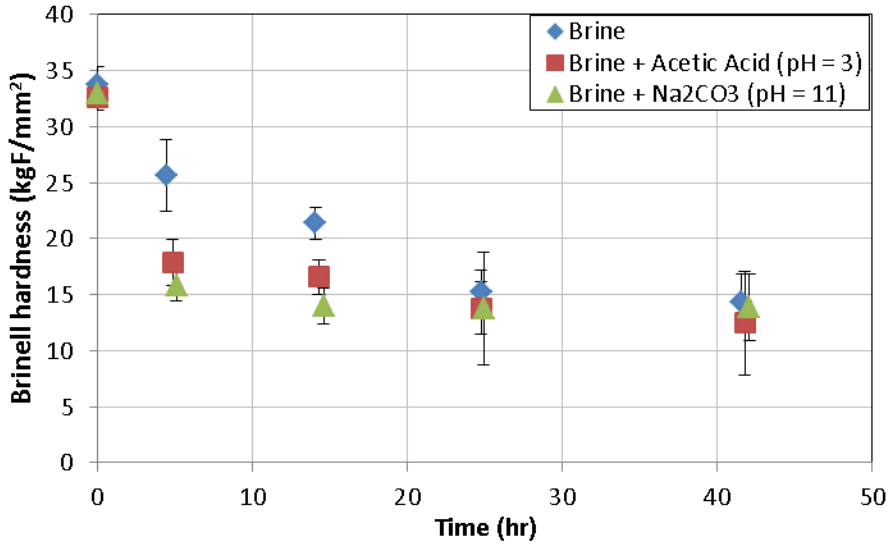

Figure 6.29: Change in the absolute Brinell hardness of the high-clay BEF-2 shale after being exposed to the field brine, an acidic fluid and a high pH fluid for over 40 hours at 175°F.

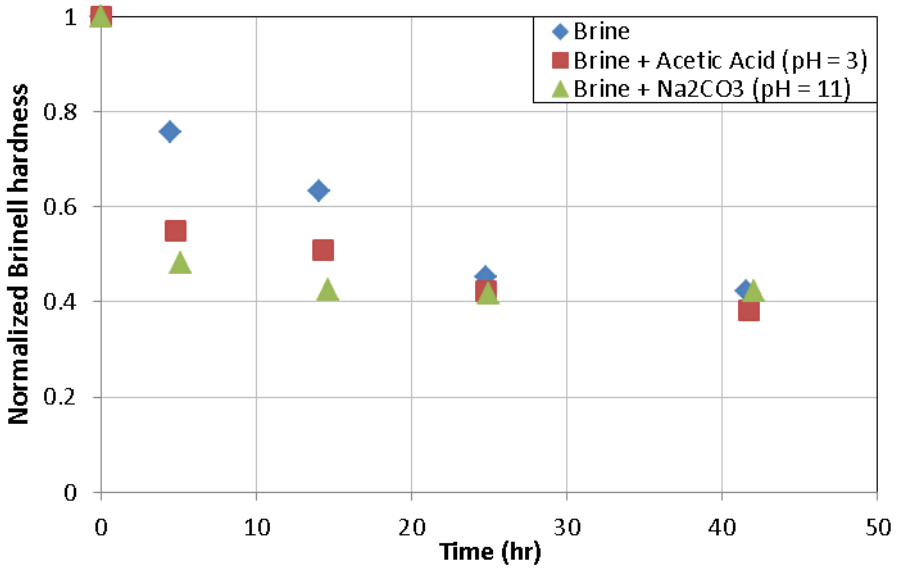

Figure 6.30: Change in the normalized Brinell hardness of the high-clay BEF-2 shale after being exposed to the field brine, an acidic fluid and a high pH fluid for over 40 hours at 175°F.

Since the high pH fluid resulted in the most softening of the BEF-2 shale, it was used as the base fluid subsequently together with various quaternary amine-based clay stabilizers. Figures 6.31 and 6.32 show the change in the absolute and normalized Brinell hardness of the BEF-2 shale after being exposed to the base high pH fluid and the fluid with various clay stabilizers for over 40 hours at 175^{o}F. It can be seen that most of the shale softening happened during the first 10 hours of fluid exposure, as the hardness of the samples stabilized afterwards. The use of the clay stabilizers did not help reduce the softening of the BEF-2 shale in a high pH environment, as the hardness of most samples were still reduced by about 60% after more than 40 hours of fluid exposure. Only PC-1955 showed some improvement with softening reduction, as the sample hardness was reduced by about 40% after over 40 hours of fluid exposure. One reason why choline chloride and TMAC were not able to mitigate shale softening was probably because the amount of these stabilizers added to the high pH fluid was very low. Patel (2009) pointed out that up to 3% of these monocationic amine additives were needed to stabilize shales. A concentration of 0.5 gpt, equivalent to 0.05% by volume, of these additives was probably too low to reduce shale softening. Moreover, these additives are known as temporary clay stabilizers, and their shale inhibition capability deteriorates with time. According to Braun (2004), choline chloride has a half-life of only 6.9 hours when exposed to the atmosphere. TMAC as a shale inhibitor also has temperature and pH limitations (Patel, 2009). These characteristics of choline chloride and TMAC might render them ineffective in reducing the softening behavior of the high-clay BEF-2 samples at high temperature and pH. The exact chemical composition of PC-1955 and PC-1952 were unknown as such information was proprietary. However, we do know that they are quaternary amines.

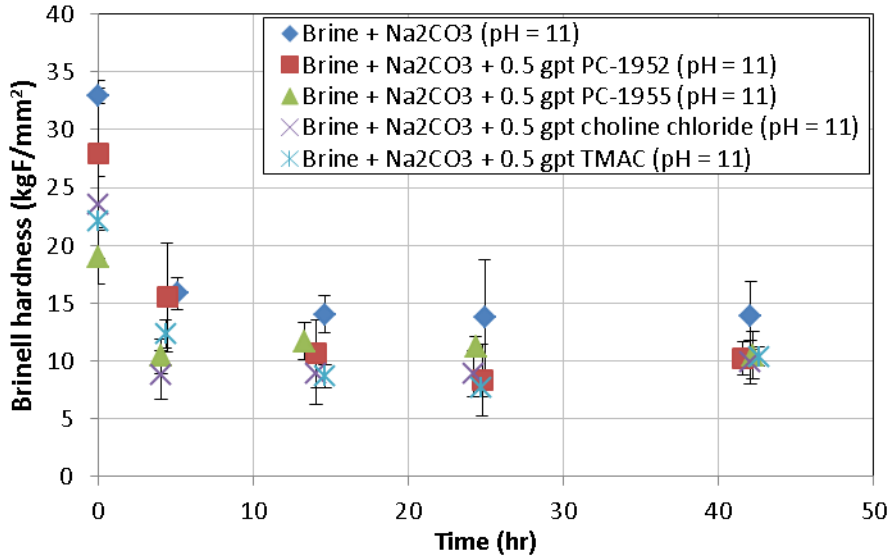

Figure 6.31: Change in the absolute Brinell hardness of the high-clay BEF-2 shale after being exposed to a high pH fluid and the fluid with various clay stabilizers for over 40 hours at 175°F.

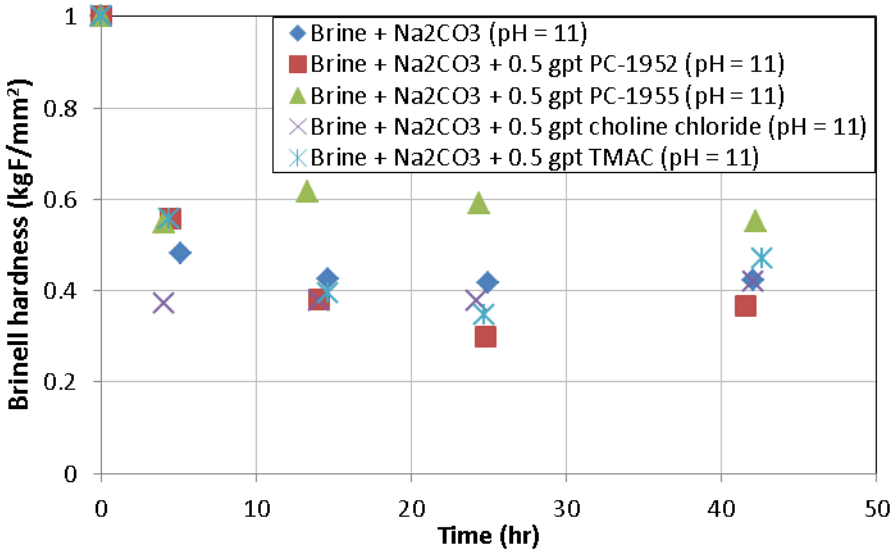

Figure 6.32: Change in the normalized Brinell hardness of the high-clay BEF-2 shale after being exposed to a high pH fluid and the fluid with various clay stabilizers for over 40 hours at 175°F.

Figure 6.33 shows a cross-plot of the change in normalized fracture permeability and change in normalized Brinell hardness of the BEF-2 shale after being exposed to various types of fluids. The fracture conductivity experiments were performed by Pratik Kakkar in our research group. The fracture permeability was measured at 175^{o}F and with a confining pressure of 5000 psi. Details of the experimental procedure can be found in Pedlow (2013) and Pedlow and Sharma (2014). The fracture permeability of fresh preserved cores was measured with nitrogen gas. The fractured cylindrical cores were then exposed to the testing fluids for a period of time and their permeability was re-measured with nitrogen to evaluate the reduction caused by unfavorable shale-fluid interactions. The fluids used in the fracture permeability measurement included brine, the high pH fluid, and the high pH fluid with 0.5 gpt TMAC, choline chloride, PC-1952 and PC-1955. The fracture permeability after fluid exposure was normalized against the permeability before fluid exposure.

It can be seen from Figure 6.33 that there was a large variation in the fracture permeability of the BEF-2 shale after fluid exposure. The greatest retained fracture permeability was almost one order of magnitude greater than that of the sample with the largest permeability reduction. On the other hand, the hardness of the samples was reduced by about 60% in all the cases. While shale softening is certainly one significant contributor to the decrease in fracture permeability, other factors such as fines generation and migration can have a greater impact on the fracture permeability reduction. Borchardt (1989) attributed a majority of the formation damage in clay-containing rock formations to fines mobilization as a result of the weakened cementing bond due to clay swelling that previously holds fines together. All the major shale minerals, which include silica, feldspar, calcite, swelling and non-swelling clays have been found to produce mobile fine particles that damage the permeability of clay-containing rocks.

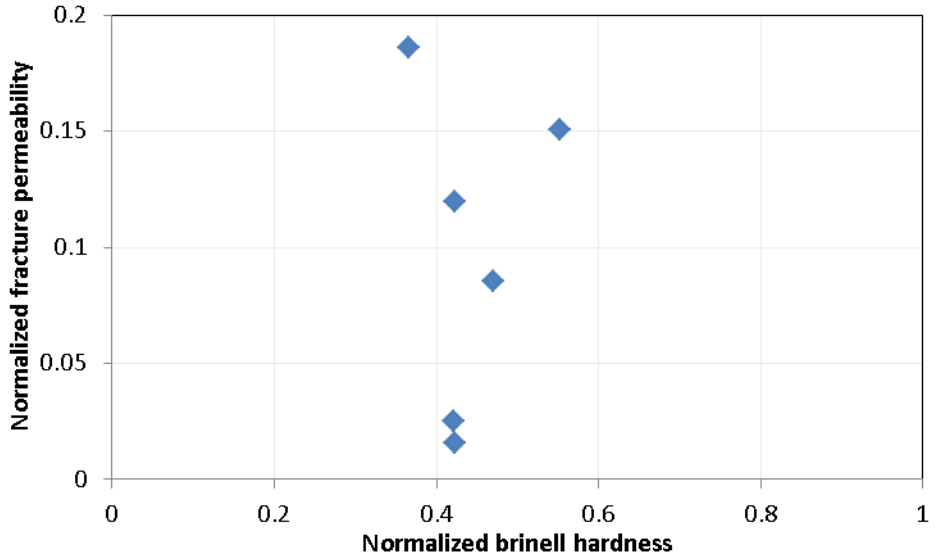

Figure 6.33: Cross-plot of change in normalized fracture permeability and change in normalized Brinell hardness of the BEF-2 shale after being exposed to various types of fluids.

To investigate the components of the mobile fines in the bulk fluid after the immersion of the BEF-2 samples, the inductively coupled plasma mass spectrometry (ICP-MS) was used to measure the concentration of metals in the fluid. Majority of the fines would not dissolve in the bulk fluid and would exist in solid form. However, the change in the concentration of metals could still be useful in identifying the specific minerals that produce fines. The concentrations of Ca and Mg in the high pH fluid with various clay stabilizers are shown in Figure 6.34. As expected, their concentrations were low because these metal ions can form precipitates with the CO_3^{2-} ions in the high-pH fluid. The original concentrations of Mg^{2+} and Ca^{2+} were 5 ppm and 48 ppm in the field water respectively, much higher than the concentrations shown in Figure 6.34.

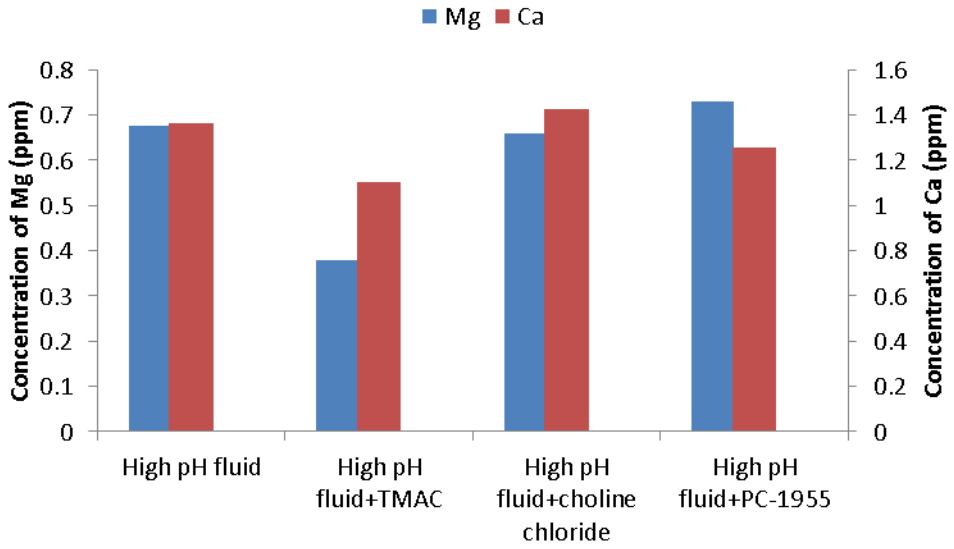

Figure 6.34: Concentrations of the Mg and Ca in the high pH fluid and the fluid with various quaternary amine-based clay stabilizers.

Figure 6.35 shows the concentration of the Al and Si in different fluids after the immersion of the BEF-2 samples. No Al was present in the acidic fluid, suggesting that the dissolved particles were not from the clay minerals. On the other hand, noticeable amount of Al and Si, especially Si, were present in the high pH fluid with various clay stabilizers. These metal ions could be from the fines produced from minerals such as clay and quartz. The fact that the concentration of Al was much greater in the high pH fluid without the clay stabilizers than that with the clay stabilizers suggests that the clay stabilizers were effective in reducing the mobilization of fines from the shale samples.

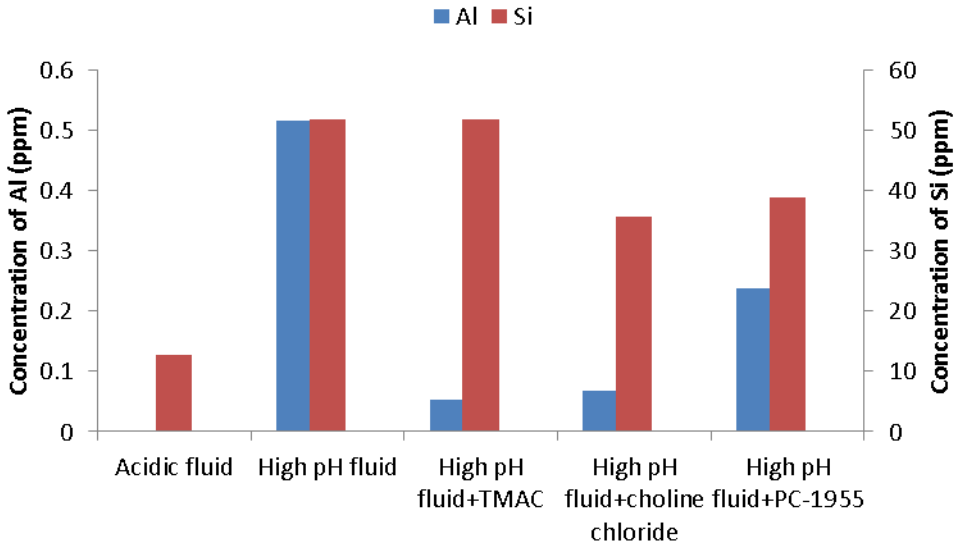

Figure 6.35: Concentrations of the Al and Si in the acidic fluid, the high pH fluid and the high pH fluid with various quaternary amine-based clay stabilizers.

Figures 6.36 – 6.38 show the cross-plots of the Brinell hardness and the relative abundance of clay, calcite and quartz of the BEF-2 shale before fluid exposure. It is evident that a good linear correlation exists between the shale hardness and the clay and calcite content. The shale hardness increased with the calcite content and decreased with the clay content. On the other hand, there is no good correlation between the hardness and the quartz content of the shale. Therefore, the shale mechanical properties such as the hardness are mainly affected by the clay and calcite content of the sample.

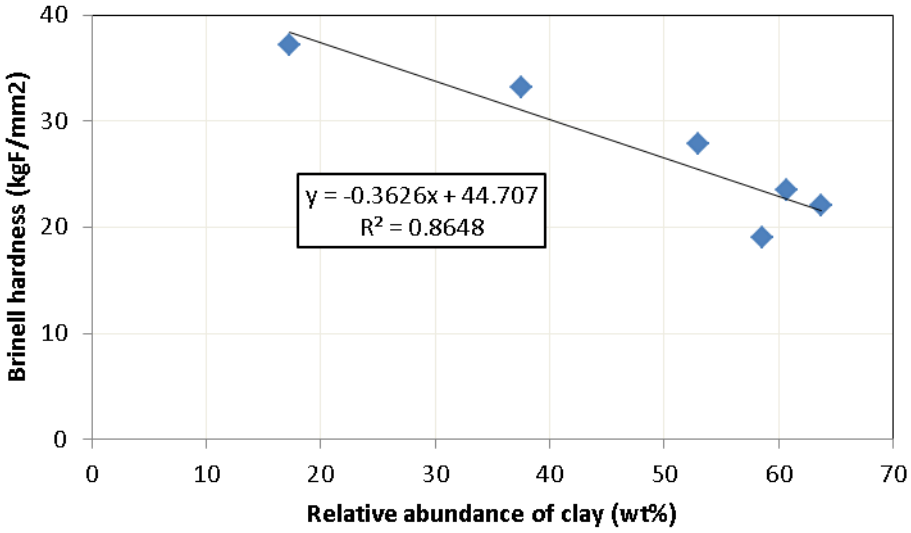

Figure 6.36: Cross-plot of the Brinell hardness and the relative abundance of clay of the BEF-2 shale before fluid exposure.

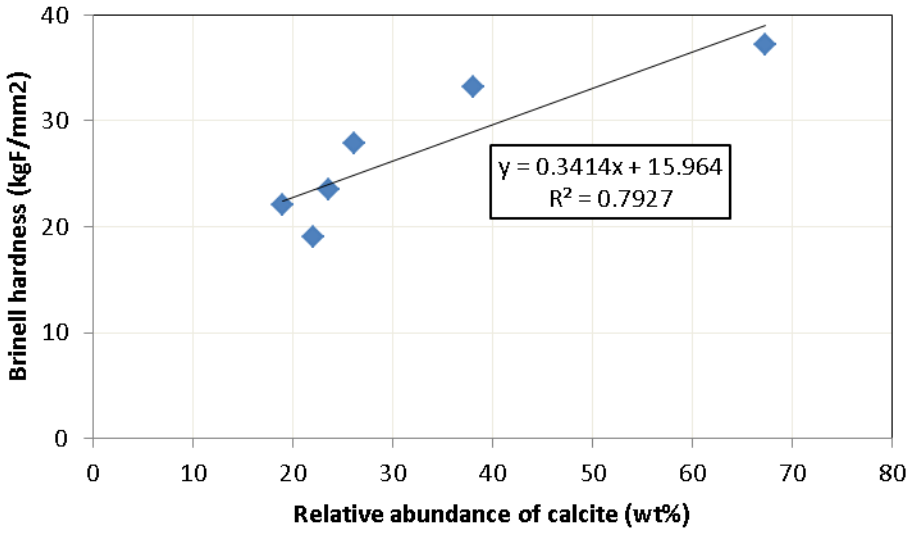

Figure 6.37: Cross-plot of the Brinell hardness and the relative abundance of calcite of the BEF-2 shale before being exposed to fluids.

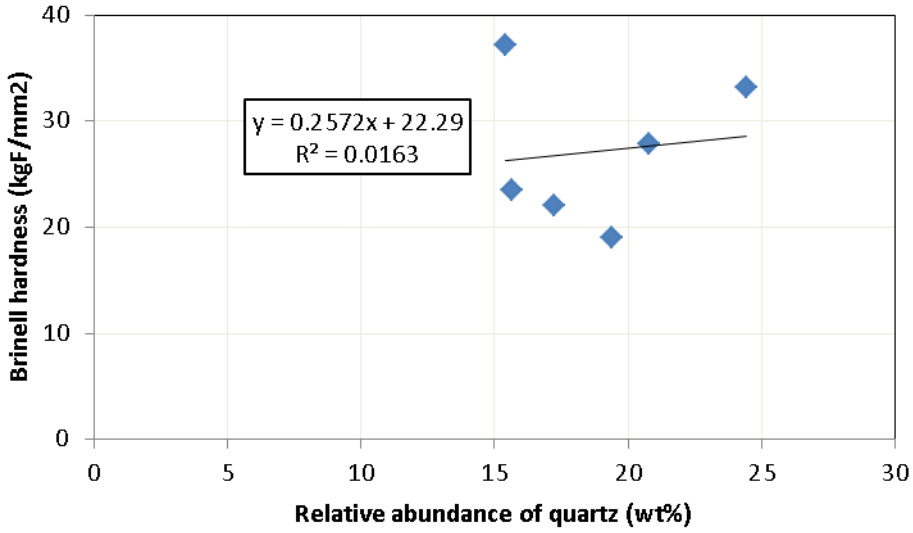

Figure 6.38: Cross-plot of the Brinell hardness and the relative abundance of quartz of the BEF-2 shale before being exposed to fluids.

Figures 6.39 – 6.41 show the cross-plots of the Brinell hardness and the relative abundance of clay, calcite and quartz of the BEF-2 shale before and after fluid exposure. The red points in Figures 6.39 and 6.40 represent the samples after exposure to the high pH fluid with 0.5 gpt TMAC, choline chloride, PC-1952 and PC-1955 clay stabilizers. The shale mineralogy could change after fluid exposure. Calcite dissolution might occur, which could reduce the relative abundance of calcite and increase the relative clay content. The fines mobilization could also alter the mineralogical makeup of the shale samples. It can be seen from Figures 6.39 and 6.40 that a good linear correlation still exists between the shale hardness and the clay and calcite content after fluid exposure. The exceptions are the samples exposed to the high pH fluid with the clay stabilizers. If these samples follow the linear trend, their hardness should have been higher. This suggests that other mechanisms rather than the alteration in the shale mineralogy might render the clay stabilizers ineffective in reducing the softening of the BEF-2 samples. On

the other hand, as Figure 6.38 shows, there was no good correlation between the shale hardness and the quartz content of the samples after fluid exposure.

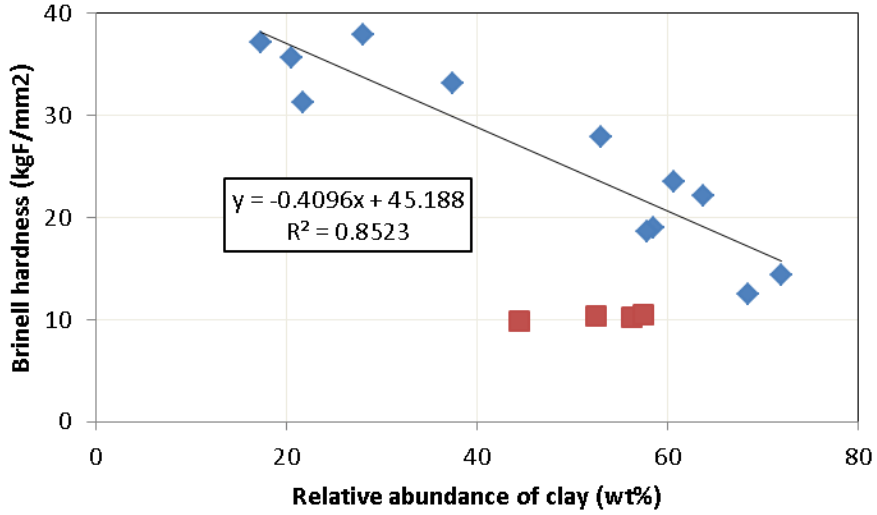

Figure 6.39: Cross-plot of the Brinell hardness and the relative abundance of clay of the BEF-2 shale before and after fluid exposure. Red represents the samples exposed to high pH fluids with the clay stabilizers.

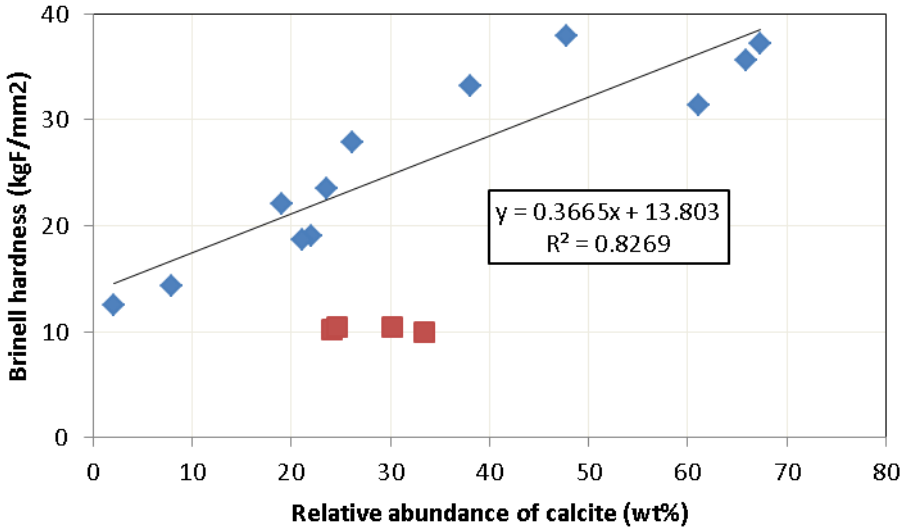

Figure 6.40: Cross-plot of the Brinell hardness and the relative abundance of calcite of the BEF-2 shale before and after fluid exposure. Red represents the samples exposed to high pH fluids with the clay stabilizers.

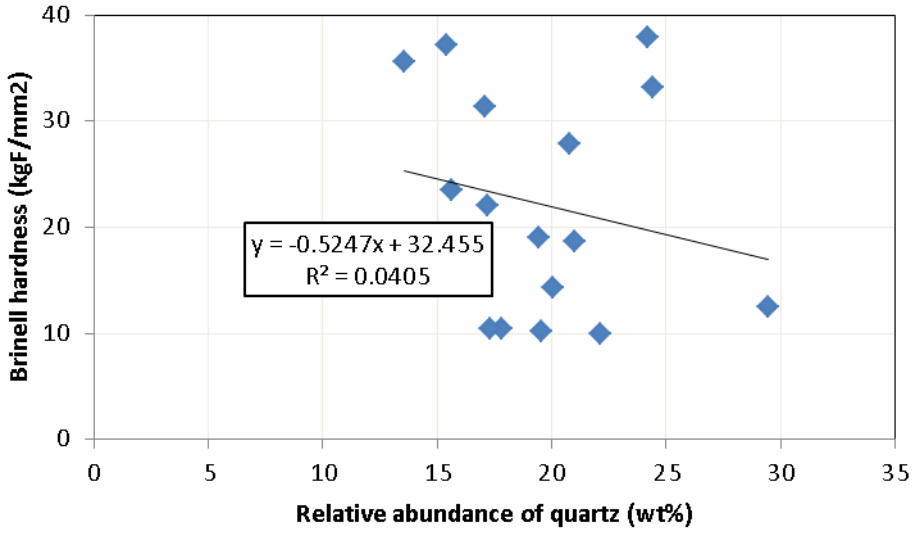

Figure 6.41: Cross-plot of the Brinell hardness and the relative abundance of quartz of the BEF-2 shale before and after fluid exposure.

6.3.4 Dynamic versus Static Young's Modulus

The relationship between the dynamic and static Young's modulus of the same sample at various stages of shale-fluid interactions was investigated using the acoustic wave velocity measurement and the indentation test. The TGS-F shale was exposed to 2% $CaCl_2$ brine while the BUT samples were immersed in various fracturing fluids. One inch cubic samples were used so as to facilitate the acoustic wave velocity measurement. All the measurements were performed on surfaces parallel to bedding planes at room temperature.

Figure 6.42 shows the comparison of the dynamic and static Young's modulus of the TGS-F shale exposed to 2% $CaCl_2$ for 24 hours. It can be seen that before and after fluid exposure, the dynamic Young's modulus was consistently higher than the corresponding static indentation Young's modulus. Similar trend was also observed on the BUT shale samples exposed to Solution 1 up to four days and brine and Solutions 1, 2

and 4 over a month respectively, as shown in Figures 6.43 and 6.44. Figure 6.45 shows the cross-plot of the dynamic and static Young's modulus of these TGS-F and BUT samples exposed to these water-based fluids. The gray dotted line represents the one-to-one correspondence of the two moduli. The data points always lie above the gray dotted line, again indicating the dynamic moduli were consistently higher than the static moduli. This is because of the viscoelastic nature of the rocks. Similar correlation between the dynamic and static moduli of shale rocks was also reported by Kumar et al. (2012). However, Kumar et al. (2012)'s measurements were performed on native shale samples, and the degree of shale preservation was not discussed.

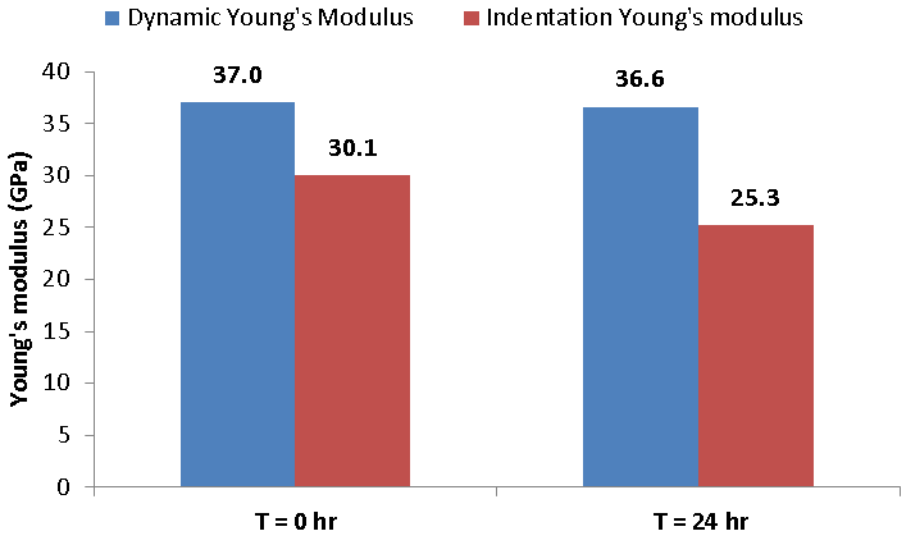

Figure 6.42: Comparison of the dynamic and static Young's modulus of the TGS-F shale exposed to 2% $CaCl_2$ for 24 hours.

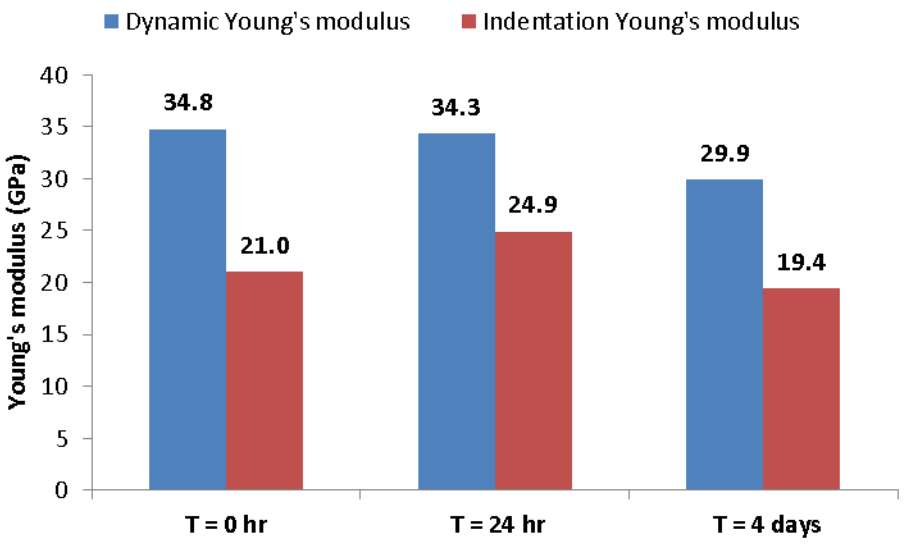

Figure 6.43: Comparison of the dynamic and static Young's modulus of the BUT shale exposed to Solution 1 for four days.

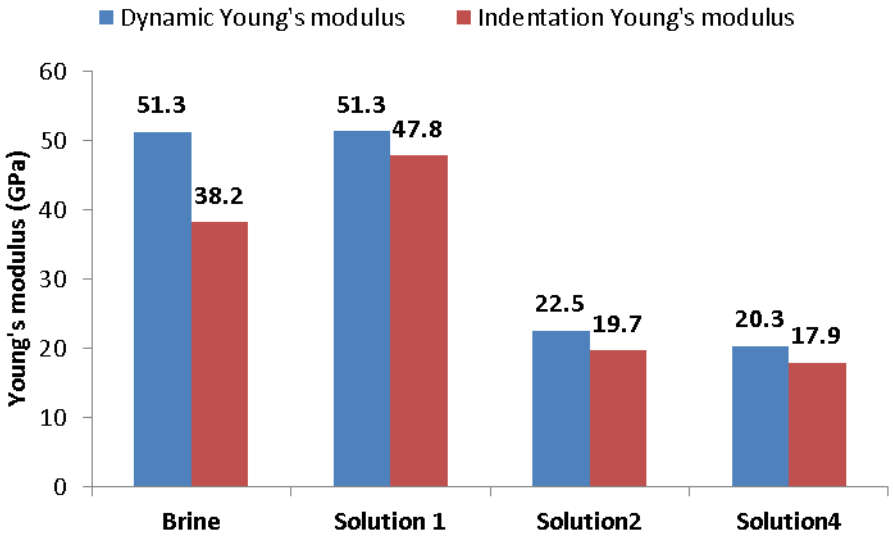

Figure 6.44: Comparison of the dynamic and static Young's modulus of the BUT shale exposed to brine, Solutions 1, 2 and 4 for over a month.

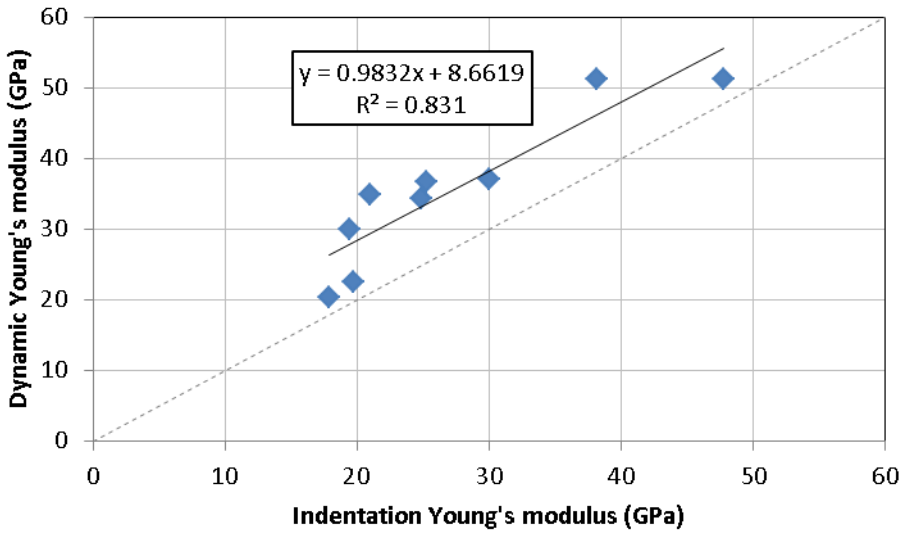

Figure 6.45: Cross-plot of the dynamic and static Young's modulus of the TGS-F and BUT shales exposed to various types of water-based fluids.

6.3.5 Fracture Width and Conductivity

As shale softens after coming into contact with water-based fracturing fluids, proppant embedment will occur, causing reductions in both fracture width and conductivity. The effect of shale softening on the decrease in fracture width and conductivity is quantified in this section.

Figure 6.46 shows a schematic picture of the embedment of one proppant particle on the fracture face. The shaded volume represents the part of the proppant that is embedded in the shale. If we assume the proppant is a rigid spherical with a diameter of d_p and the packing of proppant in the fracture is a cubic close pack, the number of proppant particles per square inch, N, can be calculated as:

$$N = \frac{1}{d_p^2} \tag{6.1}$$

If σ is the confining stress, the force exerted on one side of one proppant particle, F, can be expressed as:

$$F = \frac{\sigma}{N} = \sigma d_p^2 \tag{6.2}$$

According to Eq. 3.5, the Brinell hardness (BHN) of a shale is a function of the load and the corresponding depth of penetration. Therefore, the depth of penetration d on one side of the fracture face can be calculated as:

$$d = \frac{F}{\pi d_p BHN} = \frac{\sigma d_p}{\pi BHN} \tag{6.3}$$

If there are n layers of proppant in the fracture, the width of the fracture w_f after proppant embedment can be expressed as:

$$w_f = nd_p - 2d = nd_p - \frac{2\sigma d_p}{\pi HBN} \tag{6.4}$$

The fracture conductivity is commonly defined as the product of the fracture permeability and the fracture width. To calculate the fracture permeability using the Carman-Kozeny equation, the porosity of the proppant pack needs to be determined. The porosity of cubic packing without embedment is 47.6%. To calculate the porosity of the proppant pack with embedment on the fracture face, the volume of the spherical cap embedded into the fracture face is expressed as:

$$V_{cap} = \frac{1}{3}\pi d^2 (3R - d) = \frac{1}{3}\pi d^2 \left(\frac{3d_p}{2} - d \right) \tag{6.5}$$

The porosity ø of the proppant pack can be calculated as:

$$\phi = 1 - \frac{\frac{4}{3} n\pi \left(\frac{d_p}{2} \right)^3 - 2V_{cap}}{d_p^2 \left(nd_p - 2d \right)} \tag{6.6}$$

Using the Carman-Kozeny equation, the fracture permeability k_f is expressed as:

$$k_f = \frac{\phi^3 d_p^2}{72(1-\phi)^2 \tau} \tag{6.7}$$

Here τ is the tortuosity of the porous media. For simplicity, it is taken as unity in the calculations in this section. Combining Eq. 6.4 and Eq. 6.7, the fracture conductivity can be calculated as:

$$F_c = k_f w_f = \frac{\phi^3 d_p^2}{72(1-\phi)^2 \tau}\left(nd_p - \frac{2\sigma d_p}{\pi HBN}\right) \tag{6.8}$$

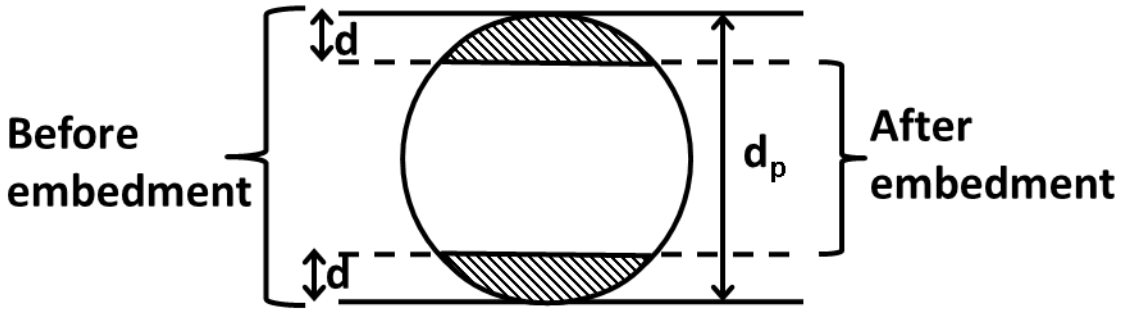

Figure 6.46: Schematic picture of the embedment of one proppant particle on the fracture face.

Figures 6.47 – 6.49 show the fracture width and conductivity as a function of confining stress for a monolayer, three layers and five layers of proppant in the fracture. Three shale hardness states, namely BHN = 50 kgF/mm^2, 30 kgF/mm^2 and 10 kgF/mm^2, are used in these calculations. As expected, the fracture width and conductivity decrease with increasing confining stress regardless of the hardness of the shale. It can be seen from the plots that the fracture width decreases more rapidly with increasing confining stress when the shale is softer, indicating a more severe proppant embedment problem. Similarly, the fracture conductivity damage is also greater with softer shales. However, unlike the linear relationship between the fracture width and confining stress, the fracture conductivity reduces exponentially with increasing confining stress.

To understand the effect of shale softening on the reduction in fracture width and conductivity, a confining stress of 8000 psi is used as an example. When the shale Brinell hardness decreases from 50 kgF/mm^2 to 10 kgF/mm^2, the fracture width decreases from 0.279 mm to 0.193 mm for the case of a monolayer of proppant. This is equivalent to 30.9% reduction in fracture width. In comparison, the fracture width is reduced by 9.8% and 5.8% respectively when there are three and five layers of proppant in the fracture respectively. It is evident that shale softening has a much greater impact on the fracture width reduction when the proppant pack is monolayer rather than multilayer. Similarly, for a monolayer proppant pack, when the shale Brinell hardness decreases from 50 kgF/mm^2 to 10 kgF/mm^2, the fracture conductivity decreases from 314 md·ft to 58 md·ft, equivalent to an 81.5% reduction in fracture conductivity. In comparison, the fracture conductivity is reduced by 30.9% and 18.8% respectively with the same degree of shale softening for three and five layers of proppant. Therefore, it is clear that shale softening can be very detrimental to fracture conductivity, especially with monolayer coverage of proppant in the fracture. Methods and techniques that can mitigate shale softening after fluid exposure will greatly help sustain the fracture conductivity.

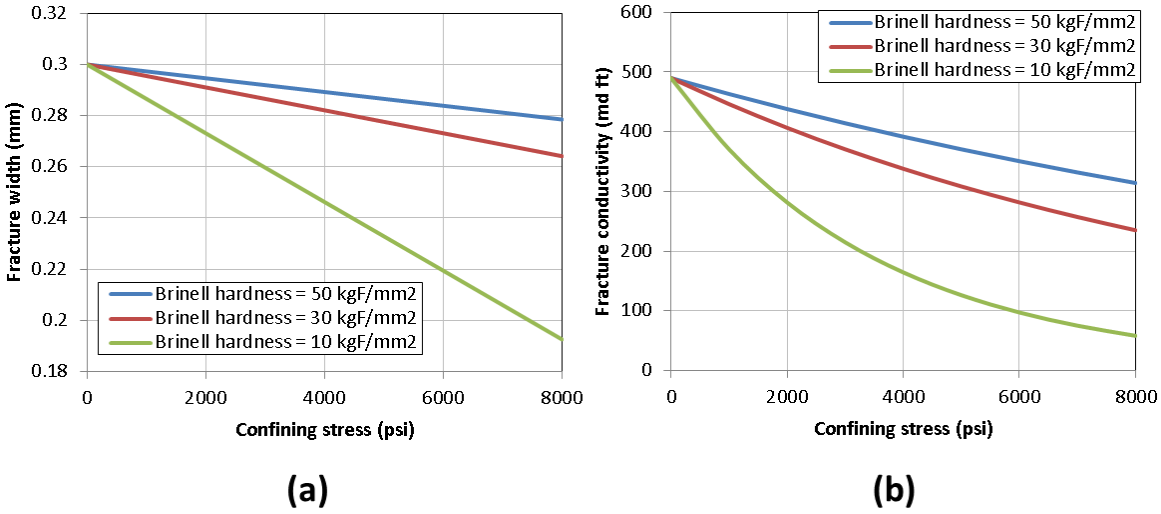

Figure 6.47: (a) Fracture width and (b) conductivity as a function of confining stress for a fracture with monolayer coverage of proppant.

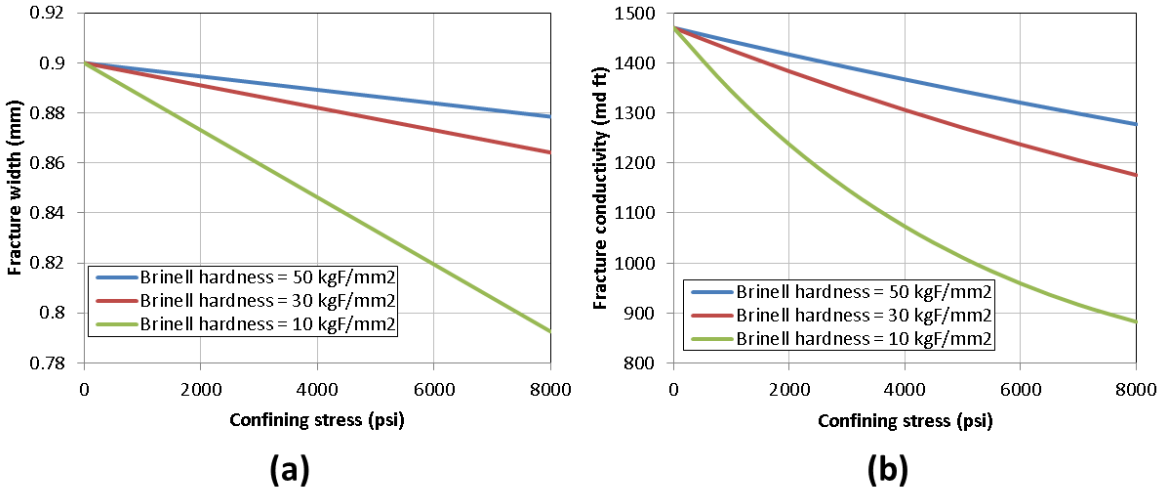

Figure 6.48: (a) Fracture width and (b) conductivity as a function of confining stress for a fracture with three layers of proppant.

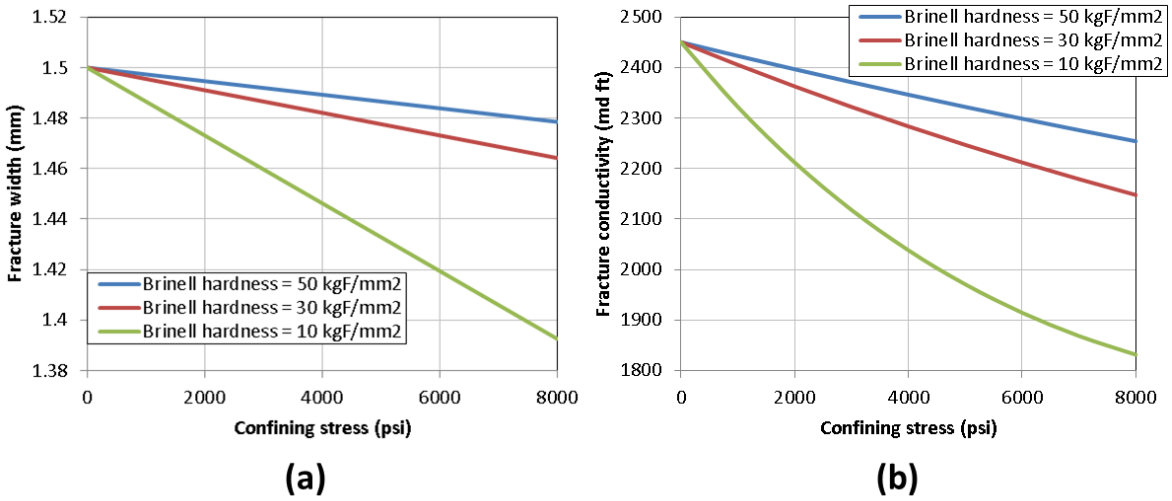

Figure 6.49: (a) Fracture width and (b) conductivity as a function of confining stress for a fracture with five layers of proppant.

Figure 6.50 shows the cross-plot of measured fracture permeability damage and calculated fracture permeability damage due to proppant embedment alone. The fracture permeability was measured at 175^{o}F and with a confining stress of 5000 psi. The theoretical fracture permeability damage was calculated based on the monolayer coverage of proppant arrangement. The much greater fracture permeability damage observed during the fracture conductivity experiment again suggests that mechanisms other than proppant embedment are contributing to the fracture conductivity damage after shale's contact with water-based fluids.

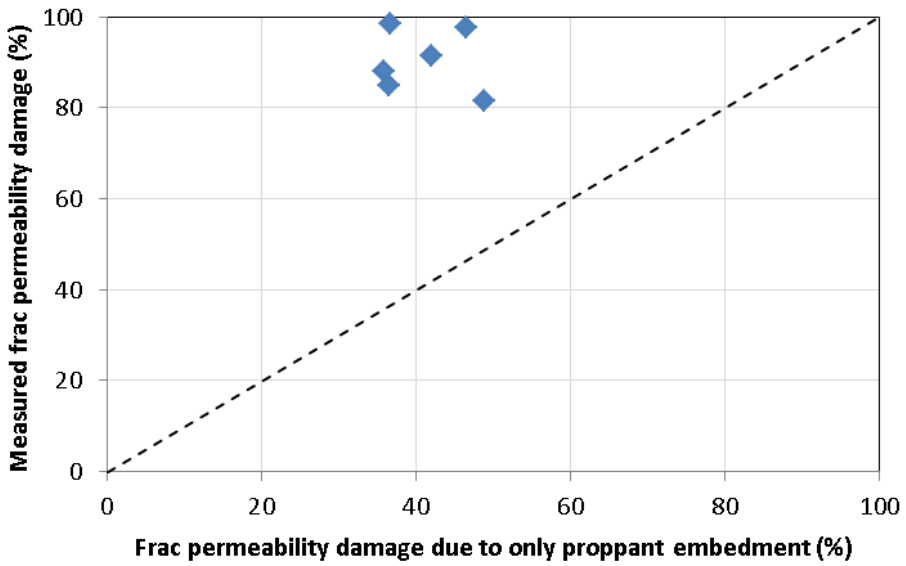

Figure 6.50: Cross-plot of measured fracture permeability damage and calculated fracture permeability damage due to proppant embedment alone.

6.4 CONCLUSIONS

In this chapter, the change in the mechanical properties of organic-rich shales after exposure to various water-based fracturing fluids was investigated using the indentation test. The effect of shale mineralogy, temperature, fluid pH and clay stabilizers on the reduction in shale hardness and Young's modulus after fluid exposure was examined.

Very little water movement was observed in the desiccator test. Less than 0.5 wt% of the water was removed from shale samples when the humidity was decreased from 96% to 50.5%. This was probably due to the small permeability of the shale. The shale hardness and Young's modulus were found to both increase. with water removal and decrease when water was added to shale samples. The change in the Young's modulus of shale was greater than the corresponding change in the hardness when water movement occurred. Shale samples with higher clay content experienced greater change

in mechanical properties when water movement happened. A reversible change in the shale mechanical properties was observed with low-clay shale while the change was irreversible when the clay content was high. The shale mechanical stability could be improved if more water could be removed from samples.

When shale samples were in contact with various water-based fracturing fluids, the fluid pH and temperature had a significant impact on the change in the mechanical properties. High-pH fluids could cause the most reduction in shale mechanical stability. Shale softening was also found to be more severe at high temperature. On the other hand, the shale with the higher clay content experienced greater hardness reduction when exposed to water-based fracturing fluids. The effect of pH on shale softening was also more pronounced with high-clay samples.

A good linear correlation was established between the shale hardness and Young's modulus. The Young's modulus tends to change more rapidly than the hardness as a result of fluid exposure. A good linear correlation also existed between the dynamic Young's modulus from the acoustic wave velocity measurement and the static modulus from the indentation test.

The impact of proppant embedment on fracture width and conductivity damage in shales was found to be the most severe with monolayer coverage of proppant in fractures. However, a comparison between the measured fracture permeability damage and the calculated fracture permeability damage due to proppant embedment alone show that proppant embedment is only partially responsible for fracture conductivity damage. The larger reduction in fracture permeability during the conductivity experiments indicates that mechanisms such as fines mobilization might be a more dominant factor than proppant embedment for controlling fracture permeability reduction. The fact that a noticeable amount of Al and Si was found in the bulk fluid suggests that fines from clay

and quartz were removed from the shale rock after the samples were exposed to water-based fluids.

The change in shale mechanical properties after fluid exposure can be used to screen drilling and fracturing fluids for their compatibility. The troublesome shales can be identified with this series of measurements. The shale that experiences large mechanical stability reduction after fluid contact is likely to encounter more problems during drilling and fracturing. More extensive testing with shale inhibitors should be planned for such shale to evaluate their performance for enhancing wellbore stability and reducing fracture conductivity damage. Meanwhile, the fracturing fluid that results in the least damage to shale mechanical stability should be preferred if it satisfies the criteria for other fluid properties. Together with other shale properties such as mineralogy and swelling behavior, the change in mechanical properties after fluid exposure gives us the first insight into the reactivity of shale with water-based fluids and allows us to develop solutions to counter the adverse effects of shale-fluid interactions during field operations.

Chapter 7: Conclusions and Future Work

7.1. CONCLUSIONS

Horizontal drilling and hydraulic fracturing are two key technologies that have helped propel the shale revolution in the U.S. and other parts of the world. The interactions of organic-rich shale with water-based drilling and fracturing fluids play a critical role in the success of these operations, ultimately affecting the well productivity. In this dissertation, the unique properties of shale and their characterization techniques are reviewed. The shale swelling mechanisms and their impact on wellbore stability and proppant embedment in fractures are discussed. A systematic approach to the characterization of shale petrophysical and mechanical properties is developed to study shale-fluid interactions and screen drilling and fracturing fluids for their compatibility.

XRD and XRF were employed to measure shale mineralogy and were shown to yield consistent results. This shows that the elemental composition obtained with the XRF measurement can accurately quantify the shale mineralogy. A large variation in shale mineralogy was observed for samples from different plays in the U.S. Even the mineralogy of samples from the same well can vary significantly at different depths. Hence, detailed mineralogical studies are needed for understanding the correlation with other shale properties and shale-fluid interactions. The quartz, calcite and clay content of the Utica shale was shown to have a good linear correlation with depth.

Simultaneous NMR T_1-T_2 measurements were performed on preserved shale samples to distinguish the pore fluids based on their viscosity and the associated pore size. The T_1/T_2 ratio is a good indication of the pore fluid viscosity while the T_2 secular relaxation time reflects the pore size. A good correlation was observed between the total clay content and the porosity attributed to small pores containing low viscosity fluid, indicating that the water-saturated microporosity was in clay minerals.

N_2GA (nitrogen gas adsorption) and MICP (mercury injection capillary pressure) were jointly utilized to construct the complete pore size distribution of low porosity and ultra-low permeability shales. Most of the shale pores were in the micropore to mesopore range. Desorption hysteresis was observed with all shale samples, indicating the pore blockage phenomenon during desorption caused by the presence of ink-bottle type of pores. Sample compressibility effect was demonstrated with large peaks in the small mesopore range and a greater fraction of small pores detected with MICP than with N_2GA.

The transverse surface relaxivity was calculated by peak matching the NMR T_2 distribution curve and the combined pore size distribution curve from N_2GA and MICP. It was shown to have a good correlation with the total clay content, suggesting the presence of paramagnetic ions in the clay mineral.

Gravimetric tests, swelling tests, and mechanical property measurements were performed systematically to study shale-fluid interactions after samples were exposed to various water-based fluids. Overall, the organic-rich shales were shown to be only slightly water-sensitive, as little changes in weight and mechanical properties were observed after the samples were brought into contact with water-based fluids. The degree of shale swelling was also very small.

The salt concentration and the difference in water activity of the bulk fluid and the shale sample were shown to play an important role in the ion and water movement when shale comes to contact with water-based fluids. Since shales usually act like leaky membranes permitting the transfer of ions across it, the bulk fluid with a higher salt concentration tends to drive more ions into the shale because of the large ionic potential between the shale and the bulk fluid. Meanwhile, water will be removed from the shale if an osmotic potential arises when the water activity of the sample is greater than that of

the fluid. Increasing the salt concentration in the bulk fluid further lowers its water activity, causing a larger amount of water to be removed from the sample. This forms the basis of enhancing shale stability through the addition of salts such as KCl and NaCl. On the other hand, if the shale sample is not well preserved, its low water activity tends to trigger the inflow of water into the shale matrix.

The degree of swelling experienced by all organic-rich shale samples in this study was less than 0.2% perpendicular to bedding planes. This is probably due to diagenesis that transformed the expandable smectite clays into the less reactive illite clays. The degree of swelling behavior was consistent with the sample weight change after shale-fluid contact. Anisotropic swelling, where the samples swelled perpendicular to bedding planes and shrank parallel to bedding planes, was observed. This type of swelling behavior was probably caused by the preferential layering of the clay platelets perpendicular to bedding planes.

The mechanical properties measurements revealed that the mechanical stability of shales generally decreased after exposure to water-based fluids. However, the reduction in Brinell hardness, acoustic wave velocities and the Young's modulus was not significant, indicating that the samples were only slightly sensitive to fluid exposure. On the other hand, the unpreserved shale sample experienced a greater change in weight and mechanical properties than the preserved sample after fluid contact. This demonstrates the importance of using preserved shale samples for studying shale-fluid interactions and screening drilling and fracturing fluids for their compatibility. Proper handling and preservation of shale cores in the well-site and in the laboratory are extremely crucial in obtaining the in-situ properties of shale downhole.

The indentation test was used to investigate the change in mechanical properties of organic-rich shales after exposure to various water-based fracturing fluids. Less than

0.5 wt% of water was removed from shale samples when the humidity was decreased from 96% to 50.5%. This was probably due to the small reactivity and permeability of these shales. The shale hardness and Young's modulus were both observed to decrease with water addition and increase with water removal in desiccator tests. The change in the Young's modulus of shale was greater than the corresponding change in the hardness when water movement occurred. A much greater change in mechanical properties was observed with high-clay shale samples than with low-clay samples when water was added or removed. The change in mechanical properties was reversible with low-clay shale and was irreversible when the clay content was high. These results show that shale mechanical stability could be improved if more water could be removed from samples.

The shale mineralogy, fluid pH and temperature were shown to have a significant impact on the reduction in shale hardness and Young's modulus after fluid exposure. High-pH fluids caused the most reduction in shale mechanical stability. This was due to the excess negative charges on the crystal lattice of clay. The dissolution of calcite with acidic fluids also caused a significant reduction in shale hardness. Shale softening was found to be much more severe at high temperature. High clay content shales are more prone to hardness reduction than low-clay shale when exposed to water-based fracturing fluids. The effect of pH on shale softening was also more pronounced with high-clay samples.

Shale hardness was found to increase with calcite content and decrease with clay content. A good linear correlation was also established between the hardness and Young's modulus. This suggests that both hardness and Young's modulus were affected by the alteration of shale mineralogy. The Young's modulus tends to change more rapidly than the hardness as a result of fluid exposure. A good linear correlation also existed

between the dynamic Young's modulus from the acoustic wave velocity measurement and the static modulus from the indentation test.

The reduction in shale hardness was expected to correlate with a reduction in fracture conductivity. However, when such a comparison was made with fracture conductivity tests, the damage to the shale fracture conductivity was uncorrelated with the reduction in hardness. This indicates that mechanisms other than proppant embedment might be the dominant factor for fracture permeability reduction. The fact that a noticeable amount of Al and Si was found in the bulk fluid suggests that fines from clay and quartz minerals were removed from the shale after the samples' exposure to water-based fluids.

The shale petrophysical and mechanical properties are very important parameters for formation evaluation and the design and optimization of drilling and fracturing operations. The systematic approach to shale characterization presented in this dissertation improved our understanding of shale petrophysical properties and the impact of shale-fluid interactions on its mechanical stability. The shale mineralogy directly affects the porosity, permeability and the reduction in shale mechanical stability after fluid exposure. The pore size distribution measured with N_2GA and MICP can be used to model shale permeability. The successful use of XRF for elemental analysis of shale and NMR for pore fluid distribution interpretation indicates the potential for such tools to be used for a relatively rapid evaluation of preserved shale core samples. The handheld XRF has already been used in the field for rapid mineralogy studies of shale cores and cuttings.

The primary objective of performing these mechanical property measurements was to screen drilling and fracturing fluids for their compatibility with a particular shale. The effectiveness of shale inhibitors in mitigating the reduction in shale stability can also be evaluated with these tests. If the reduction in shale mechanical stability is minimal

with a particular fluid system, it is likely that the fluid system is compatible with the shale. If a shale is found to be sensitive to fluid exposure, further testing needs to be conducted to investigate the degree of damage and to develop solutions to counter the adverse effects. The native shale mechanical properties and the change in these properties after exposure to water-based fluids offer valuable insights for hydraulic fracturing design and optimization. The change in shale hardness contributes to the reduction in fracture width and conductivity. The mechanical properties are usually input parameters in fracture simulators. The effect of shale-fluid interactions on the well productivity decline can also be represented by reductions in the shale hardness and Young's modulus.

7.2. FUTURE WORK

This dissertation presents a systematic approach to characterize shale petrophysical properties and to measure changes in the mechanical properties after shales are brought into contact with fluids. Together these measurement techniques enhance our capability to evaluate reservoir quality and optimize drilling and fracturing design. Some recommendations for future research related to this dissertation are described below:

1. The cutoff values of the T_1/T_2 ratio and T_2 secular relaxation for shale porosity quantification are still preliminary. Characterization of the NMR T_1-T_2 response of different hydrocarbons is needed to better understand the effect of fluid viscosity and other factors on the T_1 and T_2 relaxation time. Shale porosity and fluid saturation need to be measured independently to validate the methodology. Meanwhile, the NMR measurements presented in this dissertation were performed at room temperature. The effect of temperature on the T_1-T_2 response of preserved shale samples should also be investigated. Fluid movement into and out of shale

can also be quantified with the NMR T_1-T_2 measurements before and after shale's exposure to water-based fluids.

2. Natural shale core samples from the field were used to study the change in shale mechanical properties after fluid exposure. To better understand the effect of fluid exposure on the mechanical stability of individual minerals, synthetic homogenous mineral samples such as quartz and different types of clay can be used. Furthermore, the shale mechanical properties were measured at ambient conditions. The effect of stress on the reduction in shale mechanical properties as a result of fluid exposure can also be investigated.
3. Since fines mobilization was postulated to be the main cause for fracture conductivity damage when shale comes into contact with water-based fluids, more extensive characterization on the fines and solutes collected in the effluent and the fines recovered at the end of the fracture conductivity measurement should be performed. ICP-MS can be used to identify the origins of the fines dissolved in fluids. The elemental composition of the solid fines measured with XRF can also be used to determine their identity. The development of more effective permanent inhibitors to stabilize fines and reduce shale softening is of great interest to the petroleum industry and needs to be continued.

References

Ali, S.A., England, K.W., Waters, G. 2011. Methods of Stabilizing Shale Surface to Minimize Proppant Embedment and Increase Proppant-Pack Conductivity. U.S. Patent 13/091,741, April 21.

Alramahi, B., Sundberg, M.I. Proppant Embedment and Conductivity of Hydraulic Fractures in Shales. 2012. ARMA 12-291 presented at the 46th US Rock Mechanics/Geomechanics Symposium in Chicago, June 24 – 27.

American Petroleum Institute (API). 1998. Recommended Practices for Core Analysis. Recommended Practice 40. 2nd edition. Dallas, TX: API.

Anderson, R.L., Ratcliffe, I., Greenwell, H.C., Williams, P.A., Cliffe, S., Coveney, P.V. 2010. Clay Swelling – A Challenge in the Oilfield. *Earth-Science Reviews,* 98 (3-4): 201-216.

Atkinson, H. 1993. Hardness Tests for Rock Characterization. *Comprehensive Rock Engineering. Principles, Practice & Projects*, 3: 105-117.

Barrett, E.P., Joyner, L.G., Halenda, P.P. 1951. The Determination of Pore Volume and Area Distributions in Porous Substances. I. Computations from Nitrogen Isotherms. *Journal of the American Chemical Society*, 73 (1): 373-380.

Ballard, T.J., Beare, S.P., Lawless, T.A. 1994. Fundamentals of Shale Stabilization: Water Transport through Shales. *SPE Formation Evaluation*, 9: 129-129.

Bates, R.L., Jackson, J.A. 1984. *Dictionary of Geological Terms*. NY: American Geological Institute.

Beihoffer, T.W., Dorrough, D.S., Schmidt, D.D. 1990. The Development of an Inhibitive Cationic Drilling Fluid for Slim-Hole Coring Applications. SPE 19953 presented at SPE/IADC Drilling Conference in Houston, Texas, USA, February 27 – March 2.

Beihoffer, T.W., Dorrough, D.S., Deem, C.K., Schmidt, D.D., Bray, R.P. 1992. Cationic Polymer Drilling Fluid Can Sometimes Replace Oil-Based Mud. *Oil and Gas Journal,* 90 (11): 42-47.

Blauer, R.E., Mitchell, B.J., Kohlhaas, C.A. 1974. Determination of Laminar, Turbulent, and Transitional Foam Flow Losses in Pipes. SPE 4885 presented at the SPE California Regional Meeting in San Francisco, California, April 4 – 5.

Bol, G.M., Wong, S.W., Davidson, C.J., Woodland, D.C. 1994. Borehole Stability in Shales. *SPE Drilling & Completion*, 9 (02): 87-94.

Borchardt, J.K. 1989. Chapter 10: Cationic Organic Polymer Formation Damage Control Chemical. *Oil-Field Chemistry: Enhanced Recovery and Production Stimulation.* American Chemical Society.

Borysenko, A., Clennell, B., Sedev, R., Burgar, I., Ralston, J., Raven, M., Dewhurst, D., Liu, K. 2009. Experimental Investigations of the Wettability of Clays and Shales. *Journal of Geophysical Research: Solid Earth (1978–2012)*, 114 (B7).

Boutrid, A., Bensehamdi, S., Chaib, R. 2013. Investigation into Brinell Hardness Test Applied to Rocks. *World Journal of Engineering*, 10 (4): 367-380.

Bowker, K.A. 2007. Development of the Barnett Shale Play, Fort Worth Basin. *AAPG Bulletin,* 91 (4).

Brady, M.E., Craster, B., Getliff, J.M., Reid, P.I. 1998. Highly Inhibitive, Low-salinity Glycol Water-base Drilling Fluid for Shale Drilling in Environmentally Sensitive Locations. SPE 46618 presented at the SPE International Conference on Health, Safety, and Environment in Oil and Gas Exploration and Production in Caracas, Venezuela, June 7 – 10.

Braun, C. 2004. Experimental DIDS Initial Assessment Report for SIAM 19. Berlin, Germany, 19-22 October. UNEP Publication.

Breeden, D., Shipman, J. 2004. Shale Analysis for Mud Engineers. AADE-04-DF-HO-30 presented at the AADE 2004 Drilling Fluids Conference in Houston, Texas, April 6 – 7.

Brinell. J.A. 1990. Way of Determining the Hardness of Bodies and Some Applications of the Same. *Teknisk Tidskrift*, 5: 69 – 87.

Britt, L. K., Schoeffler, J. 2009. The Geomechanics of a Shale Play: What Makes a Shale Prospective. SPE 129925 presented at the SPE Eastern Regional Meeting. In Charleston, West Virginia, USA, Sept. 23 – 25.

Brumsack, H.J. 1989. Geochemistry of Recent TOC-rich Sediments from the Gulf of California and the Black Sea. *Geologische Rundschau*, 78 (3), 851-882.

Brunauer, S., Emmett, P.H., Teller, E. 1938. Adsorption of Gases in Multimolecular Layers. *Journal of the American Chemical Society*, 60 (2): 309-319.

Bustin, R.M., Bustin, A., Ross, D., Chalmers, G., Murthy, V., Laxmi, C., Cui, X. 2009. Shale Gas Opportunities and Challenges. *Search and Discovery Articles,* 40382: 20-23.

Cai, J., Chenevert, M.E., Sharma, M.M., Friedheim, J. 2011. Decreasing Water Invasion into Atoka Shale Using Nonmodified Silica Nanoparticles. *SPE Drilling & Completion,* 27 (01): 103 – 112.

Caenn, R., Darley, H.C., Gray, G.R. 2011. *Composition and Properties of Drilling and Completion Fluids*. Waltham, MA, USA: Gulf Professional Publishing.

Cambridge University Engineering Department. 2003. *Materials Data Book*

Chandler, H. (Ed.). 1999. *Hardness Testing*. 2nd edition. ASM International.

Chenevert, M.E. 1970a. Shale Alteration by Water Adsorption. *Journal of Petroleum Technology*, 22 (9): 1141-1148.

Chenevert, M.E. 1970b. Shale Control with Balanced-Activity Oil-Continuous Muds. *Journal of Petroleum Technology,* 22 (10): 1309-1316.

Chenevert, M.E., Dwarakanath, V. 1993. Shale Strength Measurements Using a Penetrometer. *International Journal of Rock Mechanics and Mining Sciences & Geomechanics Abstracts*, 30 (7), 703-706.

Clarkson, C.R., Wood, J., Burgis, S., Aquino, S., Freeman, M. 2012a. Nanopore-Structure Analysis and Permeability Predictions for a Tight Gas Siltstone Reservoir by Use of Low-Pressure Adsorption and Mercury-Intrusion Techniques. *SPE Reservoir Evaluation & Engineering*, 15 (06): 648-661.

Clarkson, C.R., Jensen, J.L., Chipperfield, S. 2012b. Unconventional Gas Reservoir Evaluation: What Do We Have to Consider? *Journal of Natural Gas Science and Engineering,* 8: 9-33.

Clarkson, C.R., Solano, N., Bustin, R.M., Bustin, A.M.M., Chalmers, G.R.L., He, L., Melnichenko, Y.B., Radliński, A.P., Blach, T. P. 2013. Pore Structure Characterization of North American Shale Gas Reservoirs using USANS/SANS, Gas Adsorption, and Mercury Intrusion. *Fuel*, 103: 606-616.

Comisky, J.T., Newsham, K.E., Rushing, J.A., Blasingame, T.A. 2007. A Comparative Study of Capillary-Pressure-Based Empirical Models for Estimating Absolute Permeability in Tight Gas Sands. SPE 110050 presented at the SPE Annual Technical Conference and Exhibition in Anaheim, California, Nov. 11 – 14.

Comisky, J.T., Santiago, M., McCollom, B., Buddhala, A., Newsham, K.E. 2011. Sample Size Effects on the Application of Mercury Injection Capillary Pressure for Determining the Storage Capacity of Tight Gas and Oil Shales. SPE 149432 presented at the Canadian Unconventional Resources Conference in Calgary, Alberta, Canada, November 15 – 17.

Curtis, M.E., Cardott, B.J., Sondergeld, C.H., Rai, C.S. 2012. Development of Organic Porosity in the Woodford Shale with Increasing Thermal Maturity. *International Journal of Coal Geology*, 103: 26-31.

Daigle, H. 2014. Microporosity Development in Shallow Marine Sediments from the Nankai Trough. *Marine Geology*, 357: 293-303.

Daigle, H., Johnson, A., Gips, J.P., Sharma, M. 2014. Porosity Evaluation of Shales Using NMR Secular Relaxation. URTEC 1905272 presented at the Unconventional Resources Technology Conference in Denver, Colorado, USA, August 25 – 27.

Das, P., Achalpurkar, M.P. 2013. Impact of Rock Mechanics and Formation Softening Analysis in Shale Fracturing Fluid Design. SPE 167336 presented at the SPE

Kuwait Oil and Gas Show and Conference in Kuwait City, Kuwait, October 8 – 10.

Davidson, J.A. 1999. Application of Acoustic Measurements in Shale Stability Research. PhD Dissertation. The University of Texas at Austin.

Davis, R.A. 1992. *Depositional Systems: An Introduction to Sedimentology and Stratigraphy*. 2nd ed. Englewood Cliffs, New Jersey: Prentice-Hall.

Designation, A.S.T.M. Standard Hardness Conversion Tables for Metals Relationship among Brinell Hardness, Vickers Hardness, Rockwell Hardness, Superficial Hardness, Knoop Hardness, Scleroscope Hardness, and Leeb Hardness. *ASTM International E140-12b*, 1.

EIA. 2011. Review of Emerging Resources: US Shale Gas and Shale Oil Plays. U.S. Energy Information Administration.

Eissa, E.A., Kazi, A. 1988. Relation between Static and Dynamic Young's Moduli of Rocks. *International Journal of Rock Mechanics and Mining Sciences & Geomechanics Abstracts*, 25 (6): 479-482.

El-Monier, I.A., Nasr-El-Din, H.A. 2011. A Study of Several Environmentally Friendly Clay Stabilizers. SPE 142755 presented at the SPE Project and Facilities Challenges Conference at METS in Doha, Qatar, February 13 – 16.

Ewy, R.T., Stankovich, R.J. 2000. Pore Pressure Change due to Shale-Fluid Interactions: Measurements under Simulated Wellbore Conditions. *Proceedings Pacific Rocks*: 147-154.

Fink, D.H., Thomas, G.W. 1964. X-ray Studies of Crystalline Swelling in Montmorillonites. *Soil Science Society of America Journal*, 28 (6): 747-750.

Fonseca C.F., Chenevert, M.E. The Effect of Total Stress and Temperature on Water Activity of Shales. 1998. Paper USA-829-1 presented at the 3rd North American Rock Mechanic Symposium in Cancun, Quintana Roo, Mexico, June 3 – 5.

Foster, W.R., Savins, J.G., Waite, J.M. 1954. Lattice Expansion and Rheological Behavior Relationships in Water-Montmorillonite Systems. *Clays and Clay Minerals*, 3: 296-316.

Freedman, R., Heaton, N., Flaum, M., Hirasaki, G.J., Flaum, C., Hürlimann, M. 2003. Wettability, Saturation, and Viscosity from NMR Measurements. *SPE Journal*, 8 (04), 317-327.

Freeze, R.A., Cherry, J.A. 1979. *Groundwater*. Englewood Cliffs, New Jersey: Prentice-Hall.

Friehauf, K.E., Sharma, M.M. Fluid Selection for Energized Hydraulic Fractures. SPE 124361 presented at the SPE Annual Technical Conference and Exhibition in New Orleans, Louisiana, October 4 – 7.

Gazaniol, D., Forsans, T., Boisson, M.J.F., Piau, J.M. 1995. Wellbore Failure Mechanisms in Shales: Prediction and Prevention. *Journal of Petroleum Technology*, 47 (07): 589-595.

Geertsma, J. 1985. Some Rock-mechanical Aspects of Oil and Gas Well Completions. *Society of Petroleum Engineers Journal*, 25 (06): 848-856.

Gercek, H. 2007. Poisson's Ratio Values for Rocks. *International Journal of Rock Mechanics and Mining Sciences*, 44 (1): 1-13.

Ghorbani, A., Zamora, M., Cosenza, P. 2009. Effects of Desiccation on the Elastic Wave Velocities of Clay-Rocks. *International Journal of Rock Mechanics and Mining Sciences*, 46 (8): 1267-1272.

Gidley, J.L., Holditch, S.A., Nierode, D.E., Veatch, R.W. 1989. *Recent Advances in Hydraulic Fracturing*. SPE Monograph Series, Volume 12. Richardson, TX: Society of Petroleum Engineers.

Grape, S.G. 2006. Technology-Based Oil and Natural Gas Plays: Shale Shock! Could There Be Billions in the Bakken. *DOE Energy Information Administration Series*.

Grim, R.E. 1968. *Clay Mineralogy*. 2nd edition. New York: McGraw Hill Book Co.

Groat, C.G., Grimshaw, T.W. 2012. Fact-Based Regulation for Environmental Protection in Shale Gas Development. The Energy Institute, the University of Texas at Austin.

Groen, J.C., Peffer, L.A., Pérez-Ramírez, J. 2003. Pore Size Determination in Modified Micro-and Mesoporous Materials. Pitfalls and Limitations in Gas Adsorption Data Analysis. *Microporous and Mesoporous Materials*, 60 (1): 1-17.

Gulbis, J, Hodge, R.M. 2000. Chapter 7: Fracturing Fluid Chemistry and Proppants. *Reservoir Stimulation*. 3rd edition. New York, NY: Wiley.

Gupta, A. 1987. A Model for Estimating Formation Damage in Hydrocarbon Reservoirs Containing Swelling Clays. Master's Thesis. The University of Texas at Austin.

Hale, A.H., Mody, F.K., Salisbury, D.P. 1993. Experimental Investigation of the Influence of Chemical Potential on Wellbore Stability. *SPE Drilling and Completion,* 8 (3), 207-216.

Handwerger, D.A., Willberg, D.M., Pagels, M., Rowland, B., Keller, J. 2012. Reconciling Retort versus Dean Stark Measurements on Tight Shales. SPE 159976 presented at the SPE Annual Technical Conference and Exhibition in San Antonio, Texas, USA, October 8 – 10.

Harkins, W.D., Jura, G. 1944. Surfaces of Solids. XIII. A Vapor Adsorption Method for the Determination of the Area of a Solid without the Assumption of a Molecular Area, and the Areas Occupied by Nitrogen and other Molecules on the Surface of a Solid. *Journal of the American Chemical Society*, 66 (8): 1366-1373.

Harper, J. 2011 Activity and Potential of the Utica Shale in Pennsylvania. Pennsylvania Geological Survey.

Hendricks, S.B., Nelson, R.A., Alexander, L.T. 1940. Hydration Mechanism of the Clay Mineral Montmorillonite Saturated with Various Cations. *Journal of the American Chemical Society*, 62 (6): 1457-1464.

Hester, T.C., Schmoker, J.W., Sahl, H.L. 1990. Log-Derived Regional Source-Rock Characteristics of the Woodford Shale, Anadarko Basin, Oklahoma. U.S. Geological Survey.

Himes, R.E., Vinson, E.F. 1989. Fluid Additive and Method for Treatment of Subterranean Formations. U.S. Patent 4,8,42,073, June 27.

Hodge, R. 2011. Crosslinked and Linear Gel Composition. HF Study Technical Workshop: Chemical and Analytical Methods.

Horton, A.I., Mercer, J.C., Sawyer, W. K. 1982. Infill Drilling for Shale Gas Development: A Field Case Study. SPE 11182 presented at the 57th Annual Technical Conference and Exhibition in New Orleans, Louisiana, Sept. 26 – 29.

http://www.eia.gov/oil_gas/rpd/shale_gas.pdf

Hughes, D.S., Jones, H.J. 1950. Variation of Elastic Moduli of Igneous Rocks with Pressure and Temperature. *Geological Society of America Bulletin,* 61 (8): 843-856.

Huitt, J.L., McGlothlin Jr, B.B. 1958. The Propping of Fractures in Formations Susceptible to Propping-Sand Embedment. *Drilling and Production Practice*: 115-123.

Inamdar, A., Malpani, R., Atwood, K., Brook, K., Erwemi, A., Ogundare, T., Purcell, D. 2010. Evaluation of Stimulation Techniques Using Microseismic Mapping in the Eagle Ford Shale. SPE 136873 presented at the SPE Tight Gas Completions Conference in San Antonio, Texas, USA, November 2 – 3.

International Energy Agency. 2012. World Energy Outlook.

Jacobs, T. 2014. Shale Revolution Revisits the Energized Fracture. *Journal of Petroleum Technology*, 66: 48-56.

Javadpour, F. 2009. Nanopores and Apparent Permeability of Gas Flow in Mudrocks (Shales and Siltstone). *Journal of Canadian Petroleum Technology*, 48 (8), 16-21.

Javadpour, F., Moravvej Farshi, M., Amrein, M. 2012. Atomic-Force Microscopy: A New Tool for Gas-Shale Characterization. *Journal of Canadian Petroleum Technology*, 51 (4): 236-243.

Jenkyns, H.C. 2010. Geochemistry of Oceanic Anoxic Events. *Geochemistry, Geophysics, Geosystems*, 11 (3).

Jones, L.E., Wang, H. F. 1981. Ultrasonic Velocities in Cretaceous Shales from the Williston Basin. *Geophysics,* 46 (3): 288-297.

Josh, M., Esteban, L., Delle Piane, C., Sarout, J., Dewhurst, D.N., Clennell, M.B. 2012. Laboratory Characterisation of Shale Properties. *Journal of Petroleum Science and Engineering*, 88: 107-124.

Jung, C.M., Zhang, R., Chenevert, M.E., Sharma, M.M. 2013a. High-Performance Water-Based Mud Using Nanoparticles for Shale Reservoirs. SPE 168799/URTeC 1581549 presented at the Unconventional Resources Technology Conference in Denver, Colorado, USA, August 12 – 14.

Jung, C.M., Zhou, J., Chenevert, M.E., Sharma, M.M. 2013b. The Impact of Shale Preservation on the Petrophysical Properties of Organic-Rich Shales. SPE 166419 presented at the SPE Annual Technical Conference and Exhibition. Society of Petroleum Engineers in New Orleans, Louisiana, USA, Sep. 30 – Oct. 2.

Kaarsberg, E.A. 1959. Introductory Studies of Natural and Artificial Argillaceous Aggregates by Sound-Propagation and X-ray Diffraction Methods. *The Journal of Geology*, 67 (4): 447-472.

Kearns, T.J. 2011. Chemostratigraphy of the Eagle Ford formation. Master's Thesis. UT-Arlington.

King, H. 2011. Utica Shale – The Natural Gas Giant below the Marcellus. http://geology.com/articles/utica-shale/

Kirschbaum, M.A., Schenk, C., Cook, T.A., Ryder, R.T., Charpentier, R.R., Klett, T.R., Gaswirth, S.B., Tennyson, M.E., Whidden, K.J. 2012. Assessment of Undiscovered Oil and Gas Resources of the Ordovician Utica Shale of the Appalachian Basin Province, 2012. *US Geological Survey Fact Sheet*, *3116*.

Kleinberg, R.L. 1999. Nuclear Magnetic Resonance. *Experimental Methods in the Physical Sciences,* 35: 337-385.

Kaiser, B. 2013. Photon Physics in Geology. Presentation Slides for XRF Instrument Training.

Kargbo, D.M., Wilhelm, R.G., Campbell, D.J. 2010. Natural Gas Plays in the Marcellus Shale: Challenges and Potential Opportunities. Environmental Science & Technology, 44 (15): 5679-5684.

Kuila, U., Prasad, M. 2013a. Application of Nitrogen Gas-Adsorption Technique for Characterization of Pore Structure of Mudrocks. *The Leading Edge,* 32 (12): 1478-1485.

Kuila, U., Prasad, M. 2013b. Specific Surface Area and Pore-size Distribution in Clays and Shales. *Geophysical Prospecting*, 61 (2): 341-362.

Kumar, V., Sondergeld, C.H., Rai, C.S. 2012. Nano to Macro Mechanical Characterization of Shale. SPE 159804 presented at the SPE Annual Technical Conference and Exhibition in San Antonio, Texas, October 8 – 10.

Kurz, B.A., Schmidt, D.D., Cortese, P.E. 2013. Investigation of Improved Conductivity and Proppant Applications in the Bakken Formation. SPE 163849 presented at the SPE Hydraulic Fracturing Technology Conference in The Woodlands, Texas, USA, February 4 – 6.

Kuuskraa, V.A., Koperna, G., Schmoker, J.W., Quinn, J.C. 1998. Barnett Shale Rising Star in Fort Worth Basin. *Oil and Gas Journal*, 96: 67-76.

Labani, M.M., Rezaee, R., Saeedi, A., Al Hinai, A. 2013. Evaluation of Pore Size Spectrum of Gas Shale Reservoirs using Low Pressure Nitrogen Adsorption, Aas Expansion and Mercury Porosimetry: A case study from the Perth and Canning Basins, Western Australia. *Journal of Petroleum Science and Engineering*, 112: 7-16.

Lake, L.W. 1989. *Enhanced Oil Recovery*. Old Tappan, NJ; Prentice Hall Inc.

Loucks, R.G., Reed, R.M., Ruppel, S.C., Jarvie, D.M. 2009. Morphology, Genesis, and Distribution of Nanometer-scale Pores in Siliceous Mudstones of the Mississippian Barnett Shale. *Journal of Sedimentary Research*, 79 (12): 848-861.

Madsen, F.T., Müller-Vonmoos, M. 1989. The Swelling Behaviour of Clays. *Applied Clay Science*, 4 (2): 143-156.

Manohar, L. 1999. Shale Stability: Drilling Fluid Interaction and Shale Strength. SPE 54356 at the SPE Asia Pacific Oil and Gas Conference and Exhibition in Jakarta, Indonesia, April 20 – 22.

Marsala, A.F., Loermans, T., Shen, S., Scheibe, C., Zereik, R. 2012. Portable Energy-Dispersive X-Ray Fluorescence Integrates Mineralogy and Chemostratigraphy into Real-Time Formation Evaluation. *Petrophysics,* 53 (2): 102-109.

Mason, G. (1983). A Model of Adsorption-Desorption Hysteresis in Which Hysteresis is Primarily Developed by the Interconnections in a Network of Pores. *Proceedings of the Royal Society of London. A. Mathematical and Physical Sciences*, 390 (1798), 47-72.

Mody, F.K., Tare, U.A., Tan, C.P., Drummond, C.J., Wu, B. 2002. Development of Novel Membrane Efficient Water-Based Drilling Fluids through Fundamental understanding of Osmotic Membrane Generation in Shales. SPE 77447 presented at the SPE Annual Technical Conference and Exhibition in San Antonio, Texas, Sept. 29 – Oct 2.

Moran, L.M. 2012. High Resolution Geochemistry of The Cretaceous Eagle Ford Shale, Bee County, Texas. Master's Thesis. UT-Arlington

Muradov, A., Rowell, J., Jellison, M.J., Brock, J.N., Morgan, D. 2013. Shale Play Drilling Challenges: Case Histories and Lessons Learned. SPE/IADC 163447 presented at the SPE/IADC Drilling Conference and Exhibition in Amsterdam, the Netherlands, March 5 – 7.

Myers, R. 2008. Marcellus Shale Update. Independent Oil & Gas Association of West Virginia.

Nikhanj, M., Horvat, R., Surbey, G., Ljubojevic, A. 2014. Tap Into the Source. Utica Shale: Penn State Webinar.

Norrish, K. 1954. The Swelling of Montmorillonite. *Discuss. Faraday Soc.*, 18: 120-134.

Jarvie, D.M., Hill, R.J., Ruble, T.E., Pollastro, R.M. 2007. Unconventional Shale-Gas Systems: The Mississippian Barnett Shale of North-Central Texas as One Model for Thermogenic Shale-Gas Assessment. *AAPG Bulletin*, 91 (4): 475–499.

O'Brien, D.E., Chenevert M.E. 1973. Stabilizing Sensitive Shales with Inhibited, Potassium-Based Drilling Fluids. *Journal of Petroleum Technology*, 25 (9): 1089-1100.

O'Brien, D. 2013. Longest Lateral: Consol Innovates Efficiencies. *The Business Journal*. Nov. 16.

Odusina, E.O., Sondergeld, C.H., Rai, C.S. 2011. NMR Study of Shale Wettability. SPE 147371 presented at the Canadian Unconventional Resources Conference in Calgary, Alberta, Canada, November 15 – 17.

Olesen, N.L. 2010. Bakken Oil Resource Play Williston Basin (US) Overview and Historic Perspective.

Osisanya, S.O. 1991. Experimental Studies Of Wellbore Stability in Shale Formations. Ph.D Dissertation. The University of Texas at Austin.

Ozen, A.E., Sigal, R.F. 2013. T_1/T_2 NMR Surface Relaxation Ratio for Hydrocarbons and Brines in Contact with Mature Organic-Shale Reservoir Rocks. *Petrophysics*, 54 (01), 11-19.

Padhy, G.S., Lemaire, C., Amirtharaj, E.S., Ioannidis, M.A. 2007. Pore Size Distribution in Multiscale Porous Media as Revealed by DDIF–NMR, Mercury Porosimetry and Statistical Image Analysis. *Colloids and Surfaces A: Physicochem. Eng. Aspects,* 300 (1): 222–234.

Passey, Q.R., Bohacs, K.M., Esch, W.L., Klimentidis, R., Sinha, S. 2010. From Oil-Prone Source Rock to Gas-Producing Shale Reservoir – Goelogic and Petrophysical Characterization of Unconventional Shale-Gas Reservoirs. SPE 131350 presented at the CPS/SPE International Oil & Gas Conference and Exhibition in China held in Beijing, China, June 8 – 10.

Patel, A., Thaemlitz, C.J., McLaurine, H.C., Stamatakis, E. 1999. Drilling Fluid Additive and Method for Inhibiting Hydration. U.S. Patent 5,908,814, June 1.

Patel, A.D. 2009. Design and Development of Quaternary Amine Compounds: Shale Inhibition with Improved Environmental Profile. SPE 121737 presented at the SPE International Symposium on Oilfield Chemistry in The Woodlands, TX, April 20 – 22.

Pedlow, J.W. 2013. A Study of the Effect of Stress and Fluid Sensitivity on Propped Fracture Conductivity in Preserved Reservoir Shales. Master's Thesis. The University of Texas at Austin.

Pedlow, J., Sharma, M. 2014. Changes in Shale Fracture Conductivity due to Interactions with Water-Based Fluids. SPE 168586 presented at the SPE Hydraulic Fracturing Technology Conference in The Woodlands, Texas, USA, February 4 – 6.

Piroozian, A., Ismail, I., Yaacob, Z., Babakhani, P., Ismail, A.S.I. 2012. Impact of Drilling Fluid Viscosity, Velocity and Hole Inclination on Cuttings Transport in Horizontal and Highly Deviated Wells. *Journal of Petroleum Exploration and Production Technology*, 2 (3), 149-156.

Popp, N. G. 2004. Acoustic Properties of Shale with Variant Water Activity. Master's Thesis. The University of Texas at Austin.

Pruett, J.O. 1987. A Potassium-Base Derivative of Humic Acid Proves Effective in Minimizing Wellbore Enlargement in the Ventura Basin. SPE/IADC 16080 presented at the SPE/IADC Drilling Conference in New Orleans, LA, March 15 – 18.

Quintero, L. 2002. An Overview of Surfactant Applications in Drilling Fluids for the Petroleum Industry. *Journal of Dispersion Science and Technology*, 23 (1-3), 393-404.

Ravikovitch, P.I., Neimark, A.V. 2002. Experimental Confirmation of Different Mechanisms of Evaporation from Ink-bottle Type Pores: Equilibrium, Pore Blocking, and Cavitation. *Langmuir*, 18 (25): 9830-9837.

Remvik, F., Skalle, P. 1993. Shale-Fluid Interaction under Simulated Downhole Conditions, and its Effect on Borehole Stability. *International Journal of Rock Mechanics and Mining Sciences & Geomechanics Abstracts*, 30 (7): 1115-1118.

Ribeiro, L.H.N. 2013. Development of a Three-dimensional Compositional Hydraulic Fracturing Simulator for Energized Fluids. PhD Dissertation. The University of Texas at Austin.

Rickman, R., Mullen, M., Petre, E., Grieser, B., Kundert, D. 2008. A Practical Use of Shale Petrophysics for Stimulation Design Optimization - All Shale Plays are not Clones of the Barnett Shale. SPE 115258 presented at the SPE Annual Technical Conference and Exhibition in Denver, Colorado, USA, September 21 – 24.

Robinson, R.A., Sinclair, D.A. 1934. The Activity Coefficients of the Alkali Chlorides and of Lithium Iodide in Aqueous Solution from Vapor Pressure Measurements. *J. Am. Chem. Soc.*, 56 (9), 1830-1835.

Robinson, R.A., Stokes, R.H. 1959. *Electrolyte Solutions*. 2nd ed. London: Butterworths Scientific Publications.

Rouquerol, J., Rouquerol, F., Llewellyn, P., Maurin, G., Sing, K.S. 2014. *Adsorption by Powders and Porous Solids: Principles, Methodology and Applications*. Oxford, UK: Academic Press.

Rowe, H., Hughes, N., Robinson, K. 2012. The Quantification and Application of Handheld Energy-Dispersive X-ray Fluorescence in Mudrock Chemostratigraphy and Geochemistry. *Chem. Geol.*, 324: 122-131.

Ruessink, S.H., Harville, D.G., 1992. Quantitative Analysis of Bulk Mineralogy: The Applicability and Performance of XRD and FTIR. SPE 23828 presented at the SPE International Symposium on Formation Damage Control in Lafayette, Louisiana, February 26-27.

Rylander, E., Singer, P., Jiang, T., Lewis, R., Mclin, R.H., Sinclair, S. 2013. NMR T_2 Distributions in the Eagle Ford Shale: Reflections on Pore Size. SPE 164554 presented at the SPE Unconventional Resources Conference in the Woodlands, Texas, USA, April 10 – 12.

Sandler, S.I. 2006. *Chemical, Biochemical, and Engineering Thermodynamics.*4th edition. Hoboken, NJ: John Wiley & Sons.

Santarelli, F.J., Detienne, J.L., Zundel, J.P. 1991. The Use of a Simple Index Test in Petroleum Rock Mechanics. ARMA 91-647 presented at the The 32nd US Symposium on Rock Mechanics (USRMS) in Norman, Oklahoma, July 10 – 12.

Santos, H.M. 1997. A New Conceptual Approach to Shale Stability. PhD Dissertation. The University of Oklahoma.

Schein, G. 2005. The Application and Technology of Slickwater Fracturing. SPE Distinguished Lecturer Series.

Schlumberger. 1990. Drilling Fluids for Horizontal Wells. *Oilfield Review,* 2 (3), 8-10.

Schlemmer, R., Friedheim, J.E., Growcock, F.B., Bloys, J.B., Headley, J.A., Polnaszek, S.C. 2003. Chemical Osmosis Shale and Drilling Fluids. *SPE Drilling & Completion*, 18 (4): 318-331.

Schmitt, M., Fernandes, C.P., da Cunha Neto, J.A., Wolf, F.G., dos Santos, V. S. 2013. Characterization of Pore Systems in Seal Rocks using Nitrogen Gas Adsorption Combined with Mercury Injection Capillary Pressure Techniques. *Marine and Petroleum Geology*, 39 (1): 138-149.

Schuster, G. 2007. Basics of Seismic Wave Theory. University of Utah.

Sensoy, T., Chenevert, M.E., Sharma, M.M. 2009. Minimizing Water Invasion in Shales Using Nanoparticles. SPE 124429 presented at the Annual Technical Conference and Exhibition in New Orleans, Louisiana, October 4 – 7.

Sharma, M.M. 2004. Near Wellbore Problems. PGE 383 notes. The University of Texas at Austin.

Sigal, R.F. 2013. Mercury Capillary Pressure Measurements on Barnett Core. *SPE Reservoir Evaluation & Engineering*, 16 (4): 432-442.

Sing, K.S.W., Everett, D.H., Haul, R.A.W., Moscou, L., Pierotti, R.A., Rouquérol, J., Siemieniewska, T. 1985. Reporting Physisorption Data for Gas/Solid Systems with Special Reference to the Determination of Surface Area and Porosity (Recommendations 1984). *Pure and Applied Chemistry*, 57 (4): 603-619.

Smith, K.W. 2003. Treating Shale and Clay in Hydrocarbon Producing Formations. U.S. Patent 6,502,637, Jan. 7.

Soeder, D.J. 1988. Porosity and Permeability of Eastern Devonian Gas Shale. *Society of Petroleum Engineers Formation Evaluation*, 3 (2): 116-124.

Sondergeld, C.H., Newsham, K.E., Comisky, J.T., Rice, M.C., Rai, C.S. 2010. Petrophysical Considerations in Evaluating and Producing Shale Gas Resources. SPE 131768 presented at the SPE Unconventional Gas Conference in Pittsburgh, Pennsylvania, USA, February 23 – 25.

Starks, P.H. 2003. Horizontal Drilling – A Global Perspective, T. R. Carr, E. P. Mason, and C. T. Feazel, eds., *Horizontal Wells: Focus on the Reservoir: AAPG Methods in Exploration,* No. 14: 1-7.

Stegent, N.A., Ingram, S.R., Callard, J.G. 2011. Hydraulic Fracture Stimulation Design Considerations and Production Analysis. SPE 139981 presented at the SPE Hydraulic Fracturing Technology Conference in the Woodlands, Texas, USA, Jan. 24 – 26.

Steiger, R.P., Leung, P.K. 1992. Quantitative Determination of the Mechanical Properties of Shales. *SPE Drilling Engineering*, 7 (3): 181-185.

Stenson, J.D., Sharma, M.M. 1989. A Petrophysical Model for Shaly Sands. SPE 19574 presented at the SPE Annual Technical Conference and Exhibition in San Antonio, Texas, October 8 – 11.

Straley, C., Roosini, D., Vinegar, H.J., Tutunjian, P., Morriss, C.E. 1997. Core Analysis by Low-field NMR. *Log Analyst*, 38 (2): 84-94.

Szwedzicki, T. 1998. Indentation Hardness Testing of Rock. *International Journal of Rock Mechanics and Mining Sciences*, 35 (6): 825-829.

Trembath, A., Jenkins, J., Nordhaus, T., Shellenberger, M. 2012. Where the Shale Gas Revolution Came From – Government's Role in the Hydraulic Fracturing of Shale. The Breakthrough Institute, Oakland.

Tutuncu, A.N. 1992. Velocity Dispersion and Attenuation of Acoustic Waves in Granular Sedimentary Media. PhD Dissertation. The University of Texas at Austin.

Tutuncu, A.N., Sharma, M.M. 1992a. Relating Static and Ultrasonic Laboratory Measurements to Acoustic Log Measurements in Tight Gas Sands. SPE 24689 presented at the SPE Annual Technical Conference and Exhibition in Washington, DC, Oct. 4 – 7.

Tutuncu, A.N., Sharma, M.M. 1992b. The Influence of Fluids on Grain Contact Stiffness and Frame Moduli in Sedimentary Rocks. *Geophysics*, 57 (12): 1571-1582.

Van der Vlis, A.C. 1970. Rock Classification by a Simple Hardness Test. *Proc. 2nd Int. Symp. Rock Mech*, 1 (1-19).

Van Oort, E., Hale, A.H., Mody, F.K. 1995. Manipulation of Coupled Osmotic Flows for Stabilisation of Shales Exposed to Water-Based Drilling fluids. SPE 30499 presented at the SPE Annual Technical Conference and Exhibition in Dallas, Texas, Oct. 22 – 25.

Van Oort, E, Hale, A.H., Mody, F.K., Roy, S. 1996. Transport in Shales and the Design of Improved Water Based Shale Drilling Fluids. *SPE Drilling & Completion*, 11 (3): 137-146.

Van Oort, E. 2003. On the Physical and Chemical Stability of Shales. *Journal of Petroleum Science and Engineering*, 38 (3): 213-235.

Vernik, L., Liu, X. 1997. Velocity Anisotropy in Shales: A Petrophysical Study. *Geophysics*, 62 (2): 521-532.

Volk, L.J., Raible, C.J., Carroll, H.B., Spears, J.S. 1981. Embedment of High Strength Proppant into Low-Permeability Reservoir Rock. SPE/DOE 9867 presented at the SPE/DOE Low Permeability Gas Reservoirs Symposium in Denver, Colorado, May 27 – 29.

Wang, F.P., Gale, J.F.W. 2009. Screening Criteria for Shale-Gas Systems. *Gulf Coast Association of Geological Societies Transactions*, 59: 779–793.

Washburn, E.W. 1921. The Dynamics of Capillary Flow. *Physical Review*,17 (3): 273.

Winston, P.W., Bates, D.H. 1960. Saturated Solutions for the Control of Humidity in Biological Research. *Ecology*, 41*:* 232-237.

Wong, R.C.K. 1998. Swelling and Softening Behaviour of La Biche Shale. *Canadian Geotechnical Journal*, 35 (2): 206-221.

Wood, S.G. 2013. Lithofacies, Depositional Environments, and Sequence Stratigraphy of the Pennsylvanian (Morrowan-Atokan) Marble Falls Formation, Central Texas. Master's Thesis. The University of Texas at Austin.

Yale, D. P., Jameison Jr, W. H. 1994. Static and Dynamic Rock Mechanical Properties in the Hugoton and Panoma Fields, Kansas. SPE 27939 presented at the SPE Mid-Continent Gas Symposium in Amarillo, Texas, May 22 – 24.

Yu, M., Chen, G., Chenevert, M.E., Sharma, M.M. 2001. Chemical and Thermal Effects on Wellbore Stability of Shale Formations. SPE 171366 presented at the SPE Annual Technical Conference and Exhibition in New Orleans, Louisiana, September 30 – October 3.

Zhang, J., Chenevert, M. E., AL-Bazali, T., Sharma, M. 2004. A New Gravimetric-Swelling Test for Evaluating Water and Ion Uptake in Shales. SPE 89831 presented at the SPE Annual Technical Conference and Exhibition in Houston, Texas, September 26 – 29.

Zhang, J. 2005. The Impact of Shale Properties on Wellbore Stability. PhD Dissertation. The University of Texas at Austin.

Zhang, J., Al-Bazali, T.M., Chenevert, M.E., Sharma, M.M. 2008. Factors Controlling the Membrane Efficiency of Shales when Interacting with Water-Based and Oil-Based Muds. *SPE Drilling & Completion,* 23 (02): 150-158.

Zhang, J., Rojas, J.C., Clark, D.E. 2008. Stressed Shale Drilling Strategy-Water Activity Design Improves Drilling Performance.

Zhang, J., Ouyang, L., Hill, A.D., Zhu, D. 2014. Experimental and Numerical Studies of Reduced Fracture Conductivity due to Proppant Embedment in Shale Reservoirs. SPE 170775 at the SPE Annual Technical Conference and Exhibition in Amsterdam, The Netherlands, October 27 – 29.

Zhang, Z.Z., Low, P.F. 1989. Relation between the Heat of Immersion and the Initial Water Content of Li-, Na-, and K-montmorillonite. *Journal of Colloid and Interface Science*, 133 (2): 461-472.

Zhou, J., Jung, C.M., Chenevert, M.E., Sharma, M.M. 2013a. Petrophysical Characterization of Organic-Rich Shales: A New Standardized Protocol. ARMA 13-546 presented at the 47th US Rock Mechanics/Geomechanics Symposium in San Francisco, California, USA, June 23 – 26.

Zhou, J., Jung, C.M., Chenevert, M.E., Sharma, M.M. 2013b. A Systematic Approach to Petrophysical Characterization of Organic-Rich Shales in Barnett and Eagle Ford Formations. SPE 168792/URTeC 1581323 presented at the Unconventional Resources Technology Conference in Denver, Colorado, USA, August 12 – 14.

Zhou, J., Jung, C.M., Pedlow, J.W., Chenevert, M.E., Sharma, M.M. 2013c. A New Standardized Laboratory Protocol to Study the Interaction of Organic-Rich Shales

with Drilling and Fracturing Fluids. SPE 166216 presented at the SPE Annual Technical Conference and Exhibition in New Orleans, Louisiana, USA, Sep. 30 – Oct. 2.

Vita

Junhao Zhou was born in Ningbo, China and graduated from Xiaoshi Middle School in 2001. He was awarded a full scholarship by the Ministry of Education, Singapore to pursue high school education in Singapore. He subsequently finished his O-Level and A-Level at the Chinese High School and Raffles Junior College respectively. He came to the U.S. for college in 2006 and graduated with a B.A. degree in Physics from Bard College in May 2009. In the fall of 2009, he joined the Department of Petroleum and Geosystems Engineering at the University of Texas at Austin for his graduate studies.

Permanent email address: junhao.zhou@utexas.edu

This dissertation was typed by the author.